Estimating Turbulence Modeling Uncertainty for Turbomachinery Flows Using Physics-Constrained Eigenspace Perturbations of the Reynolds Stress Tensor

Dissertation
zur
Erlangung des Grades
Doktor-Ingenieur

der
Fakultät für Maschinenbau
der Ruhr-Universität Bochum

von

Marcel Matha

aus Bad Mergentheim

Bochum 2025

Dissertation eingereicht am: 07.03.2025
Tag der mündlichen Prüfung: 04.07.2025
Erstgutachter: Prof. Dr.-Ing. Florian Herbst
Zweitgutachter: Prof. Dr. Heng Xiao

Abstract

The synthesis of RANS (Reynolds-averaged Navier-Stokes) equations and the required modeling of turbulence entails certain uncertainties in CFD (Computational Fluid Dynamics). Currently, engineers employ safety factors to address these uncertainties in turbomachinery design processes, which lead to overly conservative designs and result in missed opportunities to optimize the performance. Therefore, understanding the uncertainties in CFD and establishing methods to analyze the credibility of numerical simulations is crucial to achieve robust designs for future turbomachinery components and to create virtual certification processes.

This cumulative dissertation investigates a framework to account for the uncertainty stemming from the turbulence closure model, a primary source of the overall uncertainty in RANS simulations. Although there are a variety of approaches to assess the uncertainty associated with turbulence models, the appropriate estimation of the epistemic uncertainty inherent in turbulence models is demanding. Therefore, the establishment of a methodology capable of reasonably assessing this model-form uncertainty in the context of RANS-based design of turbomachinery components is a major objective of the present thesis.

The EPF (Eigenspace Perturbation Framework), designed to add physics-constrained perturbations to the eigenspace of the Reynolds stress tensor and provide a systematic approach to quantifying its inherent uncertainty, is implemented in the CFD solver TRACE and evaluated in the scope of this thesis. The current research includes an extensive verification of the numerical implementation as well as a scrutiny of the conceptual idea of the EPF. This thesis proposes enhancements related to the consistency and applicability of the methodology, while exploring its general capabilities and limitations. Additionally, the introduction of machine learning to reduce user-defined input and prevent overly conservative estimations of the turbulence modeling uncertainty is discussed and results are presented. Moreover, the eigenvalue perturbation is applied to the TUDa compressor stage, presenting the first application of the EPF to multi-row turbomachinery flows. Finally, the ability to quantify, analyze and interpret the uncertainties associated with turbulence closure models, provides a valuable starting point for next-generation enhancements in modeling turbulent effects for complex configurations and flow phenomena. Overall, by refining the EPF and critically assessing its capabilities, this dissertation contributes to the development of reliable methods to consider the uncertainties in CFD.

Kurzfassung

Die Reynolds-gemittelten Navier-Stokes (RANS: Reynolds-averaged Navier-Stokes) Gleichungen in Verbindung mit der notwendigen Modellierung von Turbulenz bringen inhärente Unsicherheiten in die numerische Strömungssimulation (CFD: Computational Fluid Dynamics). Gegenwärtig verwenden Ingenieurinnen und Ingenieure Sicherheitsfaktoren, um diese Unsicherheiten im Rahmen von Turbomaschinenauslegungsprozessen zu berücksichtigen. Dies führt jedoch häufig zu konservativen und deshalb suboptimalen Auslegungen, wodurch mögliche Potenziale zur Steigerung der Leistungsfähigkeit ungenutzt bleiben. Es ist daher von entscheidender Bedeutung, die Unsicherheiten der CFD einerseits zu verstehen und andererseits Methoden zu entwickeln, um die Verlässlichkeit numerischer Simulationen analysieren zu können, sodass robuste Designs und virtuelle Zertifizierungsprozesse zukünftiger Turbomaschinenkomponenten ermöglicht werden.

Diese kumulative Dissertation untersucht eine Methodik zur Berücksichtigung von Unsicherheiten, die aus der Modellierung der Turbulenz resultieren. Diese Turbulenzmodellunsicherheit ist eine der wesentlichen Unsicherheiten in RANS-Simulationen. Obwohl es verschiedene Ansätze zur Bewertung der Unsicherheiten in Verbindung mit Turbulenzmodellen gibt, stellt eine adäquate Abschätzung dieser epistemischen Unsicherheiten eine besondere Herausforderung dar. Daher ist die Entwicklung, Bereitstellung und Demonstration einer Methodik, die diese Modellunsicherheiten im Kontext der simulationsgestützten Auslegung von Turbomaschinenkomponenten angemessen bewerten kann, ein zentrales Ziel dieser Arbeit.

Die Eigenraumstörmethode (EPF: Eigenspace Perturbation Framework), welche darauf abzielt, den Eigenraum des Reynoldsspannungstensors innerhalb physikalisch motivierter Grenzen zu modifizieren, stellt einen systematischen Ansatz zur Quantifizierung der inhärenten Unsicherheiten von Turbulenzmodellen dar. Diese Methode wird im Rahmen dieser Arbeit in den Strömungslöser TRACE implementiert und evaluiert. Die vorliegende Forschung umfasst eine umfangreiche Verifikation der numerischen Implementierung sowie eine kritische Untersuchung des konzeptionellen Ansatzes der Eigenraumstörmethode. Diese Dissertation enthält dabei Verbesserungen der Methodik in Bezug auf Konsistenz und Anwendbarkeit, während die Vor- und Nachteile kritisch analysiert werden. Darüber hinaus wird der Einsatz von Methoden des maschinellen Lernens im Kontext der Unsicherheitsquantifizierung untersucht, um die Störung des Reynoldsspannungstensors zu automatisieren und gleichzeitig konservativen Unsicherheitsabschätzungen vorzubeugen. Die Störung der Eigenwerte des Reynoldsspannungstensors wird zudem auf die TUDa-Verdichterstufe angewendet, was die erste Anwendung dieser Methodik auf eine derartige mehrreihige Turbomaschinenkonfiguration darstellt. Letztendlich stellt die Fähigkeit, die mit Turbulenzmodellen verbundenen Unsicherheiten zu quantifizieren, zu analysieren und zu interpretieren, ebenfalls einen wertvollen Ausgangspunkt für zukünftige Weiterentwicklungen von Turbulenzmodellen dar. Diese Dissertation leistet einen wichtigen Beitrag zur Entwicklung zuverlässiger Methoden für die Berücksichtigung von Unsicherheiten in der numerischen Strömungssimulation, insbesondere durch die Modifikationen der Eigenraumstörmethode, aber auch durch die kritische Auseinandersetzung mit der Methodik selbst.

Preface and acknowledgments

This dissertation was developed during my time as a research associate in the Department of Numerical Methods at the Institute of Propulsion Technology of the German Aerospace Center (DLR). The journey of completing this work was both enriching and challenging, and I owe my gratitude to many individuals and institutions who supported me throughout this process.

First and foremost, I would like to express my sincere thanks to Prof. Dr. Florian Herbst for taking on the supervision of my doctoral thesis. His determined guidance, readiness to provide assistance, and valuable insights were pivotal in the successful completion of this work. Furthermore, my thanks are extended to Prof. Dr. Heng Xiao, who kindly agreed to act as the co-referee during uncertain times. His willingness to engage in discussions and provide constructive feedback whenever needed is greatly appreciated.

The presented research was supported by multiple internal and external projects and partners. I gratefully acknowledge the insightful collaborations and funding provided by the internal DLR projects under the leadership of Robin G. Brakmann. Additionally, this research was based on a project funded by MTU Aero Engines AG and the German Federal Ministry for Economic Affairs and Climate Action under the funding code 03EE5041A.

I am deeply indebted to Dr. Edmund Kügeler for his trust in my work, his unwavering support, his confidence and his commitment to shielding me when circumstances demanded it.

The Department of Numerical Methods deserves special recognition for its exceptional researching environment. From my very first day, I experienced an atmosphere characterized by openness, determination and mutual support. This collegiality, paired with a shared drive for excellence in research, has been immensely inspiring.

I would like to extend my heartfelt thanks to my group leader and closest advisor in matters of this dissertation, Dr. Christian Morsbach. His constant availability, thoughtful advice and readiness to engage in close collaboration have been invaluable. Working and researching alongside him was a source of growth.

My time at DLR would not have been the same without my colleagues Dr. Michael Bergmann, Felix Möller, Dr. Daniel Schlüß and Pierre Sivel, who became true friends. Together, we shared not only the challenges of work but also countless memorable moments outside of it. The bonds of our friendship formed during this period turned it into an unforgettable and truly remarkable experience, one that will be cherished forever.

Like most doctoral journeys, mine was marked by its share of highs and lows, both professionally and personally. In these moments, the unwavering support of my family has been indispensable. My heartfelt gratitude goes to my parents, Angelika and Gerhard Matha, who made it possible for me to study after leaving school at the University of Stuttgart and who have always believed in me and will continue to do so.

Finally, I want to express my deepest thanks to my wife, Vivian Matha. She stood by my side through every high and low of this journey, offering her unyielding support and ensuring that I had the space and peace needed to focus on my research. Her presence and encouragement, particularly in moments of doubts, made all the difference. This thesis owes much to her love and partnership.

Oberzissen, March 2025 Marcel Matha

Contents

1. Introduction **1**
1.1. Motivation and background 1
1.2. Research objectives 5
1.3. Structure and content 6
1.4. Contributions 8
1.4.1. Research contribution 8
1.4.2. Article contribution statement 9

2. Uncertainties in CFD **11**
2.1. Uncertainties vs. errors 11
2.2. Aleatoric vs. epistemic uncertainties 12

3. Turbulence closures and uncertainties **15**
3.1. Statistical turbulence modeling 15
3.2. Origin of uncertainties in RANS turbulence models 17
3.3. Closure via linear eddy viscosity assumption 20
3.4. Need for quantifying the intrinsic uncertainties in RANS models 21
3.5. Estimating uncertainty with the Reynolds stress tensor perturbations . . . 22
3.5.1. Overview of the fundamental concept and physical rationale of the EPF 22
3.5.2. Demonstration of the core functionality and credibility of the Eigenspace Perturbation Framework (EPF) 26
3.5.3. Literature review of the applications of the eigenspace perturbations and their fundamentals 31
3.5.4. Details on the implementation in TRACE 32

4. Evaluation of physics-constrained data-driven methods for turbulence model uncertainty quantification **37**
4.1. Introduction 37
4.2. Details of the Eigenspace Perturbation Framework 39
4.2.1. Motivation and goal 39
4.2.2. Data-free approach 40
4.2.3. Data-driven approach 41
4.2.4. Integration of UQ computation in CFD solver suite TRACE 44
4.2.5. Data sets for training, testing and applying the machine learning model 47
4.3. Hyperparameter selection based on generalization study 51
4.4. Verification of trained machine learning model 52
4.5. Application of UQ perturbation framework 58
4.6. Conclusion & outlook 62
4.A. Mathematical effect of the moderation factor f in case of pure eigenvalue perturbation 64

5. Improved self-consistency of the Reynolds stress tensor eigenspace perturbation for uncertainty quantification 67
5.1. Introduction . . . 67
5.2. Reynolds stress tensor perturbation to estimate uncertainties . . . 69
  5.2.1. Reynolds stress anisotropy and visualization . . . 69
  5.2.2. Perturbation of eigenspace representation . . . 71
  5.2.3. Self-consistent formulation of perturbation . . . 74
  5.2.4. Application to plane turbulent channel flow . . . 79
5.3. Conclusion & outlook . . . 82
5.A. Properties of the sum of two tensors featuring identical eigenvectors in terms of eigenspace . . . 82
5.B. Transferability of definiteness with respect to the sum of two positive semi-definite tensors . . . 83
5.C. Interpolation properties of two scaled tensor with respect to its location in barycentric coordinates . . . 83
5.D. Example tensors used in this paper . . . 84

6. Physically constrained eigenspace perturbation for turbulence model uncertainty estimation 85
6.1. Introduction . . . 85
6.2. Accounting for turbulence modeling uncertainty using the tensor perturbation framework . . . 87
  6.2.1. Eigenvalue perturbation . . . 89
  6.2.2. Eigenvector perturbation . . . 90
6.3. Adherence to realizable Reynolds stress tensors and realizable Reynolds stress tensor dynamics . . . 91
  6.3.1. Insights from the Reynolds stress tensor's eigenspace perturbation and implications for turbulent boundary layers . . . 91
  6.3.2. Simplified derivation of realizable eigenvector perturbation dynamics for wall-bounded flows . . . 93
  6.3.3. *A posteriori* validation of the suggested constraint on the eigenvector perturbation . . . 95
6.4. Application of physically constrained eigenvector perturbation . . . 96
6.5. Conclusion & outlook . . . 101
6.A. Rotation properties of eigenvector permutation . . . 101
6.B. Schematics of converging-diverging flow example . . . 103
6.C. Instability introduced by former eigenvector permutation . . . 103

7. Advanced methods for assessing flow physics of the TU Darmstadt compressor stage: Uncertainty quantification of RANS turbulence modeling 105
7.1. Introduction . . . 105
7.2. Eigenspace perturbation method . . . 107
7.3. TUDa-GLR-OpenStage compressor . . . 109
  7.3.1. Test case description . . . 109
  7.3.2. CFD setup . . . 109
  7.3.3. Creating uncertainty estimates based on Reynolds stress tensor perturbation . . . 112
7.4. Turbulence model uncertainty for a multi-row compressor application . . . 113
  7.4.1. Perturbation magnitude and effect on anisotropy . . . 113
  7.4.2. Overall compressor performance . . . 114
  7.4.3. Details on local flow physics . . . 115

7.4.4. Effect of anisotropy on turbulent kinetic energy level 123
7.4.5. Shock-boundary layer interaction 124
7.4.6. Capabilities and limitations of the EPF 125
7.5. Conclusion 126

8. Discussion 127
8.1. Methodological coherence and development across publications 127
8.2. Summary of the research findings 128
8.2.1. Additional six perturbed simulations required and effects on attainable solution space for Quantity of Interest (QoI) 129
8.2.2. Convergence issues and their consequences 130
8.2.3. Local vs. non-local perturbations and derived insights for the turbulence modeling community 131
8.2.4. Eigenspace perturbation and its effect on the turbulence production 132

9. Conclusions and outlook 135
9.1. Conclusions 135
9.2. Outlook 136

Nomenclature 139

List of figures 145

List of tables 151

Bibliography 153

A. RANS equations implemented and solved within this thesis 165

B. Relationship between the turbulence production and the eigenspace of the Reynolds stress tensor 167

C. Physical rationale of the eigenspace perturbations of the Reynolds stress tensor 169
C.1. Eigenvalue perturbation 169
C.2. Eigenvector perturbation 170

1. Introduction

1.1. Motivation and background

As turbomachinery is integral to both the aviation and energy sector, its future designs are intrinsically linked to the challenges posed by the global climate change. The European Green Deal, which aims to make Europe the first climate-neutral continent by 2050, significantly impacts the turbomachinery industry [37]. It necessitates a massive decarbonization, as well as the reduction of non-carbon emissions. Although the world's energy consumption is expected to remain at a high level until 2050, the energy sector is striving to meet the ambitious goal of achieving climate neutrality (net-zero greenhouse gas emissions) by the year 2050 primarily by exploiting renewable energy sources [67]. Nevertheless, there will be a demand for highly flexible storage technology to compensate for fluctuations in electricity production. As turbomachinery components provide such scalable and flexible power generation from various sources, the turbomachinery industry can contribute to the development of the next generation, efficient engines for future energy supply, alongside all efforts in sustainable energy solutions. At the same time, the aviation sector faces a parallel challenge, with global air traffic expected to continue growing, potentially leading to a devastating exponential increase in CO_2 emissions [43, 26]. Therefore, the aviation industry is exploring new strategies such as the electrification of the propulsion system and evaluating the potential of alternative fuels like hydrogen or Sustainable Aviation Fuels (SAF). In addition to low-emission propulsion systems, there is a persistent need for innovations that improve fuel efficiency and performance flexibility. Both inevitably contribute to reducing direct and indirect greenhouse gas emissions and making turbomachinery more sustainable. The Original Equipment Manufacturers (OEMs) of the propulsion systems have to address these requirements through advanced concepts, such as multi-shaft engines, variable cycle engines, ultra-high bypass engines, open rotor concepts and last but not least the usage of intercoolers or recuperators.

To create and assess such drastic conceptual changes of future turbomachinery designs, digitalization is supposed to be a catalyst, significantly accelerating these developments. The German Aerospace Center (DLR) aligns its strategy when aiming for efficient next generation designs by positioning itself as a virtual OEM [26]. Unlike past technology developments, which often relied on experimental testing and extensive expert knowledge, computer-based simulations have already started to pave the way towards faster design cycles. Before industrial products, such as aircraft or turbomachinery components, can be marketed, they must comply with stringent safety and environmental regulations in general. Besides the actual optimization in the design, meeting these standards through traditional methods can be both time-consuming and costly. Hence, the DLR aims to reduce costs, mitigate risks and expedite market entry through simulation-based certification, also known as virtual certification [26]. This approach not only optimizes the design process, but also ensures that new technologies meet regulatory requirements more efficiently and effectively.

The capabilities of modern Computational Fluid Dynamics (CFD) software are of utmost importance in the pursuit of designing efficient revolutionary turbomachinery for the

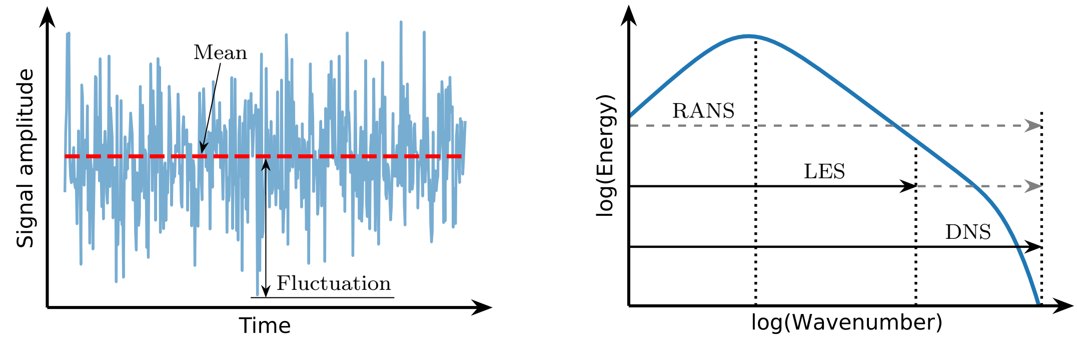

(a) A time series of a turbulent signal showing its fluctuating part and the representative mean value.

(b) Characteristic turbulent energy spectrum, where the wavenumber is inversely proportional to the size of the vortices (large scales) and turbulent eddies (smaller scales). Black arrows indicate the resolved portion of the spectrum for different modeling approaches, while the gray dashed arrows highlight its modeled part.

Figure 1.1.: Schematic representation of key aspects of turbulence.

energy sector as well as the aviation industry. CFD approximates solutions of the governing equations of continuum fluid flow - the Navier-Stokes equations - numerically, making it one of the engineer's key tools for predicting the flow field and the resulting performance of turbomachinery components [25]. The advancement of CFD has been profoundly influenced by an exponential growth in computational power, allowing for the execution of increasingly complex and detailed analyses. The Department of Numerical Methods at DLR's Institute of Propulsion Technology provides TRACE (Turbomachinery Research Aerodynamics Computational Environment), a CFD software developed in strong cooperation with MTU Aero Engines AG with special focus on the issues and characteristics of turbomachinery flows. TRACE fits into the portfolio of the DLR, as it meets the demand for simulation-based design optimization and virtual certification.

With few exceptions, the flow inside turbomachinery components is typically affected by turbulence. The flow's turbulent character develops, if inertial forces dominate over the viscous ones. This ratio is expressed via the Reynolds number $\mathrm{Re} = \frac{\rho||\boldsymbol{u}||L}{\mu}$, based on a certain characteristic length L, density ρ, magnitude of the velocity vector $\boldsymbol{u}$ and dynamic viscosity μ. If the flow features a sufficiently high Reynolds number, it is generally referred to as turbulent flow or turbulence. Although there is no general definition of turbulent flows, they are typically described as irregular (chaotic), three-dimensional, unsteady, diffusive, dissipative and featuring cascading energy transfer between different turbulent scales (eddies with different sizes and energy) [123] (cf. Fig. 1.1b). This is reflected in the fact, that the mean flow quantities are superimposed with fluctuations as schematically illustrated in Fig. 1.1a for an arbitrary turbulent signal. Probing such a signal at a certain time results in a random value with reproducible temporal mean.

The above-mentioned Navier-Stokes equations completely describe turbulent flows as well. However, accounting numerically for the entire range of length and time scales in turbulent flows is challenging in two respects. Either an appropriate resolution of space and time is required to resolve these occurring turbulent scales, or adequate modeling of their effect on the mean flow field is needed. The first approach, known as Scale-

Resolving Simulations (SRS), involves methods such as Direct Numerical Simulations (DNS) or Large Eddy Simulations (LES), which resolve large parts of the turbulent energy spectrum (as schematically illustrated in Fig. 1.1b). The contrary approach involves solving the equations for the average flow field instead of the instantaneous one, which is the fundamental idea of the Reynolds-averaged Navier-Stokes (RANS) equations. The derivation of the RANS equations requires a split of the flow quantities occurring in the Navier-stokes equations into an average and a fluctuating part (see Fig. 1.1a). This is followed by averaging the set of equations, which leads to the appearance of unknown correlations of fluctuating velocity components, known as Reynolds stresses. Unfortunately, the set of equations has to be closed by introducing turbulence models for these Reynolds stresses, addressing what is known as the turbulence closure problem. Hereby, the entire range of the spectrum in Fig. 1.1b is modeled, applying the steady-state RANS approach and employing turbulence modeling. Unsteady RANS simulations, relying on turbulence models as well, try to resolve the largest scales (corresponding to low wavenumbers) by the application of an adequate temporal resolution. In turbomachinery flows these scales are associated with the deterministic unsteadiness such as blade row interactions (i.e. blade passing frequencies) [133]. In order to adequately resolve these lower frequencies and, even more importantly, to correctly model the higher frequencies using a turbulence model, there needs to be a spectral gap between the deterministic and the turbulent, stochastic contributions [154]. As this thesis focuses on steady RANS computations, the emphasis in Fig. 1.1b is on the full range of the spectrum being modeled. Due to the imposed challenges to computational resources for simulating flow phenomena in turbomachinery (and the resulting high costs) using SRS [16], these methods are not expected to replace RANS simulations in the daily design processes of turbomachinery industry, although they might be employed at certain stages in the design, e.g. to deepen the understanding of causality between observed deficits and benefits (such as global efficiency) of a design and the underlying detailed flow physics. Since information on the mean flow is considered to be sufficient for most of the design relevant questions in industrial processes, particularly for design iterations and optimizations, the numerical approximation based on the RANS equations will be the dominant method in the foreseeable future.

Nevertheless, a significant challenge persists in the accurate representation of physical modeling [119]. Given the necessity to rely on RANS equations and closures due to their computational efficiency, it is important to acknowledge that when mapping physical phenomena, such as the mean transport of momentum due to turbulence represented by the Reynolds stresses, onto a mathematical model, an inherent lack of knowledge inevitably introduces uncertainties. This is in contrast to SRS approaches, which are typically known for incorporating no or minor modeling, leading to a reduction in modeling uncertainties. In this vein, RANS turbulence models, while essential to solve the underlying Navier-Stokes equations efficiently, may result in oversimplifications or inadequate representations of the real-world physics. This limitation becomes particularly pronounced with the emergence of drastic but advanced future turbomachinery concepts that go beyond the calibration cases of turbulence models.

A key focus for the future of turbomachinery CFD simulations is on Uncertainty Quantification (UQ) becoming an integral and systematic framework for assessing the confidence in the predictions that drive innovations [111]. Besides the aspiration to highly accurate numerical simulation techniques (such as SRS), UQ can play a pivotal role in advancing the reliability and predictive capabilities of state-of-the-art CFD, especially but not only for low fidelity simulations, such as RANS [132]. UQ approaches seek to identify and quantify uncertainties arising from various sources[1]. In CFD these sources may be inaccurate representation or simplification of the geometry (such as omitting cavity flows or approximating three-dimensional (3D) flows to lower dimensionality), deviating geometry due to manufacturing tolerances, unspecified or even varying boundary conditions during operations, simplifying assumptions as a compromise between computational effort and accuracy (such as the RANS approach in contrast to SRS) and describing physical phenomena by mathematical models (such as turbulence modeling). The capabilities of UQ techniques will be particularly important for optimizing simulation-based designs relying on Design Under Uncertainty (DUU) approaches in industry, where reliable predictions ensure robustness under varying conditions[2] [88]. With the help of UQ, engineers will be able to establish more realistic safety margins supporting informed decision-making to push the boundaries of turbomachinery technology further in the future. However, before UQ becomes an integral part of standard industrial workflows, its primary role in CFD will be to assist designers in interpreting and judging numerical results. UQ can also provide valuable insights when comparisons with other data sources, such as experiments or high-fidelity simulations, are drawn. Primarily, UQ approaches will enhance the credibility of simulation results by either quantifying their probability and variance, by highlighting certain upper and lower bounds in terms of intervals or simply by presenting realizable solutions under diverse plausible circumstances.

Although there are multiple uncertainties to be accounted for in CFD, this thesis focuses on accounting for the uncertainty due to the reliance on turbulence models, as they are a major contributor to the overall uncertainty in RANS simulations [169]. Ongoing enhancements in the development and calibration of these turbulence models highlight the critical need for a method to quantify their uncertainties, without requiring constant modifications to improve the model accuracy. By quantifying the uncertainty associated with the chosen turbulence model in RANS-based simulations of turbomachinery flows, designers can confidently assess the plausibility of their results and better communicate the degree of certainty in their predictions, while being aware of the fact, that there might be other uncertainties involved as well. This motivates the necessity of providing, demonstrating and evaluating a methodology to address turbulence modeling uncertainties as a foundational step towards comprehensive UQ in CFD integrating miscellaneous sources of uncertainties in the future.

Throughout this thesis (see detailed information on its structure and content in Section 1.3), the Eigenspace Perturbation Framework (EPF) for the Reynolds stress tensor is employed to appropriately account for the model-form uncertainties of RANS turbulence closures models, relying on the linear eddy viscosity assumption [33, 66]. The EPF adds physics-constrained selective perturbation to the eigenspace (eigenvalues and eigenvectors) of the Reynolds stress tensor to cover its potential realizable variations reflecting the inherent uncertainty in the turbulence model due to lack of knowledge. Since different Reynolds stress tensors lead to varying solutions for QoI, the EPF simply aims to sample from the possible solution space and provide meaningful intervals based on resultant additional but discrete simulations. The presented research within this thesis involves comprehensive

---

[1] Some UQ techniques, such as Bayesian inference, also mitigate the *a priori* uncertainties using available data. However, as it is difficult to completely eliminate uncertainty in general design tasks, UQ can help to understand and manage the uncertainties that do exist.

[2] That is, optimizing the design under uncertainties in order to reduce the variability of the Quantity of Interest (QoI), represented by the inverse design problem, which intends to maximize the tolerable uncertainties, such as manufacturing tolerances.

Verification and Validation (V&V)[3] efforts to ensure its reliability and accuracy for practical applications. Although the underlying methodology has been described in detail and applied to a variety of flows by previous researchers (see the review of the available literature in Section 3.5.3), its integration to TRACE has revealed several shortcomings that had not been addressed so far. Consequently, besides the theoretical introduction, implementation and application of the EPF, there remain opportunities to improve the framework.

1.2. Research objectives

The primary objective of this thesis is the advancement of the physics-constrained EPF enabling researchers and engineers to estimate the uncertainty with respect to the underlying RANS turbulence model, especially for complex turbomachinery applications. This study is guided by the main research question, whether the EPF is able to account adequately for the turbulence modeling uncertainty.

A key aspect of this research is the development of novel physics-constrained modifications to the EPF, improving both numerical accuracy and the core concept of perturbing the eigenspace of the Reynolds stress tensor. Moreover, the suitability of the approach for practical applications is critically examined, with particular attention to its strengths but also its inherent limitations.

The practical reliability of the EPF is assessed in both generic and complex flow scenarios, culminating in the most advanced turbomachinery case studied using the EPF to date. The estimation of the turbulence modeling uncertainty for a multi-row turbomachinery test case demonstrates the capabilities of the EPF and enables lessons to be learned for an application of the framework in such contexts.

In addition, as machine learning strategies are emerging to support the determination of the turbulence modeling uncertainties, this research also investigates whether these recent promising approaches, as reported in the literature, offer verifiable benefits, how they can be effectively used, and if not, the reasons for the lack of such benefits.

Finally, the capability of the eigenspace perturbations to bridge the gap between RANS simulations and high-fidelity simulations or experimental measurements is examined. If closing the gap is not feasible, guidance is provided on how to consider the conceptual idea that results in the inevitable limitations.

In pursuit of the research question, this thesis establishes a deeper understanding of the eigenspace perturbation methodology, offers insights into its effective use and interpretation of the obtained uncertainty intervals and contributes to improving the quantification of the turbulence modeling uncertainty relying on the EPF.

Table 1.1.: Summary of the considered articles in this thesis.

Authors	Title	Journal	Reference	Chapter
M. Matha K. Kucharczyk C. Morsbach	Evaluation of physics constrained data-driven methods for turbulence model uncertainty quantification	Computers & Fluids	[99]	4
M. Matha C. Morsbach	Improved self-consistency of Reynolds stress tensor eigenspace perturbation for uncertainty quantification	Physics of Fluids	[96]	5
M. Matha C. Morsbach	Physically constrained eigenspace perturbation for turbulence model uncertainty estimation	Physics of Fluids	[97]	6
M. Matha F. M. Möller C. Bode C. Morsbach E. Kügeler	Advanced methods for assessing flow physics of the TU Darmstadt compressor stage: Uncertainty quantification of RANS turbulence modeling	Journal of Turbomachinery	[101]	7

1.3. Structure and content

The research findings, which were already published in peer-reviewed journals, are included in Chapter 4 to Chapter 7 of this cumulative dissertation[4]. Table 1.1 provides a summary of the respective publication details, such as authors and journals. Two additional chapters precede these main chapters in order to equip the reader of this thesis with a comprehensive understanding of the theoretical and practical aspects of the uncertainties in CFD, the fundamentals of RANS turbulence modeling and the eigenspace perturbations of the Reynolds stress tensor.

Chapter 2 clarifies the term *uncertainty* in CFD through detailed classification and distinction according to common literature. As turbulence closures are the physical models of interest for the present consideration of uncertainty, Chapter 3 briefly introduces the RANS modeling approach and the origin of uncertainties. The need for quantifying these uncertainties follows the known inaccuracies of turbulence models. As the EPF is the method of choice in this thesis, the basic idea and the physical rationale are described. Subsequently, the core functionality of the EPF is demonstrated exemplarily for application in a generic test case. Additionally, a review of the available literature and details on the implementation in TRACE are given.

The data-free (without incorporating any *true* data) but physics-constrained eigenspace perturbations of the Reynolds stress tensor tend to result in uninformed, conservative estimates of the turbulence modeling uncertainty. For this reason, Chapter 4 focuses on

---

[3] Verification ensures that the implementation of a methodology aligns with the developer's conceptual idea, while validation assesses the model's accuracy in representing real-world phenomena for its intended purposes [1, 148, 120].

[4] Abbreviations are introduced where they appear for the first time. Once introduced, these abbreviations are used consistently throughout the dissertation. Additionally, a single bibliography is used for the entire dissertation instead of creating separate bibliographies for each chapter to ensure consistency and ease of reference. Consequently, previous publications in Chapter 4 to Chapter 7 were adapted accordingly. Moreover, minor adjustments in the form of corrections and alignments have been made for the individual publications.

the evaluation of a data-driven approach to apply local perturbations on the basis of machine learning predicted model deficiencies. The procedure was pioneered by Heyse et al. [61]. The underlying idea is motivated by the fact that the uncertainties with respect to the closure model are not expected to be uniformly distributed across the computational domain often featuring various flow physics. Hence, a random forest is trained to predict the local variation of the perturbation of the Reynolds stress tensor's eigenvalues in order to contribute to the estimation of the turbulence modeling uncertainty using the EPF. This research uses several test cases, featuring turbulent boundary layers, adverse pressure gradient, separation and reattachment, to train and validate the machine learning model. Additionally, key points associated with machine learning strategies, such as the selection of input features, tuning of hyperparameters and judging the model's accuracy in an *a priori* and an *a posteriori* way are addressed. The latter requires the consideration of an appropriate metric that is chosen to be an extrapolation metric based on the Kernel Density Estimation (KDE) in this research. The NACA 4412 (National Advisory Committee for Aeronautics (NACA)) airfoil at near-stall conditions represents the final validation test case. Hereby, the *a priori* confidence judgement by the extrapolation metric is demonstrated and the random forest's prediction of local RANS turbulence model deficiencies is presented. Conclusions for the future can be drawn from the comparison of the data-free and the data-driven uncertainty estimation using the EPF for the NACA 4412. Moreover, Chapter 4 already summarizes the objectives but also the limitations of the EPF and the applied machine learning strategies.

The common turbulence modeling assumption that the eigenvectors of the Reynolds stress tensor and the strain-rate tensor are identical is not universally valid (see details in Chapter 3). To break out of this assumption, it requires physics-based perturbations of the orientation of the Reynolds stress tensor's eigenvectors. This enables the user of the EPF to explore a potentially greater RANS solution space and to contribute to the overall turbulence modeling uncertainty estimation. Although the need for moderating the effect of Reynolds stress tensor perturbation on the RANS equations due to numerical convergences issues is already briefly discussed in Chapter 4, Chapter 5 finally reviews the suggestion of incorporating an additional moderation factor, as suggested by Mishra et al. [107]. In-depth verification of the EPF helps to identify a flaw in the numerical implementation that is contradictory to the conceptual idea of the methodology. From this, a self-consistent implementation is proposed and integrated in TRACE, ensuring that the perturbations can be mitigated without losing the underlying concept. The correctness of the proposed procedure is evaluated for the turbulent flow in a generic channel. Besides, Chapter 5 contains fundamentals with respect to the realizability constraints of the Reynolds stresses and their ramifications for the Reynolds stress anisotropy, and introduces the concept of tensor visualizations.

Chapter 6 provides further verification concerning the proposed eigenvector perturbation approach by Iaccarino et al. [66], focusing on its implications on the dynamics resulting from the Reynolds stress tensor. This chapter utilizes the example of wall-bounded flows to illustrate the effects of the eigenvector perturbation on a commensurable effective turbulent eddy viscosity and the turbulence production term. Based on this analysis, an appropriate rotation angle for the principal axes of the Reynolds stress tensor can be derived by analyzing the generic one-dimensional (1D) turbulent boundary layer flow. This derived constraint is validated *a posteriori*, demonstrating its applicability to the flow within a converging-diverging channel, which also includes a separated flow region. Finally, the modified eigenvector perturbation procedure is applied to the same test case, confirming its effect regarding physical plausibility and numerical stability simultaneously.

Chapter 7 details the simulation of the design speedline of the Technische Universität Darmstadt (TUDa) compressor. The EPF is employed to estimate the turbulence modeling uncertainties for global compressor performance metrics as well as for QoI at specific reference locations. This chapter pioneers the application of the EPF to a multi-row turbomachinery test case, providing a comprehensive description of how to employ the Reynolds stress tensor perturbations across an entire speedline. This research is dedicated to aiming for worst case scenarios that result in the most conservative estimate of the turbulence modeling uncertainty. Contrary to previous chapters, only perturbations to the eigenvalues of the Reynolds stress tensor are considered in this research. The numerical RANS results are compared against experimental measurements from Klausmann et al. [74] and a Delayed Detached-Eddy Simulations (DDES) conducted by Möller et al. [114]. In addition to the details on the local flow physics, the analysis of the rotor's shock-boundary layer interaction and the discussion on the effects of Reynolds stress anisotropy on the turbulence production, this chapters contributes to the assessment of the overall uncertainties of simulating the TUDa compressor.

Chapter 8 of this dissertation contains the discussion, which assesses the methodological coherence across the respective studies and comprehensively summarizes the conducted research, while providing guidance for practical applications.

Finally, Chapter 9 aims to present a critical reflection on the chosen methodology and derive conclusions and recommendations for future research related to the EPF.

1.4. Contributions

The listed publications in Table 1.1 form the core of this thesis, encapsulating the primary research outcomes. This section summarizes the main contributions to the research community and a personal statement regarding the specific contribution to each paper.

1.4.1. Research contribution

Essentially, there are four major novelties presented in this dissertation, aligning with the formulated objectives in Section 1.2:

1. The research presented in Chapter 4 (cf. [99]) merges various strategies for quantifying turbulence modeling uncertainty, the application of data-driven machine learning methods and *a priori* confidence estimation. Hence, it serves as a comprehensive synthesis of contemporary research topics that have been previously examined in isolation. Moreover, the research extends the range of considered test cases used for training and validating the random forests, building upon the previous work by Heyse et al. [61]. This facilitates extensive cross-validation of the machine learning model, thereby improving its generalizability. Additionally, this research represents the first attempt to combine the data-driven eigenvalue perturbation with data-free eigenvector perturbation as suggested by Iaccarino et al. [66][5]. Besides, this publication stands out as one of the few that critically discusses the limitations of the EPF referring to the actual objectives of the methodology. It

---

[5] The following chapters (based on Matha and Morsbach [96, 97]) reveal that using the combination of eigenvector perturbation and moderation factor as suggested by Mishra and Iaccarino [106] violates the consistency of the implementation on the one hand, whereas the eigenvector perturbation of Iaccarino et al. [66] may create non-physical Reynolds stress tensor dynamics on the other hand.

is essential for future users and developers of the EPF to understand these aspects and judge the simulation outcomes appropriately.

2. Aiming at verifying the numerical model with respect to the underlying conceptual idea of the EPF lead to a fundamental and essential recommendation for the implementation and application of this method. Hereby, Chapter 5 (cf. [96]) provides a consistent implementation by omitting a moderation factor, in contrast to the previous proposal by Mishra et al. [107]. This study has the potential to shift the mindset of the community using this framework. Previously, practitioners tended to use a maximum perturbation magnitude for the eigenvalue perturbation, arguing that this approach is the only viable option in the absence of superior knowledge regarding the flow topology (such as e.g. incorporating data-driven predictions). However, the effect of tensor perturbations on the RANS equations have often required mitigation through an additional moderation factor to overcome numerical stability issues, particularly when incorporating eigenvector perturbations as well. This research suggests to prevent numerical convergence issues by directly reducing the perturbation magnitude from a model-consistent point of view. Therefore, it is inferred that choosing the strongest perturbation possible before encountering convergence issues can be considered as the worst case (most conservative) scenario for future applications.

3. Since 2017, the eigenvector perturbation approach by Iaccarino et al. [66] has been widely accepted in the research community. The verification and subsequent derivations presented in Chapter 6 (cf. [97]) establish a physics-based constraint on these eigenvector perturbations for wall-bounded flows, which are the crucial ones in turbomachinery applications. This research suggests to describe the Reynolds stress tensor's eigenvector perturbation as a tensor rotation around the second eigenvector. It is determined that a maximum rotation angle of $\pi/4$ should not be exceeded, as this may lead to the formation of non-physical Reynolds stress tensor dynamics, when applied in the RANS equations. This constraint challenges common practice up to date and improves stability and accuracy of the EPF.

4. In Chapter 7, the EPF is used to account for the RANS turbulence modeling uncertainty when simulating the TUDa-GLR-OpenStage compressor, which represents the most complex application of the EPF related to turbomachinery flows. This study represents the first application of the framework in a multi-row configuration, quantifying the uncertainties associated with structural uncertainties of the turbulence model for an entire speedline. Based on this pioneering work, this dissertation guides appropriate usage of the framework and establishes best practices for such complex applications.

1.4.2. Article contribution statement

I was the primary researcher responsible for the conceptualization, methodology and execution of the research in any of the above-mentioned publications (see Table 1.1). I did the implementation for incorporating the necessary features of the EPF in DLR's CFD solver TRACE that is developed in strong cooperation with MTU Aero Engines AG. Furthermore, simulation data collection and their subsequent analysis was done by me. Based on this, I was the one, verifying the underlying methodology, which led to the further advancements of the framework. With respect to the manuscripts, I was the lead author, who was responsible for writing and the visualizations. I also coordinated the revisions and addressed reviewers' comments during the peer-review processes.

The following individual contributions were made by the respective co-authors:

- *Dr.-Ing. Edmund Kügeler*, being the head of the Department of Numerical Methods, was instrumental in organizing funding for conference attendance and my employment in general. In addition, he was involved in discussions about the results presented in Chapter 7.
- *Dr. rer. nat. Christian Morsbach* provided guidance in the planning of each paper. He reviewed my writing and made suggestions for the appropriate presentation of results. Because of his role, as my group leader, he always took part in valuable discussions about my research in general.
- *Felix-Maximilan Möller* generated the grid and the initial RANS setups for the simulation of the TUDa compressor. In preparation of the conference paper for the American Society of Mechanical Engineers (ASME) Turbo Expo 2024 [100], to which we submitted a two-part paper, we had a gainful cooperation. He proofread the final conference and the resulting journal paper presented in Chapter 7.
- *Karsten Kucharczyk* contributed to my research progress during his Master's thesis that I was supervising. We had discussions on the usage of machine learning and the EPF. He participated in the proofreading of the conference paper for the American Institute of Aeronautics and Astronautics (AIAA) Aviation 2022 [98], the results of which form the basis for Chapter 4.
- *Dr.-Ing. Christoph Bode* was an interested observer of the capabilities of the EPF. He supported me to structure the underlying paper of Chapter 7 and reviewed my writing.

2. Uncertainties in CFD

This chapter is motivated due to the fact that the choice of an appropriate UQ approach is often dependent on the classification of the uncertainty itself. In CFD but especially in the scope of this thesis, it is important to understand and classify involved uncertainties. Therefore, uncertainties are distinguished from errors and the difference between aleatoric and epistemic uncertainties with respect to CFD is presented. An overview on these distinctions is given in Fig. 2.1 that condenses the following two sections while also giving examples.

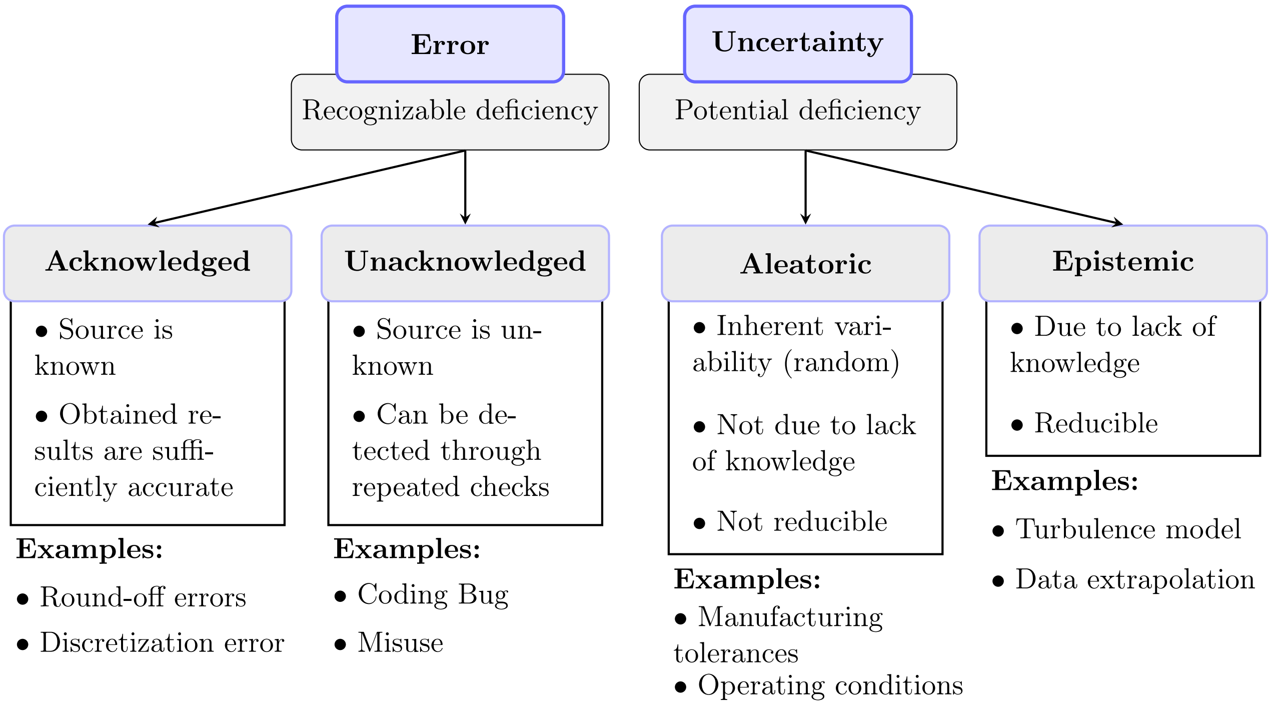
Error
Recognizable deficiency
Uncertainty
Potential deficiency
Acknowledged
• Source is known
• Obtained results are sufficiently accurate
Examples:
• Round-off errors
• Discretization error
Unacknowledged
• Source is unknown
• Can be detected through repeated checks
Examples:
• Coding Bug
• Misuse
Aleatoric
• Inherent variability (random)
• Not due to lack of knowledge
• Not reducible
Examples:
• Manufacturing tolerances
• Operating conditions
Epistemic
• Due to lack of knowledge
• Reducible
Examples:
• Turbulence model
• Data extrapolation

Figure 2.1.: Overview of errors and uncertainties in CFD.

2.1. Uncertainties vs. errors

An error is a recognizable deficiency that does not arise from a lack of knowledge [1, 121]. This concept stands in contrast to uncertainty that defines a potential inaccuracy and/or an inherent variability. While different types and sources of uncertainties are discussed in Section 2.2, errors can be categorized into two broad classes: acknowledged (recognized) and unacknowledged (not recognized) [41]. The application of additional resources, whether computational or human, can mitigate both types of errors. In the context of CFD, acknowledged errors include finite precision arithmetic (round-off error), insufficient spatial discretization (discretization error) and premature termination of the simulation (convergence error). There are also errors due to physical modeling, such as relying on a steady-state solver when the flow is obviously unsteady or modeling a compressible flow as incompressible. These errors typically result from deliberate decisions of CFD practitioners, who are capable of estimating the probable consequences and judge the numerical results as being satisfactory. Conversely, unacknowledged errors usually stem from human failure in coding or handling of CFD software. Common examples are programming errors or the use of incorrect input data. While various methods exist to account for the acknowledged errors, such as grid convergence studies or error propagation techniques, there are only a few systematic approachs, e.g. the method of manufactured solutions [8, 38, 39], to quantify the unacknowledged errors in CFD and modeling.

2.2. Aleatoric vs. epistemic uncertainties

Understanding and distinction between aleatoric and epistemic uncertainties can be crucial for incorporating these uncertainties in decision-making and risk assessment for engineering problems, as the way to account for a certain kind of uncertainty may vary due to its nature [117, 131]. Generally, the source of uncertainty leads to the classification of these two categories. While, aleatoric[1] uncertainty arises from the intrinsic randomness and natural variability present in physical systems, epistemic[2] uncertainty is presumed as a lack of knowledge about the system, phenomenon or process being modeled [73, 162]. Aleatoric uncertainty is a property of the system itself, whereas epistemic uncertainty emerges from attempts to describe and analyze the system [141]. Hence, Oberkampf et al. [121] further classify aleatoric uncertainty as the inherent variation and epistemic uncertainty as a potential inaccuracy. The latter suggests that certain phenomena might be modeled correctly even though there is incomplete understanding or information of the underlying process. Common examples of aleatoric uncertainties are manufacturing tolerances, material properties, varying environmental operating conditions or boundary conditions [41]. A straightforward way to account for these kinds of aleatoric uncertainties is by providing a probability distribution for the quantity in question. In general, aleatoric uncertainties cannot be mitigated due to their random, unbiased characteristics [141]. However, initially chosen prior probability distributions representing an uncertain parameter can be minimized by using Bayesian inference methods [115]. Conversely, mapping a mathematical model to a physical phenomenon with incomplete knowledge or simplified assumptions inevitably leads to a certain degree of epistemic uncertainty. Insights in Section 3.2 demonstrate how this is directly linked to the formulation of a RANS turbulence model, representing a prominent example of such mathematical models. Increasing knowledge would eventually reduce the degree of epistemic uncertainty. Thus, referring to Faber [40], the promising aspect for the turbulence modeling community is that these mathematical models, dominated by epistemic uncertainties, have the potential for reducing the uncertainties by adaptations and enhancements.

Although most available literature clearly distinguishes between aleatoric and epistemic uncertainty, Kiureghian and Ditlevsen [73] argue that the context and the actual application may influence how to deal with certain uncertainty. They propose that every uncertainty ultimately arises from a certain lack of knowledge, which introduces a philosophical debate. Moreover, Senge et al. [138] emphasize that the classification of an uncertain quantity as epistemic or aleatoric may also evolve over time due to increased observations, experience or applications, which contributes to knowledge gain. Even though, it is agreed on the fact that the lack of knowledge seems to be relative, in the present author's view, the aforementioned classifications offer an appropriate distinction for the purpose of this thesis. Furthermore, one might also argue that applying a particular turbulence model to flow phenomena that it might not handle well (see Section 3.4), constitutes a modeling error. However, the definition of uncertainty within this thesis adheres to the prevailing literature, as a CFD practitioner might not necessarily know *a priori* how well the assumptions and approximations in the formulation of the turbulence model fit the current problem.

---

[1] Latin *alea*: rolling of dice

[2] Greek $\epsilon\pi\iota\sigma\tau\eta\mu\eta$ *(episteme)*: knowledge

3. Turbulence closures and uncertainties

In order to ensure a consistent comprehension of the results obtained in this thesis, this chapter provides relevant background information to turbulence modeling. Based on the fundamental equations of fluid mechanics, the details of the RANS modeling approach for turbulent flows are presented. The classification of the inherent uncertainties involved in RANS simulations and the discussion on the common approach to close the set of equations is followed by the introduction of the applied UQ framework.

3.1. Statistical turbulence modeling

The basis of fluid mechanics are the Navier-Stokes equations, which can be derived from the conservation of mass, momentum and energy. In differential conservation form, the unsteady, compressible equations for mass, momentum and total energy, while neglecting volume forces such as gravity, are the following

$$\frac{\partial \rho}{\partial t} + \frac{\partial}{\partial x_i}\left(\rho u_i\right) = 0 \tag{3.1}$$

$$\frac{\partial}{\partial t}\left(\rho u_i\right) + \frac{\partial}{\partial x_j}\left(\rho u_j u_i\right) = -\frac{\partial p}{\partial x_i} + \frac{\partial \sigma_{ij}}{\partial x_j} \tag{3.2}$$

$$\frac{\partial}{\partial t}\left[\rho\left(e + \frac{u_i u_i}{2}\right)\right] + \frac{\partial}{\partial x_j}\left[u_j \rho\left(h + \frac{u_i u_i}{2}\right)\right] = \frac{\partial}{\partial x_j}\left(-q_j + u_i \sigma_{ij}\right)\ . \tag{3.3}$$

The summation convention is used here, so that sums over duplicate indices are implied.

In order to solve these equations numerically, there are several assumptions and modeling approaches required that are outlined subsequently. Based on Stokes's hypothesis for Newtonian fluids, the trace of the viscous stress tensor

$$\sigma_{ij} = \mu\left(\left(\frac{\partial u_i}{\partial x_j} + \frac{\partial u_j}{\partial x_i}\right) - \frac{2}{3}\frac{\partial u_k}{\partial x_k}\delta_{ij}\right) \tag{3.4}$$

must disappear. The dynamic viscosity μ is computed according to Sutherland [149] in this thesis. The molecular heat flux vector

$$q_j = -\kappa \frac{\partial T}{\partial x_j} = -\frac{c_p \mu}{\mathrm{Pr}}\frac{\partial T}{\partial x_j}\ , \tag{3.5}$$

occurring in the conservation of total energy (Eq. (3.3)), is typically modeled by assuming a diffusion law with a constant Prandtl number Pr. In this thesis, Pr is chosen to be 0.72 in all the considered cases. Assuming ideal gas closes the set of equations finally

$$p = \rho R T = \rho\left(h - e\right)\ , \tag{3.6}$$

while the internal energy e and enthalpy h are expressed as

$$e = c_v T \text{ and } h = c_p T\ , \tag{3.7}$$

using the specific heat at constant volume c_v and at constant pressure c_p. The ratio between the specific heats of the fluid is chosen to be $\gamma = c_p/c_v = 1.4$ in the scope of this thesis.

As already described in Section 1.1, the derivation of the compressible RANS equations requires the split of the instantaneous flow quantities into a mean and a fluctuating part

$$\phi = \overline{\phi} + \phi' \ , \tag{3.8}$$

following the approach of Reynolds [126]. In general, turbomachinery flows have to be considered being compressible, which requires a density weighted average (Favre-average)

$$\phi = \widetilde{\phi} + \phi'' \text{ and } \ \overline{\rho}\widetilde{\phi} = \overline{\rho\phi} \ . \tag{3.9}$$

Replacing all instantaneous quantities in Eq. (3.1)-Eq. (3.3) with the respective split in Eq. (3.9) except for density and pressure, which are split according to Eq. (3.8), and subsequent Reynolds-averaging (time-averaging) leads to the unsteady Favre-averaged Navier-Stokes equations

$$\frac{\partial \overline{\rho}}{\partial t} + \frac{\partial}{\partial x_i}\left(\overline{\rho}\widetilde{u}_i\right) = 0 \tag{3.10}$$

$$\frac{\partial}{\partial t}\left(\overline{\rho}\widetilde{u}_i\right) + \frac{\partial}{\partial x_j}\left(\overline{\rho}\widetilde{u}_j\widetilde{u}_i\right) = -\frac{\partial \overline{p}}{\partial x_i} + \frac{\partial}{\partial x_j}\left(\overline{\sigma}_{ij} - \overline{\rho u_i'' u_j''}\right) \tag{3.11}$$

$$\begin{aligned}\frac{\partial}{\partial t}\left[\overline{\rho}\left(\widetilde{e} + \frac{\widetilde{u}_i\widetilde{u}_i}{2} + \frac{\widetilde{u_i''u_i''}}{2}\right)\right] + \frac{\partial}{\partial x_j}\left[\widetilde{u}_j\overline{\rho}\left(\widetilde{h} + \frac{\widetilde{u}_i\widetilde{u}_i}{2} + \frac{\widetilde{u_i''u_i''}}{2}\right)\right] \\ = \frac{\partial}{\partial x_j}\left[-\overline{q}_j - \overline{\rho}\widetilde{u_j''h''} + \overline{\sigma_{ij}u_i''} - \frac{1}{2}\overline{\rho}\widetilde{u_j''u_i''u_i''}\right] \\ + \frac{\partial}{\partial x_j}\left[\widetilde{u}_i\left(\overline{\sigma}_{ij} - \overline{\rho u_i''u_j''}\right)\right] \ .\end{aligned} \tag{3.12}$$

In the scope of this thesis, we call this set RANS equations, although Reynolds-averaging was initially developed for incompressible flows [126].

The RANS equations come along with new unknown correlations of fluctuating quantities. Hereby, the term turbulence closure problem refers to the fact that equations for higher correlations invariably generate additional unknowns due to the non-linearity inherent in these equations. The focus of this thesis is on the Reynolds stresses $\overline{\rho u_i'' u_j''}$. For the sake of pragmatism and practicality,

$$\tau_{ij} = \widetilde{u_i'' u_j''} \tag{3.13}$$

is referred to as the Reynolds stress tensor even though it is actually a specific stress given its units [123]. The trace of this tensor is known as the turbulent kinetic energy

$$k = \frac{1}{2}\tau_{ii} \ . \tag{3.14}$$

Due to Favre-averaging, additional correlations appear in Eq. (3.12). While the molecular diffusion $\overline{\sigma_{ij}u_i''}$ and the turbulent transport of turbulent kinetic energy $\frac{1}{2}\overline{\rho}\widetilde{u_j''u_i''u_i''}$ can be neglected for flows with Mach numbers up to the supersonic range, the turbulent transport of heat $\overline{\rho}\widetilde{u_j''h''}$ has to be modeled [161]. All simulations within this thesis apply the simple gradient diffusion hypothesis by introducing a turbulent Prandtl number equal to 0.9 to model the turbulent heat conductivity κ_T in accordance with the laminar heat flux $\overline{q}_j$ [128]. Currently, the Favre-averaged energy conservation in Eq. (3.12) implemented in

TRACE also neglects the fluctuating velocity contribution $\widetilde{u_i''u_i''}/2$ on the total energy E. Because the test cases examined throughout this thesis can be approximated using the steady-state assumption, the derivative with respect to the physical time $\partial\square/\partial t$ must vanish for a solution of the steady RANS equations[1].
Appendix A summarizes the RANS equations implemented in TRACE. Their numerical solution forms the basis of the presented results and discussions in the current thesis.

To shorten and simplify the notation in the following sections and chapters, $\widetilde{u_i} \rightarrow U_i$ is introduced for the mean velocities, $\widetilde{T}$ is simplified as T, while the overlines for density $\overline{\rho} \rightarrow \rho$, pressure $\overline{p} \rightarrow p$ and the viscous stress tensor $\overline{\sigma_{ij}} \rightarrow \sigma_{ij}$ are omitted. Furthermore, the mean strain-rate tensor will be also denoted with a capital letter $\overline{s_{ij}} \rightarrow S_{ij} = \frac{1}{2}\left(\frac{\partial U_i}{\partial x_j} + \frac{\partial U_j}{\partial x_i}\right)$.

3.2. Origin of uncertainties in RANS turbulence models

Due to the turbulence closure problem and the absence of the fluctuating quantities in RANS simulations, turbulence (closure) models have to be introduced to account for the mean transport and dissipation of momentum induced by turbulence. Over the past century, researchers have developed and applied a wide range of turbulence models from simple algebraic relationships in order to approximate the Reynolds stresses to the most complex Reynolds Stress Models (RSMs) [161, 123]. Besides their mathematical complexity, turbulence models differ by their model parameters, also known as the coefficients. Because the adequate representation of turbulence is crucial for the accuracy of RANS simulations, functional extensions based on available models and recalibration of existing parameters have inevitably led to a variety of different models with individual advantages for specific purposes [155]. However, the turbulence modeling community has not managed to develop a single model that generalizes across the complete variety of applications. Apparently, the simpler the model (structure, terms and parameters), the more universal is its application purposes[2]. Conversely, increasing a model's accuracy for specific application necessitates greater complexity in general, which can diminish both its universality and comprehensibility.

Consequently, each model features its own advantages and drawbacks with respect to modeling accuracy and applicability. The drawbacks are mainly caused by simplifying assumptions during the formulation of RANS closures. Duraisamy et al. [29] summarized and classified these simplifications into four levels:

Level 1 Reynolds-averaging $\overline{\square}$ in combination with the non-linearity of the Navier-Stokes equations (indicated as $\mathcal{N}(\cdot)$) leads to $\overline{\mathcal{N}(\cdot)} \neq \mathcal{N}(\bar{\cdot})$ bringing along the turbulence closure problem. The resultant loss of information is due to the fact that there are infinitely many realizations of the flow field compatible with the averaged flow field by dropping the fluctuating parts. This unavoidably causes uncertainty that is even irrecoverable.

Level 2 When neglecting the modeling of the turbulent heat flux for illustration purposes, the only modeled term in $\overline{\mathcal{N}(\cdot)}$ is the Reynolds stress tensor $\boldsymbol{\tau}$ approximated via

---

[1] To be precise: The numerical solution process of the steady RANS equations require the replacement of the physical time by a cell-local pseudo-time, which is locally evaluated based on the Courant-Friedrichs-Lewy (CFL) number [9].

[2] Although the accuracy of a simpler model may suffer for certain specific applications, which can also limit its actual application rangefrom the perspective of CFD users.

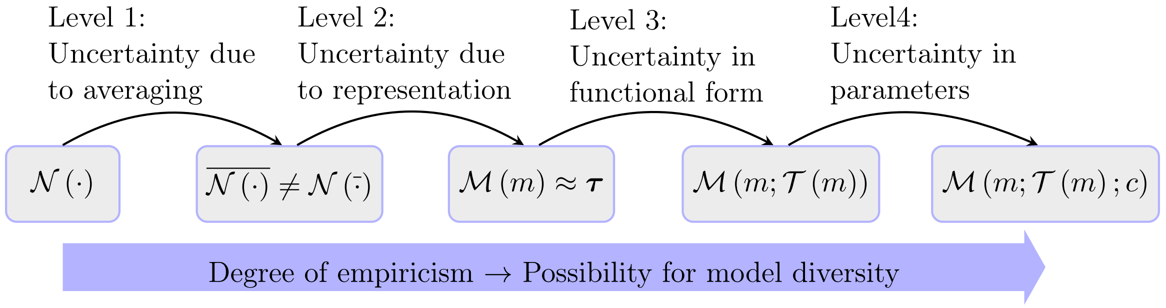
Level 1:
Uncertainty due to averaging
Level 2:
Uncertainty due to representation
Level 3:
Uncertainty in functional form
Level4:
Uncertainty in parameters
$\mathcal{N}(\cdot)$
$\overline{\mathcal{N}(\cdot)} \neq \mathcal{N}(\bar{\cdot})$
$\mathcal{M}(m) \approx \boldsymbol{\tau}$
$\mathcal{M}(m; \mathcal{T}(m))$
$\mathcal{M}(m; \mathcal{T}(m); c)$
Degree of empiricism → Possibility for model diversity

Figure 3.1.: Sources of uncertainty in RANS turbulence models at different levels according to Duraisamy et al. [29].

some model $\mathcal{M}$:

$$\overline{\mathcal{N}(\cdot)} = \mathcal{N}(\bar{\cdot}) - \nabla \begin{pmatrix} 0 \\ \rho \boldsymbol{\tau} \\ \boldsymbol{U} \rho \boldsymbol{\tau} \end{pmatrix} \approx \mathcal{N}(\bar{\cdot}) - \nabla \begin{pmatrix} 0 \\ \rho \mathcal{M} \\ \boldsymbol{U} \rho \mathcal{M} \end{pmatrix} . \tag{3.15}$$

In general, the Reynolds stress tensor is approximated as a function of a set of mean flow variables m based on the solution of the RANS equations indicated as $\mathcal{M}(m)$. This necessary choice of representing the microscopic scale (higher-order statistical moments of fluctuating velocity components) with respect to the macroscopic (low-order) averaged states introduces additional uncertainty.

Level 3 Selecting a specific functional form for the relationship between the Reynolds stresses and certain mean flow quantities adds another source of uncertainty. This typically involves transport equations accounting for convection, production, dissipation and certain redistribution of turbulent quantities, denoted here as $\mathcal{T}(m)$. The effects of the modeled Reynolds stresses on the RANS equations are derived from the solutions of the transport equations, consequently the model reads $\mathcal{M}(m; \mathcal{T}(m))$.

Level 4 Given the specific functional form of the turbulence model (such as transport equations), a set of parameters c must be determined. In general, these parameters are calibrated for certain flow scenarios, which incorporates further uncertainty.

These levels, arranged from the general set of the Navier-Stokes equations $\mathcal{N}(\cdot)$ to the final model $\mathcal{M}(m; \mathcal{T}(m); c)$, are illustrated in Fig. 3.1. The increase in empiricism from Level 1 to Level 4 is associated with a growing range of potential turbulence model formulations (model diversity). Examples for Level 2 to Level 4 are given in Section 3.3, when introducing the linear eddy viscosity assumption to close the set of equations.

While the first level is hard to assess, most of the published research focuses on the quantification of the uncertainties related to the representation of the Reynolds stresses as a function of the mean flow field (Level 2) and the uncertainties arising due to the chosen functional form (Level 3) and parameters (Level 4) of a particular model. Therefore, it is convenient to call Level 2 *structural (model-form) uncertainty* and Level 4 *parametric uncertainty*. Level 3 can be considered either as model-form or parametric uncertainty, depending on the method of accounting for it. Both uncertainties are epistemic in nature, as they stem from a lack of knowledge (see classification of uncertainties in Section 2.2). Thus, deeper understanding of turbulent flow physics could help to formulate more accurate functional representations, while increased availability of a vast amount of calibration data for the turbulence model's coefficients would lead to better fit QoI.

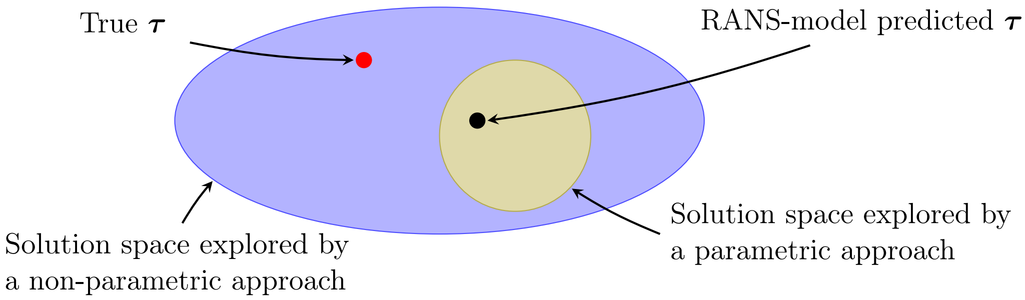
True $\boldsymbol{\tau}$
RANS-model predicted $\boldsymbol{\tau}$
Solution space explored by a parametric approach
Solution space explored by a non-parametric approach

Figure 3.2.: Conceptual difference of non-parametric and parametric approaches for assessing the uncertainty of RANS turbulence modeling to explore the possible solution space of the Reynolds stress tensor, inspired by Xiao and Cinnella [169] and Soize [142].

Xiao and Cinnella [169] comprehensively reviewed the available literature on UQ in RANS simulations. Parametric approaches primary denote methods to assess the uncertainty in turbulence models by focusing on the sensitivity of QoI to closure coefficients. Although the uncertainty is classified to be epistemic and not aleatoric nature, parametric approaches generally rely on defining probabilistic distributions, random sampling methods (Monte Carlo methods and all of their variants) and/or statistical inference.

Given the epistemic nature of turbulence model uncertainty, multi-model approaches acknowledge the strengths and weaknesses of each model, addressing uncertainty by employing a variety of models [124, 150]. Instead of just ensemble averaging individual predictions of multiple models, Bayesian statistical techniques may also help to provide a data-informed estimation on the modeling uncertainty, if accurate data for certain QoI is available [63]. In addition to parametric and multi-model approaches, non-parametric approaches aim to account for the model-form uncertainty. According to Xiao and Cinnella [169], non-parametric approaches are expected to contribute more significantly to the overall turbulence model uncertainty than parametric approaches, as the possible solution space of the Reynolds stress tensor explored by parametric approaches is a subset of the solution space obtained via non-parametric ones, illustrated schematically in Fig. 3.2. This is because approaches trying to judge the sensitivity with respect to closure coefficients always rely on an unchanged structural form of the turbulence model. Although the goal is to design non-parametric approaches, which are able to sample from the possible solution space enveloping the true Reynolds stress tensor, it cannot be guaranteed in general. More importantly, from a CFD practitioner's point of view, in the context of RANS simulations, certain true QoI, such as e.g. pressure and velocity distributions, cannot be expected to be enveloped by the sampled solution space of the Reynolds stress tensor[3]. As the goal of this thesis is to investigate a non-parametric approach to sample from the physically plausible solution space of the Reynolds stress tensor, it is reasonable to introduce the major source of the model-form uncertainty in industry relevant turbulence models in the following.

---

[3] Focusing on the solution space for certain QoI: The true data point for certain QoI (not for $\boldsymbol{\tau}$ as illustrated in Fig. 3.2) might also be located outside of the possible solution space spanned by a non-parametric approach. Finally, this will be addressed retrospectively in Section 8.2.1 and Section 9.1 for the chosen EPF in this thesis.

3.3. Closure via linear eddy viscosity assumption

Except for RSMs that solve transport equations for each individual Reynolds stress component[4], most of the available approaches apply the eddy viscosity hypothesis relying on the Boussinesq approximation [161]. The Boussinesq approximation states that the deviatoric part of the Reynolds stress tensor scaled by k, known as the anisotropy tensor,

$$a_{ij} = \frac{\tau_{ij}}{k} - \frac{2}{3}\delta_{ij} \tag{3.16}$$

can be computed in analogy to the viscous stresses (see Eq. (3.4)[5]), introducing a turbulent eddy viscosity ν_T[6]

$$\tau_{ij} = -2\nu_\mathrm{T}\left(S_{ij} - \frac{1}{3}S_{kk}\delta_{ij}\right) + \frac{2}{3}k\delta_{ij} \ , \tag{3.17}$$

given the mean strain-rate tensor $S_{ij} = \frac{1}{2}\left(\frac{\partial U_i}{\partial x_j} + \frac{\partial U_j}{\partial x_i}\right)$. Hence, the relationship in Eq. (3.17) introduces Level 2 uncertainty and shifts the closure of the RANS equations to the adequate determination of the turbulent eddy viscosity by the imposed relations of the turbulence model. Turbulence models that rely on this linear assumption between the anisotropic part of the Reynolds stress and traceless strain-rate tensor $S_{ij}^{-} = S_{ij} - \frac{S_{kk}}{3}\delta_{ij}$ are called Linear Eddy Viscosity Models (LEVMs).

Within the scope of this thesis, a two-equation turbulence model, which solves transport equations for the turbulent kinetic energy and for the turbulent dissipation rate, is considered. This type of model forms the simplest but complete turbulence model that can be applied without prior knowledge of the flow[7] [161]. By taking the trace of the transport equation of the Reynolds stresses, which manifest from the momentum equation, the transport equation for the turbulent kinetic energy can be derived following the notation of Wilcox [161]

$$\begin{aligned} \frac{\partial}{\partial t}\left(\rho k\right) + &\frac{\partial}{\partial x_j}\left(\rho U_j k\right) \\ &= \rho P_k - \rho\epsilon + \frac{\partial}{\partial x_j}\left[\overline{\sigma_{ji}u_i''} - \frac{1}{2}\rho\widetilde{u_j''u_i''u_i''} - \overline{p'u_j''}\right] - \overline{u''}\frac{\partial p}{\partial x_i} + \overline{p'\frac{\partial u_i''}{\partial x_i}} \ . \end{aligned} \tag{3.18}$$

The last two terms on the right hand side (pressure work $\overline{u''}\frac{\partial p}{\partial x_i}$ and pressure dilatation $\overline{p'\frac{\partial u_i''}{\partial x_i}}$) vanish for incompressible flows with zero density fluctuations [161]. However, they are usually neglected also for compressible flows, as considered in this thesis.
The molecular diffusion can be expressed exactly via

$$\overline{\sigma_{ji}u_i''} = \rho\nu\frac{\partial k}{\partial x_j} \ , \tag{3.19}$$

while the sum of the turbulent transport and the pressure diffusion behave similar to gradient diffusion, leading to a model of the form [161]

$$\frac{1}{2}\rho\widetilde{u_j''u_i''u_i''} + \overline{p'u_j''} \propto -\rho\nu_\mathrm{T}\frac{\partial k}{\partial x_j} \ . \tag{3.20}$$

---

[4] RSMs also solve an equation for a quantity such as the turbulent dissipation rate, which accounts for the length or timescale of turbulence.

[5] Equation (3.4) is also valid in an adapted form for σ_{ij} in the Favre-averaged equations.

[6] For simplicity, $\mu_\mathrm{T} = \rho\nu_\mathrm{T}$ is also referred to as turbulent eddy viscosity in the scope of this thesis, in analogy to the molecular viscosity, while ν_T has identical units as the kinematic viscosity.

[7] As algebraic or one-equation models, which only account for the transport of turbulent kinetic energy, require specification of the turbulent length scale in advance, associated with a certain turbulent dissipation given the turbulent kinetic energy.

The remaining terms in Eq. (3.18) are the turbulence production

$$P_k = -\tau_{ij} \frac{\partial U_i}{\partial x_j} , \tag{3.21}$$

which can be modeled by inserting the Boussinesq approximation from Eq. (3.17) for τ_{ij}, and the dissipation

$$\epsilon = \overline{\sigma_{ji} \frac{\partial u''_i}{\partial x_j}} . \tag{3.22}$$

The reason for solving a second transport equation is to model the dissipation of the turbulent kinetic energy equation. Although, it is possible to derive an exact transport equation for ϵ, for the scope of this thesis it suffices to note that the general formulation of this transport equation also features production, dissipation and diffusion terms[8].

Based on the early observations and developments by Kolmogorov [77], the use of the specific turbulent dissipation rate $\omega \propto \epsilon/k$ has been established that still forms the foundation of daily turbomachinery designs. Consequently, the dissipation of k in Eq. (3.22) is approximated via $\epsilon \propto k\omega$ (with some model-specific constant of proportionality) and the need to solve an additional transport equation for ω. The final closure of the RANS equations is done via $\nu_\mathrm{T} \propto k/\omega$. The constant of proportionality depends on the specific choice of the turbulence model and is one of many examples of introducing Level 4 uncertainty, whereas the formulation of the transport equations of the model, such as Eq. (3.18), already introduces Level 3 uncertainty. Throughout this thesis, the Menter SST k-ω turbulence model [104] is used as the underlying baseline model.

3.4. Need for quantifying the intrinsic uncertainties in RANS models

Although the linear relationship of LEVMs does not always hold true in reality [135], these models are commonly used in industrial turbomachinery design processes. Generally, the underlying turbulence for these kind of applications cannot be characterised by a linear relationship of the Reynolds stress tensor with the mean strain-rate tensor (see resulting Reynolds stress tensor in Eq. (3.17)). Hence, this simplification results in limited accuracy for flows featuring streamline curvature [23, 78] and mean rotation [5, 84, 143]. Furthermore, LEVMs fail to accurately predict flows with separation and reattachment [89]. Due to the linear relationship, these models cannot account for differences in normal Reynolds stresses, leading to an inability to predict the formation of turbulence-driven secondary flows in fully developed turbulent flow through pipes with non-circular cross sections [145, 109]. The flow inside turbomachinery is far beyond generic turbulent boundary layers, being dominated by interactions of vortex systems, such as the horse shoe, passage and tip leakage vortex, as well as secondary flows (e.g. corner separations) [81]. Monier et al. [110] demonstrated that there is significant misalignment of the Reynolds stress and strain-rate tensors in compressor secondary flow regions. Besides, the accuracy in predicting turbomachinery relevant design parameters, such as the compressor stall margin and the overall efficiency, is heavily influenced by the capabilities and limitations of turbulence models [25]. Consequently, the unknown epistemic uncertainty of the turbulence model represents a major contributor to the applied safety margins in turbomachinery designs. The violation of the linear constitutive relation of LEVMs with subsequent necessary increase of safety factors becomes even more prominent in light of future turbomachinery components, aiming for drastic designs [156]. That is because RANS models show reduced accuracy as soon as their validation range is left. To conclude, the Boussinesq approximation in Eq. (3.17) is a common example of introducing significant amount of uncertainty by choosing a functional relationship that does not coincide with actual turbulence, particularly regarding the underlying Reynolds stress tensor and its effect on the mean flow. This underscores the need to account for the model-form uncertainty of LEVMs.

---

[8] The exact derivation can be found in textbooks [161, 123].

3.5. Estimating uncertainty with the Reynolds stress tensor perturbations

Researchers have employed various techniques and approaches to assess the model-form uncertainty of RANS models (see detailed review of Xiao and Cinnella [169]). Some have assessed the model-form uncertainty on a certain budget term of the transport equation using field inversion techniques [139, 140, 10], while others have presented the uncertainty with respect to the turbulent eddy viscosity [28]. Nevertheless, it seems to be even more general to focus on the modeled quantities entering the RANS equations, which are the Reynolds stresses itself. On the one hand, this approach is motivated by the fact that trying to quantify the uncertainty of a budget term or the turbulent eddy viscosity may result in accounting for parametric uncertainty, as their effects can be expressed via an additional parameters in front of the respective terms. On the other hand and even more importantly, both approaches still rely on the linear eddy viscosity assumption, whereas targeting the Reynolds stress tensor is able to invalidate this assumption (see also Fig. 3.2).

3.5.1. Overview of the fundamental concept and physical rationale of the EPF

Emory et al. [33] pioneered the work in accounting for the inherent model-form uncertainty based on turbulence modeling assumptions by exploring the possible eigenspace of the Reynolds stress tensor. He and his co-workers in the group of Prof. Iaccarino at Stanford University aimed to create enveloping models by deriving physics-based bounds for the Reynolds stress tensor. In this vein, they postulated that the perturbations of the eigenspace of the Reynolds stress tensor can help to overcome the potential bias induced by the assumptions of LEVMs. The final uncertainty for certain QoI is deduced[9] from selective sampling from the perturbed simulations. Hence, the EPF primarily serves as a tool to assess the sensitivity of the results with respect to the eigenspace of the Reynolds stress tensor (in other words: with respect to turbulence anisotropy), a task that is acknowledged as unfeasible for unperturbed, baseline RANS models. The underlying idea forms the basis of the current work presented in this thesis. Although the method is described in any of the following chapters, as they represent individual publications on their own, the brief concept is described subsequently.

---

[9] As outlined and justified in the conclusion section (Section 9.1) of this thesis, *estimated* would be a more appropriate description.

As the deviatoric part (anisotropy tensor a_{ij}) of the Reynolds stress tensor forms a real symmetric tensor[10], the spectral decomposition

$$\tau_{ij} = k\left(a_{ij} + \frac{2}{3}\delta_{ij}\right) = k\left(v_{in}\Lambda_{nl}v_{jl} + \frac{2}{3}\delta_{ij}\right) \tag{3.23}$$

serves as the starting point, with the eigenvectors $\boldsymbol{v_k}$ being column-wise ordered in v_{in} and the traceless diagonal matrix Λ_{nl} containing the corresponding eigenvalues λ_k of a_{ij}[11].

The perturbation of the Reynolds stress tensor aims to systematically introduce physically constrained modifications to the eigenvalues, eigenvectors and turbulent kinetic energy, resulting in a perturbed Reynolds stress tensor

$$\tau^*_{ij} = k^*\left(a^*_{ij} + \frac{2}{3}\delta_{ij}\right) = k^*\left(v^*_{in}\Lambda^*_{nl}v^*_{jl} + \frac{2}{3}\delta_{ij}\right) \; . \tag{3.24}$$

Initially, as the Reynolds stress tensor has to fulfill the realizability constraints by Schumann [136], the most straightforward perturbation can be done for the eigenvalues using the transformation from the eigenvalues of the anisotropy tensor onto barycentric coordinates and exploiting the derived bounding properties of them [4]. Consequently, Emory et al. [33, 34] selected the limiting states of turbulence componentiality (the isotropic limit (3C), the two-component axisymmetric limit (2C) and the one-component limit (1C)) [93] to be the target states for the eigenvalue perturbation. These limiting states are special points as 1C, 2C and 3C represent the number (1, 2 and 3) of non-zero eigenvalues, while 2C and 3C further correspond to two or all eigenvalues of the Reynolds stress tensor being equal (see details in Table 5.1). In reality, turbulence tends to be 2C in the vicinity of walls, whereas 3C turbulence is commonly present outside of boundary layers and in undisturbed free flow regions [151]. Separated shear layers, for example, are represented by Reynolds stress tensors having only one non-zero eigenvalue (1C) [42]. In-depth information on the realizability of Reynolds stresses, implications on the eigenspace and its representation in invariant maps (such as barycentric coordinates) and tensor visualization can be found in Chapter 5.

The perturbed eigenvalues are obtained by a relative shift using a relative perturbation magnitude $\Delta_B \in [0, 1]$ according to

$$\boldsymbol{\lambda}^* = (1 - \Delta_B)\,\boldsymbol{\lambda} + \Delta_B\boldsymbol{\lambda}_{(\mathrm{t})} \; , \tag{3.25}$$

while

$$\boldsymbol{\lambda}_{(\mathrm{t})} \in \{\boldsymbol{\lambda}_{1\mathrm{C}}, \boldsymbol{\lambda}_{2\mathrm{C}}, \boldsymbol{\lambda}_{3\mathrm{C}}\} \tag{3.26}$$

represents the eigenvalues at the 1C, 2C or 3C limiting state of turbulence (see Table 5.1).

Since the eigenbasis (set of eigenvectors) of the anisotropy tensor $\mathbf{a}$ are modeled to coincide with the ones of the strain-rate tensor $\mathbf{S}$, due to the linear eddy viscosity assumption in Eq. (3.17), it is reasonable to account for this by introducing perturbations to them as well. While Thompson et al. [152] used the Reynolds stress transport equations to constrain the eigenvector perturbations, Iaccarino et al. [66] suggested to exploit the boundedness of the turbulence production term (see Eq. (3.21)) in order to modify the eigenvectors. Essentially, two extreme states (minimum and maximum) of the turbulence production term can be achieved by modifying the orientation of the Reynolds stress tensor's eigenvectors. Nevertheless, the derivations in Chapter 6 prove that the lower limit of the turbulence production may lead to implausible Reynolds stress tensor dynamics. Hence, this thesis suggests the perturbation of the eigenvectors via a rotation matrix

---

[10] The Reynolds stress and the strain-rate tensor are symmetric as well, hence they can also be diagonalized using their eigenvectors, which form an orthogonal matrix.

[11] For completeness: Every combination of $\boldsymbol{v_k}$ and λ_k satisfy the eigenvalue and eigenvector problem $\mathbf{a}\boldsymbol{v_k} = \lambda_k\boldsymbol{v_k}$ for $k = 1, 2, 3$.

$$\mathbf{R} = \begin{pmatrix} \cos(\alpha) + v_{21}^2(1-\cos(\alpha)) & v_{21}v_{22}(1-\cos(\alpha)) - v_{23}\sin(\alpha) & v_{21}v_{23}(1-\cos(\alpha)) + v_{22}\sin(\alpha) \\ v_{21}v_{22}(1-\cos(\alpha)) + v_{23}\sin(\alpha) & \cos(\alpha) + v_{22}^2(1-\cos(\alpha)) & v_{22}v_{23}(1-\cos(\alpha)) - v_{21}\sin(\alpha) \\ v_{21}v_{23}(1-\cos(\alpha)) - v_{22}\sin(\alpha) & v_{22}v_{23}(1-\cos(\alpha)) + v_{21}\sin(\alpha) & \cos(\alpha) + v_{23}^2(1-\cos(\alpha)) \end{pmatrix} , \tag{3.27}$$

describing a rotation around the second eigenvector $\boldsymbol{v_2} = (v_{21}, v_{22}, v_{23})$ with an angle $\alpha \in [0, \pi/4]$. Hence, the eigenvector matrix $\mathbf{v}$ is rotated (perturbed) according to

$$\mathbf{v}^* = \mathbf{R}\mathbf{v} \ . \tag{3.28}$$

A detailed motivation and derivations for the above mentioned equations and the proposed limitation on α, which is a major novelty of this work, are given in Chapter 6.

Unfortunately, there are no physical bounds for the turbulent kinetic energy level. However, studies by Iaccarino et al. [66] and Gorlé et al. [53, 56] revealed that the turbulence production P_k is dependent on the eigenvalues and eigenvectors of the Reynolds stress tensor, respectively of the anisotropy tensor. A summary is presented in Appendix B to support understanding and provide context in this thesis. Consequently, the indirect manipulation of the actual turbulence level by changing the eigenvalues and eigenvectors of the Reynolds stress tensor became state-of-the-art, leading to the fact that $k^* = k$ in Eq. (3.24).

To interpret the presented results in this thesis, a thorough understanding of the physical rationale behind the eigenspace perturbation of the Reynolds stress tensor is essential. Mishra and Iaccarino [106] have conducted pioneering research on this topic. While the details pertinent to the analysis in this thesis are outlined in Appendix C, the summary of the physical rational of the EPF is provided below. Symbolically, in the principal axes of the strain-rate tensor, the anisotropy tensor under eigenvalue perturbation applied to LEVMs can be expressed as

$$\mathbf{a}^*|_{\mathrm{PCS}_\mathbf{S}} = \underbrace{-2\frac{\nu_\mathrm{T}}{k}(1-\Delta_B)}_{\text{scalar}} \boldsymbol{\Psi}^- + \underbrace{\Delta_B \begin{pmatrix} \theta_1 & 0 & 0 \\ 0 & \theta_2 & 0 \\ 0 & 0 & \theta_3 \end{pmatrix}}_{\text{diagonal tensor}} \boldsymbol{\Psi}^- , \tag{3.29}$$

while $-2\frac{\nu_\mathrm{T}}{k}(1-\Delta_B)$ is a scalar, the entries of the diagonal tensor are θ_k and $\boldsymbol{\Psi}^-$ is the eigenvalue matrix of the traceless strain-rate tensor (see Appendix C.1 for detailed derivation). As each θ_k can have a different value, the eigenvalue perturbation is able to change the isotropic LEVM to an orthotropic eddy viscosity model, assigning different scalars analogous to varying turbulent eddy viscosities along the principal axes of the anisotropy tensor[12]. This is highlighted in Fig. 3.3c, as the anisotropy tensor is scaled differently along each eigenvector direction, resulting in a distorted ellipsoid compared to the traceless strain-rate tensor. In contrast, Fig. 3.3b shows the ellipsoid of the anisotropy

---

[12] The principal axes (eigenvectors) of the anisotropy tensor coincide with the ones of the Reynolds stress tensor per definition.

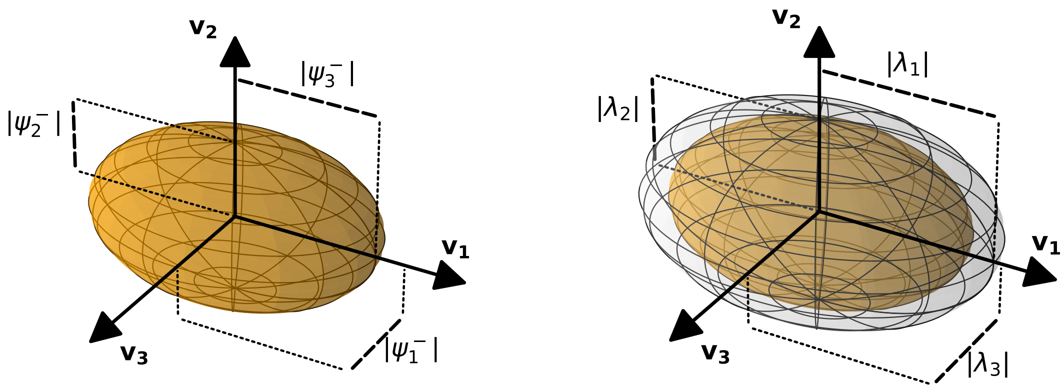

(a) Traceless strain-rate tensor

(b) Anisotropy tensor resulting from the linear eddy viscosity hypothesis (Boussinesq assumption) in Eq. (3.17)

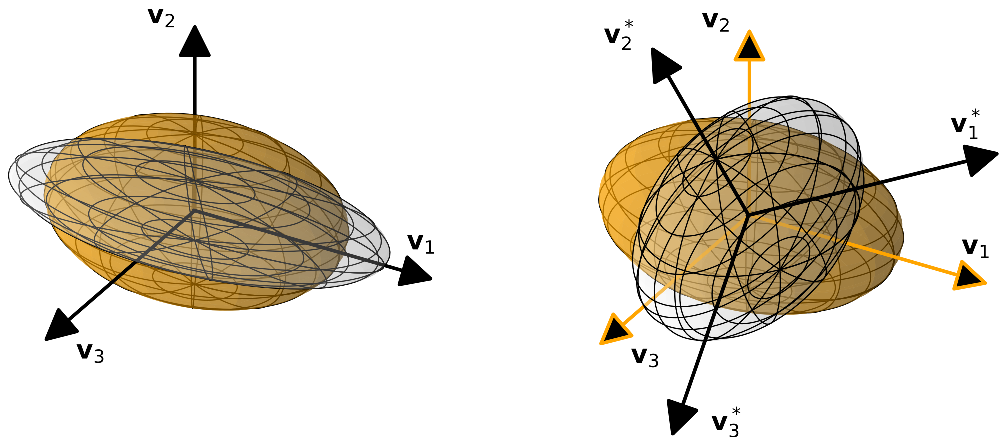

(c) Resulting anisotropy tensor under eigenvalue perturbation according to Eq. (3.25) (see also Eq. (3.29))

(d) Resulting anisotropy tensor under eigenvector perturbation according to Eq. (3.28) (see also Eq. (3.31))

Figure 3.3.: Schematic representation of the relationship between anisotropy **a** (gray) and the traceless strain-rate tensor $\mathbf{S}^{-}$ (orange) in the eigenbasis defined by the eigenvectors $\boldsymbol{v_i}$. As **a** and $\mathbf{S}^{-}$ are not positive semi-definite, the magnitude of the eigenvalues λ_i and ψ_i^{-} is plotted according to Kratz et al. [79]. The Reynolds stress tensor featuring identical principal axes as the anisotropy tensor behaves in similar manner as the anisotropy tensor.

tensor that is based on the Boussinesq assumption (see Eq. (3.17)) following the linear dependency

$$\lambda_i = -2\frac{\nu_\mathrm{T}}{k}\psi^{-}_{(4-i)} \text{ for } i = 1, 2, 3 \tag{3.30}$$

between the eigenvalues of the anisotropy tensor and the ones of the traceless strain-rate tensor in Fig. 3.3a[13].

---

[13] The negative correlation between λ_i and ψ_i^{-} results in the change of the eigenvalue order corresponding to the ordered eigenvectors of the anisotropy tensor $\boldsymbol{v_i}$.

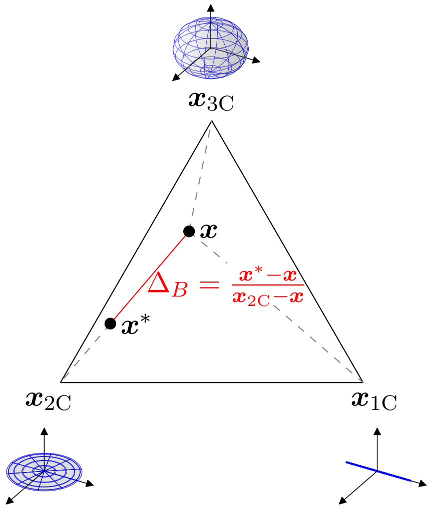
$\boldsymbol{x}_{3\mathrm{C}}$
$\boldsymbol{x}$
$\Delta_B = \frac{\boldsymbol{x}^*-\boldsymbol{x}}{\boldsymbol{x}_{2\mathrm{C}}-\boldsymbol{x}}$
$\boldsymbol{x}^*$
$\boldsymbol{x}_{2\mathrm{C}}$
$\boldsymbol{x}_{1\mathrm{C}}$

Figure 3.4.: Representation of the eigenvalue perturbation within the ABM and its effect on the shape of the Reynolds stress tensor ellipsoid. The eigenvalue perturbation towards the 2C limiting state is shown exemplarily.

According to the derivations in Appendix C.2, the perturbed anisotropy tensor under eigenvector rotation in the principal axes of the strain-rate tensor can be written as

$$\mathbf{a}^*|_{\mathrm{PCSs}} = -2\frac{\nu_{\mathrm{T}}}{k}\mathbf{G}\boldsymbol{\Psi}^{-}\mathbf{G}^T \ . \tag{3.31}$$

As $\mathbf{G}$, resulting from the tensor rotation, is typically not a diagonal matrix, the anisotropy tensor in the principal axes of the strain-rate tensor contains off-diagonal elements under eigenvector perturbation. That implies that the eigenvector perturbation is able to mimic an anisotropic eddy viscosity. For illustration purposes, Fig. 3.3d shows the schematically effect of an arbitrary rotation of the anisotropy tensor.

3.5.2. Demonstration of the core functionality and credibility of the EPF

This section aims to demonstrate the functionality of the described eigenspace perturbation approach and substantiate its credibility in applying selective perturbations to the Reynolds stress tensor to account for its model-form uncertainty, when there is actually an infinite number of realizations. The primary questions to be addressed are as follows:

1. How do the QoI respond to variations in the perturbation magnitude of the eigenvalues, represented by the relative perturbation parameter Δ_B, and the eigenvectors, represented by the rotation angle α?
2. Why is it reasonable to target the limiting states of turbulence componentiality, 1C, 2C and 3C, as representative states for estimating the model-form uncertainty of the Reynolds stress tensor?

Building on the introduced idea and theoretical foundation of the EPF outlined in Section 3.5.1, the imposed physical constraints of realizable Reynolds stress tensors, and anisotropy tensors respectively, can be used to derive the Anisotropy Barycentric Map (ABM) of physically feasible states (see Fig. 3.4). Banerjee et al. [4] and Terentiev [151] introduced barycentric coordinates

$$\boldsymbol{x} = \frac{1}{2}\boldsymbol{x}_{1\mathrm{C}}\left(\lambda_1 - \lambda_2\right) + \boldsymbol{x}_{2\mathrm{C}}\left(\lambda_2 - \lambda_3\right) + \boldsymbol{x}_{3\mathrm{C}}\left(\frac{3}{2}\lambda_3 + 1\right) \quad \text{with } \lambda_1 \geq \lambda_2 \geq \lambda_3 \tag{3.32}$$

based on the eigenvalues of the Reynolds stress anisotropy tensor. The barycentric coordinate vector $\boldsymbol{x}$ describes any state inside the barycentric triangle bounded by the limiting states of turbulence componentiality. This representation enables a linear interpolation of the barycentric coordinates with respect to the eigenvalues and equal weighting applied to these limiting states.

The perturbation of eigenvalues, as defined in Eq. (3.25), can be expressed as a relative shift in barycentric coordinates according to

$$\boldsymbol{x}^* = \boldsymbol{x} + \Delta_B \left(\boldsymbol{x}_{(\mathrm{t})} - \boldsymbol{x}\right) \text{ with } \Delta_B \in [0,1] \text{ and } \boldsymbol{x}_{(\mathrm{t})} \in \{\boldsymbol{x}_{1\mathrm{C}}, \boldsymbol{x}_{2\mathrm{C}}, \boldsymbol{x}_{3\mathrm{C}}\} \ . \tag{3.33}$$

Figure 3.4 visualizes the perturbation towards the 2C limiting state.

In order to exemplify the EPF's functionality and to answer the questions raised above, the generic test case of the converging-diverging channel, investigated by Laval and Marquillie [85][14], is considered. First of all, the effect of Δ_B, the relative shift of the eigenvalues of the anisotropy tensor towards the corners of the barycentric triangle, on the streamwise velocity profiles of the converging-diverging channel is investigated to address the first part of the first question in this section. Ten simulations are conducted with eigenvalue perturbations targeting for 1C, using $\Delta_B = [0.1, 0.2, 0.3, \ldots, 1.0]$, and compared against a baseline RANS simulation using the unperturbed Menter SST model[15]. The resulting barycentric coordinates of the perturbed Reynolds stress tensor are presented in Fig. 3.5a, while the corresponding streamwise velocity profiles are shown in Fig. 3.5b. By increasing the perturbation strength starting from the baseline simulation without any Reynolds stress tensor modification, the deformation of the velocity profiles becomes stronger. Notably, enlarged views at specific locations in the converging-diverging channel (see Fig. 3.5c to Fig. 3.5e) highlight the transition of the velocity profiles, culminating in the fully perturbed case at the 1C limiting state (applying $\Delta_B = 1$). Although only the perturbations towards the 1C state are shown here, targeting the other limiting states of turbulence componentiality yields similar trends.

To answer the second question, whether the limiting states of turbulence are adequate representatives to assess the uncertainty of the turbulence model, the barycentric triangle is discretized into 55 states, as shown in Fig. 3.6a. These states correspond to specific and individual eigenvalues of the anisotropy tensor, with samples 0, 45 and 54 representing the limiting states 3C, 1C and 2C respectively, when using $\Delta_B = 1$. Each state is propagated in a perturbed RANS simulation of the converging-diverging channel and the effects of each state on the streamwise velocity are evaluated in Fig. 3.6b to Fig. 3.6e. The simulations propagating the eigenvalues corresponding to the sampled data points 0-5, 8, 9 and 14 failed to achieve sufficiently converged steady-state results due to their reducing effect on the actual turbulence level caused by manipulating the turbulence production term (see derived relationship in Appendix B). While the perturbations aiming for the 2C (sample 54) and 1C (sample 45) corners show convergence using $\Delta_B = 1$, the perturbation towards the isotropic corner has to be adjusted iteratively by choosing $\Delta_B < 1$. After a discrete search by reducing Δ_B by 0.1, a converged simulation could be achieved for $\Delta_B = 0.2$ (see study in Section 6.4 for more information). In general, simulations featuring barycentric coordinates close to the isotropic state increase the separated flow area at the bottom wall, whereas most propagated anisotropic states of the Reynolds stress tensor tend to reduce the separated region in the diverging section of the channel compared to

---

[14] A detailed description and analysis of this test case are provided in Chapter 4 and Chapter 6. Hence, this section focuses on the demonstration of the EPF.

[15] The unperturbed baseline simulation is effectively equivalent to $\Delta_B = 0$, although the numerical procedures and solved equations differ slightly.

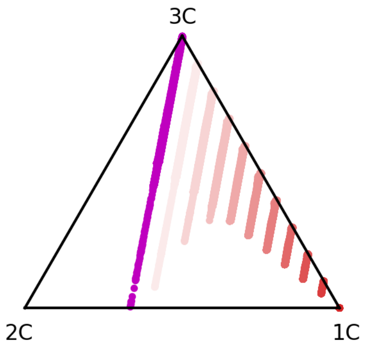

(a) Resulting barycentric coordinates; every data point indicates a single solution point of the simulation.

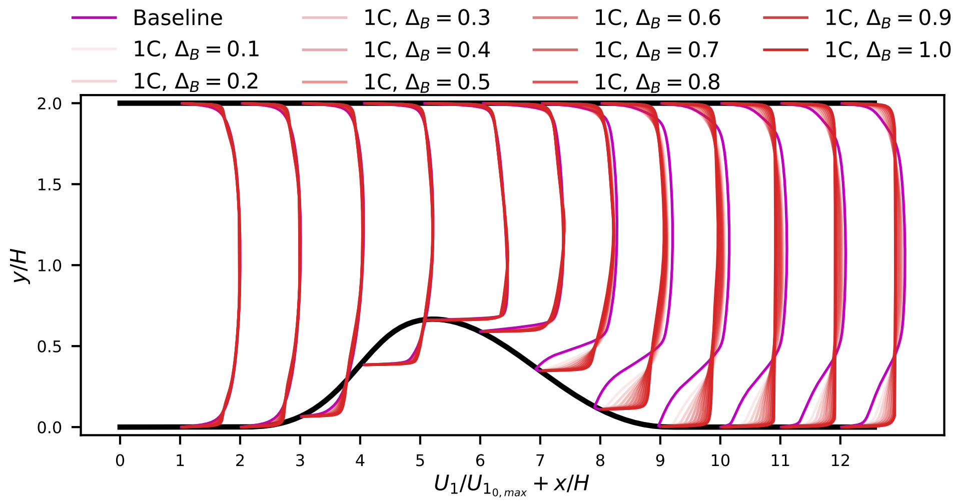

(b) Streamwise velocity U_1 inside the converging-diverging channel; $U_{1_{0,\max}}$ is the maximum streamwise velocity of the baseline simulation at x/H=0.

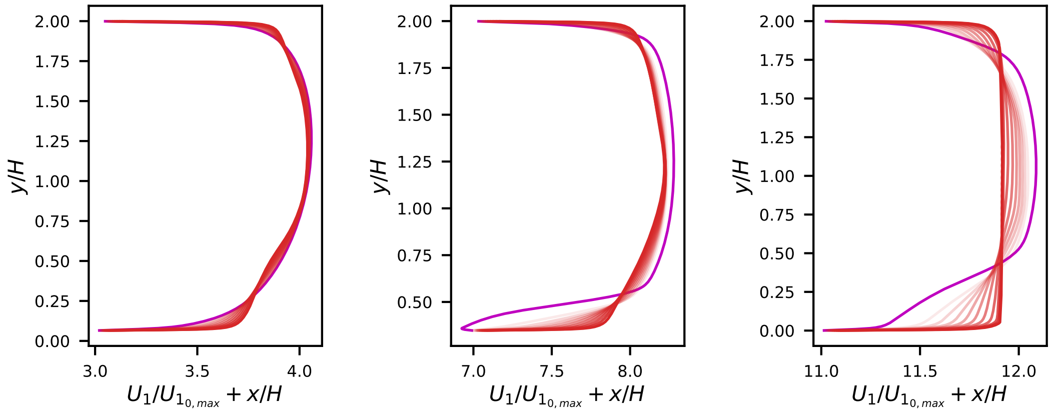

(c) Profile of U_1 at $x/H = 3$ (d) Profile of U_1 at $x/H = 7$ (e) Profile of U_1 at $x/H = 11$

Figure 3.5.: Effect of Δ_B when targeting for the 1C limiting state on the solution of the converging-diverging channel without modifying the eigenvectors of the Reynolds stress tensor; legend in (b) applies also for (a), (c), (d) and (e).

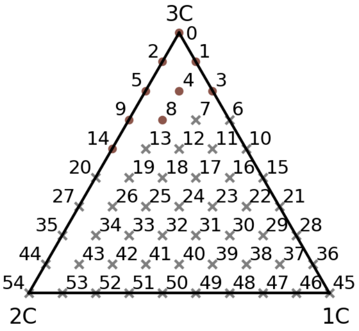
3C
2C
1C
0 1 2 3 4 5 6 7 8 9 10 11 12 13 14 15 16 17 18 19 20 21 22 23 24 25 26 27 28 29 30 31 32 33 34 35 36 37 38 39 40 41 42 43 44 45 46 47 48 49 50 51 52 53 54

(a) Sampled states of the anisotropy tensor represented by barycentric coordinates; brown data points (circles) lack convergence, while gray data points (crosses) are shown in (b), (c), (d) and (e).

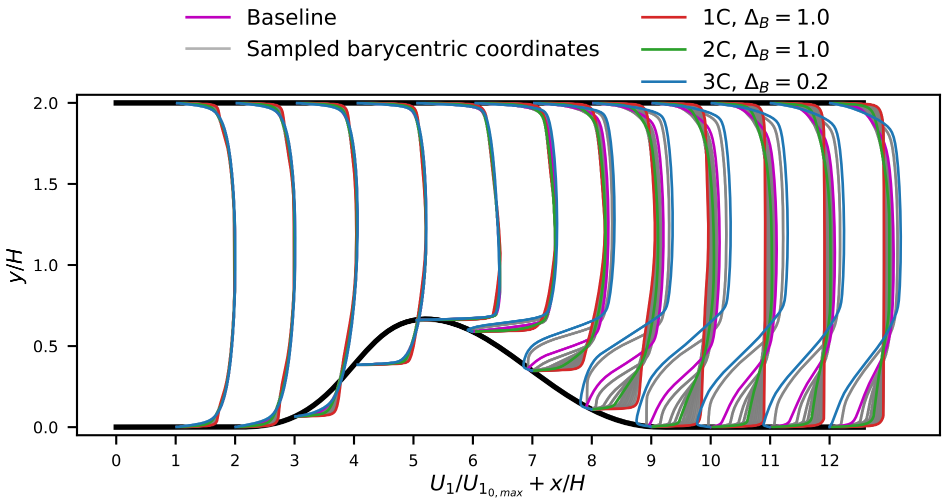

(b) Streamwise velocity U_1 inside the converging-diverging channel; $U_{1_{0,\max}}$ is the maximum streamwise velocity of the baseline simulation at $x/H{=}0$.

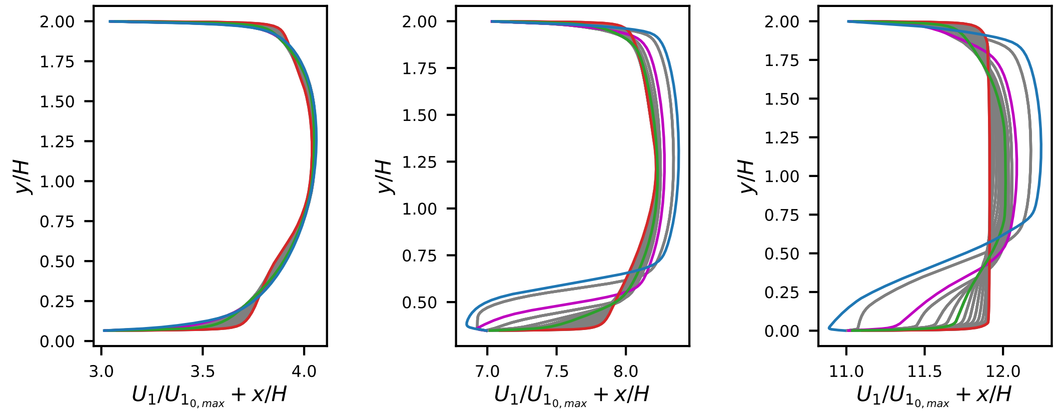

(c) Profile of U_1 at $x/H = 3$ (d) Profile of U_1 at $x/H = 7$ (e) Profile of U_1 at $x/H = 11$

Figure 3.6.: Effect of sampled states inside the barycentric triangle on the solution of the converging-diverging channel without modifying the eigenvectors of the Reynolds stress tensor; legend in (b) applies also for (c), (d) and (e).

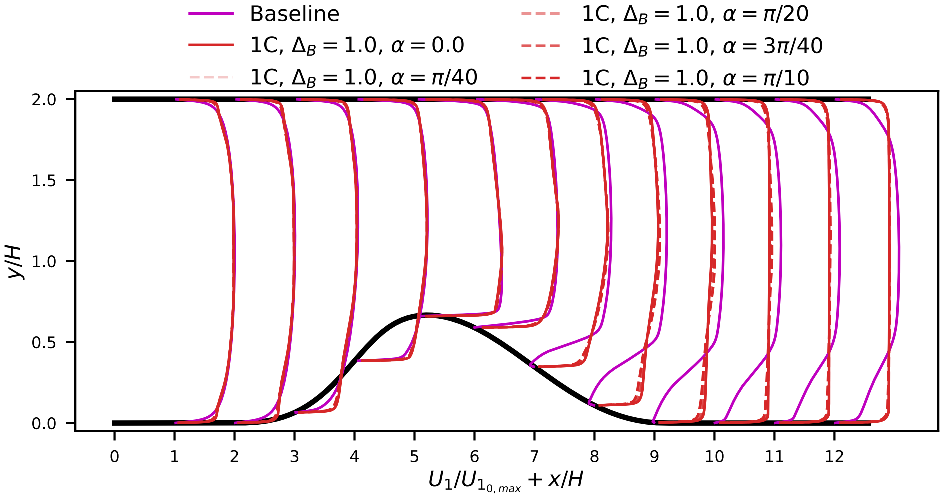

(a) Streamwise velocity U_1 inside the converging-diverging channel; $U_{1_{0,\max}}$ is the maximum streamwise velocity of the baseline simulation at $x/H{=}0$.

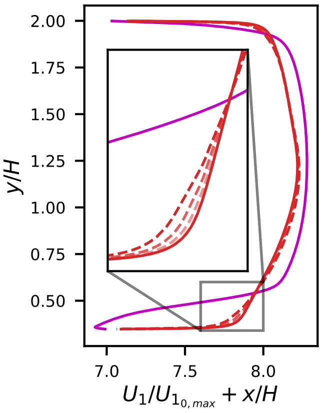

(b) Profile of U_1 at $x/H = 7$

Figure 3.7.: Effect of α when perturbing the eigenvalues to the 1C limiting state on the solution of the converging-diverging channel; legend in (a) applies also for (b).

the unperturbed Menter SST model. The 1C state exhibits the most significant gradient of the streamwise velocity at the wall, eliminating flow separation across the entire computational domain. The presented study demonstrates that simulations targeting the limiting states of componentiality (1C, 2C and 3C) effectively estimate the range of observed QoI in the majority of locations (x and y positions of 1D profiles) without necessitating full discretization of the ABM[16]. Nevertheless, there are some areas where other sampled perturbations (not the states at the corners of the barycentric triangle) or the baseline simulation form the bound on the streamwise velocity profiles, e.g. in Fig. 3.6d, where the unperturbed baseline result forms an upper bound at $y/H \approx 0.63$ (see remarks at the end of this section).

---

[16] This investigation is limited due to the fact, that it was aimed to propagate the identical barycentric state in the entire computational domain in each simulation. However, this study was also supported by additional stochastic experiments, involving random states within the barycentric triangle for each grid cell, leading to *some* intermediate result with respect to the streamwise velocity profiles. Since it was and can only be exploratory nature, and there is an infinite number of possible combinations, it is not shown in this thesis.

To finally also address the second part of the first raised question regarding the effect of the amount of eigenvector rotation, the angle of rotation around the second eigenvector is varied while the eigenvalues are perturbed towards the 1C corner using $\Delta_B = 1$. As described in Section 3.5.1, the modification of the eigenvectors according to Eq. (3.28) decreases the turbulence production term and consequently the actual level of turbulent kinetic energy. The impact of eigenvector rotation on the streamwise velocity profiles of the converging-diverging channel is presented in Fig. 3.7. As α increases, the gradient of the velocity profiles at the walls decreases, forming rounder profiles. However, it is impossible to increase the angle of rotation beyond $\pi/10$, because of convergence issues similar to those encountered when approaching the isotropic state of the Reynolds stress tensor (see derivations and study in Chapter 6 for detailed information).

The presented studies evaluate the effect of perturbing the Reynolds stress tensor and the impact of various anisotropic states. Thus, this analysis provides credibility in the EPF building on a few selective perturbations based on these observations. A user of the framework is equipped with the ability to obtain the most deviating results from an unperturbed RANS baseline simulation by applying the largest amount of perturbations possible (within the limits of numerical convergence), resulting in the most conservative uncertainty consideration for QoI. Therefore, this thesis proposes to use the three perturbations towards the limiting states of turbulence componentiality combined with a maximum possible rotation of the Reynolds stress tensor to assess the uncertainty in RANS turbulence modeling. Finally, while this analysis focuses on a single QoI, similar conclusions can be drawn for other QoI. Although, as will be examined in the following chapters, there is no linear relationship between any QoI and these perturbations due to the nature of the set of equations. Consequently, it cannot be assured, that the selective perturbations always (at every location and for every QoI) provide the bounds (minimum and maximum values) for certain QoI.

3.5.3. Literature review of the applications of the eigenspace perturbations and their fundamentals

As the Reynolds stress tensor perturbation is often described as being interpretable, physics-based and physics-constrained at the same time, the basic concept of the methodology has been integrated into various CFD solvers, like ANSYS Fluent [30], OpenFoam [24] and SU2 [107]. With this said, the methodology was applied in multiple engineering applications such as aircraft nozzle jets [105], turbomachinery [35, 125], aircraft wing-body configuration [113], civil structural design [55, 80] and wind farm design [31, 64, 32]. Different research focused on the uncertainty estimation of heat transfer [58] and even extended the framework to determine the uncertainty of turbulent scalar flux models [52]. Other researchers applied the eigenspace perturbation framework to create reliable engineering designs in design optimizations (DUU) [22, 125, 108, 51, 87]. While many applications typically assume ideal gas properties and incompressible flow conditions, Gori [49] applied the framework to non-ideal compressible flow. Most of the applications used fully turbulent RANS simulations, but Chu et al. [18, 19] applied the eigenvalue perturbation in transitional flows, which required the coupling with a dedicated transition model. Furthermore, Gori et al. [50] analyzed the sensitivity of the estimated uncertainties with respect to time and space resolution.

Even though, marker functions can be used for identifying flow regions within the simulation domain that are prone to inaccurate model-predictions to apply derived non-uniform perturbations [36, 54], the majority of researchers have favored the usage of a uniform but relative perturbation magnitude (Δ_B) for the eigenvalue perturbation. However, Huang et al. [65] introduced a novel approach by prescribing an absolute perturbation radius within the barycentric triangle, offering a distinct distance for the perturbations towards every turbulent target state. Adopting the concept of non-uniform, local perturbations, researchers also tried to improve the uncertainty estimation based on the eigenspace perturbation framework by adding data-driven machine learning techniques [61, 32]. Recently, Bidar et al. [7] applied the EPF to appropriately place probes at locations showing increased sensitivity with respect to changes in Reynolds stress tensor's eigenspace. By doing this, they were able to significantly reduce the amount of probe data points needed in order to correct the turbulence model using field inversion techniques. Moreover, other researchers aimed to broadening the view of the overall uncertainty in CFD by accounting for mixed aleatoric (e.g. boundary conditions) and epistemic (turbulence model) uncertainties in conjunction with the eigenspace perturbations [55, 57].

As the fundamentals of the eigenspace perturbation, which is the actual representation of the Reynolds stress tensor in its eigenspace, inspired another research group around Prof. Xiao to focus on Bayesian statistics to infer posterior distributions of the Reynolds stresses based on available observation data for QoI [170, 163]. Furthermore, they applied random matrix approaches relying on the realizability constraints, where the uncertainties are directly injected into the Reynolds stress tensor [159, 171]. Last but not least, the eigenspace decomposition of the Reynolds stress tensor was used to achieve more accurate RANS predictions with the help of machine learning [153, 165, 166, 69], keeping in mind the ill-conditioning of the RANS equations [167, 13].

3.5.4. Details on the implementation in TRACE

The schematic of the implemented EPF in the solver suite TRACE is presented in Fig. 3.8. The perturbation of the eigenspace happens every iteration, representing the pseudo-time for the considered steady RANS computation, on a cell-by-cell basis. The calculation of the turbulent eddy viscosity ν_T follows the solution of the RANS equations and the subsequent update of the turbulence model's transport equations for k and ω. Using the turbulence quantities k and ν_T in combination with the velocity gradients, the anisotropy tensor $\mathbf{a}$ can be determined, relying on Eq. (3.13) and Eq. (3.16). The eigenvalue problem is efficiently solved using the LAPACK library [2]. In order to obtain perturbed spectral properties, the EPF requires a couple of inputs, which are normally based on user decisions. But, as shown in Chapter 4, the inputs can also be prescribed by any kind of machine learning model. The determination of perturbed eigenvalues requires the selection of the target state with respect to the turbulence componentiality (1C, 2C, 3C) and the amount of altering the eigenvalues towards these special states. The latter is done via a relative perturbation magnitude Δ_B, ranging from 0 to 1, according to Eq. (3.25). Based on the derivations in Chapter 6, the latest version of the implementation of the EPF in TRACE requires a rotation angle α in order to rotate $\mathbf{\Lambda}$ around the second eigenvector[17]. Once the eigenspace has been perturbed, the reconstruction of the anisotropy and the Reynolds stress tensor is performed according to Eq. (3.24) by setting $k^* = k$. The perturbed Reynolds stress tensor essentially affects the subsequent solution step of the set of equations via two contributions:

---

[17] The implementation used for the simulations in Chapter 4 and Chapter 5 relied on the suggested implementation by Iaccarino et al. [66]. However, as shown in Chapter 6, their approach is equivalent to choosing $\alpha = \pi/2$.

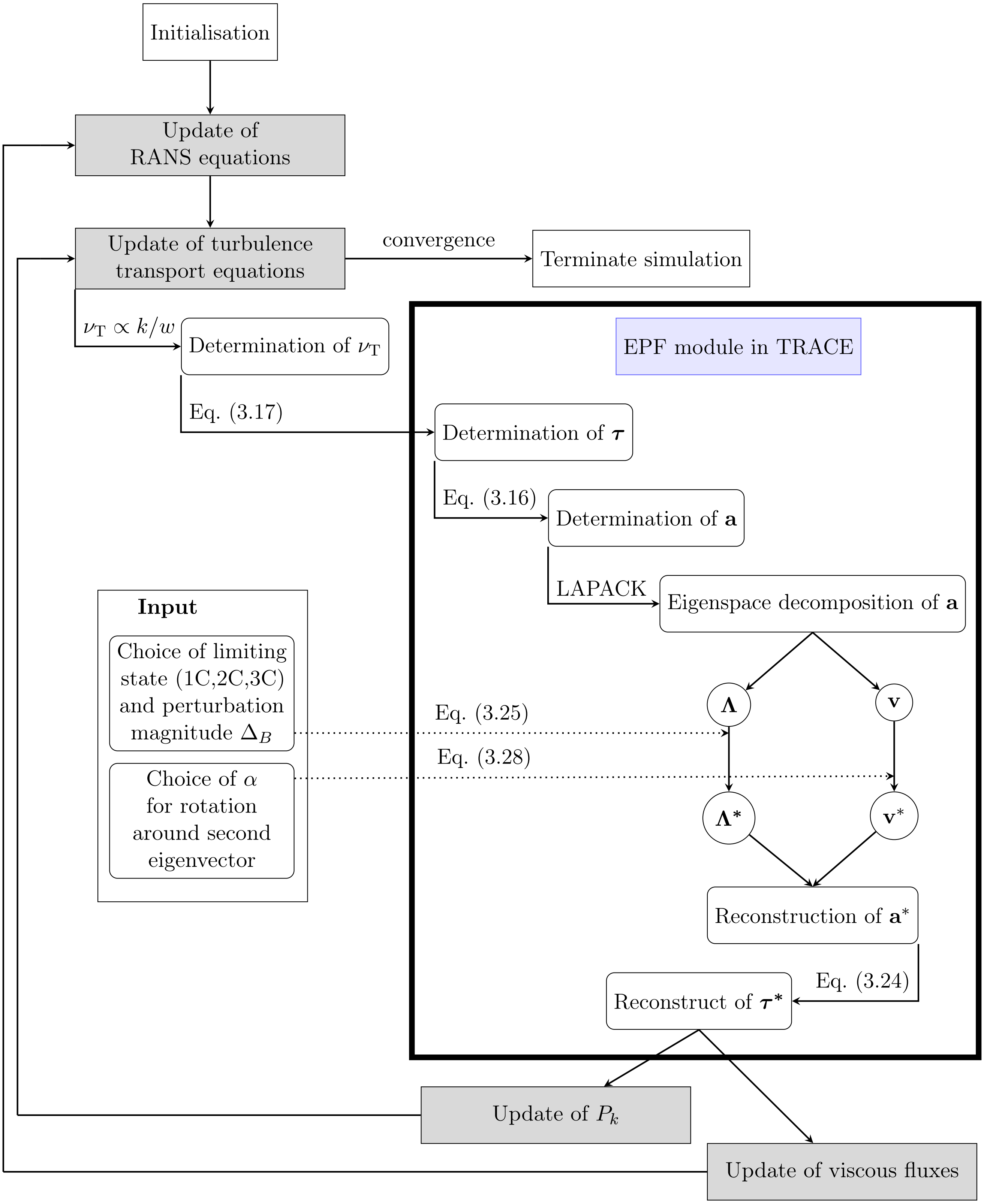
Initialisation
Update of RANS equations
Update of turbulence transport equations
convergence
Terminate simulation
$\nu_\mathrm{T} \propto k/w$
Determination of ν_T
Eq. (3.17)
EPF module in TRACE
Determination of $\boldsymbol{\tau}$
Eq. (3.16)
Determination of $\mathbf{a}$
LAPACK
Eigenspace decomposition of $\mathbf{a}$
Input
Choice of limiting state (1C,2C,3C) and perturbation magnitude Δ_B
Choice of α for rotation around second eigenvector
Eq. (3.25)
Eq. (3.28)
$\boldsymbol{\Lambda}$
$\mathbf{v}$
$\boldsymbol{\Lambda}^*$
$\mathbf{v}^*$
Reconstruction of $\mathbf{a}^*$
Eq. (3.24)
Reconstruct of $\boldsymbol{\tau}^*$
Update of P_k
Update of viscous fluxes

Figure 3.8.: Flow chart of the final implemented version of the EPF in TRACE.

- Because of the similarity of the viscous and the turbulent stresses modeled via the Boussinesq assumption (compare Eq. (3.4) and Eq. (3.17)), LEVMs usually consider only the deviatoric part of the Reynolds stress tensor (neglecting the main diagonal entries $2/3k$). Thus, the eddy viscosity is added to the dynamic viscosity of the fluid resulting in an effective viscosity[18]. However, when the EPF is applied, the Reynolds stresses occurring in the Favre-averaged momentum and energy equation are explicitly replaced by the available perturbed tensor, thus the main diagonal entries of the Reynolds stress tensor are considered as well (see Hirsch [62] and Blazek [9] for details). As TRACE solves the RANS equations using a cell-centered finite-volume method, volume sources and fluxes over the surfaces of each control volume contribute to the balance of the integral conservation formulation of the RANS equations. Consequently, it is the viscous flux, consisting of the viscous stress and the Reynolds stress tensor, which is updated using the EPF (see Fig. 3.8). Although the transport equations of the turbulence model are still updated and solved, the derived eddy viscosity does not directly affect the RANS equations anymore. Solely, the eddy viscosity is used for the implicit part of the pseudo-time derivative of the conservative variables of the momentum and energy equations, in order to stabilize the numerics[19]. As soon as the simulation reaches a converged state, this implicit part is of no consequence and the solution is only affected by the actual perturbed Reynolds stress tensor.

- The initially approximated relationship of the production term of the turbulent kinetic energy transport equation is based on the turbulent eddy viscosity and velocity gradients according to Menter et al. [104]. Relying on the actual perturbed Reynolds stresses in the EPF replaces this approximated relationship by the exact formulation in Eq. (3.21).
  According to Wilcox [161], negative source terms of the turbulence model's transport equations are linearized, while positive ones are treated explicitly. Although the eigenvector rotation, developed in Chapter 6, is derived to prevent negative contributions of P_k in boundary layers, the turbulence production term can become negative in principle. Hence, the turbulence production term needs to be linearized. Similar to the procedure proposed by Morsbach [112], differentiating the production term with respect to ρk leads to the linearized contribution

  $$\frac{\partial \rho P_k^*}{(\partial \rho k)} = \frac{\partial \left(-\rho \tau_{ij}^* S_{ij}\right)}{(\partial \rho k)} = -\left(a_{ij}^* + \frac{2}{3}\delta_{ij}\right) S_{ij} \; . \tag{3.34}$$

  The production limiter proposed by Menter et al. [104][20] for stagnation regions, limiting the actual production term to ten times the destruction term of the k transport equations, is retained in the current implementation.

Although the implemented EPF perturbs the Reynolds stress tensor on a cell-by-cell basis, some adjustments have to be included at the boundaries as well. As the framework is implemented in TRACE's block-structured, cell-centered finite-volume code (see e.g.

---

[18] To be precise: This means that the pressure in the momentum equation is now represented by $p+\frac{2}{3}\rho k$ [6]. However, the turbulent kinetic energy contribution is neglected, when considering unperturbed LEVMs in TRACE.

[19] As the consideration of perturbed Reynolds stresses is similar to the incorporation of Reynolds stresses originating from RSMs; details on the implementation in TRACE are given by Morsbach [112].

[20] Menter [103] postulated earlier that he carefully tested the limitation. He came to the conclusion that the actual production reaches a maximum level of two times the destruction term inside shear layers even for complex flows.

Section 7.3.2 for some details on the applied methods), it requires the specification of values in neighboring grid cells outside of the computational domain, called ghost cells [62]:

- **Inflow/Outflow/Far-field/Mixing plane** In order to obtain net zero viscous fluxes due to the perturbed Reynolds stress tensor for these interfaces, its values in these outer ghost cells are set to the identical ones as for the inner cells. The respective boundary conditions for k and ω of the underlying turbulence model remain unchanged at the outer boundaries of the computational domain (inlet/outlet/far-field). At mixing planes, representing the interfaces between rotating and non-rotating components used for many steady RANS studies [25], the turbulent transport quantities k and ω are circumferentially averaged at defined radial positions and communicated to the downstream component.
- **Rotational periodic boundaries/non-matching (zonal) interfaces** If neighboring panels for rotational configurations are considered, the perturbed Reynolds stresses require special treatment due to the tensor properties. Therefore, the values in the respective ghost cells are computed via a base transformation between these panels, similar to the implementation for RSMs by Morsbach [112].
- **Solid walls** Because of the no slip condition at solid wall boundaries, all the components of the Reynolds stress tensor are set to zero at the wall.

4. Evaluation of physics-constrained data-driven methods for turbulence model uncertainty quantification

(Published in *Computers & Fluids*, 255, 105837, 2023[1].)

M. Matha, K. Kucharczyk, C. Morsbach
DLR, Institute of Propulsion Technology, Cologne, Germany

Abstract

In order to achieve a virtual certification process and robust designs for turbomachinery, the uncertainty bounds for CFD have to be known. The formulation of turbulence closure models implies a major source of the overall uncertainty of RANS simulations. We discuss the common practice of applying a physics-constrained eigenspace perturbation of the Reynolds stress tensor in order to account for the model-form uncertainty of turbulence models. Since the basic methodology often leads to overly generous uncertainty estimates, we extend a recent approach of adding a machine learning strategy. The application of a data-driven method is motivated by striving for the detection of flow regions that are prone to suffer from a lack of turbulence model prediction accuracy. In this way any user input related to choosing the degree of uncertainty is supposed to become obsolete. This work especially investigates an approach, which tries to determine an *a priori* estimation of prediction confidence, when there is no accurate data available to judge the prediction. The flow around the NACA 4412 airfoil at near-stall conditions demonstrates the successful application of the data-driven EPF. Furthermore, we especially highlight the objectives and limitations of the underlying methodology.

4.1. Introduction

In previous times, engineering design applications tried to account for a variety of uncertainties in CFD simulations by applying factors of safety, margins of safety and levels of redundancy. Such heuristic methods need adjustments and recalibration for each new configuration. They are also highly empirical, especially when applied to innovative designs or new flow configurations. Nowadays, methodologies such as robust design or reliability-based design have the possibility to preempt such methods. In recent years, the interest in UQ, leading to more reliable simulation-based designs, has grown significantly [71, 119, 36, 169].

As a compromise between computational time and accuracy, RANS-based turbulence modeling is still the prevailing tool in industrial design of turbomachinery, as the replacement of RANS by SRS, e.g. DNS or LES cannot be expected for design optimization

---

[1] Copyright Elsevier

simulations in the near future. The derivation of the RANS equations reveals an unclosed term, called the Reynolds stress tensor. This tensor has to be approximated in CFD simulations by applying turbulence models. The prediction quality of the simulation is highly dependent on the accuracy of the turbulence models. However, many RANS-based models suffer from the inability to replicate fundamental turbulent processes. Throughout this paper, we consider LEVMs, which are widely used for complex engineering flows, by referring to RANS turbulence models. Due to simplifying assumptions used in the formulation of such models, the turbulence model is one of the main limitations in striving for the next generation of reliable, efficient and environmentally friendly design. These simplifications are the result of data observation, physical intuition, engineering and computational pragmatism, leading to a significant degree of epistemic uncertainty. Accounting for the uncertainties that arise due to the structural form of the turbulence model in RANS simulation is known to be the 'greatest challenge' in CFD [172]. Nevertheless, these epistemic uncertainties could, in principle, be reduced, by increasing knowledge about turbulent processes, resulting in developing advanced models. This is contrary to aleatory uncertainties, e.g. manufacturing tolerances or operating conditions, which cannot be reduced and are not considered in the current work. Different approaches try to account for the uncertainty of the turbulence model at different modeling levels [29]. Generally, one distinguishes between parametric and non-parametric approaches. While the parametric uncertainties arise from the chosen closure coefficients and their calibration process, non-parametric methodologies directly investigate the uncertainties on the modeled Reynolds stress tensor and its functional relationship. It is expected that the possible solution space, with respect to the uncertainty of the turbulence model, is larger for non-parametric approaches [169].

Iaccarino and co-workers proposed an EPF, which is based on the inability of common LEVMs to deal with Reynolds stress tensor anisotropy [34, 66]. This methodology belongs to the non-parametric approaches, as it tries to account for the uncertainty due to the closure model-form itself. The physical rationale of the EPF is discussed in-depth by Mishra and Iaccarino [106]. It enables a designer to optimize components towards an optimum design with less sensitivity to uncertainty. Successful application of DUU using the perturbation framework was already presented by Mishra et al. [108]. Moreover, this methodology was applied in multiple engineering applications such as aerospace design (aircraft nozzle [66], turbomachinery [35, 125], entire aircraft [113]), civil structural design [80] and even wind farm design [31, 64]. The increasing availability of high-fidelity simulations (such as LES and DNS) in combination with the emergence of machine learning strategies guided the path towards data-driven approaches also for the RANS turbulence modeling community [29]. Heyse et al. [61] enhanced the uncertainty estimation based on the eigenspace perturbation approach by adding a data-driven method leading to less conservative uncertainty estimates. The machine learning strategy should identify flow regions that are prone to show reduced turbulence model prediction accuracy. From our point of view, their investigations suffered under limited availability of data, most notably with respect to judging an appropriate application of a machine learning model. We consolidate the usage of a random forest regression model by investigating the credibility explicitly in the present work.

In the current work, we present details on the functionality of the eigenspace perturbation methodology, its data-driven extension and its implementation within the CFD solver suite TRACE developed by the DLR in strong cooperation with MTU Aero Engines AG. TRACE is being developed by the Institute of Propulsion Technology with focus on turbomachinery flows and offers a parallelized, multi-block CFD solver for the compressible

RANS equations [112]. In order to obtain a trustworthy quantification of uncertainties for future design application in turbomachinery flows, we investigate our implementation of the data-driven Reynolds stress tensor perturbation framework for flow configurations featuring adverse pressure gradient, flow separation and reattachment with TRACE. This procedure is reasonable, as the prediction accuracy of RANS turbulence models is significantly reduced in the presence of these complex flow phenomena. In order to further advance the data-driven prediction capabilities, additional data sets obtained by SRS of relevant test cases are used to train and validate a machine learning model. These test cases include complex flow physics such as adverse pressure gradient, separation and reattachment. In this work, we verify the application of a trained machine learning model in detail. A methodology to quantify an *a priori* estimate of prediction confidence is particularly studied as well. Finally, the data-driven perturbation approach to estimate the epistemic uncertainty of turbulence models is applied for the flow around the NACA 4412 airfoil at near-stall conditions featuring a separation zone on the suction surface. By analyzing and comparing the uncertainty estimates for certain QoI with respect to the usage of the data-free and data-driven strategy, we analyze the initial intention of the Reynolds stress tensor perturbation framework and its capabilities consequently. From our point of view, this kind of subsumption was missing in the literature oftentimes.

4.2. Details of the Eigenspace Perturbation Framework

4.2.1. Motivation and goal

RANS turbulence models are utilized in order to approximate the Reynolds stress tensor $\tau_{ij} = \widetilde{u_i'' u_j''}$ in terms of mean flow quantities, e.g. $\widetilde{u_i} = U_i = u_i - u_i''$. As already described, the formulation of turbulence models brings along certain assumptions. For example, even state-of-the-art LEVMs rely on the eddy viscosity hypothesis, also known as the Boussinesq assumption, and the gradient diffusion hypothesis. This leads to the inability to account for rotational effects, secondary flow, swirl and streamline curvature [146, 109, 23]. Besides, limited success in cases with separation and reattachment have also been reported [89]. The motivation for injecting perturbations to the eigenspace of the Reynolds stress tensor is the inability of LEVMs to account correctly for the anisotropy of Reynolds stresses. This is due to the Boussinesq assumption, approximating the turbulent stresses in similar manner to the molecular viscous stresses. The Boussinesq approximations reads

$$\tau_{ij} = -2\nu_{\mathrm{T}} \left(S_{ij} - \frac{1}{3} \frac{\partial u_k}{\partial x_k} \delta_{ij} \right) + \frac{2}{3} k \delta_{ij} \ , \tag{4.1}$$

where the turbulent kinetic energy is defined as $k = \frac{1}{2}\tau_{ii}$ and summation over recurring indices within a product is implied. The strain-rate tensor is denoted as S_{ij} and the eddy viscosity, derived from the transport equations of the turbulence model, is represented by ν_{T}.

Because of the epistemic uncertainty that is introduced into turbulence models by the choice of the actual closure model [29], the perturbation approach tries to derive and quantify the effects on QoI, e.g. the pressure field, by modifying the anisotropy of turbulence within physical limitations. The implemented framework for UQ of turbulence models seeks to sample from solutions, resulting from a modified underlying structure of the turbulence model, while aiming for extreme states of the Reynolds stress tensor [106]. In this manner a CFD practitioner may get the chance to estimate the sensitivity of some QoI regarding the uncertainty in predicting the Reynolds stress anisotropy. In the

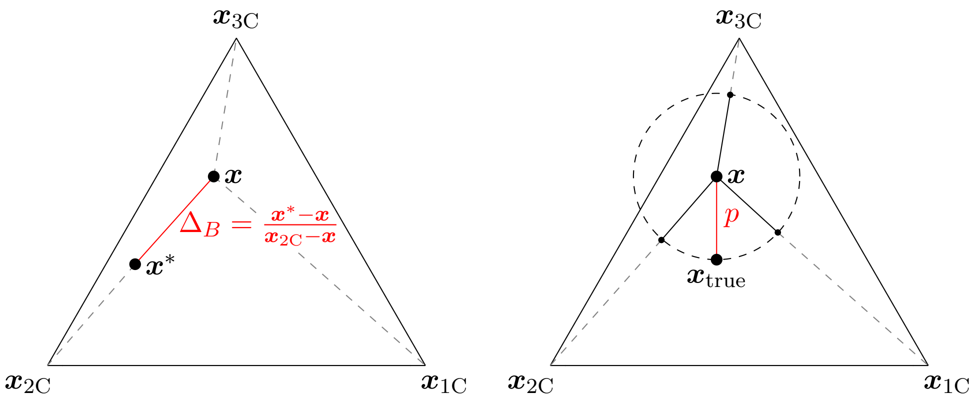
$\boldsymbol{x}_{3\mathrm{C}}$
$\boldsymbol{x}$
$\Delta_B = \frac{\boldsymbol{x}^*-\boldsymbol{x}}{\boldsymbol{x}_{2\mathrm{C}}-\boldsymbol{x}}$
$\boldsymbol{x}^*$
$\boldsymbol{x}_{2\mathrm{C}}$
$\boldsymbol{x}_{1\mathrm{C}}$
$\boldsymbol{x}_{3\mathrm{C}}$
$\boldsymbol{x}$
p
$\boldsymbol{x}_{\mathrm{true}}$
$\boldsymbol{x}_{2\mathrm{C}}$
$\boldsymbol{x}_{1\mathrm{C}}$

(a) Unperturbed and perturbed state (b) Definition of perturbation strength

Figure 4.1.: Schematic representation of the eigenvalue perturbation approach.

following section we explain how to obtain a perturbed state of the Reynolds stress tensor and how to apply machine learning in order to get a better-informed, less conservative uncertainty prediction.

4.2.2. Data-free approach

The symmetric Reynolds stress tensor can be expressed by applying an eigenspace decomposition as

$$\tau_{ij} = k\left(a_{ij} + \frac{2}{3}\delta_{ij}\right) = k\left(v_{in}\Lambda_{nl}v_{jl} + \frac{2}{3}\delta_{ij}\right) \quad . \tag{4.2}$$

Equation (4.2) includes the split into the anisotropy tensor a_{ij} and the isotopic part of τ_{ij}. The eigenspace decomposition provides the eigenvector matrix $\mathbf{v}$ and the diagonal eigenvalue matrix $\boldsymbol{\Lambda}$, where the eigenvalues represent the shape and the eigenvectors imply the orientation of the tensor. Emory et al. [34] propose a strategy to perturb the eigenvalues and eigenvectors in Eq. (4.2), resulting in a perturbed state of the Reynolds stress tensor

$$\tau^*_{ij} = k\left(v^*_{in}\Lambda^*_{nl}v^*_{jl} + \frac{2}{3}\delta_{ij}\right) \quad . \tag{4.3}$$

The eigenvalue perturbation (determining $\boldsymbol{\Lambda}^*$) makes use of the fact that every physical, realizable state of the Reynolds stress tensor can be mapped onto barycentric coordinates

$$\boldsymbol{x} = \boldsymbol{x}_{1\mathrm{C}}\frac{1}{2}\left(\lambda_1 - \lambda_2\right) + \boldsymbol{x}_{2\mathrm{C}}\left(\lambda_2 - \lambda_3\right) + \boldsymbol{x}_{3\mathrm{C}}\left(\frac{3}{2}\lambda_3 + 1\right) \quad \text{with} \quad \lambda_1 \geq \lambda_2 \geq \lambda_3 \ , \tag{4.4}$$

which is essentially a linear transformation according to $\boldsymbol{x} = \mathbf{Q}\boldsymbol{\lambda}$ (whereby three eigenvalues λ_i are represented by the vector $\boldsymbol{\lambda}$ and $\mathbf{Q}$ depends on the choice of coordinates $\boldsymbol{x}_{1\mathrm{C}}, \boldsymbol{x}_{2\mathrm{C}}$ and $\boldsymbol{x}_{3\mathrm{C}}$) [4]. Figure 4.1a shows the three limiting states of the Reynolds stress tensor, represented by the corners of the triangle ($\boldsymbol{x}_{1\mathrm{C}}, \boldsymbol{x}_{2\mathrm{C}}, \boldsymbol{x}_{3\mathrm{C}}$), corresponding to the one-, two- and three-component (isotropic) turbulent states (1C, 2C and 3C). Thus, Iaccarino and co-workers [34, 66] defined the eigenvalue perturbation as a shift in barycentric coordinates towards each of the limiting states to location $\boldsymbol{x}^*$, according to

$$\boldsymbol{x}^* = \boldsymbol{x} + \Delta_B\left(\boldsymbol{x}_{(\mathrm{t})} - \boldsymbol{x}\right) \quad . \tag{4.5}$$

The relative distance $\Delta_B \in [0, 1]$ controls the magnitude of eigenvalue perturbation towards the corner state $\boldsymbol{x}_{(\mathrm{t})} \in \{\boldsymbol{x}_{1\mathrm{C}}, \boldsymbol{x}_{2\mathrm{C}}, \boldsymbol{x}_{3\mathrm{C}}\}$. The perturbed eigenvalues λ_i^* can be remapped by

$$\boldsymbol{\lambda}^* = \mathbf{Q}^{-1}\boldsymbol{x}^* \ . \tag{4.6}$$

The creation of the perturbed eigenvector matrix $\mathbf{v}^*$ is purely motivated by manipulating the turbulence production term $P_k = -\tau_{ij}\frac{\partial U_i}{\partial x_j}$. Changing the alignment of the eigenvectors of the Reynolds stress tensor and the strain-rate tensor $\mathbf{S}$ limits the production term to a maximum and minimum value [66]. Maximum turbulence production is obtained by not changing the eigenvectors of the Reynolds stress tensor. Commuting the first and the last eigenvector of the Reynolds stress tensor leads to minimum turbulence production:

$$\begin{aligned} \mathbf{v}_{\mathrm{max}} &= \begin{pmatrix} \boldsymbol{v_1} & \boldsymbol{v_2} & \boldsymbol{v_3} \end{pmatrix} \rightarrow P_{k_{\mathrm{max}}} \\ \mathbf{v}_{\mathrm{min}} &= \begin{pmatrix} \boldsymbol{v_3} & \boldsymbol{v_2} & \boldsymbol{v_1} \end{pmatrix} \rightarrow P_{k_{\mathrm{min}}} \ . \end{aligned} \tag{4.7}$$

When combining the eigenvalue and eigenvector perturbation, not only the shape of the Reynolds stress ellipsoid is modified but also the relative alignment with the principal axes of the mean rate of the strain tensor is changed (orientation). It should be noted that targeting the 3C turbulent state with $\Delta_B = 1$ results in identical eigenvalues and consequently the eigenvector matrix cancels out with its inverse. That is the reason, why there will be no distinction between minimized and maximized turbulence production.

To sum up, the data-free perturbation framework promises to only need five distinct simulations $\in \{(1\mathrm{C}, P_{k_{\mathrm{max}}}),\ (1\mathrm{C}, P_{k_{\mathrm{min}}}),\ (2\mathrm{C}, P_{k_{\mathrm{max}}}),\ (2\mathrm{C}, P_{k_{\mathrm{min}}})$ and $3\mathrm{C}\}$, in order to get the entire information with reference to the epistemic uncertainty of the underlying turbulence model, if $\Delta_B = 1$ is chosen.

4.2.3. Data-driven approach

The eigenspace perturbation approach is a purely physics-based methodology, aiming for understandable uncertainty bounds for the turbulence modeling community. The data-free procedure applies a uniform perturbation to the entire flow domain. But the perturbation amplitude is a reflection of the inability of the turbulence model to reproduce the underlying physics with high fidelity. This discrepancies between the turbulence model's dynamics and those of the turbulence physics are not uniform, but differ between different turbulent flows and even across different regions of the same flow. Thus, enabling variation in the magnitude of the perturbations is a better reflection of the actual model-form uncertainty. As an additional advantage, if executed correctly, such a varying perturbation approach would enable more precise and less conservative uncertainty bounds on the QoI. Moreover, a user has to choose the degree of uncertainty by selecting Δ_B before each investigation, which is major drawbacks of the proposed method. This might be especially unfavorable in the design phase of turbomachinery components, when even a CFD practitioner experienced in turbulence modeling does not know *a priori* how to set the degree of uncertainty.

Consequently, the user defined bounds on the eigenspace perturbation procedure need to be replaced. Data-driven modeling approaches can be very beneficial for such surrogate modeling. Such machine learning surrogate models have found wide application in turbulence modeling [29, 68, 15]. As the amount of high-fidelity simulations (such as LES and DNS) increases, this data can be used to estimate the perturbation magnitudes. Heyse et al. [61] propose a strategy to obtain a locally varying perturbation strength by using a random forest model. Physical flow features are extracted to train a machine learning model in order to predict the local perturbation strength

$$p = ||\boldsymbol{x}_{\mathrm{true}} - \boldsymbol{x}_{\mathrm{RANS}}|| = ||\boldsymbol{x}^*_{\mathrm{RANS}} - \boldsymbol{x}_{\mathrm{RANS}}|| \ , \tag{4.8}$$

as illustrated in Fig. 4.1b. Forward propagating CFD simulations follow training the model, where the predicted perturbation strength is used to modify the Reynolds stress towards the same three limiting states as in the data-free approach.
In this work, we go several steps beyond the initial proposed strategy. First of all, Heyse et al. [61] applied pure eigenvalue perturbation of the anisotropy tensor. We combine the data-driven eigenvalue perturbation with the data-free manipulation of the eigenvectors of the Reynolds stress tensor, as already described above. From our point of view, this procedure is inevitable, as the assumption that the Reynolds stress tensor and the mean rate of strain tensor share their eigenvectors (see Eq. (4.1)), is known to be invalid in flow situations, where streamline curvature, rotational effects, flow separation or reattachment play a role [84]. We decided against utilizing machine learning to adjust the perturbations for the eigenvectors of the Reynolds stress tensor and the turbulent kinetic energy directly, as this would lead to a data-augmented, corrected turbulence model instead of obtaining uncertainty estimates. Since no justifiable bounds for the turbulent kinetic energy budget exist, the present methodology perturbs it indirectly by applying the described eigenvector manipulation. Furthermore, we evaluate the adequate usage of a machine learning model for the desired application by extending the training data set and performing certain verification checks. The latter also includes the question, how to build trust in such a trained machine learning model, when there is no accurate data available anymore to estimate the prediction error. Finally, we assess the limitations and capabilities of this method.

Choice of machine learning model

The general concept of machine learning is to approximate the relationship between input quantities (features) and output quantities (targets) to make prediction under similar conditions. There are multiple approaches to approximate these relationships. For the sake of interpretability and usability, decision trees are chosen to be the machine learning model in the present work. Decision trees (also called regression trees for solving regression problems) learn binary rules (if/else decision rules) to predict target values based on given features [11]. Decision trees are prone to overfitting, which means that the model is not able to generalize. A machine learning model is able to generalize, if it performs adequate predictions based on a feature space that is different than the feature space of the training data. Machine learning models that are prone to overfitting reveal a high variance. The potential accuracy of a machine learning model is also dependent on its bias that is characterized by the difference between the averages of the predictions and the true values. An inflexible model is not capable to fit the total number of data sufficiently, which is determined as a high bias of the model. The fact that an increasing flexibility (lower bias) comes along with worse generalization (high variance), is known as the bias-variance trade-off. This trade-off describes the aim to choose a machine learning model that has low variance and low bias simultaneously [48, 91]. Random forests are based on a number of uncorrelated regression trees and offer the possibility to handle the bias-variance trade-off, while enabling powerful predictions [91]. For this reason, we have chosen to use this ensemble learning technique. Instead of just averaging the prediction of individual regression trees, a random forest makes use of two essential key concepts:

- Bootstrapping: Random sampling (with replacement) of the training data for each individual tree, i.e. each tree is trained on a different data set with equal size.

- Feature bagging: Random subsampling of features at each decision point (also known as split) for each tree, i.e. every tree uses a different feature space at each binary decision.

In combination with bootstrap aggregation (bagging), which implies averaging the prediction of a number of bootstrapped regression trees, the variance is reduced and overfitting is avoided [12]. In this work, the python library *scikit-learn* [122] is used to train the random forests and evaluate their predictions.

Choice of flow features

The selection of input features, which are relevant for predicting more accurate perturbation magnitude p, is critical for turbulence modeling purposes. It has to be ensured that the chosen features represent physical significance with respect to the desired target (output) quantity. Wu et al. [165] identified four raw quantities

$$\mathcal{Q} = (\mathbf{S}, \boldsymbol{\Omega}, \nabla p, \nabla k) \tag{4.9}$$

to be a reasonable choice as input data for conducting machine learning based on LEVMs. The two raw input tensors $\mathbf{S}$, $\boldsymbol{\Omega}$ represent strain-rate and rotation-rate, while ∇p and ∇k are the gradients of pressure and turbulent kinetic energy. In our work, we agree on the usage of $\mathcal{Q}$ and make use of the normalization scheme, derived by Ling and Templeton [90]. A normalization by a factor β and the absolute value[2] of each element α of $\mathcal{Q}$ according to

$$\hat{\alpha} = \frac{\alpha}{|\alpha| + |\beta|} \tag{4.10}$$

lead to the determination of non-dimensional flow features, which are presented in Table 4.1.

Table 4.1.: Raw flow features for constructing the invariant basis.

Description	Normalized input $\hat{\alpha}$	raw input α	normalization factor β
Strain-rate	$\hat{\mathbf{S}}$	$\mathbf{S}$	ω
Rotation-rate	$\hat{\boldsymbol{\Omega}}$	$\boldsymbol{\Omega}$	$\lvert\lvert\boldsymbol{\Omega}\rvert\rvert$
Pressure gradient	$\widehat{\nabla p}$	∇p	$\rho\lvert\lvert\boldsymbol{U} \cdot \nabla \boldsymbol{U}\rvert\rvert$
Turbulent kinetic energy gradient	$\widehat{\nabla k}$	∇k	$\omega\sqrt{k}$

Since we are aiming for invariant features, which means that they should stay the same in different inertial frames of reference, it is essential to embed invariance properties into a machine learning model (if the model should not learn these properties during training). One method to do this is by formulating inputs and output quantities of the model such that they are invariant. In order to determine the invariant feature basis of the normalized flow features, Wu et al. [165] make use of the Hilbert basis theorem. This theorem states that a finite number of invariants belongs to each minimal integrity basis for a finite tensorial set [144]. A minimal integrity basis is the minimal set of invariants that represent all polynomial invariants associated with a tensorial set under transformation. In this manner the minimal integrity basis amounts to 47 invariants, which are in the following used as input features for training and evaluating the random forest. We add additional physical meaningful flow features to this exhaustive list of

---

[2] If α is a vector or tensor, the euclidean norm is used.

Table 4.2.: Physical flow features.

Numbering	Description	raw input α	normalization factor β
q_1	Q-criterion	$\frac{1}{2}\left(\|\|\mathbf{\Omega}\|\|^2 - \|\|\mathbf{S}\|\|^2\right)$	$\|\|\mathbf{S}\|\|^2$
q_2	Turbulent kinetic energy	k	$\frac{1}{2}U_iU_i$
q_3	Wall-distance based Reynolds Number	$\min\left(\frac{\sqrt{k}d}{50\nu}, 2\right)$	-
q_4	Pressure gradient along streamline	$U_k\frac{\partial p}{\partial x_k}$	$\sqrt{\frac{\partial p}{\partial x_j}\frac{\partial p}{\partial x_j}U_iU_i}$
q_5	Turbulent time scale	$\frac{1}{\omega}$	$\frac{1}{\|\|\mathbf{S}\|\|}$
q_6	Production term	P_k	$k\omega$
q_7	Mach number	Ma	-
q_8	Eddy viscosity	μ_T	μ
q_9	Norm of Reynolds stresses	$\|\|\widetilde{u_i''u_j''}\|\|$	k

features based on domain knowledge and physical intuition. The additional input features, which are presented in Table 4.2, can be computed by providing the turbulent kinetic energy k, the specific turbulent dissipation rate ω, the molecular viscosity μ, the eddy viscosity μ_T, the distance to the nearest wall d, the local Mach number Ma, the mean velocity $\boldsymbol{U}$ and its gradient tensor and the mean pressure p and its gradient vector. The normalization procedure is retained in accordance to Eq. (4.10). Thus, a total number of 56 input features is used for training and evaluating the random forests. Lastly, each feature is standardized by removing the mean and scaling to unit variance by applying a standard scaler preprocessing functionality of *scikit-learn* [122].

Although Wang et al. [160] reported significant improvements in prediction accuracy for using the invariant feature basis over a smaller number of features (e.g. physical motivated scalars) in a comparable study, we cannot confirm such observations in our work. We rather think that due to the limited number of data (for training and testing purposes) a smaller number of input quantities performs excellently as well. As soon as the diversity of the data starts to increase (significantly different geometries featuring various flow phenomena) the need for a large set of features may occur. Being aware of the fact that the present feature list may be needlessly large, we assure, that this exhaustive list of features does not involve any disadvantages in terms of accuracy. For this reason, we use the total amount of 56 input features in the present work.

4.2.4. Integration of UQ computation in CFD solver suite TRACE

Implementation

The aim of running a CFD simulation, propagating a perturbed Reynolds stress tensor, is to obtain a sensitivity with respect to the solution. For smooth and time-efficient simulations, it is advisable to start the perturbation from a sufficiently converged baseline RANS simulation (baseline means standard unmodified turbulence model). Mishra et al. [107] apply a factor to march the solution based on the perturbed Reynolds stress tensor to a fully converged state. In our implementation, we use a factor f for the reconstruction of Reynolds stresses in order to be able to achieve fully converged perturbed solutions as well. We discuss the necessity and the effect of this factor in Section 4.2.4. The perturbation of the Reynolds stress tensor was implemented to the existing C code of

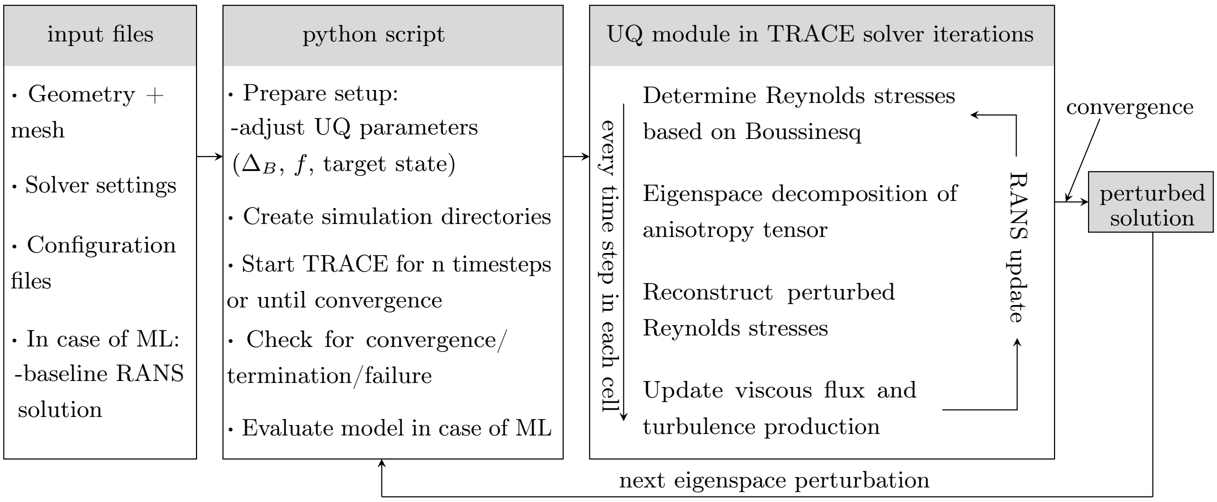
input files
· Geometry + mesh
· Solver settings
· Configuration files
· In case of ML: -baseline RANS solution
python script
· Prepare setup: -adjust UQ parameters (Δ_B, f, target state)
· Create simulation directories
· Start TRACE for n timesteps or until convergence
· Check for convergence/ termination/failure
· Evaluate model in case of ML
UQ module in TRACE solver iterations
every time step in each cell
Determine Reynolds stresses based on Boussinesq
Eigenspace decomposition of anisotropy tensor
Reconstruct perturbed Reynolds stresses
Update viscous flux and turbulence production
RANS update
convergence
perturbed solution
next eigenspace perturbation

Figure 4.2.: Implementation of the UQ framework within the CFD solver suite TRACE.

TRACE and can be subdivided in several steps within each pseudo-time step of steady simulations:

1. Calculate Reynolds stresses based on the Boussinesq approximation (see Eq. (4.1)).
2. Determine the anisotropy tensor (see Eq. (4.2)).
3. Perturb the anisotropy tensor within physical realizable limits by selecting Δ_B (see Eq. (4.5)) and whether the turbulence production term should be minimized or maximized (see Eq. (4.7)).
4. Reconstruct the perturbed Reynolds stress tensor according to

$$\tau^*_{ij_f} = \tau_{ij} + f\left[k\left(a^* + \frac{2}{3}\delta_{ij}\right) - \tau_{ij}\right], \tag{4.11}$$

   where $f \in [0,1]$ is the introduced moderation factor, adjusting the total amount of newly perturbed anisotropy tensor to be considered.

5. Update of the viscous fluxes using the perturbed Reynolds stresses explicitly.
6. Update of the turbulence production term $P_k = -\tau_{ij}\frac{\partial U_i}{\partial x_j}$ using the perturbed Reynolds stresses explicitly.

TRACE features a python interface, called pyTRACE [27], which can be used to conduct a full set of perturbed simulations and sample the results for some QoI. In case of applying a data-driven perturbation of the Reynolds stresses, the python script takes also charge of evaluating a previously in preprocessing trained machine learning model based on extracted mean flow quantities. The high-level python script takes input parameters, containing information regarding the geometry, mesh resolution and additional solver settings. Furthermore, the set of intended perturbed simulations is set up, including selecting the limiting state of turbulence ($\boldsymbol{x}_{(\mathrm{t})} \in \{\boldsymbol{x}_{1\mathrm{C}}, \boldsymbol{x}_{2\mathrm{C}}, \boldsymbol{x}_{3\mathrm{C}}\}$), the relative distance $\Delta_B \in [0,1]$, the alignment of the Reynolds stress eigenvectors with the strain-rate tensor ($\mathbf{v}_{\min}$ or $\mathbf{v}_{\max}$) and the moderation factor $f \in [0,1]$, as described earlier. As illustrated in Fig. 4.2 the integration of the UQ module in the TRACE simulation run is conducted every time step (steady simulation) in each cell of the computational domain. When the converged perturbed solution is reached, the python script takes charge of setting up the next desired perturbation.

Discussion about restrictions of the Reynolds stress tensor perturbations

The eigenspace perturbation methodology, presented in Section 4.2, is solely motivated on quantifying the epistemic uncertainties of LEVMs due to the inaccurate account for anisotropic flow phenomena. Iaccarino and co-worker [34, 66, 107] designed this method based on the mathematical derivations of Lumley [92] and Banerjee et al. [4]. These derivations map the states of the Reynolds stress tensor, when it features one, two or three non-zero eigenvalues, onto corners of a constructed triangle, called the barycentric triangle. These states are described to be the extreme states of the Reynolds stress tensor, as the turbulence is only present in one, two or three directions - the corresponding directions of the eigenvectors.

A CFD practitioner is interested in ascertain the effect of the turbulence model's uncertainty on certain QoI, which are relevant for design. However, the relation between the one-, two- and three-component corner of the Reynolds stress tensor and some QoI is anything but linear. As a consequence, modifying/perturbing the turbulent state of the Reynolds stress tensor seeks to estimate the uncertainty bounds rather than create extreme state of QoI.

Nonetheless, we analyzed the relation of barycentric coordinates and QoI for selected flow cases by sampling points inside the barycentric triangle and propagating the perturbed Reynolds stress tensor in an earlier prior investigation [94][3]. Therefore, assessed against currently available data, we agree on the fact that the corners of the barycentric coordinate produce adequate estimate of the uncertainty bounds in most of the flow regions. Although there might be areas of the flow solution, where the extreme state of turbulence is not corresponding to the extreme state of some QoI. This observation will be also discussed in Section 4.5.

Additionally, we would like to discuss the effect of the moderation factor f, which was initially mentioned by Mishra et al. [107]. The main goal of applying f is to reach a converged solution based on the perturbation approach. We agree on the fact that this factor is needed for convergence issues, as some perturbed states tend to be unstable. Understandably, this is especially the case for perturbations seeking to decrease the turbulence production term ($P_{k_{\min}}$ and/or 3C). Nevertheless, it is shown in the Appendix 4.A that the effect of applying the moderation factor is actually identical to reducing Δ_B in case of pure eigenvalue perturbation. The need for moderating the effect of Reynolds stress tensor perturbation by an additional factor according to Eq. (4.11) emerges, when combining eigenvector and eigenvalue perturbation. Generally speaking, using $f \leq 1$ stabilizes the CFD simulation by weakening the impact of perturbation. Accordingly, users are encouraged to not only state the prescribed Δ_B but also the factor f. It has to be stated, though, that damping the effects of the actual perturbation (eigenvalues and eigenvectors) weakens the interpretability of the limiting states of turbulence, represented by the corners of the barycentric triangle.

Last but not least, the data-driven extension of the EPF is build on Reynolds stress reference data, whereas other machine learning approaches in the field of turbulence modeling utilize indirect mean flow quantities like velocity and pressure. Hence, appropriate training data are mainly limited to well-resolved DNS/LES and cannot make use of experimental measurement data containing no second-moment statistics.

---

[3] As the cited paper is not part of this cumulative dissertation, the underlying study is taken over, expanded and presented in Section 3.5.2 of this thesis.

4.2.5. Data sets for training, testing and applying the machine learning model

As already described in Section 4.1, the final well-trained machine learning model should be sensitive to flow phenomena such as adverse-pressure gradient, separation and reattachment due to the known shortcomings of the LEVMs. Consequently, it is reasonable to use data sets for training that include these flow situations. We are continuously striving for extending our database, which contains various flow cases for machine learning. For the present study, we use the following flow cases:

- DNS of turbulent channel flow at $\mathrm{Re}_\tau \in \{180, 550, 1000, 2000, 5200\}$ based on Lee and Moser [86].
- DNS at $\mathrm{Re}_H \in \{2800, 5600\}$ and LES at $\mathrm{Re}_H = 10595$ of periodic hill flow based on Breuer et al. [14].
- DNS of wavy wall flow at $\mathrm{Re}_H = 6850$ based on Rossi [130].
- DNS of converging-diverging channel flow at $\mathrm{Re}_\tau = 617$ based on Laval and Marquillie [85].

All the DNS and LES data of the described test cases are generated using incompressible solvers. In order to simulate these incompressible flows using the compressible solver TRACE without low-Mach preconditioning, the simulations are scaled (adapting dimensions of the geometry and/or molecular viscosity) to an incompressible Mach number of approximately 0.1, while preserving the intended Reynolds numbers. The two-equation, linear eddy viscosity Menter SST $k-\omega$ turbulence model is selected as the baseline model for all conducted RANS simulations [104]. In order to obtain steady-state solutions, an implicit time marching algorithm is applied. A flux difference splitting approach is employed to discretize the convection terms making use of a second order accurate Roe scheme in combination with MUSCL extrapolation [129, 158].

To evaluate proper features as input parameters based on the RANS simulations, we conducted a mesh convergence study for each of the listed flow cases. Although the mesh convergence studies are not presented here due to the scope of the paper, we affirm that we only use RANS simulation data that shows sufficient grid convergence using a low-Reynolds resolution ($y^+ \leq 1$) at solid walls. The perturbation magnitude p can be determined according to Eq. (4.8) by comparing scale-resolving and RANS solutions. In order to compute the intended target quantity, the scale-resolving data has to be interpolated onto the RANS data points for every test case first. Due to numerical issues some RANS data samples may be located outside the barycentric triangle. Therefore, we included the opportunity to remove these samples from the training or testing sets. The final application of the UQ perturbation approach is presented for the airfoil test case NACA 4412 at $\mathrm{Re}_c = 1.52 \cdot 10^6$.

Turbulent channel

Although we are interested in more complex cases, the channel flow data represents one of the key properties, which the model should be able to recognize and predict: turbulent boundary layer with inaccurate anisotropy represented by the LEVM close to the wall. The configuration for simulating the turbulent boundary layer is sketched in Fig. 4.3. The characteristic Reynolds number is defined as

$$Re_\tau = \frac{\rho u_\tau H}{2\mu} \ , \tag{4.12}$$

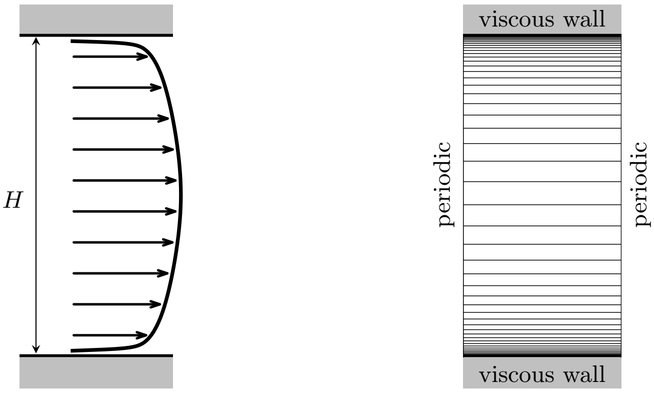

(a) Schematic sketch of a fully developed turbulent boundary layer

(b) $\mathrm{Re}_\tau = 1000$ (every fourth line shown) mesh and boundary conditions; symmetry is enforced in spanwise direction

Figure 4.3.: Schematic turbulent channel flow setup.

where H is the channel height and the friction velocity is known as $u_\tau = \sqrt{(\tau_w/\rho)}$ with $\tau_w = \mu \frac{\partial U}{\partial y}|_{y=\mathrm{wall}}$. The turbulent channel flow is homogeneous in the streamwise direction x and the spanwise direction z. A constant pressure gradient $\partial p/\partial x$ is applied to balance the skin friction at the wall. We use the available RANS grid cells in one half of the channel at the five different Reynolds numbers as subsequent data points for training the random forest.

Periodic hill

The flow over periodic hills features flow separation from curved surfaces, recirculation and a subsequent reattachment on the flat bottom of the channel. Since the Reynolds number has a strong impact on the actual size of the separation bubble, it is worthwhile to add three different Reynolds number flows to our training set.

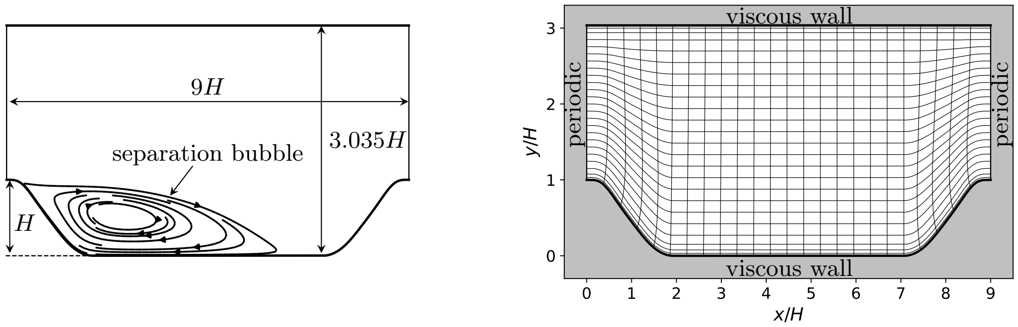

(a) Relative dimensions and sketch of the flow

(b) Mesh ($\mathrm{Re}_H = 10595$, every tenth line shown) and boundary conditions; slip conditions/inviscid walls are applied in spanwise direction

Figure 4.4.: Schematic periodic hill setup.

The Reynolds number based on the bulk velocity U_B, evaluated at the crest of the hill and the hill height H is defined as

$$Re_H = \frac{\rho U_B H}{\mu} \; . \tag{4.13}$$

For simulating the periodic hill configuration, periodic boundary conditions are applied as illustrated in Fig. 4.4. A constant pressure gradient $\partial p/\partial x$ is applied to move the fluid through the configuration. The available scale-resolving data sets of the periodic hill only contain data at certain slices ($x/H \in \{0.05, 0.5, 1.0, 2.0, \; 3.0, 4.0, 5.0, 6.0, 7.0, 8.0\}$). Consequently, the RANS solution is sliced at these locations accordingly. The scale-resolving data are interpolated onto the wall-normal RANS data positions, in order to generate the desired target quantity for the machine learning model.

Wavy wall

The wavy wall test case is confined by a plane wall and a wavy surface, which is sketched in Fig. 4.5. In former experimental settings, the desired flow situation was generated by stringing together multiple hills and valleys, described by a cosine function. For the CFD simulations (DNS and RANS) periodic boundary conditions in streamwise direction can be applied. In order to adjust the intended Reynolds number of $\mathrm{Re}_H = 6850$, based on the bulk velocity and the mean channel height evaluated on the hill crest (according to Eq. (4.13)), a constant pressure gradient $\partial p/\partial x$ is used. Since the available DNS data set is two-dimensional (2D) and covers the entire domain size, we use all available RANS grid cells as subsequent data points for training the random forest.

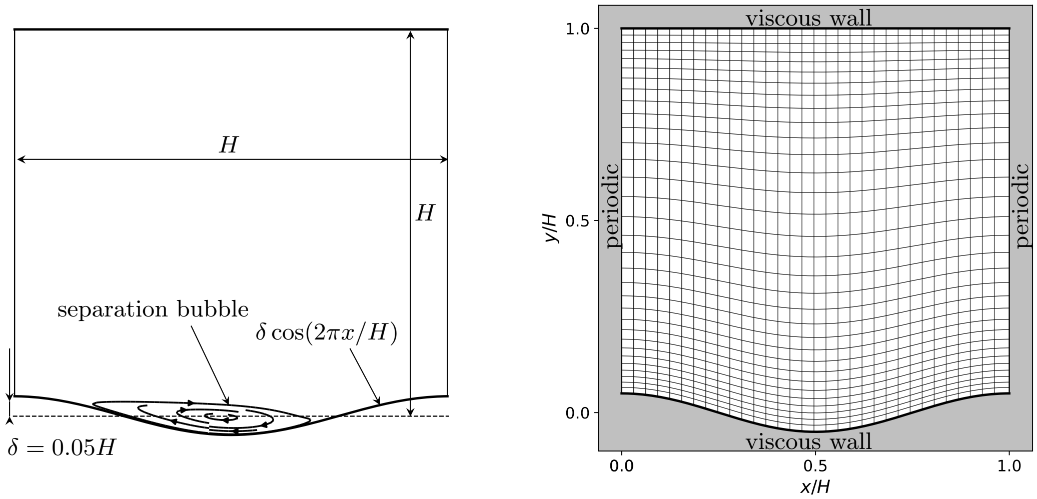

(a) Relative dimensions and sketch of the flow

(b) Mesh (every fourth line shown) and boundary conditions; slip conditions/inviscid walls are applied in spanwise direction

Figure 4.5.: Schematic wavy wall setup.

Converging-diverging channel

The configuration of a converging followed by a diverging section is an ideal test case to investigate the effect of an adverse pressure gradient with and without curvature. The

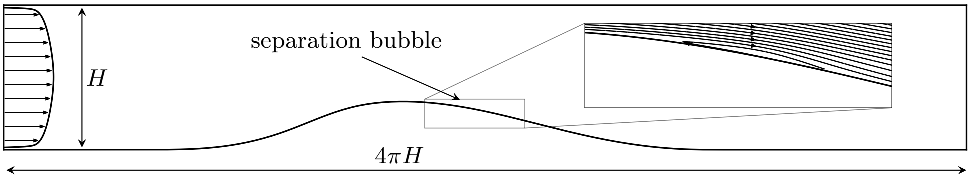

(a) Relative dimensions and sketch of the flow

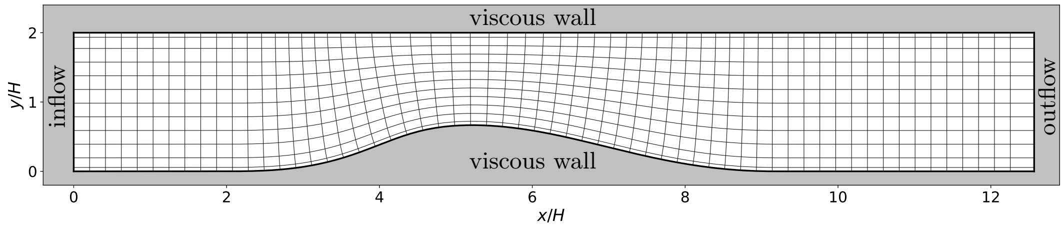

(b) Mesh (every fourth line in streamwise direction and every twentieth line in wall normal direction shown) and boundary conditions; slip conditions/inviscid walls are applied in spanwise direction

Figure 4.6.: Schematic converging-diverging setup.

flow separates slightly at the diverging part at the lower wall, but not on the flat top wall, as shown in Fig. 4.6. Similar to the DNS, the inflow boundary conditions are derived from a fully developed turbulent boundary layer at $\mathrm{Re}_\tau = 617$ (RANS predicted). A constant mass flow rate is prescribed at the outflow of the domain, which was derived based on the domain size and bulk quantities of the inflow profile (streamwise velocity and density). Since the available DNS data set is 2D as well, we are able to provide all available RANS grid solution points as subsequent data points for training the machine learning model.

NACA 4412 airfoil

To demonstrate the application of the UQ framework with and without a machine learning model, the near-stall NACA 4412 airfoil test case is chosen in the presented work. This test case is a NASA benchmark case for turbulence models, featuring boundary layer separation close to the trailing edge. This airfoil is operated at a Reynolds number of $\mathrm{Re}_c = 1.52 \cdot 10^6$ (based on the freestream velocity U_∞ and the chord length c) and a Mach number of $\mathrm{Ma} = 0.09$ (based on U_∞). The angle of attack is 13.87° as sketched in Fig. 4.7a. The CFD results are compared against experimental measurements of Coles and Wadcock [21]. In order to minimize the effect of boundary conditions on the CFD simulation, far-field conditions are applied to prescribe the specified flow conditions (see Fig. 4.7b). A turbulence intensity of 0.086% and an eddy viscosity ratio μ_T/μ of 0.009 is prescribed in accordance with the description of NASA [116]. The mesh topology is the so-called C-grid featuring a grid cell resolution of $n_x, n_y, n_z = 896, 256, 1$, which can be downloaded from NASA's turbulence database [116].

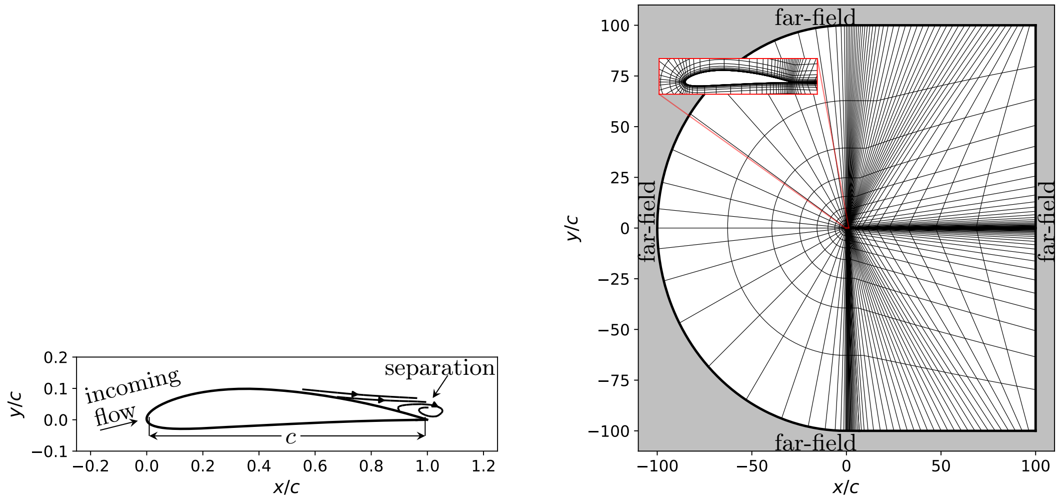

(a) Relative dimensions and sketch of the flow

(b) Mesh (every eighth line shown) and boundary conditions; slip conditions/inviscid walls are applied in spanwise direction

Figure 4.7.: Schematic NACA 4412 setup.

4.3. Hyperparameter selection based on generalization study

Before the training of the final random forest regression model is conducted, the impact of four different hyperparameters on the accuracy is evaluated:

- Maximum tree depth: maximum number of decision nodes from the root down to the furthest node allowed.
- Minimum sample count: minimum number of data samples required at a decision node allowed.
- Maximum number of features: maximum number of features randomly chosen at each decision node allowed.
- Number of trees: total number of individual decision trees used.

Since the final trained model should be able to generalize for different geometries and flow conditions, it seems to be reasonable to evaluate these hyperparameters with focus on generalization capabilities of the random forest. Therefore, we apply a leave-one-out-cross validation, which is an appropriate procedure for small data sets. This means that three out of four available training data sets (see Section 4.2.5) are used for training, while the remaining flow case is used to verify the model (see Table 4.3). Data samples featuring non-physical Reynolds stress tensors (barycentric coordinates are located outside the barycentric triangle) are removed from each data set.

For each of the first three hyperparameters several different values were studied over a range of the total amount of individual regression trees, while the other two hyperparameters were set to default values (see *scikit-learn* documentation for further information). As an example, Fig. 4.8 presents the effect of the considered hyperparameters on the accuracy of the model prediction in scenario I, where the accuracy is expressed in terms of the Root Mean Square Error (RMSE).

Table 4.3.: Scenarios for hyperparameter study: x means part of training data, ∘ means testing data.

	Scenario			
Flow cases	I	II	III	IIII
turbulent channel	x	x	x	∘
periodic hill	x	x	∘	x
wavy wall	x	∘	x	x
converging-diverging channel	∘	x	x	x

The subsequent statements made coincide with all evaluated scenarios as well. With increasing maximum depth of each individual tree, the model prediction error on the training data is reduced at the expense of increasing complexity. Increasing complexity of the tree may result in reduced generalizability capabilities (reduced test data accuracy) of the model. Because a maximum tree depth of 15 showed excellent performance for the training as well as for testing data, it is preferred compared to a higher value of 20, which increases computational costs (see Fig. 4.8a). The smaller the number of data samples for each decision node, the more accurate the performance on the training data (see Fig. 4.8b). Since the RMSE based on evaluated testing data is not significantly affected by this hyperparameter, a minimum sample count of 10 is chosen. This enables the model to generalize to a greater extend, than selecting a smaller value. A larger number of selected features for each decision node lowers the training error and increases the risk of overfitting. Since a maximum number of 7 features produces accurate prediction performance for the test data as well (see Fig. 4.8c), it is selected as inferred hyperparameter. In terms of total number of individual trees, one can observe a steep drop in RMSE for small numbers followed by an almost constant level of accuracy. The computational costs scale linearly with the number of individual trees. Although computational costs do not really play a relevant role for our application, as we only evaluate the model once before each simulation run, we sought for the minimum number of trees for maximized performance of the model. Therefore, we concluded to use a total number of 30 individual trees for the random forest by evaluating all described scenarios in Table 4.3.

4.4. Verification of trained machine learning model

Based on the choice of hyperparameters, which was discussed in the previous section, the prediction accuracy of the random forest should be evaluated on the available data (see Section 4.2.5). Ten different scenarios based on combinations of the flow data cases, listed in Table 4.4, serve as verification of functionality and present the accomplishment of the intended generalization of every model. While data samples featuring non-physical Reynolds stress tensors (barycentric coordinates are located outside the barycentric triangle) are removed from the data sets, the RMSE classifies the prediction accuracy of different scenarios. As the target quantity p can vary between zero and one (based on the construction of the equilateral triangle with edge length equals to one), the resulting RMSEs indicate less than 10% absolute prediction error except for scenario II.

As soon as a trained machine learning model should make predictions on flow cases, for which accurate data does not exist, judging the model's prediction in terms of accuracy becomes difficult. Comparing the input feature spaces of training and testing data (previously unseen case) based on extrapolation metrics in order to build confidence in

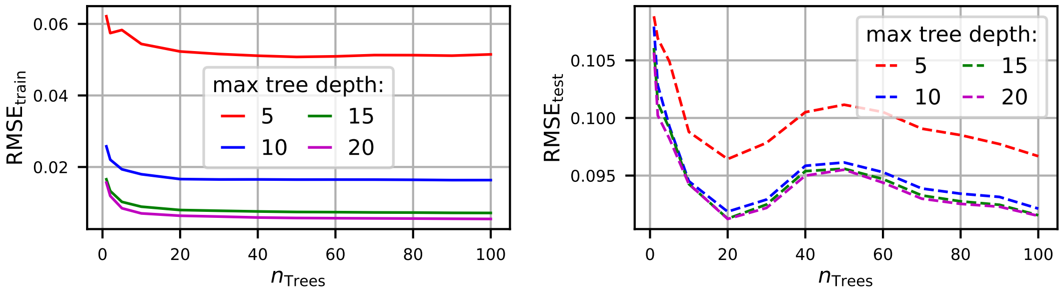

(a) Effect of maximum depth of trees over total number of individual trees

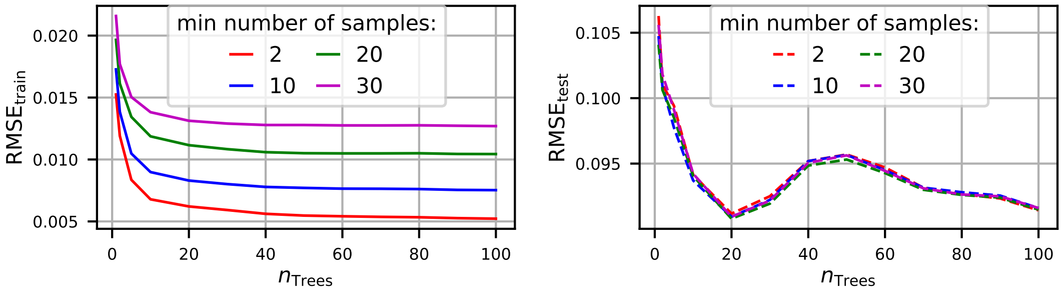

(b) Effect of the minimum number of required samples over the total number of individual trees

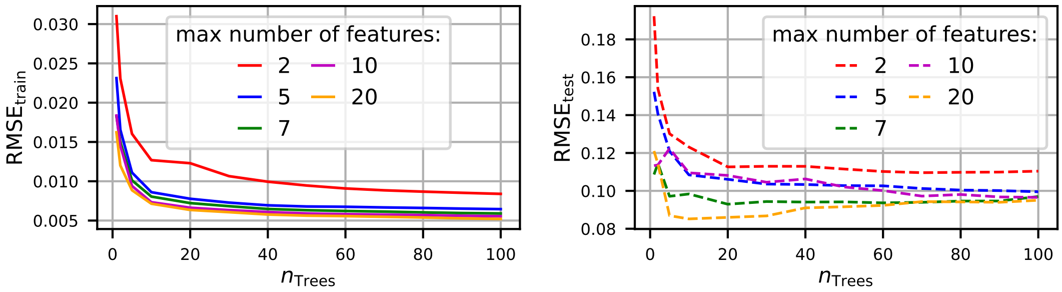

(c) Effect of the maximum number of active features over the total number of individual trees

Figure 4.8.: Training accuracy (solid / left) and testing accuracy (dashed / right) based on RMSE for selection of hyperparameters in scenario I.

a machine learning model, is a reasonable idea. An extrapolation metric measures the distance between a test point $\tilde{m}$ and the training data feature set $m^{(i)}$ for $i = 1, \ldots, n$ with n as the number of training data points. In this paper, we use the KDE to compute the distance by estimating the probability density

$$f_{\text{KDE}} = \frac{1}{n\sigma^d} \sum_{i=1}^{n} \prod_{j=1}^{d} K\left(\frac{\tilde{m}_j - m_j^{(i)}}{\sigma}\right) , \tag{4.14}$$

with the number of features d and the bandwidth σ, determined by Scott's rule [137]. According to the work of Wu et al. [164], we use a Gaussian kernel

$$K\left(\frac{\tilde{m}_j - m_j^{(i)}}{\sigma}\right) = 1/\sqrt{(2\pi)}\exp\left(-\left(\frac{\tilde{m}_j - m_j^{(i)}}{\sigma}\right)^2 /2\right) \tag{4.15}$$

and the distance is computed as follows:

$$
\begin{aligned}
d_{\mathrm{KDE}} &= 1 - \frac{f_{\mathrm{KDE}}}{f_{\mathrm{KDE}} + 1/A} \quad \text{with} \\
A &= \prod_{i}^{n} \left(\max_{j} \left(m_j^{(i)} \right) - \min_{j} \left(m_j^{(i)} \right) \right) \quad \text{for} \quad j = 1, \ldots, d \, .
\end{aligned}
\tag{4.16}
$$

The applied Gaussian kernel K ensures that the smaller the difference of $\tilde{m}_j$ and $m_j^{(i)}$, the larger the output of K. In other words, Eq. (4.14) increases, if $\tilde{m}$ becomes close to a concentrated feature space of the training data points and vice versa. The quantity A, which is only dependent on the features of the training set, can be interpreted as the volume of a cuboid with d dimensions. Thus $1/A$ is the probability density with respect to a uniform distribution inside such a cuboid. Due to the normalization of the distance in Eq. (4.16), the metric is able to measure the distance of $\tilde{m}$ to the training data with respect to a uniform distribution. Consequently, on the one hand, if $\tilde{m}$ is close to a concentrated feature space, $f_{KDE} \gg 1/A$ implies $d_{\mathrm{KDE}} \to 0$. On the other hand, $d_{\mathrm{KDE}} \to 1$ follows from $f_{KDE} \ll 1/A$. This enables a user to interpret the rate of extrapolation needed based on the training data set. Thus, two extreme scenarios are represented according to:

- $d_{\mathrm{KDE}} = 0$: No extrapolation is required ↔ the features of the training data set cover the features of the test point $\tilde{m}$.
- $d_{\mathrm{KDE}} = 1$: High extrapolation is required ↔ the features of the test point $\tilde{m}$ are far off the features of the training data.

Since the extrapolation metric only assesses the closeness of the features between training and test data sets, Wu et al. [164] demonstrate that the KDE extrapolation metric can be used to estimate the prediction confidence by quantifying the correlation between the degree of extrapolation and the prediction accuracy. In our work, the flow case of the converging-diverging channel serves to present the application of the extrapolation metric. The remaining data (turbulent channel flow, flow over periodic hills and wavy walls) is used for training individual random forests, while each random forest is evaluated on the converging-diverging channel.

Selected input features attributed with significant feature importance are considered for computing the KDE distance d_{KDE}. The individual feature importance for each of

Table 4.4.: Prediction accuracy of random forest: x means part of training data, ○ means not part of training data, red highlights data sets used for evaluation of RMSE.

	Scenario									
Flow cases	I	Ia	II	IIa	III	IIIa	IIIb	IIII	IIIIa	V
turbulent channel	x	x	x	x	x	x	x	○	x	x
periodic hill										
· $Re_H \in \{2800, 5600, 10595\}$	x	x	x	x	○	x		x	x	x
· $Re_H \in \{2800, 10595\}$							x			
· $Re_H = 5600$							○			
wavy wall	x	x	○	x	x	x	x	x	x	x
converging-diverging channel	○	x	x	x	x	x	x	x	x	x
RMSE $(p_{\mathrm{pred}}, p_{\mathrm{true}})$	0.098	0.010	0.133	0.029	0.095	0.028	0.041	0.051	0.014	0.013

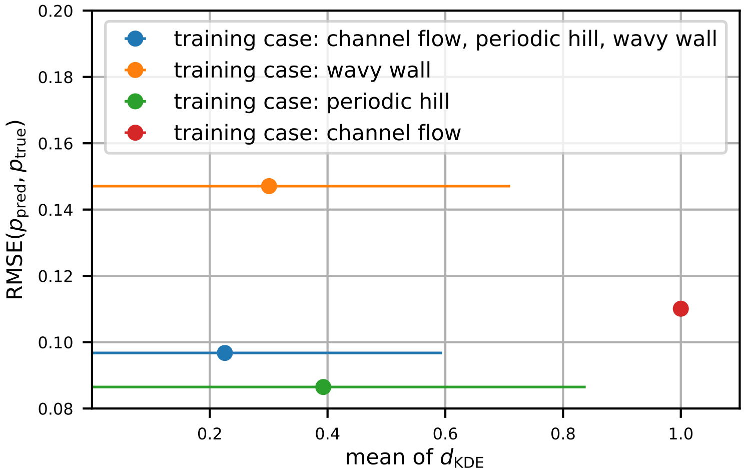

Figure 4.9.: Relationship between the RMSE of the prediction for the converging-diverging channel and the mean value of the KDE extrapolation metric (standard deviation of the extrapolation metric is shown as the horizontal bars). All 56 input features are considered for the prediction and training of the random forest models, while only q_1, q_2, q_3, q_7 and q_8 are used to compute d_{KDE}.

the 56 input features, is determined after training the final random forest (scenario V in Table 4.4) using the chosen hyperparameters (see Section 4.3). The utility of each feature is determined by the permutation feature importance approach, accounting for the reduction in the model accuracy, when the values of this feature are randomly shuffled. Consequently, the selected five most important features to be considered for determining d_{KDE} are the eddy viscosity q_8, the normalized wall-distance q_3, the Mach number q_7, the turbulent kinetic energy q_2 and the Q-criterion q_1. Contrary to the work of Wu et al. [164], we cannot confirm a strong correlation between the accuracy of the model, evaluated by predicting the perturbation magnitude p for the converging-diverging channel, and the mean of the KDE distance d_{KDE} for different training data sets, as illustrated in Fig. 4.9.

However, Fig. 4.10 presents a possible explanation for reduced prediction error, when training on the periodic hill compared to the wavy wall. The DNS data based barycentric coordinates of the converging-diverging channel and the periodic hill cover similar areas in the barycentric triangle, while true values of barycentric coordinates for the wavy wall test case are only located in the lower area of the triangle. Thus, the target quantity, which is the distance in barycentric coordinates, becomes more frequent in a similar range of absolute values for the converging-diverging channel and the periodic hill (see Fig. 4.11). Even Wu et al. [164] mention that the correlation between accuracy and extrapolation metric is less correlated, if the training set is very similar or very different from the test set, which we might be facing here as well.

Nevertheless, the result of the extrapolation metric is highly dependent on the set of considered features. Thus, it seems reasonable to limit the evaluation of the metric to certain important features for the random forest. Figure 4.12a presents the two-dimensional distribution of the KDE metric, evaluated based on the five most important features q_8, q_3, q_7, q_2 and q_1 (corresponding to the blue data point in Fig. 4.9 and scenario I in Table 4.4). Although, some spatial correlated regions between KDE distances d_{KDE} and model errors $|p_{\mathrm{pred}} - p_{\mathrm{true}}|$ in Fig. 4.12b can be recognized, their overall correlation is not strong (Pearson correlation coefficient of approx. 0.2). Nonetheless, similar observations

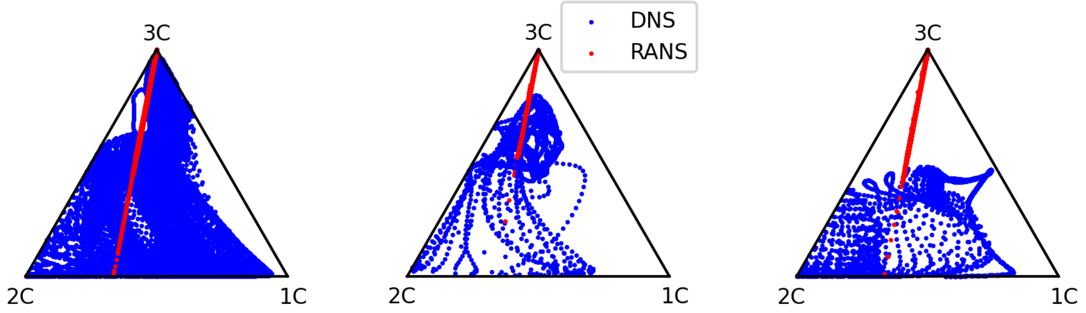

(a) Converging-diverging channel (b) Periodic hill, $\mathrm{Re}_H = 5600$ (c) Wavy wall

Figure 4.10.: Barycentric coordinates for the selected flow cases; legend of (b) corresponds to (a) and (c) as well.

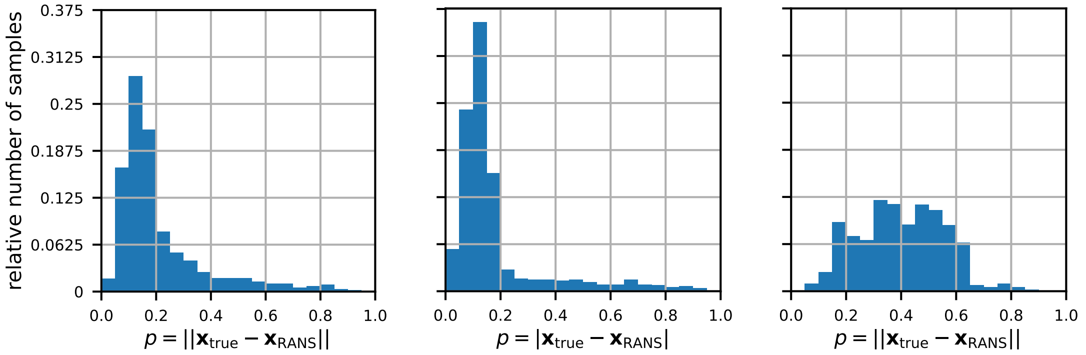

(a) Converging-diverging channel (b) Periodic hill, $\mathrm{Re}_H = 5600$ (c) Wavy wall

Figure 4.11.: Frequency of the target quantity p for the selected flow cases; vertical axis correspond to (a), (b) and (c).

based on comparable test cases as in the work of Wu et al. [164] (not shown here) reinforce the trust in the presented KDE distance, when applied in an adequate manner.

Before the actual application of the data-driven UQ perturbation framework on the flow around NACA 4412 can be conducted, the prediction of the random forest model for this case should be discussed. Figure 4.13 shows the evaluated extrapolation metric and the corresponding predicted p, when the model was trained on all available data (channel flow, wavy wall, periodic hill, converging-diverging channel). The estimated distribution of the KDE distance based on the five most important flow features q_8, q_3, q_7, q_2 and q_1 is shown in Fig. 4.13a. Solely regions close around the airfoil contain $d_{\mathrm{KDE}} \leq 1$. This is due to the substantially differing geometry, Reynolds number and flow situation compared to the training data. The feature space of NACA 4412 contains especially higher Mach numbers q_7 in regions far off the boundary layer with less turbulent kinetic energy q_2 (respective turbulent eddy viscosity q_8) and limited wall-distance based Reynolds Number q_3. This fact also manifests, when taking a look at the level of turbulence intensity for the baseline RANS solution (not shown here). Because far-field boundary conditions are used, laminar flow is present almost everywhere in the CFD domain. An area with $\mathrm{Tu} \geq 0.01\%$ can only be identified in the boundary layer around the profile, in the wake flow and around the stagnation point on the pressure side (PS) at $x/c \approx 0.035$. Consequently, the chosen

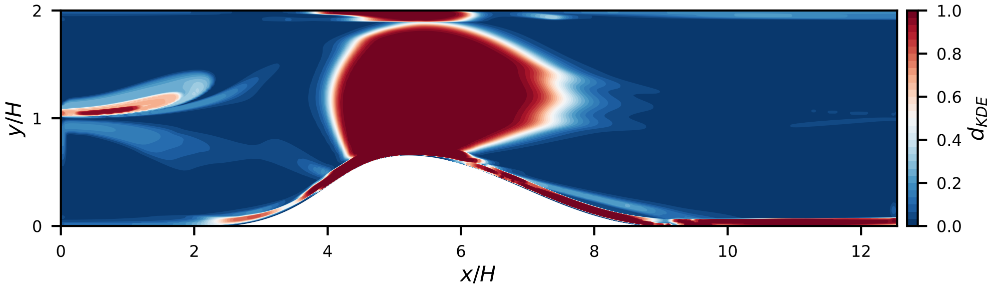

(a) Evaluated extrapolation metric

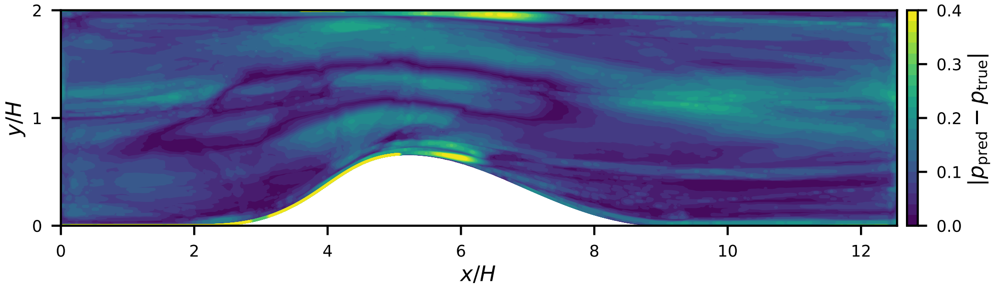

(b) Model prediction p_{pred} presented as absolute deviation based on true values

Figure 4.12.: Verification of extrapolation metric based on converging-diverging channel.

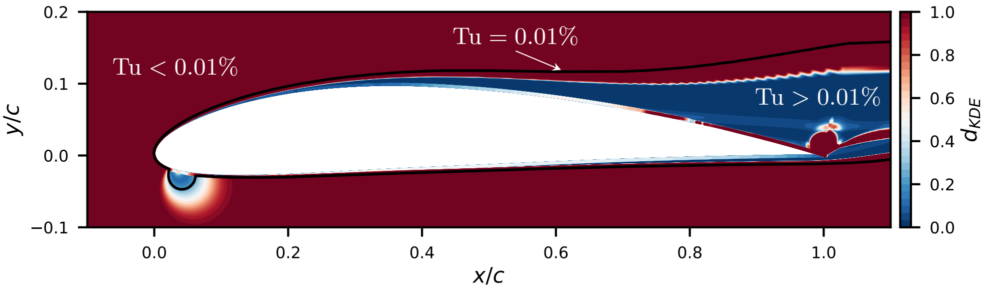

(a) Evaluated extrapolation metric, black line divides areas with higher and lower turbulence intensity Tu with a threshold of 0.01%

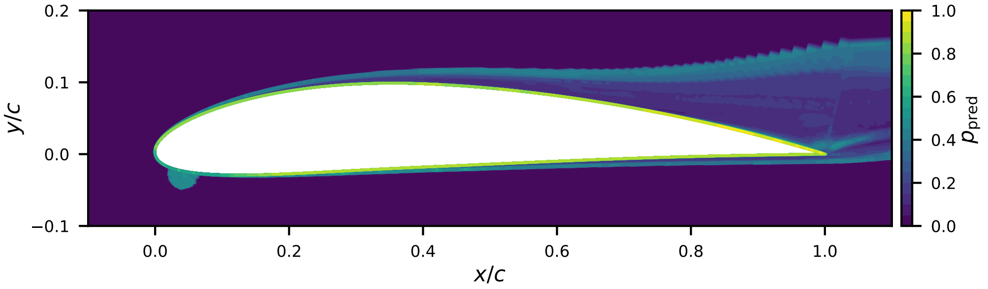

(b) Model prediction in the area of Tu $\geq$ 0.01% (p_{pred} is set to zero for area with Tu $<$ 0.01%)

Figure 4.13.: Evaluated metric and perturbation magnitude for the NACA 4412 profile.

training data does not sufficiently cover the feature space of NACA 4412 in the outer regions, leading to $d_{\mathrm{KDE}} = 1$. But since the entire mapping of the Reynolds stress tensor onto barycentric coordinates makes only sense for relevant turbulent stresses, which are significantly larger than machine precision, the random forest is restricted to predict values in the area at $\mathrm{Tu} \geq 0.01\%$ (see Fig. 4.13b). This decision is purely based on our observations and physical intuition. The verification of this procedure was numerically justified by comparing forward data-driven UQ computations based on model predicted p. Some simulations contained p, determined by the random forest, everywhere in the domain, others only in the area $\mathrm{Tu} \geq 0.01\%$. Although the random forest is able to predict certain values greater than zero in the region featuring $\mathrm{Tu} \leq 0.01\%$, the evaluated flow quantities around the NACA 4412 airfoil did not show any significant difference (not shown here). Even the KDE distance in Fig. 4.13a confirms the chosen procedure, by revealing reduced extrapolation distance in areas with increased turbulence intensity. Thus, restricting the model prediction to certain area closely around the airfoil can be justified from a physical and a machine learning perspective. However, the presented extrapolation metric and model prediction close to the separation zone ($x/c \geq 0.8$ based on RANS simulation) reveal that predicting the influence of a separated region in terms of anisotropy discrepancy is a challenging task. This issue might be only overcome with an increasing number of training data sets involving varying flow conditions and geometries.

4.5. Application of UQ perturbation framework

The flow around NACA 4412 at $\mathrm{Re}_c = 1.52 \cdot 10^6$, $\mathrm{Ma} = 0.09$ and an angle of attack of 13.87° demonstrates the general framework of the UQ perturbation approach presented in Section 4.2. Before analyzing the actual perturbed solutions and derived UQ estimates, the general performance of the Menter SST $k - \omega$ turbulence model is discussed briefly. The baseline simulation is in accordance with the presented RANS solutions using the identical turbulence model provided by NASA's turbulence modeling resource site [116]. Similar to NASA's observations, when conducting steady simulation with TRACE on the given grid resolution, $\mathrm{CFL} = 1$ has to be used in order to reach a fully converged steady-state solution. The main difference of the baseline simulation in comparison with the experimental surface pressure measurements conducted by Coles and Wadcock [21] can be observed at the trailing edge of the suction side (SS). The pressure coefficient, shown for example in Fig. 4.14a, is defined as

$$c_p = \frac{p - p_\infty}{\frac{1}{2}\rho_\infty U_\infty^2} \ , \tag{4.17}$$

while the reference quantities are those at infinity $U_\infty = 31.2$ m/s, $p_\infty = 76914.1$ Pa and $\rho_\infty = 0.9$ kg/m^3 (far-field boundary condition). Although the reference velocity is evaluated at different locations in the experiment, we apply the far-field freestream velocity instead, based on best practice guidelines and in order to retain similar CFD results compared to the NASA findings [116].

The data-free uncertainty estimates, presented in Fig. 4.14 are the result of perturbed turbulence model simulations using a relative perturbation magnitude $\Delta_B = 1$, as there is no justifiable physical reason to reduce the amount for targeting the extreme states of turbulence *a priori* without data [34]. Unfortunately, as already discussed in Section 4.2.4, the perturbed simulations, trying to minimize the turbulence production, come along with stability issues in terms of convergence or even completely diverge from steady-state solutions. An appropriate moderation factor f has to be adjusted to

Table 4.5.: Moderation factor f for every perturbed UQ simulation of NACA 4412. Application of $\Delta_B \leq 1$ in the data-driven approach necessitates a distinction between $P_{k_{\min}}$ and $P_{k_{\max}}$ for 3C.

	Data-free					
Perturbed simulation:	$(1\text{C}, P_{k_{\max}})$	$(1\text{C}, P_{k_{\min}})$	$(2\text{C}, P_{k_{\max}})$	$(2\text{C}, P_{k_{\min}})$	3C	
moderation factor	1.0	0.03	1.0	0.05	0.1	
	Data-driven					
Perturbed simulation:	$(1\text{C}, P_{k_{\max}})$	$(1\text{C}, P_{k_{\min}})$	$(2\text{C}, P_{k_{\max}})$	$(2\text{C}, P_{k_{\min}})$	$(3\text{C}, P_{k_{\max}})$	$(3\text{C}, P_{k_{\min}})$
moderation factor	1.0	0.2	1.0	0.2	1.0	0.2

retain acceptable, converged simulations. Besides examining the overall residuals of each simulation, we evaluate the mean blade force in y-direction to distinguish between an unacceptable unstable and an acceptable converged solution. Based on physical experience and consequent intuition, a threshold of 2% relative standard deviation with respect to the mean of the overall blade force in y-direction is chosen.

Put simply, as one is increasing the moderation factor f for simulations minimizing the turbulence production term ($P_{k_{\min}}$), the standard deviation of the mean blade force rises. In our investigations, a high-level python script (see Fig. 4.2) is applied to march the moderation factor as high as possible (by steps of 0.1 for $f \in [0.1, 1.0)$ and by steps of 0.01 for $f \in [0, 0.1)$). As the designated solutions may still contain small variations, we instrument probes on the airfoil surface and average the solution in order to get the mean for QoI. Due to the described convergence issues only a fraction of the perturbed Reynolds stress tensor (according to Eq. (4.11)) can be utilized to update the Navier-Stokes equations for the NACA 4412 simulations (see moderation factors in Table 4.5). To the authors knowledge, these low values are in accordance with the implementation of the eigenspace perturbation in the solver suite SU2, as their default value for the moderation factor is 0.1 [147].

Figure 4.14 presents the uncertainty estimates based on the perturbed target states, using the moderation factors presented in Table 4.5. As discussed above, the baseline Menter SST $k-\omega$ simulation shows significant deviation for the prediction of the separation zone close to the trailing edge. The results of $(1\text{C}, P_{k_{\max}})$ and $(2\text{C}, P_{k_{\max}})$ minimize this gap on the SS for $x/c < 0.7$, whereas perturbed simulations minimizing the turbulence production term by modifying the eigenvectors of the Reynolds stress tensor predict an increased static pressure on the SS for $x/c > 0.7$. Targeting for the 3C turbulent state with $\Delta_B = 1$ results in minimizing the turbulence production term as well [22], which can be seen on the presented surface quantities. Reduced turbulent kinetic energy moves the separation zone towards the front of the airfoil, indicated by the friction coefficient

$$c_f = \frac{\tau_w}{\frac{1}{2}\rho_\infty U_\infty^2} \tag{4.18}$$

in Fig. 4.14b. In contrast, the boundary layers of the perturbed solutions (1C, $P_{k_{\max}}$) and (2C, $P_{k_{\max}}$) reveal significant increased momentum transfer into the viscous sublayer, inducing complete suppression of the separation bubble. As already mentioned in Section 4.2.4, the estimated uncertainty bounds by the perturbation framework are only aiming for the extreme state of turbulence in terms of Reynolds stress tensor's shape and

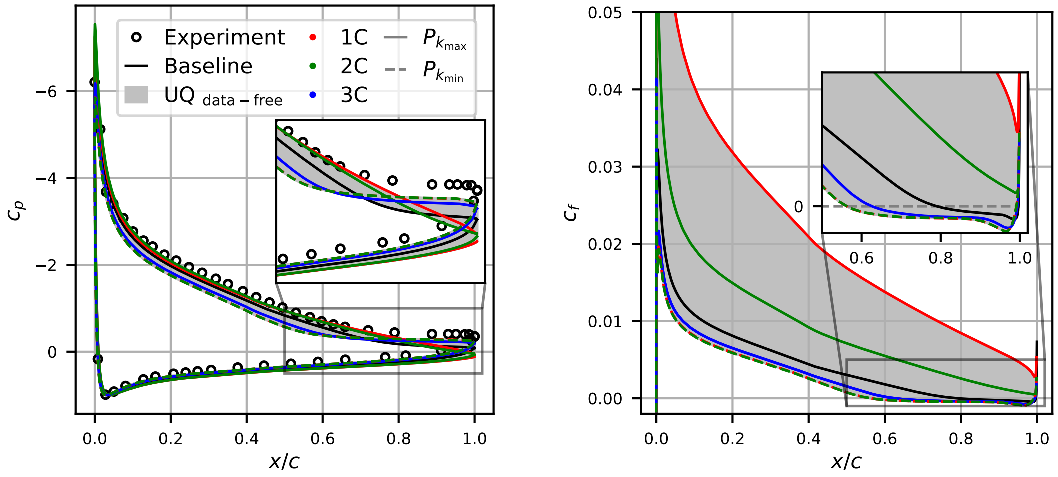

(a) Pressure coefficient c_p

(b) Friction coefficient c_f

Figure 4.14.: Surface quantities for the flow around NACA 4412 including data-free evaluation of the uncertainty estimates for the Menter SST $k-\omega$ turbulence model; legend in (a) applies also for (b).

orientation, which may not necessarily need to coincide with extreme state of some QoI. In the range of $0.72 < x/c < 0.82$ the baseline solution lies outside of the determined gray shaded UQ estimate for the pressure coefficient.

The random forest predicted perturbation magnitude p (see Fig. 4.13b) is forward propagated towards the same three limiting states as in the data-free approach, as described in Section 4.2.3. This two-dimensional distribution of p is used to determine the respective Δ_B for each target state (see Fig. 4.15 for 1C, 2C and 3C). Due to the fact that the unperturbed RANS solution data points are distributed along the plane-strain line[4], the spatially averaged relative distance Δ_B is highest for the the simulations targeting the isotropic corner (3C), followed by the two-component corner (2C) and the one-component corner (1C). In order to reach an acceptable steady-state solution for each perturbed simulation the moderation factor f is adjusted in the same manner as discussed above for the data-free procedure. Since the overall perturbation is weaker than using $\Delta_B = 1$, the moderation factor could be increased (see Table 4.5).
The estimated uncertainty bands for the surface quantities, shown in Fig. 4.16, become narrower. Especially the uncertainty estimates for the pressure coefficient based on $(1\mathrm{C}, P_{k_{\max}})$ and $(2\mathrm{C}, P_{k_{\max}})$ are very close to the baseline solution. As the overproduction of turbulent kinetic energy for the data-free 1C and 2C cases disappears, all data-driven perturbed simulations feature a separation zone on the suction surface.

Last but not least, the fact that none of the presented UQ estimates envelopes the experimental surface pressure measurements needs to be discussed. To start with, as discussed already in the beginning of this section, the CFD setup seems to come along with certain weaknesses. Moreover, the underlying intention of applying the UQ perturbation framework is not to include certain high-fidelity data, whether it originates from experiments or SRS, into its resulting envelope. The methodology seeks to produce limiting states of the Reynolds stress tensor, propagates these states and results in modified QoI. But it cannot be ensured that accurate data points for some QoI have

---

[4] Plane-strain turbulence is characterized by at least one zero eigenvalue of the anisotropy tensor.

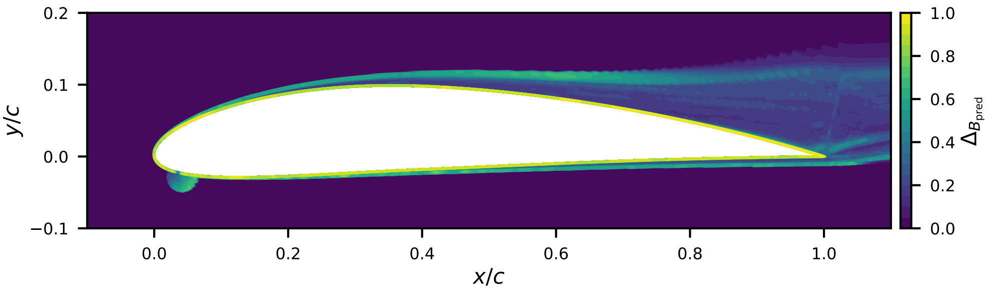

(a) Data-driven relative perturbation magnitude evaluated for the 1C target state

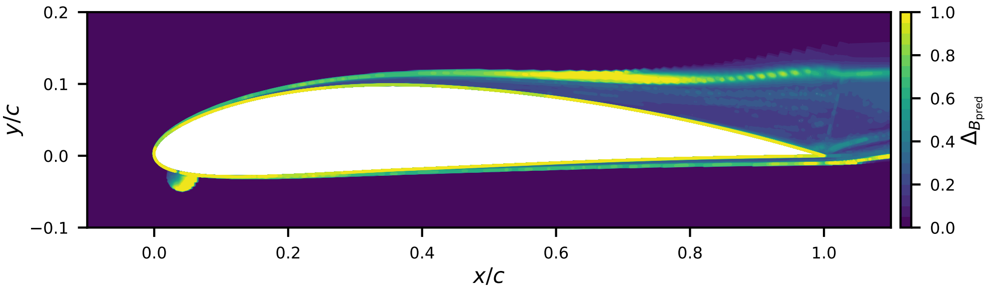

(b) Data-driven relative perturbation magnitude evaluated for the 2C target state

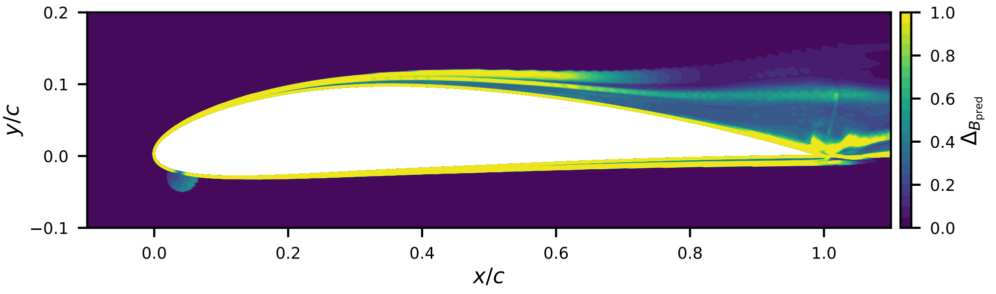

(c) Data-driven relative perturbation magnitude evaluated for the 3C target state

Figure 4.15.: Comparison of the effect of identical model predicted perturbation magnitude p on the relative perturbation magnitude Δ_B.

to be covered by the uncertainty estimates resulting from the Reynolds stress tensor perturbation framework. Therefore, we disagree with some recent publications (e.g. [32]), where the quality of the EPF is judged by covering certain QoI. As the uncertainty envelopes do not represent confidence or strict intervals at all [108], we encourage to validate the uncertainty estimates with respect to the underlying physical concept of the EPF. Analyzing simulation results related to the perturbed state of the Reynolds stress tensor should be chosen over evaluating the coverage of certain reference data. The main reason for this is that the perturbation framework is only able to account for structural uncertainties limited to the chosen RANS turbulence model in the CFD solver. However, other sources of uncertainties related to RANS simulations are not considered by the eigenspace perturbations, such as:

- approximation of 3D geometries with 2D CFD setups,

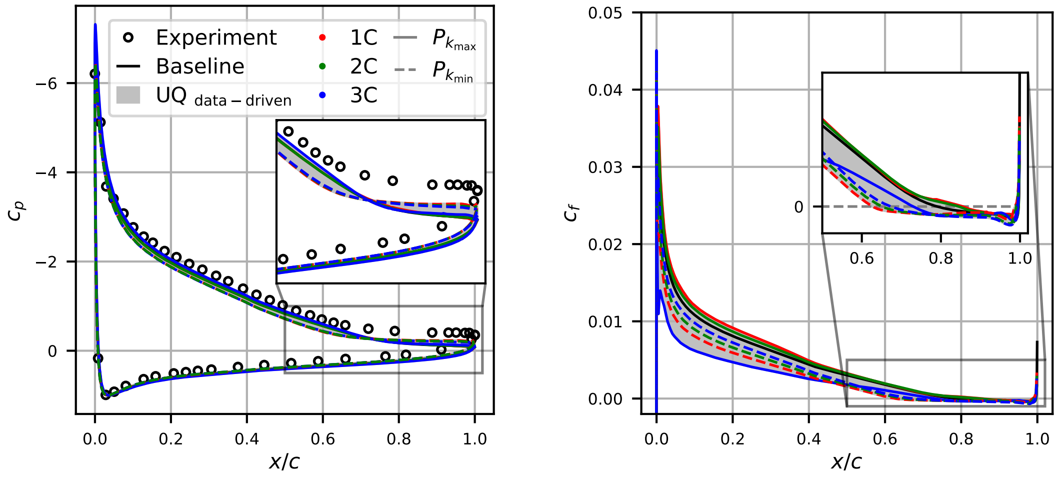

(a) Pressure coefficient c_p

(b) Friction coefficient c_f

Figure 4.16.: Surface quantities for the flow around NACA 4412 including data-driven evaluation of the uncertainty estimates for the Menter SST $k-\omega$ turbulence model; legend in (a) applies also for (b).

- neglecting of geometry and manufacturing tolerances,
- choice of boundary conditions that must not necessarily coincide with reference conditions,
- assuming steady-state flow conditions, when the flow might be already unsteady in reality,
- averaging of the Navier-Stokes equations and, thus, neglecting the unsteady nature of turbulence itself.

Consequently, it cannot be expected that the perturbed simulations envelope reference data.

The described machine learning procedure only accounts for the spatially varying deviation in the Reynolds stress anisotropy, as the turbulence model's uncertainties are not expected to be uniformly distributed across the computational domain. The impact of the discrepancy in terms of anisotropy between RANS and scale-resolving data on certain QoI, was not part of the machine learning process. Thus, with reference to the disregarded sources of uncertainty mentioned above, even the data-driven perturbed turbulence model simulations cannot account for adequate entirely enveloping bounds for selected QoI.

4.6. Conclusion & outlook

The present work aims to consolidate an arisen method in the field of turbulence model UQ. We demonstrate the possibility to estimate uncertainty bounds for turbulence models with state-of-the-art methods in the CFD solver suite TRACE. The UQ perturbation framework is described extensively, presenting its underlying idea while mentioning its limitations and what it is not able to do for industrial applications. Additionally, since TRACE is eminent in turbomachinery industry, designing and implementing a framework to easily conduct uncertainty estimation for turbulence models using TRACE was a major goal of this work.

Moreover, we applied a proposed machine learning strategy to further enhance the interpretability of generated uncertainty estimates by being less conservative and nonetheless physics-constrained simultaneously. Our extension of this data-driven eigenvalue perturbation approach is the enlargement of flow cases featuring separated flows, adverse pressure gradient and reattachment for training and testing purposes on the one hand. This enables us to check and verify the appropriate application of trained random forest regression model in-depth. On the other hand, considering eigenvector perturbation of the Reynolds stress tensor on top of the data-driven eigenvalue perturbation was the plausible next step in this specific research field.

In our investigations, we outline tools and methodologies for assessing and analyzing data-driven models, especially in the context of turbulent flows. We address key points in the field of machine learning such as selection of input features, tuning of hyperparameters, judging the model's accuracy in an *a posteriori* and and an *a priori* way.

In order to predict the desired target quantity for the selected flow cases by the random forest, we admit that we might not have to use this abundant number of input features, as described above. This is due to the fact, that the considered cases show certain similarities in terms of input and target quantities. However, if the amount of training data sets increases, covering a wider range of flow phenomena, the machine learning model will likely take advantage of a larger number of input features.

We confirm that the perturbation approach to account for turbulence model uncertainties, is a purely physics-based, comprehensible framework. Nevertheless, it suffers from reduced convergence or even divergence of steady-state solutions. The necessity to moderate certain perturbations by an arbitrary factor, seems unsatisfactory for such an advanced approach. Currently, we are not aware of any other remedy for convergence issues as well, as even the machine learning does not help to overcome this particular issue. Moreover, we also agree on the underlying idea to account for spatially varying of turbulence model uncertainties by using data-driven methodologies to determine certain areas of high deviations from accurate Reynolds stress anisotropy states. Training a machine learning model to predict an appropriate model-form uncertainty will always help CFD users to get an indication, in which regions the LEVM assumptions might be violated[5]. However, we believe, based on our experiences with the data-driven Reynolds stress tensor perturbation framework (which are not only limited to the NACA 4412 flow case), that an enhanced applicability can only be achieved, if the stability issues in terms of convergence for steady-state simulation were solved.

---

[5] More specifically, this may be of particular interest to the turbulence modeling community rather than designers, whose main concern is the overall (turbulence modeling) uncertainty on CFD results.

Appendix 4.A Mathematical effect of the moderation factor f in case of pure eigenvalue perturbation

By applying the moderation factor $f \in [0,1]$, the perturbed Reynolds stress tensor can be expressed as

$$\begin{aligned} \tau^*_{ij_f} &= \tau_{ij} + f\left[k\left(a^*_{ij} + \frac{2}{3}\delta_{ij}\right) - \tau_{ij}\right] \\ &= (1-f)\,\tau_{ij} + f\tau^*_{ij} \ , \end{aligned} \tag{4.19}$$

where τ_{ij} is the Reynolds stress tensor that was calculated based on Boussinesq assumption in step 1 (see Section 4.2.4). Based on the perturbed anisotropy tensor, the reconstructed Reynolds stress tensor is indicated by τ^*_{ij}. The anisotropy tensor related to this perturbed Reynolds stress tensor can be written as

$$\begin{aligned} a^*_{ij_f} &= \frac{\tau^*_{ij_f}}{k} - \frac{2}{3}\delta_{ij} \\ &= \frac{(1-f)\,\tau_{ij} + f\tau^*_{ij}}{k} + \frac{2}{3}\delta_{ij} \\ &= \frac{(1-f)\left[k\left(a_{ij} + \frac{2}{3}\delta_{ij}\right)\right] + f\left[k\left(a^*_{ij} + \frac{2}{3}\delta_{ij}\right)\right]}{k} - \frac{2}{3}\delta_{ij} \\ &= (1-f)\left(a_{ij} + \frac{2}{3}\delta_{ij}\right) + f\left(a^*_{ij} + \frac{2}{3}\delta_{ij}\right) - \frac{2}{3}\delta_{ij} \\ &= (1-f)\,a_{ij} + f a^*_{ij} \ . \end{aligned} \tag{4.20}$$

When just applying eigenvalue perturbation of the anisotropy tensor, a_{ij} and a^*_{ij} share identical eigenvectors. Thus, the eigenvalues of $a^*_{ij_f}$ are

$$\lambda^*_{i_f} = (1-f)\,\lambda_i + f\lambda^*_i \ . \tag{4.21}$$

The barycentric weights $C_{i\mathrm{C}}$, which are used to calculate the barycentric coordinates in Eq. (4.4), can be expressed in terms of the moderation factor:

$$\begin{aligned} C^*_{1\mathrm{C}_f} &= \frac{1}{2}\left[\lambda^*_{1_f} - \lambda^*_{2_f}\right] \\ &= \frac{1}{2}\left[(1-f)\,\lambda_1 + f\lambda^*_1 - (1-f)\,\lambda_2 + f\lambda^*_2\right] \\ &= (1-f)\,\frac{1}{2}\left(\lambda_1 - \lambda_2\right) + f\frac{1}{2}\left(\lambda^*_1 - \lambda^*_2\right) \\ &= (1-f)\,C_{1\mathrm{C}} + fC^*_{1\mathrm{C}} \end{aligned} \tag{4.22}$$

$$\begin{aligned} C^*_{2\mathrm{C}_f} &= \lambda^*_{2_f} - \lambda^*_{3_f} \\ &= (1-f)\,\lambda_2 + f\lambda^*_2 - (1-f)\,\lambda_3 + f\lambda^*_3 \\ &= (1-f)\left(\lambda_2 - \lambda_3\right) + f\left(\lambda^*_2 - \lambda^*_3\right) \\ &= (1-f)\,C_{2\mathrm{C}} + fC^*_{2\mathrm{C}} \end{aligned} \tag{4.23}$$

$$\begin{aligned} C^*_{3\mathrm{C}_f} &= \frac{3}{2}\lambda^*_{3_f} + 1 \\ &= \frac{3}{2}(1-f)\,\lambda_3 + \frac{3}{2}f\lambda^*_3 + (1-f) + f \\ &= (1-f)\left(\frac{3}{2}\lambda_3 + 1\right) + f\left(\frac{3}{2}\lambda^*_3 + 1\right) \\ &= (1-f)\,C_{3\mathrm{C}} + fC^*_{3\mathrm{C}} \ . \end{aligned} \tag{4.24}$$

The perturbed barycentric coordinates $\boldsymbol{x}^*_f$ (modified by the moderation factor f) can be written using Eq. (4.22), Eq. (4.23) and Eq. (4.24) as

$$\begin{aligned}\boldsymbol{x}^*_f &= \boldsymbol{x}_{1\mathrm{C}} C^*_{1C_f} + \boldsymbol{x}^*_{2\mathrm{C}_f} + \boldsymbol{x}_{3\mathrm{C}} C^*_{3\mathrm{C}_f} \\ &= \boldsymbol{x}_{1\mathrm{C}} \left[(1-f)\, C_{1\mathrm{C}} + f C^*_{1\mathrm{C}}\right] + \boldsymbol{x}_{2\mathrm{C}} \left[(1-f)\, C_{2\mathrm{C}} + f C^*_{2\mathrm{C}}\right] + \boldsymbol{x}_{3\mathrm{C}} \left[(1-f)\, C_{3\mathrm{C}} + f C^*_{3\mathrm{C}}\right] \\ &= (1-f)\left(\boldsymbol{x}_{1\mathrm{C}} C_{1\mathrm{C}} + \boldsymbol{x}_{2\mathrm{C}} C_{2\mathrm{C}} + \boldsymbol{x}_{3\mathrm{C}} C_{3\mathrm{C}}\right) + f\left(\boldsymbol{x}_{1\mathrm{C}} C^*_{1\mathrm{C}} + \boldsymbol{x}_{2\mathrm{C}} C^*_{2\mathrm{C}} + \boldsymbol{x}_{3\mathrm{C}} C^*_{3\mathrm{C}}\right) \\ &= (1-f)\, \boldsymbol{x} + f \boldsymbol{x}^* \ .\end{aligned} \tag{4.25}$$

Remembering Eq. (4.5) and rearranging leads to

$$\boldsymbol{x}^* = (1-\Delta_B)\, \boldsymbol{x} + \Delta_B \boldsymbol{x}_{(\mathrm{t})} \ . \tag{4.26}$$

The analogy of Eq. (4.25) and Eq. (4.26) reveals the similar effect of adjusting Δ_B or f in case of only perturbing the eigenvalues of the anisotropy tensor. Thus, one can rewrite the actual intended location inside the barycentric triangle as a relative distance towards the corners

$$\boldsymbol{x}^*_f = (1-\Delta_B f)\, \boldsymbol{x} + \Delta_B f \boldsymbol{x}_{(\mathrm{t})} \ . \tag{4.27}$$

5. Improved self-consistency of the Reynolds stress tensor eigenspace perturbation for uncertainty quantification

(Published in *Physics of Fluids*, 35(6), 065130, 2023[1].)

M. Matha and C. Morsbach
DLR, Institute of Propulsion Technology, Cologne, Germany

Abstract

The limitations of turbulence closure models in the context of RANS simulations play a significant part in contributing to the uncertainty of CFD. Perturbing the spectral representation of the Reynolds stress tensor within physical limits is common practice in several commercial and open-source CFD solvers, in order to obtain estimates for the epistemic uncertainties of RANS turbulence models. Recent research revealed that there is a need for moderating the amount of perturbed Reynolds stress tensor to be considered due to upcoming stability issues of the solver. In this paper, we point out that the consequent common implementation can lead to unintended states of the resulting perturbed Reynolds stress tensor. The combination of eigenvector perturbation and moderation factor may actually result in moderated eigenvalues, which are not linearly dependent on the originally unperturbed and targeted perturbed eigenvalues anymore. Hence, the computational implementation is no longer in accordance with the conceptual idea of the EPF. We verify the implementation of the conceptual description with respect to its self-consistency. Adequately representing the basic concept results in formulating a computational implementation to improve self-consistency of the Reynolds stress tensor perturbation.

5.1. Introduction

Industrial aerodynamic designs increasingly rely on numerical analysis based on flow simulations using CFD software. Such industrial applications usually feature turbulent flows. Due to its cost- and time-effective solution procedure, RANS equations are an appropriate approach for design optimizations and virtual certification. Unfortunately, the RANS equations are not closed and, hence, require the determination of the second-moment Reynolds stress tensor. In this context, the Reynolds stress tensor is approximated using turbulence models. These models make assumptions regarding the relationship between the Reynolds stresses and available mean flow quantities, such as the mean

---

[1] Licensed under a Creative Commons Attribute (CC BY) license

velocity gradients, which limit their applicability in terms of accuracy on the one hand. On the other hand, the assumptions made in the formulation of closure models inevitably lead to uncertainties as soon as their range of validity is left. The quantification of these model-form uncertainties for industrial purposes is a demanding task in general.

Several approaches seek to account for these uncertainties at different modeling levels [29, 169]. We focus on the EPF [34, 66], which estimates the predictive uncertainty due to limitations in the turbulence model structure, namely its epistemic uncertainty. The EPF is purely physics-based and introduces a series of perturbations to the shape, alignment and size of the modeled Reynolds stress ellipsoid to estimate its uncertainty. Because of its straightforward implementation, the EPF has been used in diverse areas of application such as mechanical engineering [125], aerospace engineering [105, 22, 108, 18, 19], civil engineering [45, 80] and wind farm design [31, 64]. The EPF is the foundation of recent confidence-based DUU approaches [51]. There have been studies showing the potential to optimize it using data-driven machine learning approaches [61, 32] and it has been applied for the virtual certification of aircraft designs [113, 118]. The EPF has been integrated into several open and closed source flow solvers [30, 56, 107, 99]. This range of applications emphasizes the importance of the EPF. Imperfections in the EPF can have a cascading ramification to all these applications and fields.

There is need for V&V of such novel methodologies. Validation focuses on the agreement of the computational simulation with physical reality [120], which has been done for the EPF in the aforementioned studies. Whereas, verification focuses on the correctness of the programming and computational implementation of the conceptual model [148]. For the EPF, this verification would involve the theory behind the conceptual model and the computational implementation. The theoretical foundations of the Reynolds stress tensor perturbations have been analyzed in detail [106]. In this investigation, we focus on the computational implementation of the EPF, analyzing the consistency between the envisioned conceptual model and the actually implemented computational model. In order to estimate the epistemic uncertainty for future design applications with respect to turbulence closure model, we review the current implementation of the framework in the CFD solver suite TRACE developed by DLR in strong cooperation with MTU Aero Engines AG. Especially, we focus on the motivation, implementation and effects of applying a moderation factor f that serves to mitigate the amount of perturbation and aid numerical convergence of CFD solution [107, 99] (in some publications f is called under-relaxation factor). The present investigation reveals a shortcoming when combining the eigenspace perturbation of the Reynolds stress tensor with the moderation factor, which has not yet been addressed in the literature. On this basis, we formulate a way of improving self-consistency of the EPF and recovering its originally intended, physically meaningful idea in the present paper. Such adherence of self-consistency is an essential component of the verification assessment stage of V&V [127] in order to ensure agreement between the conceptual and the computational model (numerical implementation) in accordance with verification as outlined by the AIAA CFD Committee [1].

The paper is structured as follows: Section 5.2 introduces the Reynolds stress tensor's eigenspace perturbation. We describe the fundamental motivation, the mathematical background and the deduced practical implementation of the EPF. In Section 5.2.1, we present the conceptual idea to apply an eigenspace decomposition of the anisotropy tensor. On this basis, the evident choice to perturb the eigenvalues and eigenvectors within physical limits is demonstrated from a practical engineering perspective in Section 5.2.2. Propagating these limiting states of turbulence enables a CFD practitioner to estimate the model-form uncertainty for certain QoI with respect to the underlying turbulence model.

Finally, we point out an inconsistency in the prevailing computational implementation of the eigenspace perturbation in CFD solvers and suggest an alternative self-consistent formulation in Section 5.2.3. The uncertainty estimation for simulations of a turbulent boundary layer serve to demonstrate the envisioned benefits of the proposed consistent implementation of the EPF in Section 5.2.4. Section 5.3 summarizes the findings of the paper and assesses their significance for future applications.

5.2. Reynolds stress tensor perturbation to estimate uncertainties

5.2.1. Reynolds stress anisotropy and visualization

The symmetric, positive semi-definite[2] Reynolds stress tensor $\tau_{ij} = \widetilde{u_i'' u_j''}$ needs to be determined by turbulence models in order to close the RANS equations. It can be decomposed into an anisotropy tensor a_{ij} and an isotropic part

$$\tau_{ij} = k\left(a_{ij} + \frac{2}{3}\delta_{ij}\right) \ , \tag{5.1}$$

where the turbulent kinetic energy is defined as $k = \frac{1}{2}\tau_{ii}$ and summation over recurring indices within a product is implied. As the Reynolds stress tensor and its symmetric anisotropic part only contain real entries, they are diagonalizable. Thus, based on an eigenspace decomposition, the anisotropy tensor can be expressed as

$$a_{ij} = v_{in}\Lambda_{nl}v_{jl} \ . \tag{5.2}$$

The orthonormal eigenvectors form the Principal Coordinate System (PCS) and can be written as a matrix v_{in} while the traceless diagonal matrix Λ_{nl} contains the corresponding ordered eigenvalues λ_k with respect to $a_{ij}|_{\mathrm{PCS}}$. Because of the definition of the anisotropy tensor in Eq. (5.1), Reynolds stress and anisotropy tensor share the same eigenvectors while the eigenvalues of the Reynolds stress tensor are $\boldsymbol{\xi} = k(\boldsymbol{\lambda} + 2/3)$. Consequently, the eigenvalues and the eigenvectors represent the shape and the orientation of the positive semi-definite 3x3-tensor and can be visualized as an ellipsoid (see Fig. 5.1).

Generally, the anisotropy tensor describes and measures the deviation of the Reynolds stress tensor from the isotropic state, where its geometric ellipsoid representation forms a

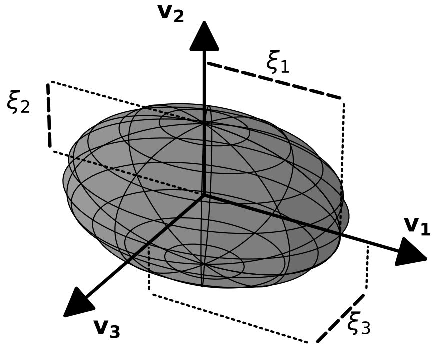

Figure 5.1.: Representation of the Reynolds stress tensor as an ellipsoid; eigenvalues ξ_i and eigenvectors $\boldsymbol{v_i}$ are highlighted.

---

[2] A tensor which is positive semi-definit has only non-negative eigenvalues.

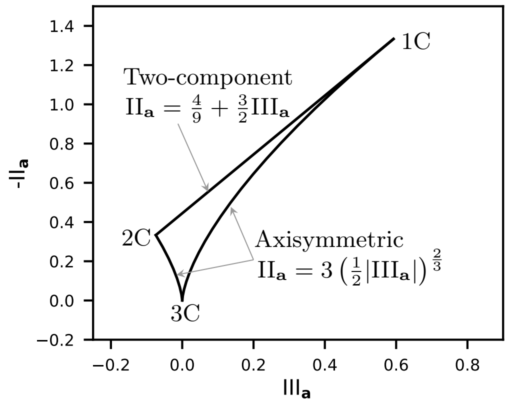

Figure 5.2.: AIM of the Reynolds stress tensor comparing second and third invariant of respective anisotropy tensor. The corners of the triangle (1C, 2C, 3C) represent the componentiality of turbulence (see Table 5.1).

perfect sphere ($\xi_1 = \xi_2 = \xi_3$). The invariants of the anisotropy tensor

$$\begin{aligned} \mathrm{I}_\mathbf{a} &= \mathrm{tr}\,(\mathbf{a}) = 0 \\ \mathrm{II}_\mathbf{a} &= -\frac{1}{2}\mathrm{tr}\left(\mathbf{a}^2\right) = \lambda_1\lambda_2 + \lambda_1\lambda_3 + \lambda_2\lambda_3 \\ \mathrm{III}_\mathbf{a} &= \det\,(\mathbf{a}) = \lambda_1\lambda_2\lambda_3 \end{aligned} \tag{5.3}$$

can be used to visualize the tensor in a coordinate-system-invariant way, called the Anisotropy Invariant Map (AIM) [93], in Fig. 5.2.

Because of the physical realizability constraints of the Reynolds stress tensor [136]

$$\tau_{\alpha\alpha} \geq 0\ , \quad \tau_{\alpha\alpha} \cdot \tau_{\beta\beta} \geq \tau_{\alpha\beta}^2\ , \quad \det\,(\boldsymbol{\tau}) \geq 0\ , \quad \alpha, \beta = 1, 2, 3 \tag{5.4}$$

and the definition of the anisotropy tensor (see Eq. (5.1)), the entries of the anisotropy tensor are bounded in the following ranges:

$$a_{ij} \in \begin{cases} \left[-\frac{2}{3}, \frac{4}{3}\right] & \text{for } i = j \\ [-1, 1] & \text{for } i \neq j \end{cases} . \tag{5.5}$$

The eigenspace decomposition of the anisotropy tensor in combination with tensor diagonalization (see Eq. (5.2)) leads to the fact that any physically realizable Reynolds stress tensor can be mapped to exactly one respective anisotropy tensor in its canonical form $\Lambda_{ij} = \mathrm{diag}(\lambda_1, \lambda_2, \lambda_3)$. When applying Eq. (5.5) to Λ_{ij}, the ordered eigenvalues

$$\begin{aligned} \lambda_1 &= \max_{\alpha}\,(a_{\alpha\alpha}|_{\mathrm{PCS}}) \\ \lambda_2 &= \max_{\beta\neq\alpha}\,(a_{\beta\beta}|_{\mathrm{PCS}}) \\ \lambda_3 &= -\lambda_1 - \lambda_2 = \min_{\gamma\neq\alpha,\beta}\,(a_{\gamma\gamma}|_{\mathrm{PCS}}) \end{aligned} \tag{5.6}$$

are bounded accordingly [151]:

$$\lambda_1 \geq \frac{3|\lambda_2| - \lambda_2}{2}\ , \ \lambda_1 \leq \frac{2}{3} - \lambda_2\ . \tag{5.7}$$

Table 5.1.: Turbulence componentiality and limiting states of turbulence with respect to the eigenvalues of the Reynolds stress tensor ξ_i and the anisotropy tensor λ_i.

States of turbulence	componentiality $\# \ \xi_i \neq 0$ or $\# \ \lambda_i \neq -\frac{2}{3}$	eigenvalues ξ_i	 λ_i
One-component (1C)	1	$\xi_1 = 2k, \xi_2 = \xi_3 = 0$	$\lambda_1 = \frac{4}{3}, \lambda_2 = \lambda_3 = -\frac{2}{3}$
Two-component	2	$\xi_1 + \xi_2 = 2k, \xi_3 = 0$	$\lambda_1 + \lambda_2 = \frac{2}{3}, \lambda_3 = -\frac{2}{3}$
Two-component axisymmetric (2C)	2	$\xi_1 = \xi_2 = k, \xi_3 = 0$	$\lambda_1 = \lambda_2 = \frac{1}{3}, \lambda_3 = -\frac{2}{3}$
Three-component	3	$\xi_1 + \xi_2 + \xi_3 = 2k$	$\lambda_1 + \lambda_2 + \lambda_3 = 0$
Three-component isotropic (3C)	3	$\xi_1 = \xi_2 = \xi_3 = \frac{2}{3}k$	$\lambda_1 = \lambda_2 = \lambda_3 = 0$

Turbulence componentiality [151] categorizes three fundamental states (one-, two- and three-component turbulence) based on the number of non-zero eigenvalues of the Reynolds stress tensor ξ_i (and respective anisotropy tensor eigenvalues λ_i), presented in Table 5.1. Besides, axisymmetric turbulence is characterized by two eigenvalues being equal, while an isotropic state features three identical eigenvalues. The corners of the AIM in Fig. 5.2 can be classified as the (three-component) isotropic limit (3C), the two-component axisymmetric limit (2C) and the one-component limit (1C) (see also Table 5.1). Moreover, due to the boundedness of the anisotropy tensor entries (and its eigenvalues, respectively), all physically plausible states of turbulence must lie within the area spanned by the corners of the triangle. Furthermore, a barycentric triangle can be constructed based on the spectral theorem [4]. Consequently, every physically realizable state of the Reynolds stress tensor can be mapped onto barycentric coordinates

$$\begin{aligned} \boldsymbol{x} &= \frac{1}{2}\boldsymbol{x}_{1\mathrm{C}}\left(\lambda_1 - \lambda_2\right) + \boldsymbol{x}_{2\mathrm{C}}\left(\lambda_2 - \lambda_3\right) + \boldsymbol{x}_{3\mathrm{C}}\left(\frac{3}{2}\lambda_3 + 1\right) \\ \boldsymbol{x} &= \mathbf{Q}\boldsymbol{\lambda} \quad \text{with } \lambda_1 \geq \lambda_2 \geq \lambda_3 \ , \end{aligned} \tag{5.8}$$

while $\mathbf{Q}$ depends on the choice of corners of the barycentric triangle. Figure 5.3 shows these three limiting states of the Reynolds stress tensor, defined by the corners of the triangle ($\boldsymbol{x}_{1\mathrm{C}}, \boldsymbol{x}_{2\mathrm{C}}, \boldsymbol{x}_{3\mathrm{C}}$) representing the one-component, two-component axisymmetric and three-component isotropic turbulent state. A great benefit of the ABM is the possibility to obtain a linear interpolation between two points with respect to their eigenvalues. The eigenspace perturbation exploits this property as well.

5.2.2. Perturbation of eigenspace representation

As the Reynolds stresses are expressed as functions of the mean flow quantities for turbulence modeling, we need to consider the nature of their relationship. A common example is the state-of-the-art LEVMs, which assume this relationship to be linear and introduce a turbulent (eddy) viscosity ν_T to approximate the Reynolds stress tensor in analogy to the viscous stresses

$$\tau_{ij} = -2\nu_\mathrm{T}\left(S_{ij} - \frac{1}{3}\frac{\partial u_k}{\partial x_k}\delta_{ij}\right) + \frac{2}{3}k\delta_{ij} \ , \tag{5.9}$$

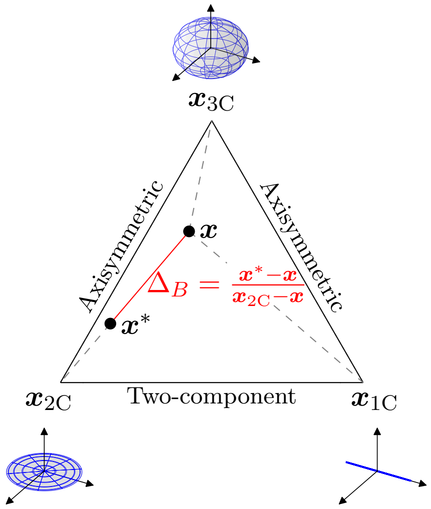
$\boldsymbol{x}_{3\text{C}}$
Axisymmetric
Axisymmetric
$\boldsymbol{x}$
$\Delta_B = \frac{\boldsymbol{x}^* - \boldsymbol{x}}{\boldsymbol{x}_{2\text{C}} - \boldsymbol{x}}$
$\boldsymbol{x}^*$
$\boldsymbol{x}_{2\text{C}}$
Two-component
$\boldsymbol{x}_{1\text{C}}$

Figure 5.3.: ABM representing the eigenvalues of the anisotropy tensor and its effect on the shape of the Reynolds stress tensor ellipsoid. The eigenvalue perturbation towards the two-component limiting state of turbulence is shown schematically.

where the strain-rate tensor is denoted as S_{ij}. In the past decades researchers have pointed out limitations of these LEVMs for flow situations that are not covered by the calibration cases [146, 109, 23, 89]. The estimated relationship between Reynolds stresses and mean rate of strain results in the inability to account correctly for its anisotropy and consequently lead to a significant degree of epistemic uncertainty. In order to account for such epistemic uncertainties due to the model-form, the perturbation approach suggests to modify the eigenspace (eigenvalues and eigenvectors) of the Reynolds stress tensor within physically permissible limits [34, 66]. The EPF of the Reynolds stress tensor implemented in TRACE creates a perturbed state of the Reynolds stress tensor defined as

$$\begin{aligned}\tau_{ij}^* &= k\left(a_{ij}^* + \frac{2}{3}\delta_{ij}\right)\\ &= k\left(v_{in}^* \Lambda_{nl}^* v_{jl}^* + \frac{2}{3}\delta_{ij}\right) \ ,\end{aligned} \tag{5.10}$$

where a_{ij}^* is the perturbed anisotropy tensor, Λ_{nl}^* is the perturbed eigenvalue matrix and v_{in}^* is the perturbed eigenvector matrix. The turbulent kinetic k energy is left unchanged. In the following sections, we will describe the mathematical and physical foundation of forming a perturbed eigenspace.

Eigenvalue perturbation

The eigenvalue perturbation utilizes the boundedness of the eigenvalues of the anisotropy tensor and their representation in terms of barycentric coordinates, as described in Section 5.2.1. As the representation of the anisotropy tensor within the ABM enables linear interpolation between a starting point $\boldsymbol{x}$ and a target point $\boldsymbol{x}_{(\text{t})}$, the perturbation methods creates a modified location $\boldsymbol{x}^*$, according to

$$\boldsymbol{x}^* = \boldsymbol{x} + \Delta_B\left(\boldsymbol{x}_{(\text{t})} - \boldsymbol{x}\right) \ , \tag{5.11}$$

with the relative distance $\Delta_B \in [0, 1]$ controlling the magnitude of eigenvalue perturbation as illustrated in Fig. 5.3. The starting point $\boldsymbol{x}$ is usually determined within the RANS simulation iteration via the relationship for the Reynolds stresses determined by the turbulence model, e.g. the Boussinesq assumption for LEVMs (see Eq. (5.9)). Due to their distinctive significance, the limiting states of turbulence at the corners act typically as the target point $\boldsymbol{x}_{(\mathrm{t})} \in \{\boldsymbol{x}_{1\mathrm{C}}, \boldsymbol{x}_{2\mathrm{C}}, \boldsymbol{x}_{3\mathrm{C}}\}$. Subsequently, the perturbed eigenvalues λ_i^* can be remapped by the inverse of $\mathbf{Q}$

$$\boldsymbol{\lambda}^* = \mathbf{Q}^{-1}\boldsymbol{x}^* \ . \tag{5.12}$$

Eigenvector perturbation

In contrast to the eigenvalues, there are no physical bounds for the orientation of the eigenvectors of the Reynolds stress tensor and there is no upper limit for the turbulent kinetic energy. Thus, the fundamental idea of perturbing the eigenvectors is to create bounding states for the production P_k of turbulent kinetic energy k in transport equation based LEVMs. Hereby, the budget of turbulent kinetic energy is indirectly manipulated. The production of turbulent kinetic energy is defined as the Frobenius inner product of the Reynolds stress and the strain-rate tensor. Since both are positive semi-definite, the bounds of the Frobenius inner product can be written in terms of their eigenvalues ξ_i and ψ_i arranged in decreasing order [83]:

$$\begin{aligned} P_k = -\tau_{ij}\frac{\partial U_i}{\partial x_j} = -\tau_{ij}\cdot S_{ij} = -\langle \boldsymbol{\tau}, \mathbf{S}\rangle_F = -\mathrm{tr}\,(\boldsymbol{\tau}\mathbf{S}) \\ \in [\xi_1\psi_3 + \xi_2\psi_2 + \xi_3\psi_1,\ \xi_1\psi_1 + \xi_2\psi_2 + \xi_3\psi_3] \ . \end{aligned} \tag{5.13}$$

Since the Reynolds stress and the strain-rate tensor share the same eigenvectors in LEVMs (see Eq. (5.9)), the lower bound of the turbulence production term can be obtained by commuting the first and third eigenvector of the Reynolds stress tensor, whereas maximum turbulence production is obtained by not changing the eigenvectors of the Reynolds stress tensor[3]:

$$\begin{aligned} \mathbf{v}_{\max} &= \begin{pmatrix} \boldsymbol{v_1} & \boldsymbol{v_2} & \boldsymbol{v_3} \end{pmatrix} \rightarrow P_{k_{\max}} \\ \mathbf{v}_{\min} &= \begin{pmatrix} \boldsymbol{v_3} & \boldsymbol{v_2} & \boldsymbol{v_1} \end{pmatrix} \rightarrow P_{k_{\min}} \ . \end{aligned} \tag{5.14}$$

Implications for CFD practitioners

The eigenspace perturbation can be divided into eigenvalue and eigenvector modifications of the Reynolds stress tensor. For practical application purposes each eigenvalue perturbation towards one of the limiting states of turbulence can be combined with minimization or maximization of the turbulence production term (eigenvector perturbation). In summary, the model-form uncertainty of LEVMs can be estimated by six additional CFD simulations if $\Delta_B < 1$ and only five perturbed simulations if $\Delta_B = 1$ is chosen. This is because the Reynolds stress ellipsoid is a perfect sphere when targeting for the 3C turbulence state with $\Delta_B = 1$ (see Fig. 5.3), making an eigenvector perturbation obsolete. As the amount of considered turbulence model uncertainty scales with the relative perturbation strength Δ_B, aiming for the corners of the barycentric triangle (applying $\Delta_B = 1$) is common practice in order to obtain the worst case estimate corresponding to the most conservative uncertainty bounds on QoI [34, 66, 107, 99]. The analysis of additional CFD simulations, propagating the effect of perturbed Reynolds stress tensors, enables a CFD practitioner to quantify the derived effect of the turbulence model perturbation on certain QoI, e.g. the pressure distribution.

---

[3] Permuting of the eigenvectors of the Reynolds stress is equivalent to changing the order of the respective eigenvalues. Both change the alignment of the Reynolds stress ellipsoid with the principal axes of the strain-rate tensor.

5.2.3. Self-consistent formulation of perturbation

The emergence of some shortcomings of the eigenspace perturbation of the Reynolds stress tensor is highlighted in this section. This forms the foundation for rethinking the computational formulation of the EPF. The present paper suggests an appropriate way of formulating the EPF, ensuring control over numerical stability while preserving the conceptual model of perturbing the eigenspace of the Reynolds stress tensor.

Need for moderating the perturbation strength

The need for moderating the effect of Reynolds stress tensor perturbation emerges, when the Reynolds stress tensor perturbation seeks to decrease the turbulent kinetic energy budget ($P_{k_{\min}}$ and/or 3C). These perturbations featuring overly reduced turbulent viscosity can lead to numerical convergence issues for example when simulating separated flows. To ensure convergence, moderating the effect of Reynolds stress tensor perturbation is required. Recent publications introduce a moderation factor f to enable the CFD solver to achieve fully converged, steady-state RANS results [107, 99]. Consequently, the propagated perturbed Reynolds stress tensor (entering the update of the viscous fluxes and the turbulence production term) can be expressed as

$$\tau^*_{ij_f} = \tau_{ij} + f\left[\tau^*_{ij} - \tau_{ij}\right], \tag{5.15}$$

where $f \in [0, 1]$ is the introduced moderation factor, adjusting the total amount of perturbed anisotropy tensor to be considered[4].

Inconsistency when combining eigenspace perturbation and moderation factor

Unfortunately, the unperturbed Reynolds stress tensor τ_{ij} and the perturbed one τ^*_{ij} do not necessarily share the same eigenvectors. When eigenvector perturbation is applied, the resulting moderated Reynolds stress tensor $\tau^*_{ij_f}$ shows unintended behaviour with respect to its projection onto barycentric coordinates. Fig. 5.4 presents the perturbation trajectory when increasing f from 0 to 1 for selected RANS data points inside the ABM towards the one-component limiting state of turbulence. The moderated Reynolds stress tensor is calculated based on Eq. (5.15) with $\tau^*_{ij} = \tau_{ij_{1\mathrm{C}}}$, while $\tau_{ij_{1\mathrm{C}}}$ is a function of $\Lambda^*_{ij_{1\mathrm{C}}}$, $\mathbf{v}^*_i$ and k_{RANS}. Each location along the perturbation trajectory results from determining the respective moderated anisotropy tensor and its barycentric coordinates related to its eigenvalues. The perturbation trajectory when τ^*_{ij} and τ_{ij} share identical eigenvectors shows the expected linear interpolation between the respective coordinates. However, when applying eigenvector perturbation (first and last column of $\mathbf{v}$ are commuted) the resulting intermediate paths do not represent the most direct connection between starting and target point. Instead, the perturbation trajectories in Fig. 5.4b point towards axisymmetric expansion (line between $\boldsymbol{x}_{3\mathrm{C}}$ and $\boldsymbol{x}_{1\mathrm{C}}$) first, head towards axisymmetric contraction (line between $\boldsymbol{x}_{3\mathrm{C}}$ and $\boldsymbol{x}_{2\mathrm{C}}$) subsequently and target the one-component limit of turbulence finally.

The mathematical explanation for this observation, when combining eigenvalue and eigenvector perturbation while moderating their effects by a factor according to Eq. (5.15) is given thereupon. Thus, the prerequisites for the accomplishment of linear interpolation properties in terms of barycentric coordinates, when adding two tensors $\mathbf{X}$ and $\mathbf{Y}$, are addressed. Assuming $\mathbf{X}$ and $\mathbf{Y}$ are positive semi-definite (as the Reynolds stress tensor),

---

[4] The effect of applying the moderation factor is identical to a reduction of Δ_B in Eq. (5.11) in case of pure eigenvalue perturbation (see Appendix 4.A in Chapter 4).

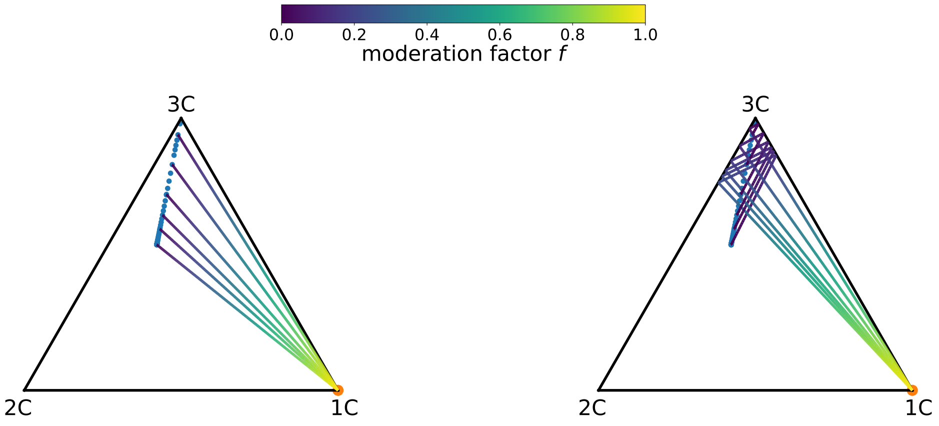

(a) Without eigenvector modification (aiming for $P_{k_{\max}}$)

(b) Perturbation including eigenvector modification (aiming for $P_{k_{\min}}$)

Figure 5.4.: Comparison of the perturbation trajectory for RANS channel flow data at $\mathrm{Re}_\tau = 1000$ (blue dots) in barycentric coordinates. The trajectories for selected RANS data points (τ_{ij}) are created by increasing $f = 0...1$ with and without eigenvector perturbation targeting the one-component limiting state of turbulence $\tau_{ij}^* = \tau_{ij_{1\mathrm{C}}}$ (orange dot).

then these tensors are realizable [136] and their projection onto barycentric coordinates has to lie within the barycentric triangle [4], following the reasons mentioned above (see Section 5.2.1). If $\mathbf{X}$ and $\mathbf{Y}$ share identical eigenvectors (commuting matrices), their sum $\mathbf{X} + \mathbf{Y}$ will feature the same eigenvectors and its eigenvalues are the sum of the individual eigenvalues of $\mathbf{X}$ and $\mathbf{Y}$ consequently (see Appendix 5.A). Moreover, if $\mathbf{X}$ and $\mathbf{Y}$ are positive semi-definite, their sum $\mathbf{X} + \mathbf{Y}$ will be positive semi-definite as well (see Appendix 5.B). This implies that the sum of two realizable Reynolds stress tensors will fulfill realizability constraints and will be located inside the ABM accordingly.
The line of argument mentioned above is also true for the summation of two scaled tensors

$$\mathbf{Z} = \mathbf{X} + f\,[\mathbf{Y} - \mathbf{X}] = (1 - f)\,\mathbf{X} + f\mathbf{Y}\ , \tag{5.16}$$

as multiplying a tensor by a scalar does not affect the eigenvectors and modifies the eigenvalues linearly. The individual scaling of the tensors is chosen, such that the first invariant of $\mathbf{Z}$ ($\mathrm{tr}\,(\mathbf{Z})$) remains identical to $\mathbf{X}$ and $\mathbf{Y}$ ($\mathrm{tr}\,(\mathbf{X}) = \mathrm{tr}\,(\mathbf{Y}) = \mathrm{tr}\,(\mathbf{Z})$). Keeping in mind that $\mathbf{X}$ and $\mathbf{Y}$ represent Reynolds stress tensors, this means that the turbulent kinetic energy remains constant. This is achieved by choosing $f \in [0, 1]$. Due to the affine transformation, the barycentric coordinates of the anisotropic part of $\mathbf{Z}$ are determined by $\boldsymbol{x}_\mathbf{Z} = (1 - f)\,\boldsymbol{x}_\mathbf{X} + f\boldsymbol{x}_\mathbf{Y}$, when $\boldsymbol{x}_\mathbf{X}$ and $\boldsymbol{x}_\mathbf{Y}$ are the initial states of the tensors $\mathbf{X}$ and $\mathbf{Y}$ in barycentric coordinates (see Appendix 5.C). Finally, if f is increased incrementally from 0 to 1, the resulting states $\boldsymbol{x}_\mathbf{Z}$ will end up forming a straight line connecting $\boldsymbol{x}_\mathbf{X}$ and $\boldsymbol{x}_\mathbf{Y}$, as illustrated in Fig. 5.5 and especially in Fig. 5.5a. For reference, Fig. 5.5b and Fig. 5.5c show the result of linear interpolation in terms of barycentric coordinates in the classical AIM and the alternative Anisotropy Invariant Map [17].

However, the summation of commuting matrices is the exception. Adding up two arbitrary, positive semi-definite matrices, eigenvector orientation is not preserved and the resulting eigenvalues are not just the sum of the original eigenvalues. As a consequence, their transformation into barycentric coordinates is not located along the shortest possible path connecting the representation of the anisotropy of the original tensors, as shown in

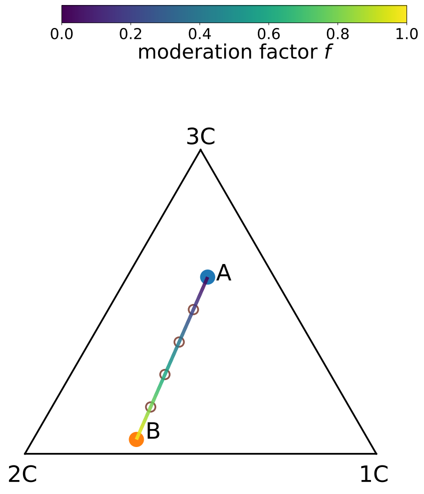

(a) Representation in ABM [4]

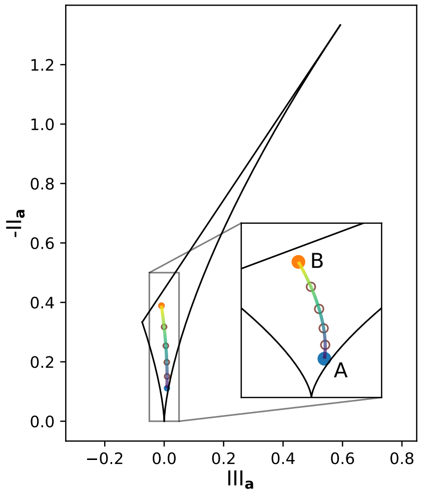

(b) Representation in AIM [93]

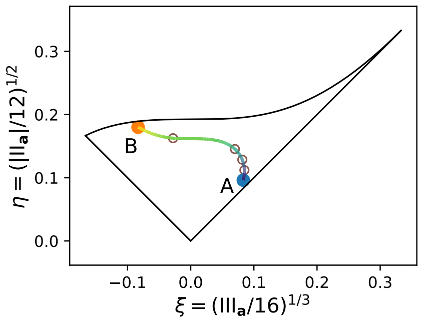

(c) Representation in alternative Anisotropy Invariant Map [17]

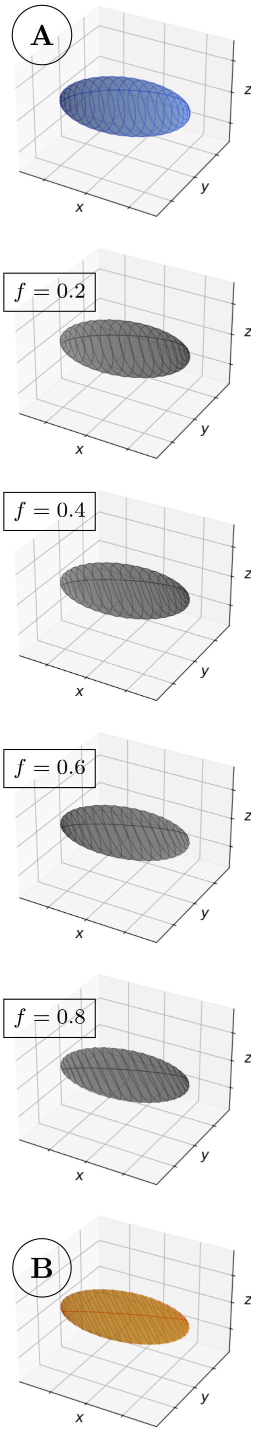

(d) Reynolds stress tensor ellipsoid

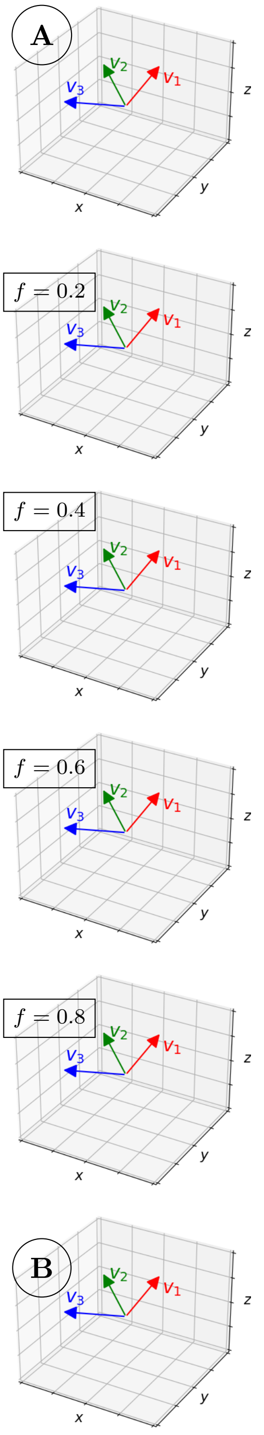

(e) Eigenvectors of Reynolds stress tensor

Figure 5.5.: Transition from tensor **A** to **B** (defined in Appendix 5.D) featuring identical eigenvectors by increasing $f = 0...1$ (see Eq. (5.16)). The intermediate brown-colored states in (a), (b) and (c) correspond to the states with $f \in [0.2, 0.4, 0.6, 0.8]$ in (d) and (e).

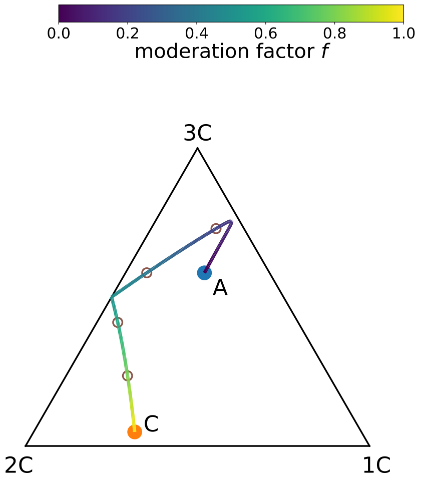

(a) Representation in ABM [4]

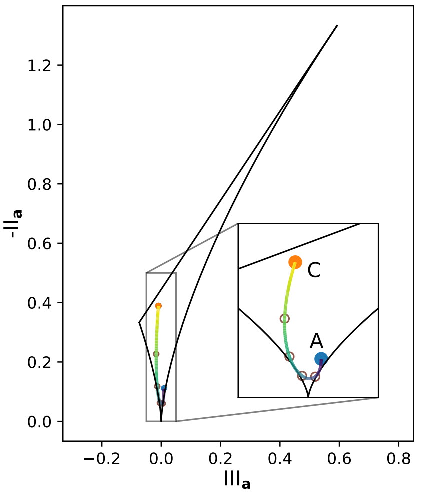

(b) Representation in AIM [93]

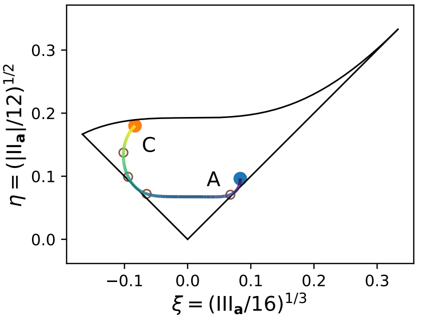

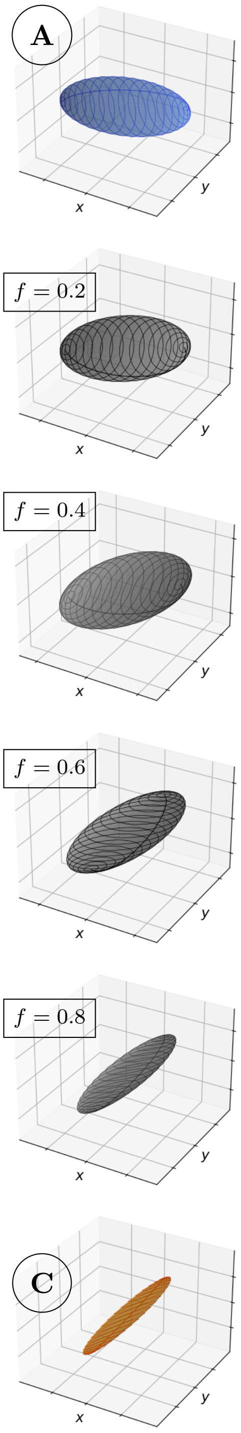

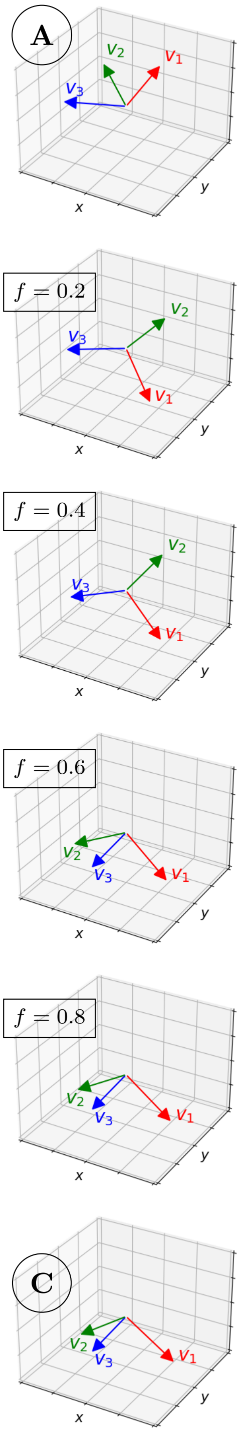

(c) Representation in alternative Anisotropy Invariant Map [17]

(d) Reynolds stress tensor ellipsoid

(e) Eigenvectors of Reynolds stress tensor

Figure 5.6.: Transition from tensor **A** to **C** (defined in Appendix 5.D) featuring different eigenvector by increasing $f = 0 ... 1$ (see Eq. (5.16)). The intermediate brown-colored states in (a), (b) and (c) correspond to the states with $f \in [0.2, 0.4, 0.6, 0.8]$ in (d) and (e).

Fig. 5.6. Analyzing the orientation of the PCS of each tensor in Fig. 5.6d and Fig. 5.6e reveals the transformation of eigenspace. The representation in barycentric coordinates shows a perturbation trajectory that connects starting and target point via the sides of the triangle (see Fig. 5.6a). Hence, the introduction of a moderation factor violates the original intent of the EPF and, in addition to that, affects the plausibility of recent data-driven machine learning approaches [61, 99], relying on the interpolation property with respect to barycentric coordinates. Moreover, the bounds of the Frobenius inner matrix product (see Eq. (5.14)) can only be achieved, if the matrices share the same eigenvectors[5]. When applying Reynolds stress eigenvector perturbation in combination with a moderation factor, the resulting turbulence production indeed yields a value within the interval of the inner product defined in Section 5.2.2, but does not reach the theoretical limits as the perturbed Reynolds stress tensor features some different eigenvectors compared to the strain-rate tensor.

To sum up, the concept of the EPF that is perturbing the eigenvalues of the Reynolds stress tensor linearly between the initial state and a certain limiting state of turbulence cannot be guaranteed if a moderation factor is introduced as in current implementations. Applying this moderation factor in combination with eigenvector perturbations results in a conceptually unintended state of the anisotropy tensor on the one hand. On the other hand, the intended minimization and maximization of the turbulence production term is no longer guaranteed.

Proposed approach to improve self-consistency

In order to resolve the issues described in Section 5.2.3 the implementation of the EPF needs to be changed. A first step is the removal of the entire idea of applying a moderation factor to adjust the amount of perturbed Reynolds stress tensor according to Eq. (5.15). As a consequence, Δ_B in Eq. (5.11), which controls the amount of perturbation towards the respective limiting state of turbulence, has to be adjusted, in order to retain converged RANS simulations (see Section 5.2.3). This is in contrast to the common practice of choosing $\Delta_B = 1$, arguing that there is no physical reason to restrict this value without the usage of data-driven methods or expert knowledge on the flow configuration. In other words, the perturbed Reynolds stress tensor, entering the update of the viscous fluxes and the turbulence production term, in the proposed self-consistent implementation is based on Eq. (5.10). Nevertheless, the fundamental idea of the individual perturbation of eigenvalues and eigenvectors, introduced in Section 5.2.2, remains the same. Hereby, the entire EPF in order to quantify the structural uncertainties of turbulence models is formulated in a verified, physics-constrained and self-consistent manner. Its implementation in TRACE can be subdivided in several steps within each pseudo-time step of steady RANS simulations:

1. Calculate the Reynolds stress tensor based on the Boussinesq approximation in Eq. (5.9).
2. Determine the respective anisotropy tensor (see Eq. (5.1)).
3. Decompose the anisotropy tensor in its eigenvalues and eigenvectors (see Eq. (5.2)).
4. Compute the barycentric coordinates based on the eigenvalues of the anisotropy tensor (see Eq. (5.8)).

---

[5] Details can be found in Appendix B.

5. Perturb the barycentric coordinates of the anisotropy tensor within physical realizable limits by chosen Δ_B (see Eq. (5.11)).
6. Determine the perturbed eigenvalues of the anisotropy tensor with respect to the perturbed barycentric coordinates (see Eq. (5.12)).
7. Perturb the eigenvectors of the anisotropy/Reynolds stress tensor if the production term of the turbulent kinetic energy should be minimized (see Eq. (5.14)).
8. Reconstruct the perturbed Reynolds stress tensor according to Eq. (5.10).
9. Update the viscous fluxes using the reconstructed perturbed Reynolds stress tensor.
10. Update the turbulence production term using the reconstructed perturbed Reynolds stress tensor explicitly.

It should be noted that different types and magnitudes of the perturbations (1C, 2C or 3C; $P_{k_{\min}}$ or $P_{k_{\max}}$; chosen Δ_B and/or f) result in different solutions of the RANS equations from a mathematical point of view regardless of the EPF formulation (non-consistent or consistent). However, not every mathematical solution represents a physically meaningful solution (e.g. a solution giving laminar flow in a clearly turbulent domain, or unsteady flow in steady-state conditions). Hence, the EPF requires certain expert knowledge and engineering practice to determine the appropriate amount of perturbation magnitude (Δ_B in the consistent formulation) leading to meaningful, converged RANS solutions.

5.2.4. Application to plane turbulent channel flow

The uncertainty estimates based on the non-consistent and self-consistent eigenspace perturbation are compared when applied to a canonical turbulent channel flow at $\mathrm{Re}_\tau = 1000$. The channel flow is homogeneous in streamwise and spanwise direction. A constant streamwise pressure gradient $\partial p/\partial x$ is applied to balance the skin friction at the walls. The configuration for simulating this wall-bounded flow is sketched in Fig. 5.7. The mesh has a low-Reynolds resolution ($y^+ \leq 1$) at the solid walls with 100 cells up to the symmetry line in wall-normal direction. The two-equation Menter SST k-ω turbulence model [104], which belongs to the group of LEVMs, is considered as the baseline model for the present simulations. The discrepancies with respect to barycentric coordinates of the RANS turbulence model when compared with available DNS data of Lee and Moser [86] are moderate in the channel center and start to increase close to the wall due to the strong anisotropy of turbulence (see Fig. 5.8). Due to the fact that the turbulence model relies on the Boussinesq assumption Eq. (5.9) and that a velocity gradient in spanwise direction is missing, the Reynolds stress tensor has at least one zero eigenvalue. Hence, the resulting barycentric coordinates are known to be the plane-strain line in the ABM.

The turbulence model-form uncertainty is quantified applying the EPF. In order to demonstrate the implications of using the proposed consistent formulation a relative perturbation strength of $\Delta = 0.5$ is used for the consistent formulation, while $\Delta = 1.0$ is used for the non-consistent formulation. Consequently, a factor of $f = 0.5$ is applied for the non-consistent formulation to moderate the strength for eigenvalues and eigenvector perturbation and to obtain comparable results to the consistent formulation. The streamwise pressure gradient, which was adjusted for the baseline simulation to match the Reynolds number, remains constant throughout the perturbed simulations. This is comparable to the procedure of Emory et al. [34] for a similar test case. The comparison of the uncertainty estimated by the EPF for the streamwise velocity profile of the boundary layer is presented in Fig. 5.9. The simulations featuring eigenvector perturbation are

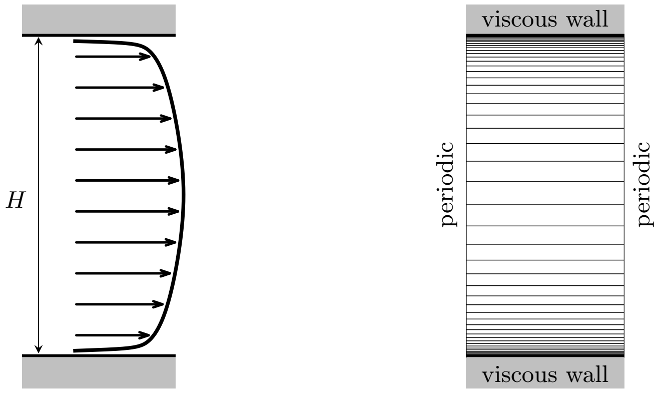

(a) Schematic sketch of a fully developed turbulent boundary layer

(b) $\mathrm{Re}_\tau = 1000$ (every fourth line shown) mesh and boundary conditions; symmetry is enforced in spanwise direction

Figure 5.7.: Schematic turbulent channel flow setup.

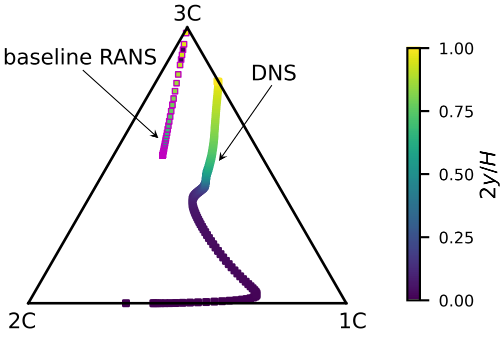

Figure 5.8.: Barycentric coordinates of DNS data and RANS simulation using the Menter SST k-ω model. Data points are colored according to their distance from the wall.

indicated by $P_{k_{\mathrm{min}}}$ (aiming for minimized turbulence production), while no eigenvector permutation is applied for $P_{k_{\mathrm{max}}}$ (see Eq. (5.14)). Overall, the uncertainty estimate (gray shaded area) of the boundary layer profile are identical for both formulations. On the one hand, this is because the simulations without any eigenvector perturbation are mathematically equivalent, leading to identical results for QoI. On the other hand, applying eigenvector permutation for the channel flow results in laminarization of the boundary layer. Hence, the laminar velocity profile driven by the selected constant streamwise pressure gradient bounds the uncertainty estimation, regardless of the EPF formulation or target barycentric coordinate $\boldsymbol{x}_{(\mathrm{t})}$. Overall, the uncertainty intervals are smaller for previous investigations of the channel flow by Emory et al. [34]. To the authors' knowledge and experience, this is because of the fact that Emory et al. [34] do not explicitly update the turbulence production term based on the perturbed Reynolds stresses. Additionally, as the perturbations for both formulations are uniform throughout the computational domain, it is expected that by applying an appropriate amount of perturbation strength (e.g. locally varying perturbations with the help of machine learning) the uncertainty estimates would be more adequate.

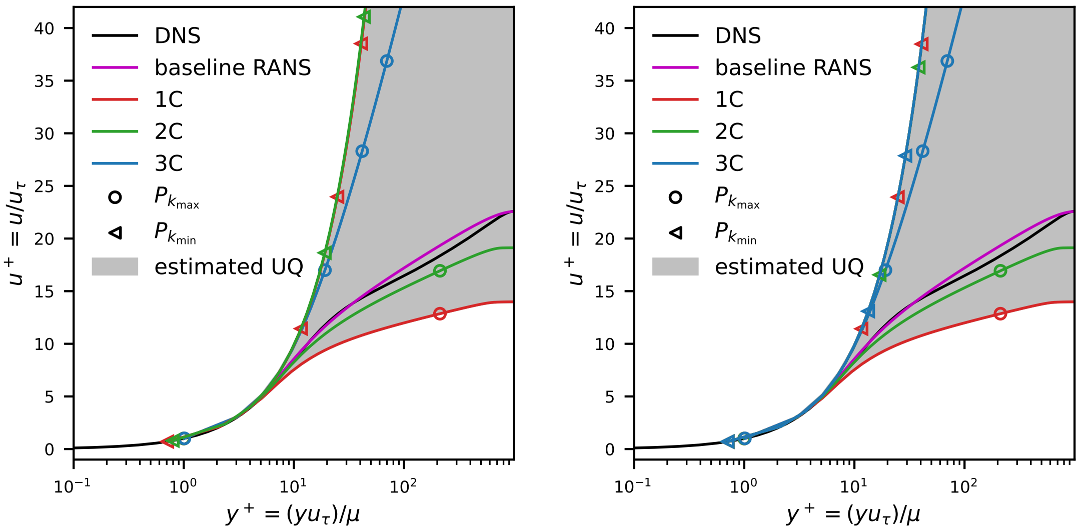

(a) Application of non-consistent formulation of EPF using $\Delta_B = 1.0$ and $f = 0.5$

(b) Application of consistent formulation of EPF using $\Delta_B = 0.5$

Figure 5.9.: Comparison of the resulting uncertainty bounds for the streamwise velocity profile of turbulent channel flow simulation derived by the EPF.

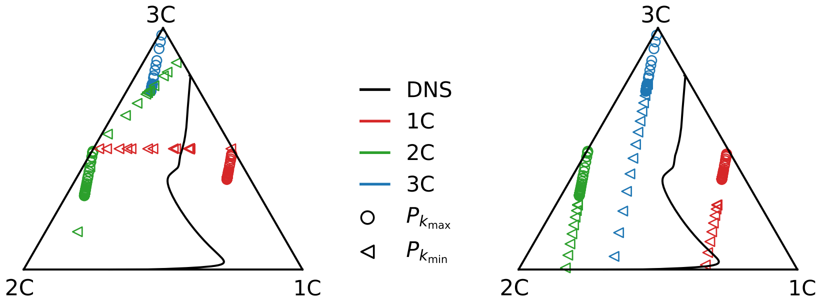

(a) Application of non-consistent formulation of EPF using $\Delta_B = 1.0$ and $f = 0.5$

(b) Application of consistent formulation of EPF using $\Delta_B = 0.5$

Figure 5.10.: Comparison of the resulting barycentric coordinates of the perturbed Reynolds stress tensors for the turbulent boundary layer profiles.

In terms of conceptual model verification, the proposed self-consistent formulation guarantees to maintain agreement between the theoretical idea of the EPF and the simulation results, which are shown in Fig. 5.10. The final perturbed states of the Reynolds stress anisotropy tensor for simulations aiming at $P_{k_{\max}}$ show the expected identical perturbed anisotropic states for both EPF formulations. Fig. 5.10a reveals the initial motivation for scrutinizing the consistency of the formulation using a moderation factor in combination with eigenvector perturbation, as the RANS solution points for the turbulent boundary layer do not show the intended behaviour for $P_{k_{\min}}$. If a CFD practitioner runs a perturbed RANS simulation aiming for one of the corners of the barycentric triangle, it is expected that the resulting anisotropic states show respective shifts towards that limiting state of turbulence. The boundary layer solution points of $(1\text{C}, P_{k_{\min}})$ and $(2\text{C}, P_{k_{\min}})$ are located at some unintended states inside the barycentric triangle in Fig. 5.10a due to summation of two non-commuting tensors. In contrast, the respective simulations using the consistent formulation produces anisotropic states of the Reynolds stress tensor, which are entirely perturbed towards one of the corners of the triangle (keeping in mind that the unperturbed Reynolds stress tensor is represented by the plane-strain line as in Fig. 5.8).

Besides, the self-consistent formulation of the EPF framework, presented in Section 5.2.3, enables the user to additionally perform the perturbed RANS simulation aiming for $(3\text{C}, P_{k_{\min}})$, which was obsolete in the non-consistent formulation using $\Delta_B = 1$.

5.3. Conclusion & outlook

The EPF, which creates perturbed states of the Reynolds stress tensor in order to quantify the structural uncertainties of RANS turbulence models, is described in detail, presenting its underlying idea and discussing its practical implementation and usage. The present work highlights one shortcoming in the commonly proposed implementation of this framework. Due to numerical convergence issues, researchers have suggested to weaken the effect of perturbed Reynolds stress by introducing a moderation factor in previous publications. The assessment of the common computational implementation reveals that the basic concept of the EPF is not correctly represented in that case. The introduction of a separate moderation factor may cause unintended behaviour and violate EPF's self-consistency. Therefore, the present paper presents a self-consistent way of formulating the Reynolds stress tensor perturbation framework, as the significance of reasonable physics-constrained UQ methodologies is indisputable. This formulation has recently been implemented in the CFD solver suite TRACE. The analysis of the results based on the proposed eigenspace perturbation formulation when applied to turbulent channel flow verifies its benefits with respect to the interpretability of the uncertainty estimates. In the near future the framework will be applied to quantify the uncertainties for more complex flows for which the differences between the non-consistent and the self-consistent formulation are expected to be greater for QoI. Moreover, ongoing research focusing on determining the Reynolds stress tensor perturbation by the use of data-driven machine learning practises will benefit from verified self-consistent implementation of the framework as well.

Appendix 5.A Properties of the sum of two tensors featuring identical eigenvectors in terms of eigenspace

Let $\xi_{i_\mathbf{X}}$ be the eigenvalues of tensor $\mathbf{X}$ and $\xi_{i_\mathbf{Y}}$ be the eigenvalues of tensor $\mathbf{Y}$. Both tensors share the same eigenvectors $\boldsymbol{v_i}$. Therefore, we know that the relationships

$$\begin{aligned} \mathbf{X}\boldsymbol{v_i} &= \xi_{i_\mathbf{X}}\boldsymbol{v_i} \quad i = 1,2,3 \\ \mathbf{Y}\boldsymbol{v_i} &= \xi_{i_\mathbf{Y}}\boldsymbol{v_i} \quad i = 1,2,3 \end{aligned} \tag{5.17}$$

are satisfied. The summation of $\mathbf{X}$ and $\mathbf{Y}$ leads to:

$$\begin{aligned} (\mathbf{X}+\mathbf{Y})\,\boldsymbol{v_i} &= \mathbf{X}\boldsymbol{v_i} + \mathbf{Y}\boldsymbol{v_i} \quad i = 1,2,3 \\ &= \xi_{i_\mathbf{X}}\boldsymbol{v_i} + \xi_{i_\mathbf{Y}}\boldsymbol{v_i} \text{ (cf. Eq. (5.17))} \\ &= (\xi_{i_\mathbf{X}} + \xi_{i_\mathbf{Y}})\,\boldsymbol{v_i}\ . \end{aligned} \tag{5.18}$$

Consequently, the resulting sum features identical eigenvectors as well and its eigenvalues are the sum of the individual eigenvalues.

Appendix 5.B Transferability of definiteness with respect to the sum of two positive semi-definite tensors

Tensor $\mathbf{X}$ and tensor $\mathbf{Y}$ are positive semi-definite, which means

$$\forall \boldsymbol{n} \in \mathbb{R}^n,\ \boldsymbol{n}^T \mathbf{X} \boldsymbol{n} \geq 0,\ \boldsymbol{n}^T \mathbf{Y} \boldsymbol{n} \geq 0\ . \tag{5.19}$$

The sum of $\mathbf{X}$ and $\mathbf{Y}$ can be distributed based on the laws of tensor multiplication

$$\forall \boldsymbol{n} \in \mathbb{R}^n, \boldsymbol{n}^T \left(\mathbf{X} + \mathbf{Y}\right) \boldsymbol{n} = \boldsymbol{n}^T \mathbf{X} \boldsymbol{n} + \boldsymbol{n}^T \mathbf{Y} \boldsymbol{n} \geq 0\ . \tag{5.20}$$

Consequently, the sum of two positive semi-definite tensors is positive semi-definite as well.

Appendix 5.C Interpolation properties of two scaled tensor with respect to its location in barycentric coordinates

Let $\lambda_{1_\mathbf{X}} \geq \lambda_{2_\mathbf{X}} \geq \lambda_{3_\mathbf{X}}$ be the eigenvalues of the anisotropic part of the 3x3-tensor $\mathbf{X}$ and $\lambda_{1_\mathbf{Y}} \geq \lambda_{2_\mathbf{Y}} \geq \lambda_{3_\mathbf{Y}}$ be the eigenvalues of the anisotropic part of the 3x3-tensor $\mathbf{Y}$. The eigenvalues of the summation of the scaled tensors

$$\mathbf{Z} = (1-f)\,\mathbf{X} + f\mathbf{Y} \tag{5.21}$$

are $\lambda_{i_\mathbf{Z}} = (1-f)\,\lambda_{i_\mathbf{X}} + f\lambda_{i_\mathbf{Y}}$.

The barycentric coordinates are

$$\boldsymbol{x}_\mathbf{Z} = \boldsymbol{x}_{1\mathrm{C}} \frac{1}{2}\left[\lambda_{1_\mathbf{Z}} - \lambda_{2_\mathbf{Z}}\right] + \boldsymbol{x}_{2\mathrm{C}}\left[\lambda_{2_\mathbf{Z}} - \lambda_{3_\mathbf{Z}}\right] + \boldsymbol{x}_{3\mathrm{C}}\left[\frac{3}{2}\lambda_{3_\mathbf{Z}} + 1\right] \tag{5.22}$$

$$\begin{aligned} =&\boldsymbol{x}_{1\mathrm{C}} \frac{1}{2}\left[\left((1-f)\,\lambda_{1_\mathbf{X}} + f\lambda_{1_\mathbf{Y}}\right) - \left((1-f)\,\lambda_{2_\mathbf{X}} + f\lambda_{2_\mathbf{Y}}\right)\right] \\ &+ \boldsymbol{x}_{2\mathrm{C}}\left[\left((1-f)\,\lambda_{2_\mathbf{X}} + f\lambda_{2_\mathbf{Y}}\right) - \left((1-f)\,\lambda_{3_\mathbf{X}} + f\lambda_{3_\mathbf{Y}}\right)\right] \\ &+ \boldsymbol{x}_{3\mathrm{C}}\left[\frac{3}{2}\left((1-f)\,\lambda_{3_\mathbf{X}} + f\lambda_{3_\mathbf{Y}}\right) + 1\right] \end{aligned} \tag{5.23}$$

$$\begin{aligned} =&\boldsymbol{x}_{1\mathrm{C}} \frac{1}{2}\left[\left((1-f)\,\lambda_{1_\mathbf{X}} + f\lambda_{1_\mathbf{Y}}\right) - \left((1-f)\,\lambda_{2_\mathbf{X}} + f\lambda_{2_\mathbf{Y}}\right)\right] \\ &+ \boldsymbol{x}_{2\mathrm{C}}\left[\left((1-f)\,\lambda_{2_\mathbf{X}} + f\lambda_{2_\mathbf{Y}}\right) - \left((1-f)\,\lambda_{3_\mathbf{X}} + f\lambda_{3_\mathbf{Y}}\right)\right] \\ &+ \boldsymbol{x}_{3\mathrm{C}}\left[\frac{3}{2}\left((1-f)\,\lambda_{3_\mathbf{X}} + f\lambda_{3_\mathbf{Y}}\right) + 1 - f + f\right] \end{aligned} \tag{5.24}$$

$$\begin{aligned}
=&\boldsymbol{x}_{1\mathrm{C}}\frac{1}{2}\left[(1-f)\left(\lambda_{1_\mathbf{X}}-\lambda_{2_\mathbf{X}}\right)\right]\\
&+\boldsymbol{x}_{2\mathrm{C}}\left[(1-f)\left(\lambda_{2_\mathbf{X}}-\lambda_{3_\mathbf{X}}\right)\right]\\
&+\boldsymbol{x}_{3\mathrm{C}}\left[\frac{3}{2}(1-f)\left(\lambda_{3_\mathbf{X}}+1\right)\right]\\
&+\boldsymbol{x}_{1\mathrm{C}}\frac{1}{2}\left[f\left(\lambda_{1_\mathbf{Y}}-\lambda_{2_\mathbf{Y}}\right)\right]\\
&+\boldsymbol{x}_{2\mathrm{C}}\left[f\left(\lambda_{2_\mathbf{Y}}-\lambda_{3_\mathbf{Y}}\right)\right]\\
&+\boldsymbol{x}_{3\mathrm{C}}\left[\frac{3}{2}f\left(\lambda_{3_\mathbf{Y}}+1\right)\right]
\end{aligned}\tag{5.25}$$

$$=(1-f)\,\boldsymbol{x}_\mathbf{X}+f\boldsymbol{x}_\mathbf{Y}\ . \tag{5.26}$$

Consequently, the projection onto barycentric coordinates preserves the ability to interpolate linearly between two initial states in the ABM.

Appendix 5.D Example tensors used in this paper

The positive semi-definite tensor **A** is defined as

$$\mathbf{A}=\begin{pmatrix}2 & 0.5 & -0.5\\ 0.5 & 2.5 & -0.5\\ -0.5 & -0.5 & 1.5\end{pmatrix}\ , \tag{5.27}$$

with a set of eigenvalues $\xi_{i_\mathbf{A}}$ and eigenvectors $\boldsymbol{v}_{\boldsymbol{i}_\mathbf{A}}$.
Tensor **C**, that is also positive semi-definite and features identical trace as **A**, reads

$$\mathbf{C}=\begin{pmatrix}1 & 0.5 & 1.5\\ 0.5 & 2 & 0\\ 1.5 & 0 & 3\end{pmatrix}\ . \tag{5.28}$$

The respective set of eigenvalues is $\xi_{i_\mathbf{C}}$ and eigenvectors are $\boldsymbol{v}_{\boldsymbol{i}_\mathbf{C}}$.
Tensor **B** is constructed using the PCS defined by the eigenvectors of **A** and the eigenvalues of **C**

$$\mathbf{B}=v_{in_\mathbf{A}}\begin{pmatrix}\xi_{1_\mathbf{C}} & 0 & 0\\ 0 & \xi_{2_\mathbf{C}} & 0\\ 0 & 0 & \xi_{3_\mathbf{C}}\end{pmatrix}v_{jl_\mathbf{A}}\approx\begin{pmatrix}2.19 & 0.55 & -1.11\\ 0.55 & 3.02 & -0.83\\ -1.11 & -0.83 & 0.79\end{pmatrix}\ . \tag{5.29}$$

6. Physically constrained eigenspace perturbation for turbulence model uncertainty estimation

(Published in *Physics of Fluids*, 36(2), 025153, 2024[1].)

M. Matha and C. Morsbach
DLR, Institute of Propulsion Technology, Cologne, Germany

Abstract

Aerospace design is increasingly incorporating DUU-based approaches to lead to more robust and reliable optimal designs. These approaches require dependable estimates of uncertainty in simulations for their success. The key contributor of predictive uncertainty in CFD simulations of turbulent flows are the structural limitations of RANS models, termed model-form uncertainty. Currently, the common procedure to estimate turbulence model-form uncertainty is the EPF, involving perturbations to the modeled Reynolds stress tensor within physical limits. The EPF has been applied with success in design and analysis tasks in numerous prior works from the industry and academia. Owing to its rapid success and adoption in several commercial and open-source CFD solvers, in-depth Verification and Validation of the EPF is critical. In this work, we show that under certain conditions, the perturbations in the EPF can lead to Reynolds stress dynamics that are not physically realizable. This analysis enables us to propose a set of necessary physics-based constraints, leading to a realizable EPF. We apply this constrained procedure to the illustrative test case of a converging-diverging channel, and we demonstrate that these constraints limit physically implausible dynamics of the Reynolds stress tensor, while enhancing the accuracy and stability of the uncertainty estimation procedure.

6.1. Introduction

As computational resources continue to advance, the aerospace industry is experiencing a notable increase in the degree of digitization, leading to faster design cycles with the help of CFD. In order to accelerate the optimization of designs and streamline virtual certification procedures, numerical approximations of the RANS equations is a judicious choice. This choice not only upholds an acceptable level of fidelity but also computational efficiency for its purposes in design. However, the RANS equations necessitate the modeling of the second-moment Reynolds stress tensor $\boldsymbol{\tau}$. Closure models, commonly referred to as turbulence models, attempt to express the Reynolds stresses as a function of measured quantities such as the local mean rate of strain. While turbulence modeling offers practicality and facilitates efficient simulations, it also imposes inherent limitations

---

[1] Licensed under a Creative Commons Attribute (CC BY) license

in achieving high levels of accuracy. Moreover, the assumptions made in the functional representation of turbulence models introduce model-form (epistemic) uncertainties as soon as their applicability range is exceeded [29, 169]. This is particularly relevant for complex engineering flows such as the ones encountered in turbomachinery components. To provide a few examples, the prediction accuracy of common LEVMs suffers in flows characterized by adverse pressure gradient, separation and reattachment, surface curvature and secondary flow. Due to the definition of the Reynolds stresses in LEVMs (see also introduction of Boussinesq approximation in Section 6.2), the tensor only carries information on the mean rate of strain, hence the model is unable to account for rotational effects and streamline curvature [146, 23]. Additionally, in the isotropic eddy viscosity hypothesis, excluding representation of any anisotropic normal Reynolds stresses hinders the accurate consideration of secondary flow [109].

Accounting for the inherent uncertainties in simulations is key towards robust designs. That is why approaches to quantify the uncertainties associated with turbulence closure models play an important role, especially in industrial applications with turbulent flows. The only approach capable of addressing the epistemic uncertainty inherent in turbulence closure modeling is the EPF that was initially proposed by Emory [33]. This methodology builds upon the limited functional relationship of the Reynolds stresses. Selective perturbation of the Reynolds stress tensor within physical bounds combined with sampling from the resulting CFD solutions is an innovative model-form UQ approach [34, 52, 36, 66]. The underlying modeling structure of the tensor perturbation involves perturbations in both eigenvalues and eigenvectors, which is comprehensively described in Section 6.2. These perturbations can be interpreted as altering the shape and the orientation of the Reynolds stress tensor ellipsoid [66, 106, 96]. Due to its unique characteristics and persuasive interpretability of its simulation outcomes, the EPF has been used in various engineering applications [45, 35, 105, 56, 80, 22, 125, 108, 113, 64, 31, 152, 19, 51, 49]. For this reason, the ability of perturbing the eigenspace of the Reynolds stresses has been integrated into numerous CFD solvers [30, 107, 56, 99]. In addition to that, the emergence of machine learning strategies guided the path towards data-driven enhancements of the EPF [30, 61, 32, 99].

As there is the need for V&V of novel CFD methods, this paper addresses the underlying modeling rationale of this framework. Recently, we have already proposed a novel advancement in the context of the EPF that focuses on ensuring realizable Reynolds stresses and consistency between the envisioned conceptual and the implemented computational model [96]. While the theoretical modeling structure and limitations of the eigenvalue perturbation have been exhaustively discussed [106], the analysis of the eigenvector perturbation remains incomplete so far.

In this article, we undertake a detailed examination of the foundation and ramifications of the eigenvector perturbations. This thorough analysis of the Reynolds stress tensor's eigenvector perturbation in the context of RANS equations, enables us to show that eigenvector perturbation, as they are currently implemented, may lead to non-realizable Reynolds stress tensor dynamics. Moreover, we highlight numerical stability issues that may arise as a consequence, potentially preventing broader application of this approach. Therefore, we derive and propose a novel idea to prevent implausible Reynolds stress tensor dynamics in the current paper.

6.2. Accounting for turbulence modeling uncertainty using the tensor perturbation framework

Despite the ongoing increase in computational resources, solving the set of Navier-Stokes equations for turbulent flows by SRS in the design phase for industrially relevant devices operating at high Reynolds numbers cannot be expected in the near future. As engineers and system designers are rather interested in rapid iteration cycles, the ability to make decisions based on statistical consideration of the mean flow is still industrial practice. Hence, all flow quantities can be split into a mean and a fluctuating part, according to $\phi = \overline{\phi} + \phi'$. To accommodate this need for compressible flows, a density weighted average (Favre-average) is performed, whereby

$$\phi = \widetilde{\phi} + \phi'' \text{ and } \overline{\rho}\widetilde{\phi} = \overline{\rho\phi} \tag{6.1}$$

holds for all instantaneous quantities except density ρ and pressure p. In the scope of this paper, we will use the term RANS for the Favre-averaged Navier-Stokes equations, although *Reynolds-averaging* was initially developed for incompressible flows. The statistically Favre-averaged momentum equation

$$\frac{\partial}{\partial t}\left(\overline{\rho}\widetilde{u}_i\right) + \frac{\partial}{\partial x_j}\left(\overline{\rho}\widetilde{u}_j\widetilde{u}_i\right) = -\frac{\partial \overline{p}}{\partial x_i} + \frac{\partial}{\partial x_j}\left(\sigma_{ij} - \overline{\rho}\widetilde{u'_i u'_j}\right) \tag{6.2}$$

describes the change of the mean momentum in both time and space, attributed to acting mean forces such as pressure gradients and divergence of viscous stresses (for the sake of simplicity, gravitational forces and forces due to rotating frames of reference are neglected).

To shorten and simplify the notation, we denote the mean velocities by a capital letter $\widetilde{u}_i \to U_i$ and omit the overline for density $\overline{\rho} \to \rho$ and pressure $\overline{p} \to p$. Additionally, we use x, y, z for x_1, x_2, x_3 in the following.

Based on Stokes' hypothesis the mean viscous stresses $\boldsymbol{\sigma}$ depend on the strain-rate tensor $S_{ij} = \frac{1}{2}\left(\frac{\partial U_i}{\partial x_j} + \frac{\partial U_j}{\partial x_i}\right)$ and kinematic viscosity denoted as ν:

$$\sigma_{ij} = 2\rho\nu\left(S_{ij} - \frac{1}{3}S_{kk}\delta_{ij}\right) \ . \tag{6.3}$$

In addition to these stresses, the right hand side of the equation contains unknown correlations of fluctuating velocities $\tau_{ij} = \widetilde{u''_i u''_j}$, called the turbulent stresses or Reynolds stresses [123]. To close the set of equations and facilitate computational simulations, there exist numerous approximation methods. A widely used modeling assumption is the representation of Reynolds stresses as an isotropic function of the scalar eddy viscosity ν_T and the mean rate of strain tensor, drawing an analogy to the representation of viscous stresses

$$\tau_{ij} = -2\nu_\mathrm{T}\left(S_{ij} - \frac{1}{3}S_{kk}\delta_{ij}\right) + \frac{2}{3}k\delta_{ij} \ . \tag{6.4}$$

The equation mentioned above, also known as the Boussinesq approximation, ensures that the trace of the resulting tensor is twice the turbulent kinetic energy $k = \frac{1}{2}\tau_{ii}$. State-of-the-art two-equation turbulence models, such as the Menter SST $k-\omega$ model [104], typically solve additional partial differential transport equations for the turbulent kinetic energy and the turbulent dissipation rate and reconstruct the eddy viscosity afterwards to close the set of equations. The assumed linear relationship between Reynolds stresses and strain-rate tensor, however, is not universally valid, as already discussed in Section 6.1. Consequently, any simulation using the Boussinesq assumption contains inherent epistemic uncertainty. The perturbation of Reynolds stress tensor's eigenspace [33] is the method of choice in order to account for turbulence modeling uncertainty on QoI. The underlying methodology is described in the following.

The symmetric, positive semi-definite Reynolds stress tensor τ_{ij} can be decomposed into an anisotropy tensor a_{ij} and an isotropic component

$$\tau_{ij} = k\left(a_{ij} + \frac{2}{3}\delta_{ij}\right) \ . \tag{6.5}$$

Eddy viscosity based turbulence models assume that the tensorial characteristics of the anisotropy tensor are solely dictated by the mean rate of strain tensor (see Eq. (6.4))

$$a_{ij} = -2\frac{\nu_\mathrm{T}}{k}\left(S_{ij} - \frac{1}{3}S_{kk}\delta_{ij}\right) \ . \tag{6.6}$$

The epistemic discrepancy in the evaluation of Reynolds stresses can be represented by the tensor D_{ij}, such that the true Reynolds stresses are

$$\begin{aligned} \tau_{ij}^{\text{true}} &= \tau_{ij}^{\text{modeled}} + D_{ij} \\ &= -2\nu_\mathrm{T}\left(S_{ij} - \frac{1}{3}\frac{\partial u_k}{\partial x_k}\delta_{ij}\right) + \frac{2}{3}k\delta_{ij} + D_{ij} \\ &= ka_{ij} + \frac{2}{3}k\delta_{ij} + D_{ij} \ . \end{aligned} \tag{6.7}$$

Building upon the concept of the eigenspace perturbation approach, the structural uncertainty of the Reynolds stress tensor can be split into contributors of shape, alignment and amplitude of the tensor. Therefore, the anisotropy tensor can be represented by an eigenspace decomposition

$$a_{ij} = v_{in}\Lambda_{nl}v_{jl} \ . \tag{6.8}$$

The orthonormal eigenvectors form the matrix v_{in} while the traceless diagonal matrix Λ_{nl} contains the corresponding ordered eigenvalues λ_k. When the Boussinesq approximation is used, the eigenvectors of the anisotropy tensor coincide with those of the strain-rate tensor, while the eigenvalues λ_i are solely dependent on the strain-rate tensor's eigenvalues ψ_i and its trace

$$\lambda_i = -2\frac{\nu_\mathrm{T}}{k}\left(\psi_{(4-i)} - \frac{\mathrm{tr}\,(\mathbf{S})}{3}\right) \ \text{for } i = 1, 2, 3 \ . \tag{6.9}$$

Evidently, the Reynolds stress tensor features identical eigenvectors as well, however the eigenvalues of the Reynolds stress tensor are

$$\boldsymbol{\xi} = k\left(\boldsymbol{\lambda} + \frac{2}{3}\right) \ . \tag{6.10}$$

Inserting Eq. (6.8) into Eq. (6.7) leads to:

$$\tau_{ij}^{\text{true}} = k\left(v_{in}\Lambda_{nl}v_{jl}\right) + \frac{2}{3}k\delta_{ij} + D_{ij} \ . \tag{6.11}$$

Because of the tensorial properties, the tensor $\mathbf{D}$ can be decomposed into

$$D_{ij} = \Delta k\left(\Delta v_{in}^a \Delta\Lambda_{nl}^a \Delta v_{jl}^a\right) + \frac{2}{3}\Delta k\delta_{ij}, \tag{6.12}$$

whereby Δ describe the discrepancy terms for turbulent kinetic energy (amplitude), alignment (eigenvectors) and shape (eigenvalues).

As precisely quantifying the uncertainty of the turbulence model in representing the modeled Reynolds stress tensor is a challenging task, the developers and founders of the methodology rather try to estimate the uncertainty by sampling from possible solution space. Hence, it is not the aim to apply a correct Reynolds stress tensor τ_{ij}^{true} but a perturbed, physically realizable one, which is called τ_{ij}^* [99]. Following the line of argument above, the EPF, considered in this work, creates a perturbed state of the Reynolds stress tensor defined as

$$\begin{aligned}\tau_{ij}^* &= k\left(a_{ij}^* + \frac{2}{3}\delta_{ij}\right)\\ &= k\left(v_{in}^*\Lambda_{nl}^*v_{jl}^* + \frac{2}{3}\delta_{ij}\right)\ ,\end{aligned} \tag{6.13}$$

where a_{ij}^* indicates the perturbed anisotropy tensor, Λ_{nl}^* represents its perturbed eigenvalue matrix and v_{in}^* is the perturbed eigenvector matrix. Adhering to the procedure established in the majority of previously published works, there is no explicit modification of the turbulent kinetic k energy. Instead, the level of turbulence is manipulated indirectly by altering the production of turbulence due to affirmative perturbations of eigenvalues and eigenvectors, as will be clarified in subsequent sections.

6.2.1. Eigenvalue perturbation

As the components of the symmetric anisotropy tensor are bounded according to the realizability constraints [136][2], the respective eigenvalues can be transformed into barycentric coordinates [4]. By defining the vertices $\boldsymbol{x}_{1\mathrm{C}}, \boldsymbol{x}_{2\mathrm{C}}, \boldsymbol{x}_{3\mathrm{C}}$ of an equilateral triangle, representing the componentiality of turbulence (three-component, isotropic limit (3C), two-component axisymmetric limit (2C) and the one-component limit (1C)) [151], the mapping from anisotropy eigenvalues to barycentric coordinates is defined as

$$\begin{aligned}\boldsymbol{x} =& \frac{1}{2}\boldsymbol{x}_{1\mathrm{C}}\left(\lambda_1 - \lambda_2\right) + \boldsymbol{x}_{2\mathrm{C}}\left(\lambda_2 - \lambda_3\right) + \boldsymbol{x}_{3\mathrm{C}}\left(\frac{3}{2}\lambda_3 + 1\right)\\ \boldsymbol{x} =& \mathbf{Q}\boldsymbol{\lambda} \quad \text{with } \lambda_1 \geq \lambda_2 \geq \lambda_3\ .\end{aligned} \tag{6.14}$$

The perturbation of the eigenvalues of the anisotropy tensor within physically permissible limits is grounded on shifting the barycentric state within the borders of the barycentric triangle [33]. Using the pseudoinverse of $\mathbf{Q}$, any perturbed eigenvalues are expressed through remapping

$$\boldsymbol{\lambda}^* = \mathbf{Q}^{-1}\boldsymbol{x}^*\ , \tag{6.15}$$

where the relocated position $\boldsymbol{x}^*$ results from linear interpolation between starting point $\boldsymbol{x}$ and target point $\boldsymbol{x}_{(\mathrm{t})} \in \{\boldsymbol{x}_{1\mathrm{C}}, \boldsymbol{x}_{2\mathrm{C}}, \boldsymbol{x}_{3\mathrm{C}}\}$

$$\boldsymbol{x}^* = \boldsymbol{x} + \Delta_B\left(\boldsymbol{x}_{(\mathrm{t})} - \boldsymbol{x}\right)\ . \tag{6.16}$$

The relative distance $\Delta_B \in [0,1]$ controls the magnitude of eigenvalue perturbation as presented in Fig. 6.1. Traditional eddy viscosity-based turbulence models assume that this eddy viscosity is a scalar, known as the isotropic eddy viscosity. Thus, turbulence behaves as an isotropic medium. The eigenvalue perturbation modulates this to an orthotropic medium, where turbulence behaves differently along each eigen-direction [106], accounting for the sensitivity of the model with respect to the anisotropic characteristics of turbulence[3].

---

[2] See Section 5.2.1 for details in this thesis.

[3] See Section 3.5.1 and Appendix C for details in this thesis.

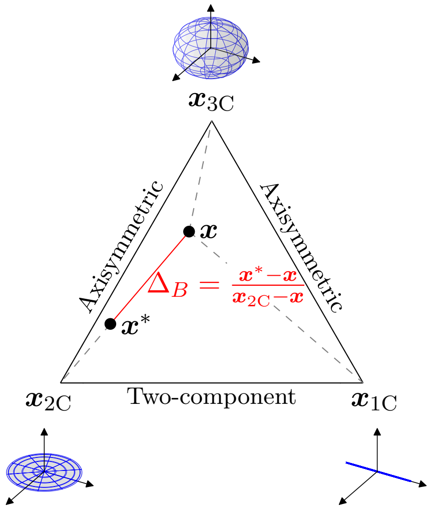
$\boldsymbol{x}_{3\mathrm{C}}$
Axisymmetric
Axisymmetric
$\boldsymbol{x}$
$\Delta_B = \frac{\boldsymbol{x}^* - \boldsymbol{x}}{\boldsymbol{x}_{2\mathrm{C}} - \boldsymbol{x}}$
$\boldsymbol{x}^*$
$\boldsymbol{x}_{2\mathrm{C}}$
Two-component
$\boldsymbol{x}_{1\mathrm{C}}$

Figure 6.1.: Representation of the eigenvalue perturbation within the barycentric triangle and its effect on the shape of the Reynolds stress tensor ellipsoid.

6.2.2. Eigenvector perturbation

Given that LEVMs rely on the Boussinesq approximation in Eq. (6.4), the Reynolds stress, the anisotropy and the strain-rate tensor share identical eigendirections, as already discussed in Section 6.2. However, this relationship results in inaccuracies in predicting certain flows, e.g. involving flow separation and reattachment. Nevertheless, even for simple turbulent boundary layer flows there is a significant misalignment between SRS (such as DNS) and RANS model predicted eigenvectors of the Reynolds stress tensor [95]. Hence, the eigenspace perturbation idea adds a perturbation to the eigenvectors. In contrast to the eigenvalues, there are no actual bounds for the orientation of the Reynolds stress tensor ellipsoid. To address this issue, Iaccarino et al. [66] suggest to make use of the boundedness of the Frobenius inner product of the Reynolds stress and the strain-rate tensor, called the turbulence production P_k of the turbulent kinetic energy transport equation. Based on the relationship of the strain-rate and Reynolds stress tensor for LEVMs (see Eq. (6.4)), the bounds of the turbulence production term can be written in terms of their eigenvalues ψ_i and ξ_i[83]:

$$P_k = -\tau_{ij}\frac{\partial U_i}{\partial x_j} \in \left[\xi_1\psi_3 + \xi_2\psi_2 + \xi_3\psi_1,\ \xi_1\psi_1 + \xi_2\psi_2 + \xi_3\psi_3\right] \ . \tag{6.17}$$

As the Reynolds stress and the strain-rate tensor share the same eigenvectors for LEVMs, the lower bound of the turbulence production term can be obtained by commuting the first and third eigenvector of the Reynolds stress tensor that manipulates the relationship between eigenvalues and respective eigendirections. The permutation of first and third eigenvector results in a reconstructed Reynolds stress tensor based on Eq. (6.13), which is equivalent to the one obtained by rotating the eigenvector matrix $\mathbf{v}$ around the second eigenvector by $\pi/2$, see Appendix 6.A. Whereas keeping the ordering of eigenvectors in case of LEVMs evidently leads to the upper limit of the turbulence production. In the subsequent section, we outline, why the eigenvector perturbation can lead to implausible dynamics of the Reynolds stress tensor combined with an unrealistically derived turbulence production term.

6.3. Adherence to realizable Reynolds stress tensors and realizable Reynolds stress tensor dynamics

6.3.1. Insights from the Reynolds stress tensor's eigenspace perturbation and implications for turbulent boundary layers

The significant advantage of the EPF lies in its ability to generate a perturbed and realizable Reynolds stress tensor from an unperturbed one. This is accomplished by ensuring that the realizability condition, saying that the Reynolds stress tensor must be positive semi-definite, is met [136]. To illustrate, when perturbing the eigenvalues of the modeled Reynolds stress tensor, choosing $\Delta \leq 1$ (see Fig. 6.1) inevitably leads to fulfillment of the realizability condition as the perturbed Reynolds stress anisotropy eigenvalues remain inside the barycentric triangle. Recently, we addressed an appropriate way to incorporate eigenvector perturbations in a self-consistent manner in order to obtain the desired realizable Reynolds stresses [96]. However, while the current formulation of the realizability principle is valuable, it is not comprehensive or adequate in ensuring that the evolution of the Reynolds stress, from one physically permissible state to another, remains physically plausible. Indeed, under certain conditions, the realizable Reynolds stress tensor, obtained through eigenspace perturbation, may become physically implausible leading to turbulent stress dynamics, which are rather unrealizable.

An exemplary case to illustrate these conditions is the turbulent boundary layer, whereby we consider the flow to be steady, 1D and fully developed. This is equivalent to analyzing half of a symmetric infinite channel flow, as sketched in Fig. 6.2. Hence, by setting $\frac{\partial \square}{\partial t} = 0$, $U_2 = U_3 = 0$, $\frac{\partial \square}{\partial x} = \frac{\partial \square}{\partial z} = 0$ (except $\frac{\partial p}{\partial x} \neq 0$), Eq. (6.2) simplifies to

$$\frac{\partial p}{\partial x} = \frac{\partial}{\partial y}\left(\sigma_{12} - \rho \tau_{12}\right) \ . \tag{6.18}$$

The diffusion based on viscous stresses has to be balanced by a source term, associated with a streamwise pressure gradient. Applying the isotropic eddy viscosity assumption (see Eq. (6.4)), the Reynolds stress tensor for 1D boundary layer flow becomes

$$\boldsymbol{\tau} = \begin{pmatrix} \frac{2}{3}k & -\nu_\mathrm{T}\frac{\partial U_1}{\partial y} & 0 \\ -\nu_\mathrm{T}\frac{\partial U_1}{\partial y} & \frac{2}{3}k & 0 \\ 0 & 0 & \frac{2}{3}k \end{pmatrix} \ . \tag{6.19}$$

The eigenvalues $\xi_1 = \frac{2}{3}k + \nu_\mathrm{T}\frac{\partial U_1}{\partial y}$, $\xi_2 = \frac{2}{3}k$, $\xi_3 = \frac{2}{3}k - \nu_\mathrm{T}\frac{\partial U_1}{\partial y}$ come along with the respective eigenvectors $\boldsymbol{v_1} = \left(\frac{-1}{\sqrt{2}}, \frac{1}{\sqrt{2}}, 0\right)^T$, $\boldsymbol{v_2} = (0,0,1)^T$ and $\boldsymbol{v_3} = \left(\frac{1}{\sqrt{2}}, \frac{1}{\sqrt{2}}, 0\right)^T$. By

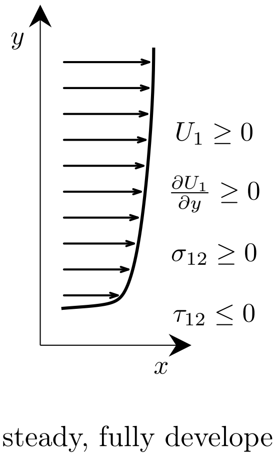

Figure 6.2.: Schematics of steady, fully developed 1D boundary layer flow.

means of the eigenspace decomposition $\tau_{ij} = v_{in}\Xi_{nl}v_{jl}$ and employing the eigenvector matrix $\mathbf{v} = (\boldsymbol{v_1}, \boldsymbol{v_2}, \boldsymbol{v_3})$, the shear stress component of the Reynolds stress tensor can be reformulated

$$\tau_{12} = v_{11}v_{12}\xi_1 + v_{21}v_{22}\xi_2 + v_{31}v_{32}\xi_3 \ . \tag{6.20}$$

Inserting the unperturbed eigenvectors and eigenvalues of the Reynolds stress tensor, as outlined above, into Eq. (6.20) results in a strictly negative Reynolds shear stress component $\tau_{12} = \frac{1}{2}\left(\xi_3 - \xi_1\right) \leq 0$ as $\xi_1 \geq \xi_3$. However, when perturbing the eigenspace orientation according to the approach of Iaccarino et al. [66], we obtain $\tau_{12}^* = \frac{1}{2}\left(\xi_1 - \xi_3\right) \geq 0$ as $\xi_1 \geq \xi_3$[4]. Hence, the simple permutation of first and third eigenvector leads to different sign of the relevant shear stress shaping the boundary layer profile. At first glance, this already seems to violate obvious flow physics.

Nevertheless, we aim to present a conceptual explanation for this phenomenon. In order to qualitatively assess the physical relationships related to a change in sign of the Reynolds shear stress, we insert Stokes' hypothesis (see Eq. (6.3)) and the eddy viscosity hypothesis (see Eq. (6.4)) into Eq. (6.18)

$$\frac{\partial p}{\partial x} = \frac{\partial}{\partial y}\left(\rho\left(\nu + \nu_{\mathrm{T}}\right)\frac{\partial U_1}{\partial y}\right) \ . \tag{6.21}$$

Consequently, a change in sign of the Reynolds stress component τ_{12} would equate to an effective negative turbulent eddy viscosity ν_{T}. Negative eddy viscosity means that the momentum flux from regions of lower momentum is transported to regions of higher momentum. This implies a countergradient transport that is physically implausible. Additionally, this phenomenon is associated with positively correlated Reynolds stresses and mean velocity gradients. Following the example of steady, fully developed 1D boundary layer, the turbulence production $P_k = -\tau_{ij}\frac{\partial U_i}{\partial x_j} = -\tau_{12}\frac{\partial U_1}{\partial y}$[5] will be negative, if τ_{12} becomes positive because of eigenvector permutation. Such negative turbulence production denotes transferring energy from the turbulent scales to the mean kinetic energy, a process that is deemed physically implausible in fully developed boundary layers and especially in the entire computational domain (which would result from the described eigenvector permutation) [46][6]. In contrast to the eigenvector perturbation, a pure eigenvalue perturbation is incapable of inducing a change in the sign of τ_{12} for fully developed boundary layer flow. Indeed, Fig. 6.3b additionally serves to illustrate the observation that applying eigenvector perturbation leads to negative turbulence production and, consequently, negative effective eddy viscosity for any eigenvalue perturbation that falls within the bounds of the barycentric triangle. As depicted in Fig. 6.3, the absolute value of the turbulence production reaches its maximum at the one-component limiting state of turbulence, whereas it becomes zero[7] for an isotropic Reynolds stress tensor, which is in accordance to the finding of Gorlé et al. [56][8]. This illustrative example demonstrates that, in the context of wall-bounded, boundary layer like flows, the suggested eigenvector permutation of first and third eigenvector can give rise to non-realizable Reynolds stress

---

[4] As already described in Section 5.2.2: Iaccarino et al. [66] propose to permute the first and third eigenvectors of the Reynolds stress tensor. This is equivalent to changing the order of the respective eigenvalues.

[5] As $\frac{\partial U_1}{\partial y} \geq 0$ for the sketched boundary layer flow in Fig. 6.2.

[6] Although negative production of turbulent kinetic energy can occur e.g. at leading edges featuring separation and reattachment areas [20].

[7] This is only valid for this specific type of flow.

[8] Details can be found in Appendix B.

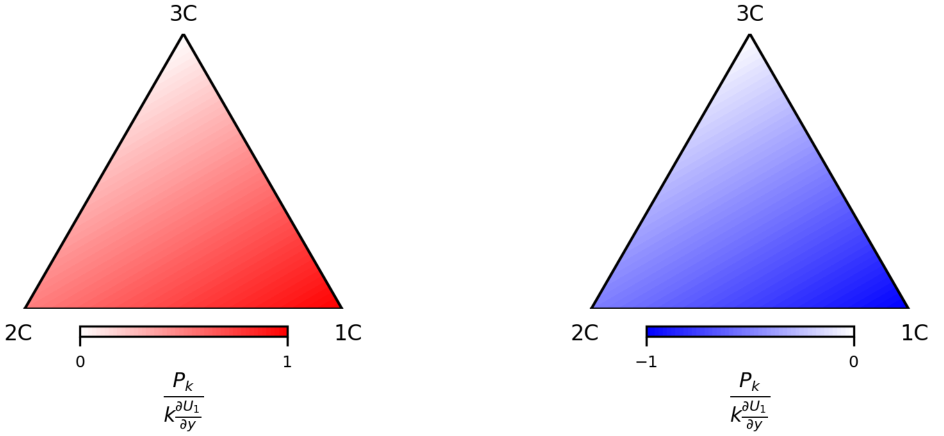

(a) Turbulence production under eigenvalue perturbation

(b) Turbulence production under eigenvalue and eigenvector perturbation

Figure 6.3.: Comparison of the effect of the eigenspace perturbation on the turbulence production term P_k in case of fully developed boundary layer flow. Effect of pure eigenvalue perturbation is shown in (a), while (b) presents the effect, when combining the permutation of the eigenvectors $\boldsymbol{v_1}$ and $\boldsymbol{v_3}$ and eigenvalue perturbation within the barycentric triangle.

tensor dynamics in the set of RANS equations. Therefore, there is the need for a physics-based constraint that ensures not only realizable Reynolds stresses but also plausible Reynolds stress tensor dynamics. Subsequently, we derive this constraint, verify its validity and suggest its future usage within the EPF.

6.3.2. Simplified derivation of realizable eigenvector perturbation dynamics for wall-bounded flows

As the second eigenvector of the Reynolds stress tensor in Eq. (6.19) is $\boldsymbol{v_2} = (0,0,1)^T$, the rotation matrix for any rotation around this eigenvector simplifies to

$$\mathbf{R} = \begin{pmatrix} \cos(\alpha) & -\sin(\alpha) & 0 \\ \sin(\alpha) & \cos(\alpha) & 0 \\ 0 & 0 & 1 \end{pmatrix} \tag{6.22}$$

(choosing $\alpha = \pi/2$ results in Iaccarino's permutation of first and third eigenvector [66] see Appendx 6.A). The general rotation of the Reynolds stress tensor ellipsoid around its second eigenvector is sketched in Fig. 6.4a.

The objective is to derive a condition that evidently causes a change of sign for the shear Reynolds stress component τ_{12}, ultimately resulting in non-realizable Reynolds stress tensor dynamics. Therefore, we formulate the rotated eigenvector matrix based on the unperturbed eigenvector matrix $\mathbf{v}$ for 1D boundary layer flow

$$\begin{aligned} \mathbf{v}^* &= \mathbf{R}\mathbf{v} \\ &= \frac{1}{\sqrt{2}} \begin{pmatrix} -\sin(\alpha) - \cos(\alpha) & 0 & \cos(\alpha) - \sin(\alpha) \\ -\sin(\alpha) + \cos(\alpha) & 0 & \cos(\alpha) + \sin(\alpha) \\ 0 & \sqrt{2} & 0 \end{pmatrix} . \end{aligned} \tag{6.23}$$

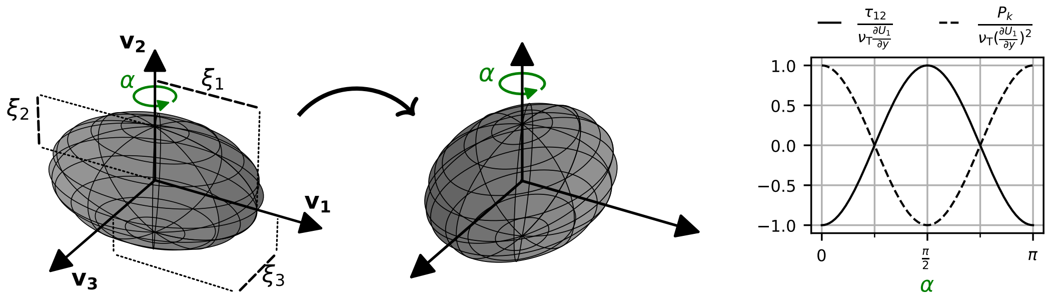
v_2
α
ξ_1
ξ_2
v_1
v_3
ξ_3
α
$\frac{\tau_{12}}{\nu_T \frac{\partial U_1}{\partial y}}$
$\frac{P_k}{\nu_T (\frac{\partial U_1}{\partial y})^2}$
1.0
0.5
0.0
−0.5
−1.0
0
$\frac{\pi}{2}$
π
α

(a) (b)

Figure 6.4.: Rotation of the eigenvector matrix of the Reynolds stress tensor around second eigenvector $\boldsymbol{v_2}$ by α. The schemtical impact of the rotation on the Reynolds stress tensor ellipsoid is shown in (a). (b) shows the effect of eigenvector rotation on the Reynolds shear stress component and the turbulence production. This plot is created based on assuming 1D boundary layer flow, as sketched in Fig. 6.2. The eigenvectors of τ_{ij} presented in Eq. (6.19) are rotated by α. The resulting τ_{12} and P_k (see Eq. (6.17)) are evaluated subsequently.

Hence, the resulting Reynolds shear stress based on Eq. (6.20) becomes

$$\tau_{12}^* = \frac{1}{2}\left(\xi_3 - \xi_1\right)\cos\left(2\alpha\right) \overset{!}{=} 0 \ . \tag{6.24}$$

Consequently, Eq. (6.24) holds true for isotropic turbulence, as $\xi_1 = \xi_3$ and any rotation angle $\alpha = \frac{\pi}{2}n - \frac{\pi}{4}$ with $n \in \mathbb{N}$. The relationship of the rotation angle and the shear stress component is verified by a step-by-step analysis presented in Fig. 6.4b. The resulting dependency of the Reynolds shear stress component is exactly the analytically derived one in Eq. (6.24). As the rotation of the Reynolds stress tensor is symmetric to $\pi/2$, which means that any rotation around $\pi/2 - \delta$ results in the same tensor as any rotation around $\pi/2 + \delta$, $\alpha = \pi/4$ is the appropriate choice as the smallest angle at which a sign change occurs.

The mean of the cosine in Fig. 6.4b has to be zero in order to obtain zero crossing of the turbulence production at exactly $\alpha = \pi/4$. In other words, it is required that the maximum and the minimum value of the turbulence production have equal absolute magnitude but opposite signs. Equating the lower and upper bound of the inner Frobenius product Eq. (6.17) leads to

$$\begin{aligned} -P_{k_{min}} &= P_{k_{max}} \\ -\xi_1\psi_3 - \xi_2\psi_2 - \xi_3\psi_1 &= \xi_1\psi_1 + \xi_2\psi_2 + \xi_3\psi_3 \\ \xi_1\left(\psi_1 + \psi_3\right) + 2\xi_2\psi_2 + \xi_3\left(\psi_1 + \psi_3\right) &= 0 \ . \end{aligned} \tag{6.25}$$

Thus, rotating the orthogonal eigenvectors around the second eigenvector by an angle of $\pi/4$, results in zero turbulence production if $\psi_1 = -\psi_3$ and $\psi_2 = 0$. This conditions always holds true for fully developed 1D boundary layers, as there is only a single velocity gradient present in the flow. However, any 2D flow featuring vanishing divergence of the velocity field does also satisfy Eq. (6.25). This means that $\frac{\partial U_1}{\partial x} = -\frac{\partial U_2}{\partial y}$, given that U_3 is the vanishing velocity component.

6.3.3. *A posteriori* validation of the suggested constraint on the eigenvector perturbation

To corroborate our findings, we analyze another generic flow scenario, which is the 2D converging-diverging channel flow [85]. This test case consists of viscous walls with and without curvature as sketched in Fig. 6.12a. Our numerical setup uses inlet boundary conditions extracted from a fully developed turbulent boundary layer at $\mathrm{Re}_\tau = 617$. The derived mass flow rate is forced using a boundary controller, which adjusts the static pressure at the outlet of the computational domain. We conducted a RANS grid independence study (not shown here) using a low-Reynolds resolution ($y^+ \leq 1$) at solid walls and by applying the Menter SST $k-\omega$ LEVM [104]. Based on this, we conduct analyses in post processing for the finest mesh featuring a resolution of 242x242x1 grid points (see Fig. 6.12b). The resulting velocity gradients, the eddy viscosity and the turbulent kinetic energy are used to determine the Reynolds stress tensor following Boussinesq's approximation (see Eq. (6.4)). According to our derivation above, the eigenvectors of these Reynolds stress tensors are rotated around the second eigenvector by $\alpha = \pi/4$ in the entire domain as a first step. The rotated Reynolds stress tensors are composed using Eq. (6.13). Subsequently, we can compare the resulting turbulence production term (see Eq. (6.17)) after rotating the eigenvectors with the one based on the initial Reynolds stress tensor. The comparison, presented in Fig. 6.5, reveals a reduction in the effective turbulence production due to the rotation as expected. This observation confirms the exemplarily derived relationship of the turbulence production term with respect to eigenvector rotation of the Reynolds stress tensor. Nevertheless, due to the existing divergence of the velocity field in this configuration, a rotation around $\pi/4$ may also lead to negative turbulence production in the converging section of the channel[9]. As a second step, we further validate the derivations by solving an optimization problem for achieving zero turbulence production by an eigenvector rotation of the Reynolds stress tensor given the velocity gradients of the previously performed RANS simulation of the 2D converging-diverging channel. Figure 6.6 shows the appropriate rotation angle $\alpha|_{P_k=0}$ relative to $\pi/4$ that would lead to zero turbulence production term. The deviations from to the derived α under idealised conditions of a 1D boundary layer flow, can be ascribed to the fact that the flow is not fully divergence-free in the outer parts of the boundary layers. The regions indicating $\alpha|_{P_k=0} \neq \pi/4$ are directly related to the areas shown in Fig. 6.5

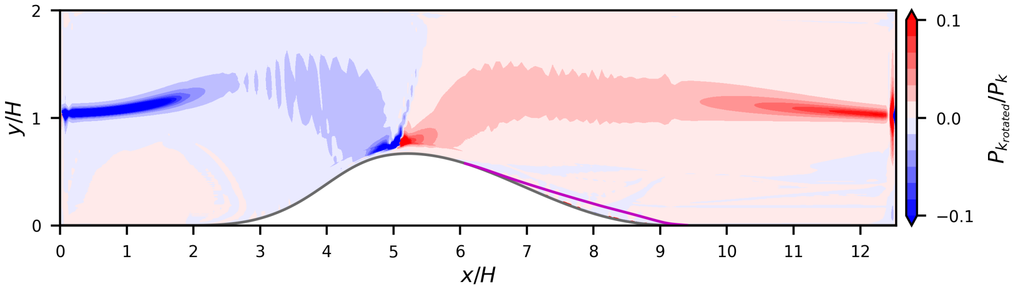

Figure 6.5.: Distribution of the turbulence production term $P_{k_{\text{rotated}}}$, when rotating the eigenvectors of the Reynolds stress tensor around the second eigenvector by $\alpha = \pi/4$. For better interpretability the resulting production is scaled by the unperturbed turbulence production P_k. The magenta line indicates $U_1 = 0$.

---

[9] This refers to the fact, that $\alpha = \pi/4$ might have to be smaller to achieve zero production. As discussed in the next section (Section 6.4), the rotation needs to be mitigated anyway because of stability issues. A reduction of α makes the production rather stay positive.

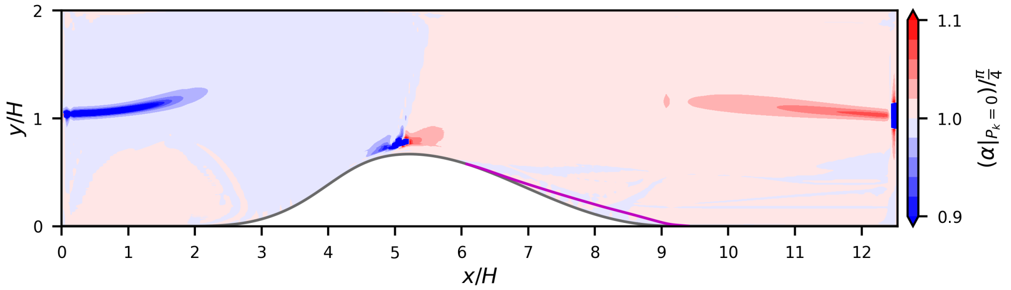

Figure 6.6.: Rotation around the second eigenvector of the Reynolds stress tensor by $\alpha|_{P_k=0}$ leads to zero turbulence production. In order to better classify the discrepancy from $\pi/4$, the determined angle $\alpha|_{P_k=0}$ is presented as a fraction of $\pi/4$. The magenta line indicates $U_1 = 0$.

where the production term under rotation does not exactly equal zero[10]. However, as the optimized $\alpha|_{P_k=0}$ differs by only 10% at maximum from $\pi/4$, we believe that restricting the eigenvector rotation of the Reynolds stress tensor to $\pi/4$ is a reasonable choice also for more complex flows.

To sum up, we have shown through mathematical analysis that a simple eigenvector perturbation involving permuting the first and third eigenvector may lead to implausible, unrealizable Reynolds stress tensor dynamics. Based on that, a constraint that facilitates physically meaningful Reynolds stress tensor perturbations with respect to rotation of the eigenspace has been derived for wall-bounded, boundary layer like flows. Additionally, we have substantiated the derivations by presenting illustrative proofs. In the next section, we apply the proposed eigenvector rotations in the EPF[11].

6.4. Application of physically constrained eigenvector perturbation

The idea of the EPF is to sample from the possible solution space for certain QoI attributed to perturbing the Reynolds stress tensor within the discussed physical bounds. The entire framework was implemented in DLR's in-house CFD solver TRACE [47]. TRACE is a parallel Navier-Stokes flow solver that has been developed at DLR's Institute of Propulsion Technology in close cooperation with MTU Aero Engines AG. In the present work, we use the finite-volume method to discretize the compressible RANS equations. The EPF and can be subdivided in several steps within each pseudo-time step of steady simulations:

1. Determine the anisotropy tensor (see Equation Eq. (6.5)).
2. Perturb the eigenvalues of the anisotropy tensor by choosing the relative perturbation strength Δ_B (cf. Eq. (6.15) and Eq. (6.16)).

---

[10] The unperturbed turbulence production is always positive.

[11] Although, as described, negative turbulence production and derived negative turbulent eddy viscosity can happen in unsteady flows, it remains desirable to prevent negative production and countergradient transport of momentum in the entire computational domain. Additionally, a negative turbulence production term would result in a rapid destruction of the turbulence level, ending up in laminar solutions only.

3. Perturb the eigenvectors of the anisotropy (Reynolds stress) tensor by choosing the rotation angle α. The rotation is done by rotating the eigenvector matrix around the second eigenvector $\mathbf{v}^* = \mathbf{R}\mathbf{v}$ with $\mathbf{R}$ according to Eq. (6.26).
4. Reconstruct the perturbed Reynolds stress tensor τ_{ij}^* according to Eq. (6.13).
5. Update of the viscous fluxes using τ_{ij}^*.
6. Update of the turbulence production term $P_k = -\tau_{ij}^* \frac{\partial U_i}{\partial x_j}$.

The simulations of the flow within a converging-diverging channel serve to exemplify the application of the EPF and further validate the proposed constraint on the eigenvector perturbation. We compare against DNS data by Laval and Marquillie [85]. The two-equation Menter SST $k-\omega$ [104] LEVM is chosen to be the baseline model in the present investigation. Hence, the uncertainty estimates presented subsequently based on the EPF can be attributed to the structural uncertainties within this particular turbulence model. As the amount of considered structural uncertainty increases with increasing eigenvalue perturbation, the most conservative estimation of the modeling uncertainty is obtained by choosing $\Delta_B = 1$. Nevertheless, according to latest publications [99], intense Reynolds stress tensor perturbations may cause numerical convergence issues.

Following the approach proposed in our previous work [96], the relative perturbation magnitude with respect to the relative shift in barycentric coordinates Δ_B has to be adjusted as a consequence of the convergence issues. In the present study, we seek to apply Δ_B as large as possible by steps of 0.1. Consequently, while the full Reynolds stress tensor perturbation could be used for the 2C and 1C corners, the perturbation towards the isotropic corner had to be adjusted by $\Delta_B < 1$, as approaching the isotropic state results in a reduction of turbulent kinetic energy production.

Although, we have just derived that the maximum eigenvector rotation angle has to be $\alpha \leq \pi/4$, this constraint is necessary but not sufficient for practical applications. The eigenvector modification by applying $\alpha \leq \pi/4$ may result in states of the Reynolds stress tensor that are indeed realizable and physically plausible but still lead to numerical stability issues. Therefore, we iteratively decrease the rotation angle by fractions of 10% with respect to the maximum value of $\pi/4$. Besides examining the overall residuals and convergence of the static outlet pressure (controlled to maintain the prescribed mass flow outlet boundary condition) of each simulation, we evaluate the evolution of the the streamwise velocity. Therefore, we record iterative data at $x/H \in [0.5, 1, 2, 3, 4, 5, 6, 7, 8, 9, 10, 11, 12]$ every 1000 iterations and evaluate the relative error (standard deviation divided by the mean) over the last 100 snapshots. In order to distinguish between an unacceptable unstable and an acceptable converged solution, we use a maximum tolerable relative error of 1.5% in each considered location. The numerically achievable perturbations leading to converged RANS results for this study of the convergence-divergence channel flow are

Table 6.1.: Selected turbulent target states (componentiality), Δ_B for the eigenvalue modifications and α for the eigenvector rotations of the Reynolds stress tensor perturbation applied to the flow within the converging-diverging channel.

simulation	#1	#2	#3	#4	#5	#6
target turbulent state	1C	1C	2C	2C	3C	3C
Δ_B	1.0	1.0	1.0	1.0	0.2	0.2
α	0.0	$\frac{\pi}{10}$	0.0	$\frac{\pi}{8}$	0.0	$\frac{\pi}{20}$

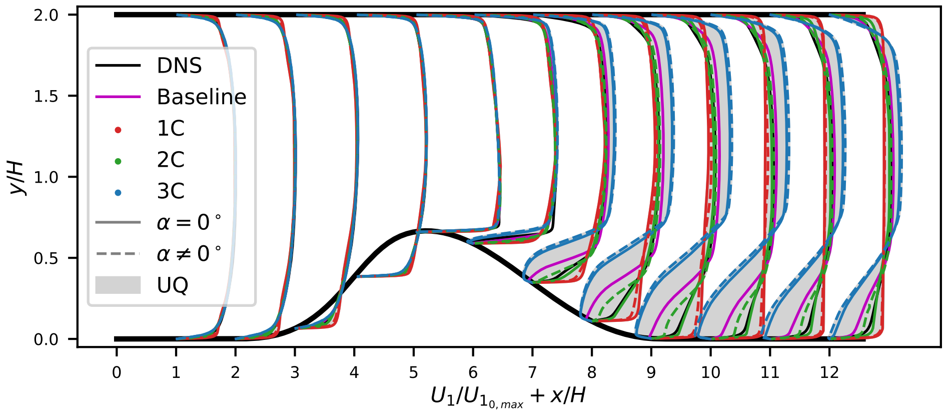

Figure 6.7.: Estimated turbulence model uncertainty for the streamwise velocity inside the converging-diverging channel based on the EPF. $U_{1_{0,\max}}$ is the maximum streamwise velocity of the baseline simulation at $x/H{=}0$. The settings for every eigenspace perturbation of the Reynolds stress tensor can be found in Table 6.1.

summarized in Table 6.1. In order to verify that the eigenvector perturbation proposed by Iaccarino et al. [66] leads to unstable CFD simulations as a result of non-realizable Reynolds stress tensor dynamics, we have conducted one exemplary simulation, presented in Appendix 6.C, applying eigenvector permutation without any eigenvalue perturbation.

In the subsequent section, we discuss the resulting estimated uncertainty intervals based on the eigenspace perturbation. The analysis refers to the presented QoI in Fig. 6.7 to Fig. 6.10. The estimated uncertainty for the streamwise velocity field is shown in Fig. 6.7. Perturbing the eigenspace of the Reynolds stress tensor has minor effect upstream of the diverging section ($x/H \approx 5$), where the baseline RANS simulation closely aligns with the DNS data. Due to the increased turbulence production at the one- and two-component limiting state of turbulence (as can be observed in the turbulent kinetic energy distributions in Fig. 6.10), the velocity profiles become sharper with an increased gradient at the wall. This is also reflected in higher friction coefficients in Fig. 6.8 at the bottom and top wall compared to the baseline simulation. Conversely, the simulations featuring more isotropic Reynolds stresses (simulation #5 and #6 with $\Delta_B = 0.2$), lead to rounder velocity profiles and reduced friction coefficients. Larger deviations between RANS and DNS results arise, when the flow experiences the adverse pressure gradient in the diffusor section. This is further reflected in an increased sensitivity of the velocity field with respect to the shape and orientation of the Reynolds stress tensor. Due to the indirectly manipulated turbulence production behaviour, the turbulent kinetic energy evolves differently in the simulation domain for every perturbation (see Fig. 6.10). This is also in accordance with the described dependency of the production term of turbulent kinetic energy on the eigenvalues in the front section of the diffusor (see also Section 6.2.1). The turbulent kinetic energy production significantly affects the size of the separation bubble due to the adverse pressure gradient. While the simulations aiming for the one- and two-component turbulence state completely suppress the separation zone at the lower wall, the simulations #5 and #6, featuring more isotropic turbulence both separate early and overpredict the reattachment length (see Fig. 6.8). While the static wall pressure reduction in the converging section is not affected by the eigenspace perturbation, the pressure recovery in the diffusor section shows growing turbulence model uncertainty (see Fig. 6.9). These uncertainty intervals on the pressure coefficient, underline the

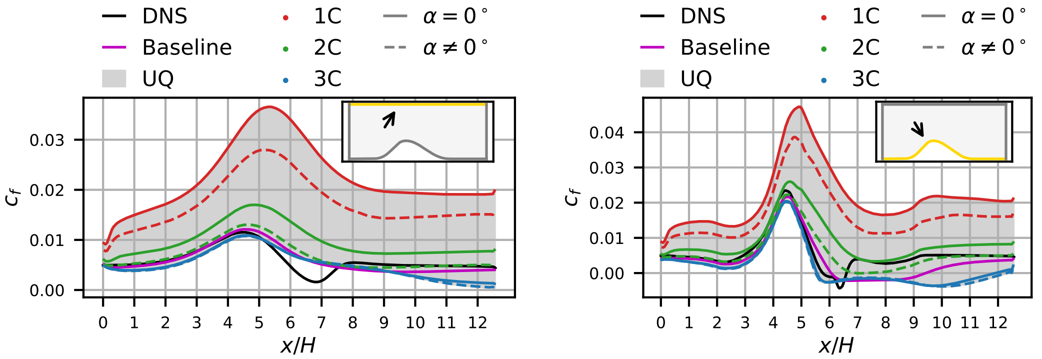

(a) Upper wall

(b) Bottom wall

Figure 6.8.: Turbulence model uncertainty based on the EPF for the friction coefficient $c_f = \tau_w / \left(\frac{1}{2}\rho_0 U_{1_{0,\max}}^2\right)$ at upper and bottom wall of the converging-diverging channel. The quantities with subscript 0 indicate that they are extracted at $x/H = 0$. The settings for every eigenspace perturbation of the Reynolds stress tensor can be found in Table 6.1.

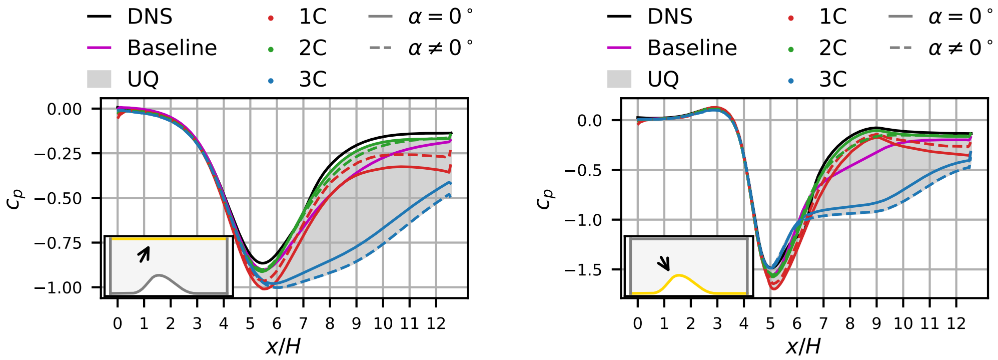

(a) Upper wall

(b) Bottom wall

Figure 6.9.: Turbulence model uncertainty based on the EPF for the pressure coefficient $c_p = (p - p_0) / \left(\frac{1}{2}\rho_0 U_{1_{0,\max}}^2\right)$ at upper and bottom wall of the converging-diverging channel. The quantities with subscript 0 indicate that they are extracted at $x/H = 0$. The settings for every eigenspace perturbation of the Reynolds stress tensor can be found in Table 6.1.

increased model-form uncertainty when it comes to adverse pressure gradient flows. The reduced turbulence production of the simulations #5 and #6 in the converging section $x \leq 5$ results in increased turbulent kinetic energy in the massively separated section (see Fig. 6.10). As already described in the theoretical parts of this paper (see Section 6.2.2 and Section 6.3), the rotation of the eigenvector matrix mainly affects the turbulence production process indirectly. This is especially highlighted by decreased turbulent kinetic energy patterns in the upstream section of the domain.

It is noticeable that the simulations aiming for the two-component limiting state of the Reynolds stress tensor show the best agreement with the DNS data in the diffusor section for the considered QoI. Additionally, the DNS data are included in the turbulence model

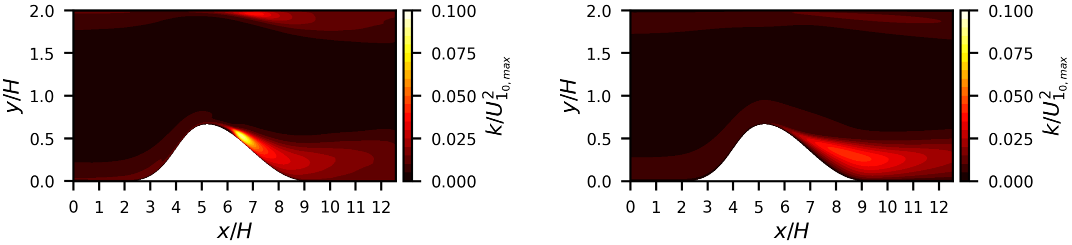

(a) DNS [85]

(b) RANS Baseline

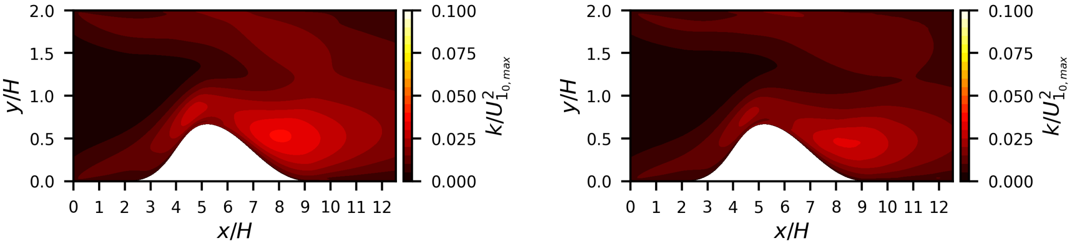

(c) Aiming for 1C without eigenvector rotation (#1)

(d) Aiming for 1C with eigenvector rotation (#2)

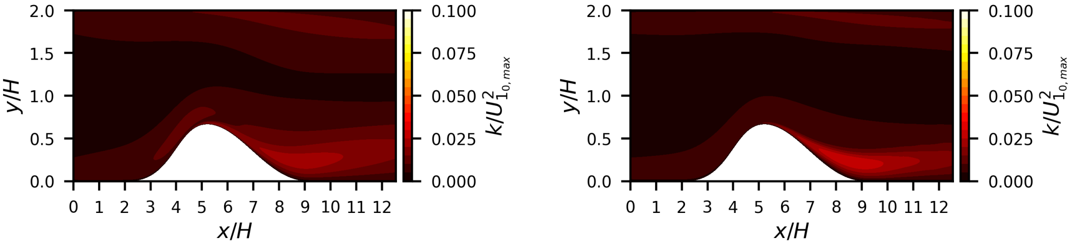

(e) Aiming for 2C without eigenvector rotation; (#3)

(f) Aiming for 2C with eigenvector rotation (#4)

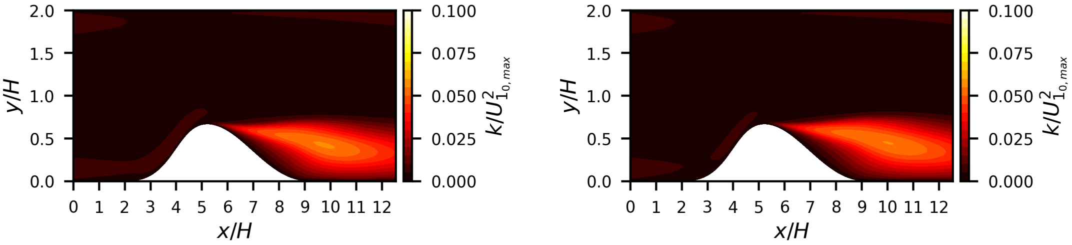

(g) Aiming for 3C without eigenvector rotation (#5)

(h) Aiming for 3C with eigenvector rotation (#6)

Figure 6.10.: Evolution and comparison of the turbulent kinetic energy within the converging-diverging channel between DNS data [85] (a), RANS baseline (b) and EPF simulations applying perturbed Reynolds stress tensors (c)-(h) (see Table 6.1).

uncertainty estimates in most of the plots, which also validates the EPF to a certain extent, although the authors are aware of the fact that this is not the main goal of the perturbation methodology. The interested reader is referred to the discussion on the restrictions and capabilities of the framework in Matha et al. [99]. Regarding the potentially large uncertainty intervals concerning the considered QoI, we must note that the eigenspace perturbations of the Reynolds stress tensor were chosen to be sufficiently large, allowing the CFD solver to handle it just well enough to produce a convergent solution. On the one hand, this enables exploring the capabilities of the considered EPF, and on the other hand, it represents the most conservative estimate of turbulence model uncertainty. For upcoming design decisions considering this framework, design engineers would likely aim for a non-overly conservative estimate of turbulence model uncertainty, as they may introduce expert knowledge into the analysis.

6.5. Conclusion & outlook

Uncertainty estimation in the context of RANS turbulence modeling is crucial in industrial applications as it provides a quantifiable measure of the reliability of CFD simulations. Accurate assessment of physically plausible uncertainties ensures the credibility of simulation results, allowing engineers and designers to make informed decisions under uncertainty. The EPF has established itself as the only physics-based UQ approach for turbulence model uncertainty. It has been applied to problems in aerospace, civil, environmental and mechanical Engineering. It is widely used in leading CFD software. This underscores the need to ensure V&V of this framework. However, due to its newness, in-depth verification of the rationale and application of this framework have not been conducted. This need is addressed by our investigation.

In this work, our primary focus centers on the eigenvector perturbation of the Reynolds stress tensor that has received limited attention in the literature. We systematically analyze that the eigenvector perturbation may violate Reynolds stress tensor dynamics under specific conditions. The present study derives and introduces physics-based constraints for eigenvector perturbations, adhering to the realizability and stability of the uncertainty estimation procedure. The application of these constraints to the flow within a converging-diverging channel illustrates improved stability and accuracy in capturing the turbulent behavior. The flow characteristics of this case encompass turbulent boundary layer, separation and reattachment regions, revealing deviations of RANS and DNS results. Applying the EPF unveils significant sensitivity of the considered QoI based on Reynolds stress anisotropy and its eigenvector alignment with the strain-rate tensor. Based on the present paper and our previous research [96], we have successfully identified challenges in the application and interpretability and proposed potential solutions. Our future investigations will focus on implications of the physics-constrained Reynolds stress tensor perturbation method for more complex engineering flows, such as those encountered in turbomachinery components. This will provide valuable insights into the method's practical utility.

Appendix 6.A Rotation properties of eigenvector permutation

In this section, we show that the eigenvector permutation (first and third eigenvector) according to Iaccarino et al. [66] is identical to the rotation around second eigenvector with $\pi/2$. Any rotation around an arbitrary vector $\boldsymbol{v} = (v_1, v_2, v_3)^T$ by α can be described via the rotation matrix

$$\mathbf{R} = \begin{pmatrix} \cos(\alpha) + v_1^2(1-\cos(\alpha)) & v_1 v_2(1-\cos(\alpha)) - v_3\sin(\alpha) & v_1 v_3(1-\cos(\alpha)) + v_2\sin(\alpha) \\ v_1 v_2(1-\cos(\alpha)) + v_3\sin(\alpha) & \cos(\alpha) + v_2^2(1-\cos(\alpha)) & v_2 v_3(1-\cos(\alpha)) - v_1\sin(\alpha) \\ v_1 v_3(1-\cos(\alpha)) - v_2\sin(\alpha) & v_2 v_3(1-\cos(\alpha)) + v_1\sin(\alpha) & \cos(\alpha) + v_3^2(1-\cos(\alpha)) \end{pmatrix} . \tag{6.26}$$

The eigenvector matrix contains column-wise orthogonal, normalized eigenvectors $\boldsymbol{v_1}, \boldsymbol{v_2}, \boldsymbol{v_3}$

$$\mathbf{v} = \begin{pmatrix} v_{11} & v_{21} & v_{31} \\ v_{12} & v_{22} & v_{32} \\ v_{13} & v_{23} & v_{33} \end{pmatrix} . \tag{6.27}$$

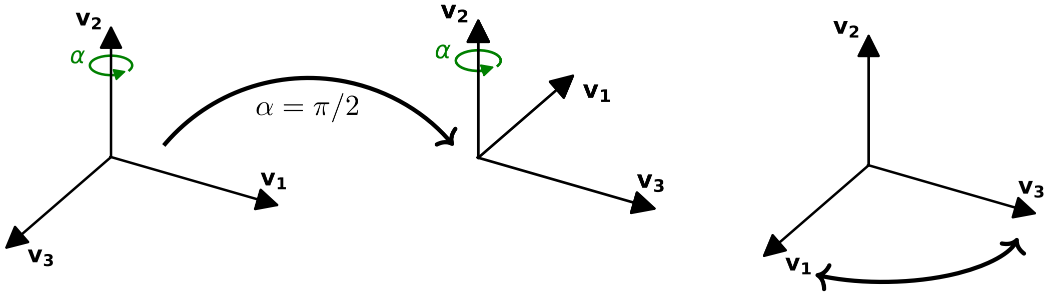

(a) Rotation of the eigenvector matrix around the second eigenvector $\boldsymbol{v_2}$ by $\alpha = \pi/4$

(b) Schematic representation of the eigenvector perturbation by permuting the first and third eigenvector [66]

Figure 6.11.: Comparison of modifying eigenvectors of the Reynolds stress tensor.

The eigenvectors are ordered with respect to the respective eigenvalues in descending order. Rotating $\mathbf{v}$ around $\boldsymbol{v_2}$ with $\alpha = \pi/2$ leads to:

$$
\begin{aligned}
\mathbf{v}^* &= \mathbf{R}\mathbf{v} \\
&= \begin{pmatrix} v_{21}^2 & v_{21}v_{22} - v_{23} & v_{21}v_{23} + v_{22} \\ v_{21}v_{22} + v_{23} & v_{22}^2 & v_{22}v_{23} - v_{21} \\ v_{21}v_{23} - v_{22} & v_{22}v_{23} + v_{21} & v_{23}^2 \end{pmatrix} \begin{pmatrix} v_{11} & v_{21} & v_{31} \\ v_{12} & v_{22} & v_{32} \\ v_{13} & v_{23} & v_{33} \end{pmatrix} \\
&= \begin{pmatrix} (v_{21}\,(\boldsymbol{v_2}\cdot\boldsymbol{v_1}) - (\boldsymbol{v_1}\times\boldsymbol{v_2})_1) & (v_{21}|v_2|^2) & (v_{21}\,(\boldsymbol{v_2}\cdot\boldsymbol{v_3}) + (\boldsymbol{v_2}\times\boldsymbol{v_3})_1) \\ (v_{22}\,(\boldsymbol{v_2}\cdot\boldsymbol{v_1}) + (\boldsymbol{v_1}\times\boldsymbol{v_2})_2) & (v_{22}|v_2|^2) & (v_{22}\,(\boldsymbol{v_2}\cdot\boldsymbol{v_3}) - (\boldsymbol{v_2}\times\boldsymbol{v_3})_2) \\ (v_{23}\,(\boldsymbol{v_2}\cdot\boldsymbol{v_1}) - (\boldsymbol{v_1}\times\boldsymbol{v_2})_3) & (v_{23}|v_2|^2) & (v_{23}\,(\boldsymbol{v_2}\cdot\boldsymbol{v_3}) + (\boldsymbol{v_2}\times\boldsymbol{v_3})_3) \end{pmatrix} \\
&= \begin{pmatrix} -v_{31} & v_{21} & v_{11} \\ -v_{32} & v_{22} & v_{12} \\ -v_{33} & v_{23} & v_{13} \end{pmatrix} .
\end{aligned}
\tag{6.28}
$$

As it can be seen in Eq. (6.28), the rotation results in permuting $\boldsymbol{v_1^*} = -\boldsymbol{v_3}$ and $\boldsymbol{v_3^*} = \boldsymbol{v_1}$. This is illustrated in Fig. 6.11 and compared with the formerly proposed eigenvector permutation. In contrast to rotating the eigenvectors, simple permutation of $\boldsymbol{v_1}$ and $\boldsymbol{v_3}$ evidently leads to a left-handed oriented eigenvector matrix. The resulting Reynolds stress tensor, when reconstructed based on Eq. (6.13), is identical due to the characteristic of the spectral decomposition.

Appendix 6.B Schematics of converging-diverging flow example

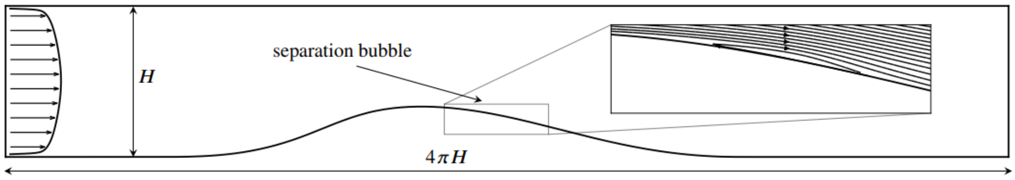

(a) Relative dimensions and sketch of the flow based on DNS data [85]

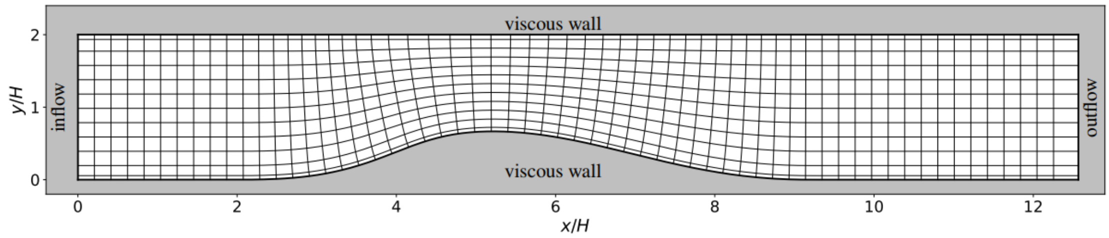

(b) Mesh consisting of 242x242x1 grid points (every fourth line in streamwise direction and every twentieth line in wall normal direction shown) and boundary conditions; slip conditions/inviscid walls are applied in spanwise direction

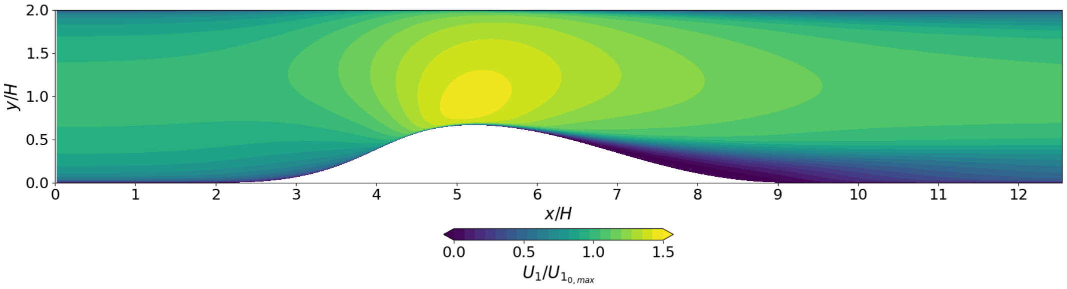

(c) Streamwise velocity based on the RANS baseline computation using the Menter SST turbulence model and the mesh presented in (b)

Figure 6.12.: Introduction of the converging-diverging setup.

Appendix 6.C Instability introduced by former eigenvector permutation

We apply the eigenvector permutation [66] in the former implementation of the EPF without any eigenvalue perturbation ($\Delta_B = 0$). When checking the evolution of the outlet pressure in Fig. 6.13 (specified mass flow rate is specified as outlet boundary condition), it becomes evident that the simulation is unstable. As a consequence, the streamwise velocity reveals significant variations at each snapshot in Fig. 6.14. Additionally, the application of non-realizable Reynolds stress tensor dynamics, creates non-physical countergradient transport (see Section 6.3), which results in the zigzag like velocity profiles. In contrast, the streamwise velocity snapshots of the perturbed simulations, used in Section 6.4, converge over runtime of the simulations (Fig. 6.15 presents one example).

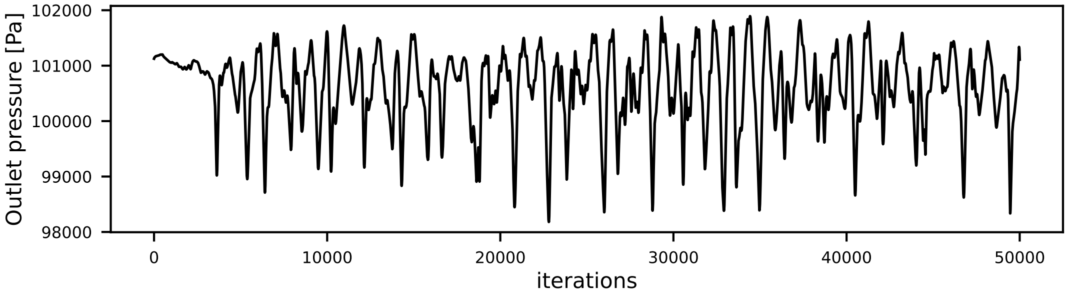

Figure 6.13.: Evolution of the area averaged outlet pressure over iteration count for the simulation using eigenvector permutation without any eigenvalue perturbation.

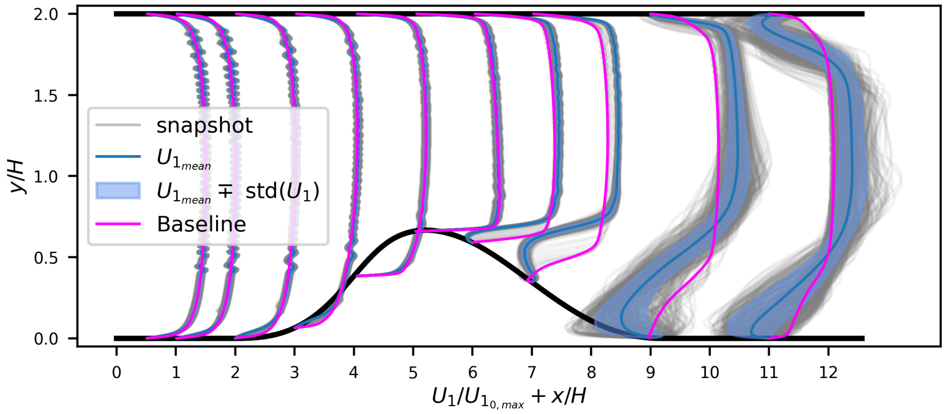

Figure 6.14.: Streamwise velocity inside the converging-diverging channel based on pure eigenvector permutation without any eigenvalue perturbation. The snapshots are taken every 1000 iteration, while the mean $U_{1_{\mathrm{mean}}}$ and the standard deviation $\mathrm{std}(U_1)$ are determined between 400.000 to 500.000 iterations.

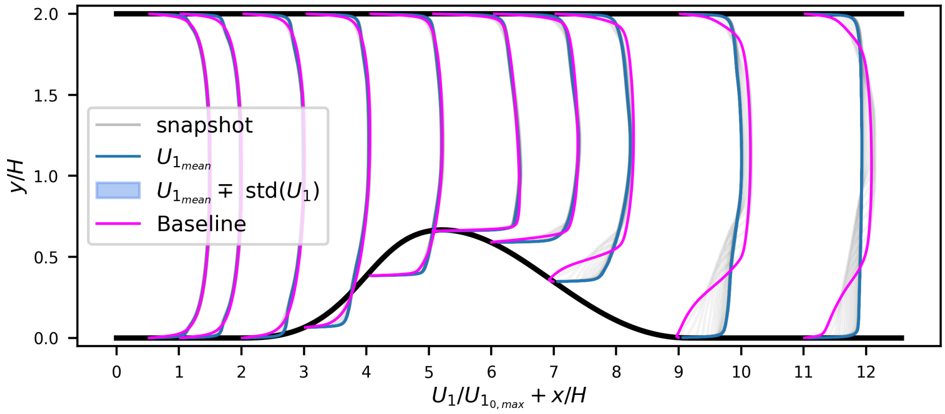

Figure 6.15.: Streamwise velocity inside the converging-diverging channel for simulation #2 (see Table 6.1) using moderated eigenvector perturbation and eigenvalue modification towards the one-component limiting state. The snapshots are taken every 1000 iteration, while the mean $U_{1_{\mathrm{mean}}}$ and the standard deviation $\mathrm{std}(U_1)$ are determined between 400.000 to 500.000 iterations.

7. Advanced methods for assessing flow physics of the TU Darmstadt compressor stage: Uncertainty quantification of RANS turbulence modeling

(Published in *Journal of Turbomachinery*, 147(8), 081004, 2025[1].)

M. Matha*, F. M. Möller**, C. Bode***, C. Morsbach*, E. Kügeler*
*DLR, Institute of Propulsion Technology, Cologne, Germany
**DLR, Institute of Test and Simulation for Gas Turbines, Cologne, Germany
***TU Braunschweig, Institute of Jet Propulsion and Turbomachinery, Germany

Abstract

In this paper, we quantify the turbulence modeling uncertainty for the transonic TUDa compressor. The present work applies the EPF, as it is the only published physics-based framework capable of addressing the model-form uncertainty in turbulence closure modeling. To sample from the possible solution space and obtain the modeling uncertainty, we perform simulations perturbing the eigenvalues of the Reynolds stress tensor in addition to simulations using an unperturbed turbulence model. We show that the shape of the Reynolds stress tensor ellipsoid has significant impact on the evolution of turbulence, flow separation, vortex systems, shock-boundary layer interaction and finally the overall performance of the compressor. We compare the estimated uncertainties with available measurements and transitional DDES. This allows us to assess the confidence of the chosen turbulence model and to evaluate the sharpness and coverage of the resulting uncertainty bounds. Thus, the EPF is comprehensively validated and suggestions for its future applicability with respect to turbomachinery components are made.

7.1. Introduction

The design of turbomachinery components is heavily dependent on the prediction capabilities of RANS simulations. However, the RANS equations require the modeling of the second-moment Reynolds stress tensor $\boldsymbol{\tau}$. While Reynolds stress tensor modeling, known as turbulence modeling, provides practicality and enables efficient simulations, it also comes with inherent limitations that hinder the attainment of high levels of accuracy. Over the last decade, researchers have highlighted the limitations of the commonly applied LEVM assumption for flow situations not covered by the calibration cases [146, 109, 23, 89].

---

[1] Copyright @ASME

Due to the lack of knowledge, these LEVMs are characterized by modeling assumptions derived from data observation, engineering intuition and computational pragmatism, leading to a significant degree of model-form (epistemic) uncertainty. This is in contrast to potential errors in CFD that are not due to the general lack of knowledge, such as discretization or round-off errors, which could in principle be reduced by exploiting extra resources [119]. Theoretically, epistemic uncertainties could also be mitigated through a better understanding of turbulent processes, facilitating the development of advanced models. This contrasts with aleatory uncertainties, such as manufacturing tolerances or uncertain operating conditions, which cannot be reduced and are not within the scope of the present study. In the past, efforts in engineering design applications aimed to address uncertainties in CFD simulations through the use of safety margins, levels of redundancy and similar heuristic approaches. As computational resources continue to increase, the turbomachinery industry is undergoing substantial advancements in digitization. Methodologies such as robust design or reliability-based design offer the potential to supersede the traditional approaches for addressing uncertainties in CFD. In recent years, there has been a growing interest in UQ, paving the way for more reliable simulation-based designs [71].

The usage of turbulence closure models represents a major source of the overall uncertainty observed in RANS simulations, assuming a known set of boundary conditions and precise geometry information. In addition, the quantification of model-form uncertainty is described to be the 'greatest challenge' in CFD [172]. Following Duraisamy's categorization, the uncertainty is introduced at several modeling levels [29]. These include uncertainties arising from information loss during the averaging of the Navier-Stokes equations, uncertainties associated with representing Reynolds stress as a function of mean flow quantities, uncertainties stemming from the selection of a particular function (mainly transport equations) and uncertainties associated with choosing and calibrating certain parameters. Two broad categories are recognized: parametric and non-parametric approaches. Parametric uncertainties originate from the selection and calibration of closure coefficients, whereas non-parametric methodologies explore uncertainties related to the mathematical relationships for representing the Reynolds stress tensor [169]. As the modeled Reynolds stress tensor is the only term that links the turbulence model equations to the RANS equation, it plays a unique role. Hence, our current research focuses on the appropriate estimation of turbulence modeling uncertainty related to the functional representation of Reynolds stresses (non-parametric approach). In this paper, we introduce selective perturbed states of the Reynolds stress tensor based on the concept of realizability. This physics-based approach developed by Emory et al. [34] is able to address the epistemic uncertainty inherent in turbulence closure modeling. As the modifications of the Reynolds stress tensor rely on perturbing its eigenspace (described in Section 7.2), the entire framework is called the EPF.

Due to its unique characteristics and persuasive interpretability of its simulation outcomes, the EPF has been used in various engineering applications, such as aircraft design [113], civil structural design [80], wind farms [64, 31] and turbomachinery flows [35]. For this reason, the EPF has also been integrated into TRACE [47, 99], which is developed by the DLR in strong cooperation with MTU Aero Engines AG. We have already verified the conceptual idea behind the methodology and its computational implementation and applied the EPF to generic test cases in recent publications [96, 97]. Although the aforementioned applications of the EPF have provided some validation of the framework, this paper applies and consequently validates the methodology to the most complex configuration related to turbomachinery applications to date. The capabilities of the EPF are demonstrated on the TUDa compressor [74]. The TUDa-GLR-OpenStage compressor is a single-stage, transonic axial compressor, which is introduced in Section 7.3.

Hence, the novelty of this paper lies in the application of the Reynolds stress tensor perturbation to a complex rotational multi-row test case on the one hand. With respect to physical flow phenomena, this means shock-boundary layer interaction in the rotor section, formation of a rotor tip vortex and general rotor-stator interaction. On the other hand, the current research offers the physically constrained estimation of the turbulence modeling uncertainty for RANS simulations of this test case. Hereby this paper contributes to the ongoing assessment of the overall uncertainties of simulating the TUDa compressor [60, 168, 59].

7.2. Eigenspace perturbation method

State-of-the-art LEVMs close the RANS equations by introducing a scalar turbulent eddy viscosity ν_T to express the Reynolds stress tensor

$$\tau_{ij} = -2\nu_\mathrm{T}\left(S_{ij} - \frac{1}{3}\frac{\partial u_k}{\partial x_k}\delta_{ij}\right) + \frac{2}{3}k\delta_{ij}\ , \tag{7.1}$$

where $k = \frac{1}{2}\tau_{ii}$ represents the turbulent kinetic energy and the strain-rate tensor is denoted as S_{ij}. This modeling assumption, known as the Boussinesq assumption, assumes turbulence to behave as an isotropic medium. Hence, LEVMs are not able to account correctly for the anisotropy of Reynolds stresses by definition, leading to a significant degree of epistemic uncertainty. Following the modeling assumption in Eq. (7.1), the eigenspace of the Reynolds stress tensor only depends on the eigenspace of the strain-rate tensor (identical eigenvectors and linear dependency between eigenvalues). The EPF, described in the following, assesses this uncertainty within physical constraints. The underlying methodology is based on the spectral decomposition of the anisotropic part, represented by the anisotropy tensor $\mathbf{a}$, of the Reynolds stress tensor

$$\tau_{ij} = k\left(a_{ij} + \frac{2}{3}\delta_{ij}\right) = k\left(v_{in}\Lambda_{nl}v_{jl} + \frac{2}{3}\delta_{ij}\right)\ . \tag{7.2}$$

The eigenvectors $\boldsymbol{v_k}$ of a_{ij} are contained column-wise in v_{in}, while the traceless diagonal matrix Λ_{nl} contains the corresponding eigenvalues λ_k.

Generally speaking, perturbing the Reynolds stress tensor means changing the amount of turbulent kinetic energy (k), the spectral energy distribution of the anisotropy tensor (λ_k) and the orientation of the principal components of the anisotropy tensor (v_{in}) [33, 66]. The eigenspace perturbation, considered in this study, modifies solely the shape of the Reynolds stress tensor ellipsoid by creating perturbed states of the eigenvalues λ_k^*, while the other two attributes of the Reynolds stress tensor are kept constant. Changing the shape of the Reynolds stress tensor ellipsoid means modifying the turbulence model to an orthotropic eddy viscosity model, where turbulence behaves differently along each eigendirection [106][2]. This is equivalent to assigning different turbulent eddy viscosities along every eigendirection. Consequently, the uniform linear dependency between the eigenvalues of the strain-rate tensor and the Reynolds stress tensor is overridden. Accordingly, the perturbed Reynolds stress tensor is defined as

$$\tau_{ij}^* = k\left(v_{in}\Lambda_{nl}^*v_{jl} + \frac{2}{3}\delta_{ij}\right)\ . \tag{7.3}$$

---

[2] See Section 3.5.1 and Appendix C for details in this thesis.

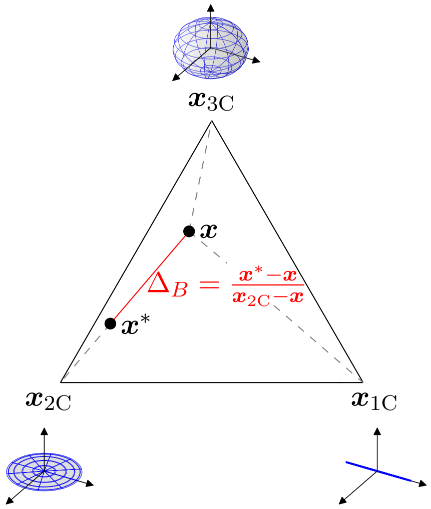
$\boldsymbol{x}_{3\mathrm{C}}$
$\boldsymbol{x}$
$\Delta_B = \frac{\boldsymbol{x}^* - \boldsymbol{x}}{\boldsymbol{x}_{2\mathrm{C}} - \boldsymbol{x}}$
$\boldsymbol{x}^*$
$\boldsymbol{x}_{2\mathrm{C}}$
$\boldsymbol{x}_{1\mathrm{C}}$

Figure 7.1.: Representation of the Reynolds stress tensor's eigenvalue perturbation within the barycentric triangle. Its effect on the shape of the Reynolds stress tensor is shown by the ellipsoid visualizations, when approaching the vertices of the triangle.

The realizability constraints manifest limits for the eigenvalues of the Reynolds stress tensor and the anisotropy tensor, respectively [136]. The mapping of eigenvalues onto barycentric coordinates, based on Banerjee et al. [4],

$$\boldsymbol{x} = \frac{1}{2}\boldsymbol{x}_{1\mathrm{C}}\left(\lambda_1 - \lambda_2\right) + \boldsymbol{x}_{2\mathrm{C}}\left(\lambda_2 - \lambda_3\right) + \boldsymbol{x}_{3\mathrm{C}}\left(\frac{3}{2}\lambda_3 + 1\right) \tag{7.4}$$

is used to explore the realizable eigenvalue space within a 2D projection, where $\boldsymbol{x}_{1\mathrm{C}}, \boldsymbol{x}_{2\mathrm{C}}, \boldsymbol{x}_{3\mathrm{C}}$ are the coordinates of the vertices of an equilateral triangle, as illustrated in Fig. 7.1. The states of the Reynolds stress tensor that are defined by these vertices represent the limiting states of turbulence componentiality based on the number of non-zero eigenvalues of the Reynolds stress tensor: the three-component, isotropic limit (3C), the two-component axisymmetric limit (2C) and the one-component limit (1C). As the representation of eigenvalues in barycentric coordinates enables linear interpolation between two states, Emory et al. [33] propose to obtain the perturbed location as a relative shift towards the vertices $\boldsymbol{x}_{(\mathrm{t})} \in \{\boldsymbol{x}_{1\mathrm{C}}, \boldsymbol{x}_{2\mathrm{C}}, \boldsymbol{x}_{3\mathrm{C}}\}$ according to

$$\boldsymbol{x}^* = \boldsymbol{x} + \Delta_B\left(\boldsymbol{x}_{(\mathrm{t})} - \boldsymbol{x}\right) \text{ with } \Delta_B \in [0, 1]. \tag{7.5}$$

This is shown by way of example in Fig. 7.1 for the perturbation towards the 2C state. As Eq. (7.4) can be expressed as $\boldsymbol{x} = \mathbf{Q}\boldsymbol{\lambda}$, the resulting perturbed eigenvalues are determined via

$$\boldsymbol{\lambda}^* = \left(1 - \Delta_B\right)\boldsymbol{\lambda} + \Delta_B \boldsymbol{\lambda}_{(\mathrm{t})} \text{ , while} \tag{7.6}$$

$\boldsymbol{\lambda}_{(\mathrm{t})} \in \{\boldsymbol{\lambda}_{1\mathrm{C}}, \boldsymbol{\lambda}_{2\mathrm{C}}, \boldsymbol{\lambda}_{3\mathrm{C}}\} = \left\{\left(\frac{4}{3}, -\frac{2}{3}, -\frac{2}{3}\right)^T, \left(\frac{1}{3}, \frac{1}{3}, -\frac{2}{3}\right)^T, \left(0, 0, 0\right)^T\right\}$ depends on the chosen componentiality of the target state [106]. While the choice of $\Delta_B = 0$ results in unaltered eigenvalues, $\Delta_B = 1$ changes the eigenvalues to the ones of the target state $\boldsymbol{\lambda}_{(\mathrm{t})}$. Whereas previous studies tried to account for spatially varying perturbations [34, 52, 61, 99], we assume a uniform distribution of the relative perturbation magnitude Δ_B in the computational domain. Although LEVMs produce sufficiently accurate predictions in the majority of the computational domain, except for separation, reattachment, secondary flows and wakes, we are exploring the worst case scenario by applying uniform, non-local perturbations. This procedure results in the most conservative uncertainty estimates.

The eigenspace perturbation takes place in every grid point within each pseudo-time step of the steady simulations. The coupling with the RANS equations is done by updating the viscous fluxes via the perturbed Reynolds stress tensor. To incorporate the effect on the turbulence model's turbulent kinetic energy transport equation, the production of turbulent kinetic energy is computed according to

$$P_k = -\tau^*_{ij} \frac{\partial U_i}{\partial x_j} \ , \tag{7.7}$$

incorporating the perturbed Reynolds stresses explicitly. Finally, the uncertainty on certain QoI attributed to the uncertainty of the turbulence model can be determined by propagating the perturbed Reynolds stress tensors in additional RANS simulations and sample from the attainable possible solution space.

7.3. TUDa-GLR-OpenStage compressor

7.3.1. Test case description

The single stage transonic axial compressor is an open test case of the Global Power and Propulsion Society (GPPS) providing detailed information on the geometry and a comprehensive set of measurement data by the Technical University of Darmstadt [74]. The original stage consists of 16 rotor blades, 29 stator blades and 5 outlet guide vanes. At the corrected[3] design speed of $n_{\mathrm{corr}} = n_{\mathrm{real}}\sqrt{\frac{T_{\mathrm{ISA}}}{T_{\mathrm{t},15}}} = 20\,000$ rpm and a corrected mass flow rate of $\dot{m}_{\mathrm{corr}} = \dot{m}_{\mathrm{real}}\frac{p_{\mathrm{ISA}}}{p_{\mathrm{t},15}}\sqrt{\frac{T_{\mathrm{t},15}}{T_{\mathrm{ISA}}}} = 16.00\,\mathrm{kg/s}$, a total pressure ratio of 1.5 is achieved.

7.3.2. CFD setup

TRACE is a parallel Navier-Stokes flow solver. In the present work we use the finite-volume method to discretize the compressible RANS equations. We apply Roe's upwind scheme combined with MUSCL extrapolation to ensure second-order accuracy [129, 158]. Large gradients are smoothed using a van Albada-type flux limiter [157]. This ensures the total variation diminishing property of the scheme, which is important for transonic flows. The attainment of steady-state solutions is facilitated through the utilization of an implicit time-marching algorithm. Furthermore, for the transport equations governing turbulence quantities, we apply a segregated solution method that is second-order accurate and conservative [112]. The two-equation Menter SST $k-\omega$ [104] LEVM is chosen to be the underlying turbulence model in the present investigation. As already described in Section 7.2, the viscous fluxes and the turbulence production term are modified when applying the EPF.

We simulate a single passage of the compressor without considering the outlet guide vanes (see Fig. 7.2). Previous studies already presented a comprehensive analysis of various important aspects when simulating the compressor stage [60, 168]. Based on recent adjustments of the geometry provided by the GPPS, our numerical setup incorporates the latest hub and shroud contour, the rotor tip gap of 0.75 mm, a constant fillet radius at the rotor hub of 5 mm and approximated fillet radii at stator hub and tip. We stick to using 16 rotor blades but scale to 32 stator blades in order to compare the RANS uncertainty estimates with the transitional DDES data of Möller et al. [114]. By comparing CFD with CFD results, we are able to eliminate potential geometrical errors. The inlet section of the

---

[3] Corrected with reference to International Standard Atmosphere (ISA) conditions.

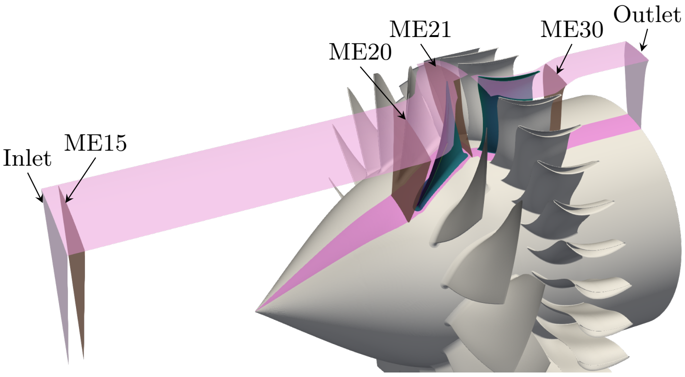

Figure 7.2.: 3D illustration of the considered TUDa compressor configuration. The simulated single passage is colored in pink, while reference locations are highlighted as well.

Table 7.1.: Number of grid points / 10^6 used for the RANS grid convergence study presented in Fig. 7.3.

	Total	Rotor	Stator
Ultra-coarse	0.70	0.30	0.29
Coarse	1.87	0.78	0.80
Medium	3.97	1.64	1.69
Fine	5.38	2.21	2.30
Ultra-fine	18.06	7.35	7.76

computational domain is located 3% upstream of ME15 with respect to the compressor core axial length (ME20 to ME30). Experimentally measured total temperature and pressure profiles based on the experiment by Klausmann et al. [74] are prescribed at the inlet. Similar to previously published RANS studies (e.g. by He et al. [60]), we assume axial inflow direction, while the level of turbulence intensity is set to 4% and the turbulent length scale is assumed to be $L_\mathrm{T} = \sqrt{k}/\omega = 0.09\,\mathrm{mm}$. The rotor-stator interface is accomplished by a mixing plane approach [134]. The domain's outlet is located at $+58\%$ downstream of ME30 with respect to the compressor core axial dimension. In order to compare RANS results at the experimental operating points, the respective mass flow rates are realized by using a boundary controller that adjusts the static pressure at the outlet of the computational domain. If the simulation, enforcing a certain mass flow rate, does not converge, an iterative process decreasing the backpressure in steps of 100 Pa is conducted. Hereby, we are able to examine the numerical stall limit of the RANS simulations appropriately[4].

Finally, given the geometry information by GPPS, the low-Reynolds mesh is generated using our in-house tool PyMesh. A grid convergence study based on five grids helps to identify the influence of grid resolution on the prediction of design relevant integral quantities. The considered grids are summarize in Table 7.1. As the goal of the conducted grid study is only to select a resolution that serves practical purposes for subsequent UQ simulations while still remaining computationally feasible, all simulations are based on the mass flow controller aiming for the experimental mass flow rates. Figure 7.3 shows

---

[4] Klausmann et al. [76] proved experimentally that rotating stall occurs for the actual TUDa compressor configuration.

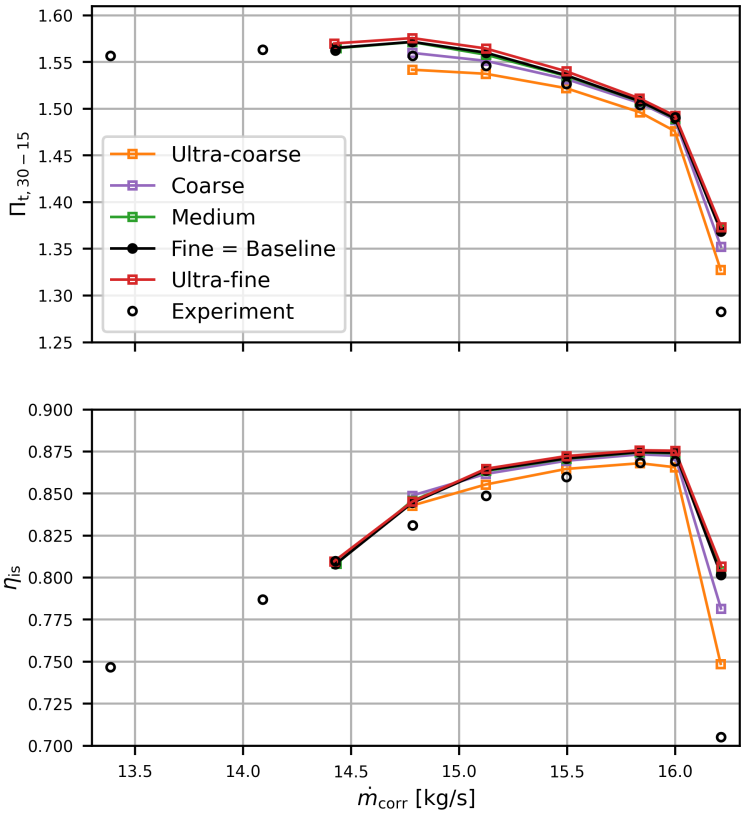

Figure 7.3.: Effect of the grid resolution on the prediction of the total pressure ratio (top) and the isentropic efficiency (bottom) by RANS simulations at design speed.

the sensitivity with respect to the chosen grid resolution on the total pressure ratio

$$\Pi_{\mathrm{t},30-15} = \frac{p_{\mathrm{t},30}}{p_{\mathrm{t},15}} \tag{7.8}$$

and on the isentropic efficiency

$$\eta_{\mathrm{is}} = \frac{\Pi_{\mathrm{t},30-15}^{((\gamma-1)/\gamma)} - 1}{\zeta_{\mathrm{t},30-15} - 1} \ , \tag{7.9}$$

where the total temperature ratio is defined as

$$\zeta_{\mathrm{t},30-15} = \frac{T_{\mathrm{t},30}}{T_{\mathrm{t},15}} \ . \tag{7.10}$$

These integral quantities are computed using the area-averaged total pressure and total temperature at ME30 and ME15.

The general trend indicates that mesh refinement results in an increase in both total pressure ratio and isentropic efficiency. Simultaneously, this is reflected in the ability to approach the experimentally determined stall limit. It also becomes evident that coarser meshes increase the matching with absolute values of the total pressure ratio and the isentropic efficiency ascertained in the experiment by Klausmann et al. [74]. This is in accordance with the observed grid analysis by He et al. [60]. Nevertheless, as we want to choose an appropriate level of grid convergence, we choose the fine mesh for the subsequent analysis and call the obtained results to be the baseline simulation in the following sections. Choosing the fine mesh leads to a 0.17% deviation in predicting the total pressure ratio and 0.13% difference in predicting the isentropic efficiency compared with the ultra-fine mesh at the design (peak efficiency) operation point. When we compare the prediction of the fine with the ultra-fine mesh resolution across all considered mass flow rates, the mean relative deviation is 0.26% for $\Pi_{\mathrm{t},30-15}$ and 0.2% for η_t.

7.3.3. Creating uncertainty estimates based on Reynolds stress tensor perturbation

We perform simulations propagating Reynolds stresses that are perturbed towards the one-component (1C), two-component (2C) and isotropic limit of turbulence (3C). Following the approach proposed in our previous work [96, 97], the relative perturbation magnitude with respect to the relative shift in barycentric coordinates Δ_B (see Fig. 7.1) is adjusted as a consequence of occurring convergence issues. Selecting a uniform Δ_B for 1C, 2C and 3C perturbation would be a conceivable and equally valid approach. Furthermore, it is also possible to moderate the Δ_B based on expert knowledge, marker functions [34] or machine learning [61, 99]. In the present investigation, we apply Δ_B as large as possible non-uniformly towards $\boldsymbol{x}_{1\mathrm{C}}, \boldsymbol{x}_{2\mathrm{C}}, \boldsymbol{x}_{3\mathrm{C}}$ in order to obtain the worst case scenario with respect to the inherent turbulence modeling uncertainty and to account for physically plausible variation in perturbation magnitude across the limiting states. As already described in Section 7.3.2, we aim for approaching the experimental operating points (in terms of mass flow rates) at the design rotational speed. As previous studies (e.g. [36, 56]) reveal, there is a general trend indicating more conservative uncertainty estimates when increasing the eigenvalue perturbation strength, we seek for the largest possible Δ_B for each individual operation point. Considering that, we limited the iterative search to gradually decreasing Δ_B by 0.1 for $\Delta_B \in [0.1, 1.0]$ and by 0.01 for $\Delta_B \in [0, 0.1]$. Additionally, we employ an initially arbitrarily chosen search points at $\Delta_B = 0.25$. As soon as we switch the boundary condition at the outlet from mass flow controller to constant backpressure for approaching the stall limit (described in Section 7.3.2) and some near choke operation point beyond the design point, we keep the relative perturbation magnitude constant and evaluate the attainable backpressure adjustment.

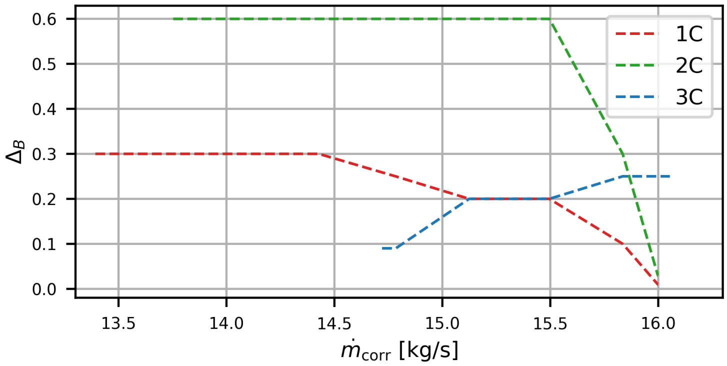

Figure 7.4.: Attainable relative perturbation magnitude Δ_B over corrected mass flow rate for eigenvalue perturbation of the Reynolds stress tensor towards the three limiting states of turbulence.

7.4. Turbulence model uncertainty for a multi-row compressor application

7.4.1. Perturbation magnitude and effect on anisotropy

Following the procedure described in Section 7.3.3, Fig. 7.4 shows the attainable perturbation magnitude for each speedline simulation of 1C, 2C and 3C. Throttling the compressor enables increased perturbation magnitude for 1C and 2C perturbations, while Δ_B needs to be reduced for 3C simulations. To give an idea of what perturbing the eigenvalues means for the converged states of the Reynolds stress tensor, Fig. 7.5 presents the analysis of the Reynolds stress anisotropy at ME30 with respect to RGB coloring in Fig. 7.5a and the barycentric coordinates in Fig. 7.5b. Evaluating the anisotropy tensor for the unperturbed baseline simulation using the Menter SST $k-\omega$ LEVM reveals the Reynolds stress tensor to be rather isotropic aligning the barycentric coordinates around the plane-strain line [4]. Except for the wakes and the secondary flow structures (see later

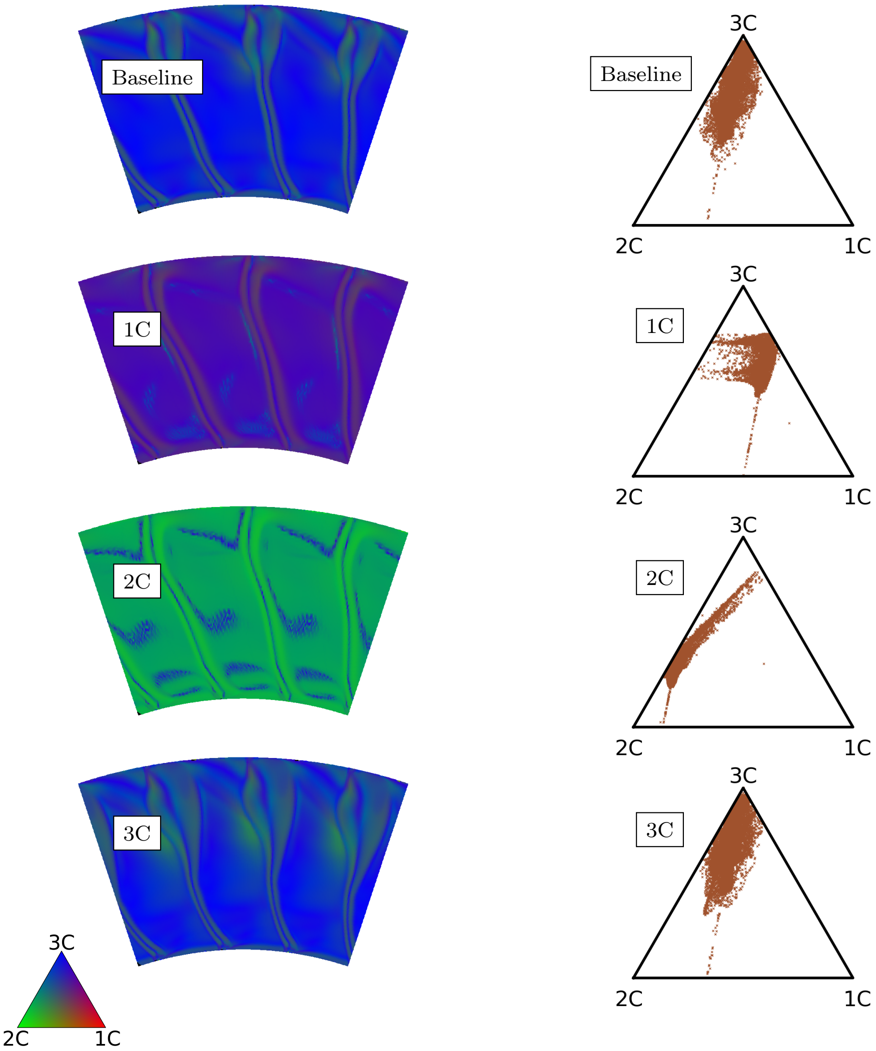

(a) Red Green Blue (RGB) coloring (b) Barycentric coordinates

Figure 7.5.: Illustration of the turbulent state of the Reynolds stress tensor at ME30 and $\dot{m}_{\text{corr}} = 14.78$ kg/s. (a) presents the RGB coloring according to the location of each data point inside the barycentric triangle, which is shown in (b).

analysis on secondary flows referring to Fig. 7.10 and Fig. 7.11), where some areas tend towards the two-component corner of the barycentric triangle (green regions in Fig. 7.5a). At the chosen mass flow rate $\dot{m}_{\mathrm{corr}} = 14.78\,\mathrm{kg/s}$, Δ_B is 0.25, 0.6 and 0.09 for 1C, 2C and 3C perturbation respectively (cf. Fig. 7.4). This results in the expected shift of the barycentric coordinates in the direction of the respective vertex. The perturbation of the eigenvalues of the Reynolds stress tensor has to be done iteratively, allowing the mean flow quantities to change over simulation time until converged states are reached. The same holds true for the unperturbed state of the Reynolds stress tensor derived from the respective velocity gradients, turbulent kinetic energy and turbulent eddy viscosity (see Boussinesq assumption in Eq. (7.1)). Since the perturbation of the eigenvalues depends on the unperturbed state of the current iteration step, each converged perturbed data point in Fig. 7.5b is not simply shifted towards the corners by the relative perturbation magnitude starting from the baseline computation.

7.4.2. Overall compressor performance

Changing the eigenvalues of the Reynolds stress tensor towards the one- and two-component limiting state of turbulence, stabilizes the RANS for low mass flow rates, as can be seen in Fig. 7.6. This leads to the possibility of further throttling the compressor compared with the baseline and 3C simulation. Unfortunately, we were not able to

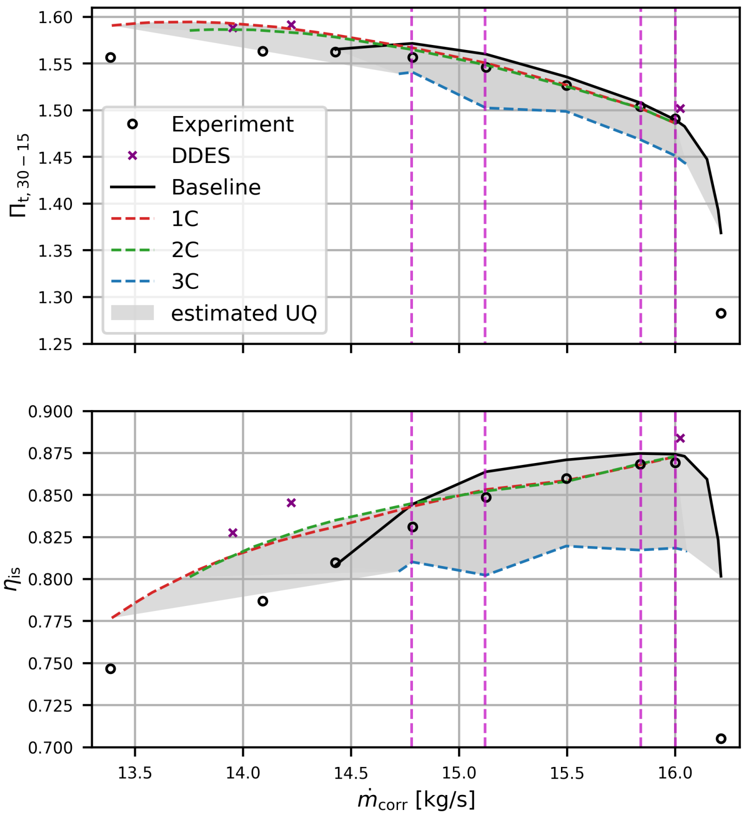

Figure 7.6.: Estimated turbulence modeling uncertainty for the global compressor performance quantities total pressure ratio (top) and isentropic efficiency (bottom) at 100% speedline and comparison with experimental data. The mass flow rates for subsequent detailed analysis are highlighted by magenta dashed lines ($\dot{m}_{\mathrm{corr}} \in [14.78\ \mathrm{kg/s}, 15.12\ \mathrm{kg/s}, 15.84\ \mathrm{kg/s}, 16.00\ \mathrm{kg/s}]$).

achieve converged steady-state RANS solutions significantly above the design mass flow rate, when perturbing the Reynolds stress tensor. On the one hand, this was already looming for 1C and 2C simulations, as we had to reduce Δ_B when approaching the design point to achieve converged solutions. On the other hand, 3C perturbation beyond the design point lead to undesired instabilities, which may potentially be identified as choking. The predictions of the compressor performance based on the 3C simulations show reduced total pressure ratios and isentropic efficiencies over the entire speedline. Overall, the chosen perturbation magnitude seems to be too large for 3C. However, as mentioned in Section 7.3.3, we are aiming for worst case scenarios of the attainable turbulent states rather than accurate sharpness (appropriate bounding of CFD predictions) of the uncertainty estimation. Consequently, we continue to analyze the obtained results based on the isotropic perturbations throughout this paper. Generally, the estimated uncertainty intervals for the integral compressor performance parameters include most of the experimental measurements, constituting a good coverage of the considered EPF. Applying the unperturbed (baseline) turbulence model yields mostly increased efficiency and total pressure ratios compared with the considered perturbed ones. However, close to the numerical stall limit the baseline simulation reveals a rather abrupt reduction in compressor performance, whereas perturbing the Reynolds stress tensor towards the one- and two-component turbulence allows stable operations of the compressor with increased efficiency. Increased performance of the compressor enables a shift of the numerical stall limit to reduced mass flows by $\dot{m}_{\mathrm{corr}_{1\mathrm{C,stall}}} - \dot{m}_{\mathrm{corr}_{3\mathrm{C,stall}}} \approx -1.33\,\mathrm{kg/s}$. Thus, perturbing towards 1C is beneficial for the prediction of the compressor's stall limit, as the difference between experimental and numerical stall mass flow rate becomes $\dot{m}_{\mathrm{corr}_{\mathrm{exp,stall}}} - \dot{m}_{\mathrm{corr}_{1\mathrm{C,stall}}} \approx -0.01\,\mathrm{kg/s}$. The performance maps in Fig. 7.6 also show the considered operation points by Möller et al. [114] using transitional DDES modeling. Besides the increased number of grid points, the applied geometrical model of the compressor is identical to the one used in the present RANS study. However, the transitional DDES are combined with the stagnation point anomaly fix by Kato and Launder [72] and the rotational effects extension by Bardina et al. [5], which is per se a numerical setup deviating from the one used in the current study. Since conducted preliminary RANS studies (not shown in this paper) indicate that especially the rotational effects extension lead to increased isentropic efficiencies, the observed performance improvement near the stall limit predicted by the DDES can be attributed to this modification.

7.4.3. Details on local flow physics

For further comparison with experimental measurements by Klausmann et al. [74], we analyze the flow at the reference locations ME21 and ME30. Figure 7.7 and Fig. 7.8 show the effect of turbulence modeling uncertainty on the total pressure and temperature ratios and draw the comparison with experimental data at ME30 downstream of the stator. The baseline simulation underpredicts the total pressure ratio for the design mass flow rate in Fig. 7.7 between 30% and 80% span, while an overprediction can be seen at the hub and tip. This overprediction of the total pressure ratio in the hub region is also present with decreasing mass flow rates from Fig. 7.7b to Fig. 7.7d. The baseline simulation rather coincides with the measurements at the mid-range mass flows, but tends to overpredict the total pressure ratio for $\dot{m}_{\mathrm{corr}} = 14.78\,\mathrm{kg/s}$. The contour plots in Fig. 7.8, showing the total pressure ratio at ME30 with reference to the integral area-averaged value at ME15, reveals that none of the RANS simulations is able to reproduce the corner separation in the hub region, which is observed in the experiments. This is in accordance with the RANS studies by He et al. [60]. Recently Klausmann

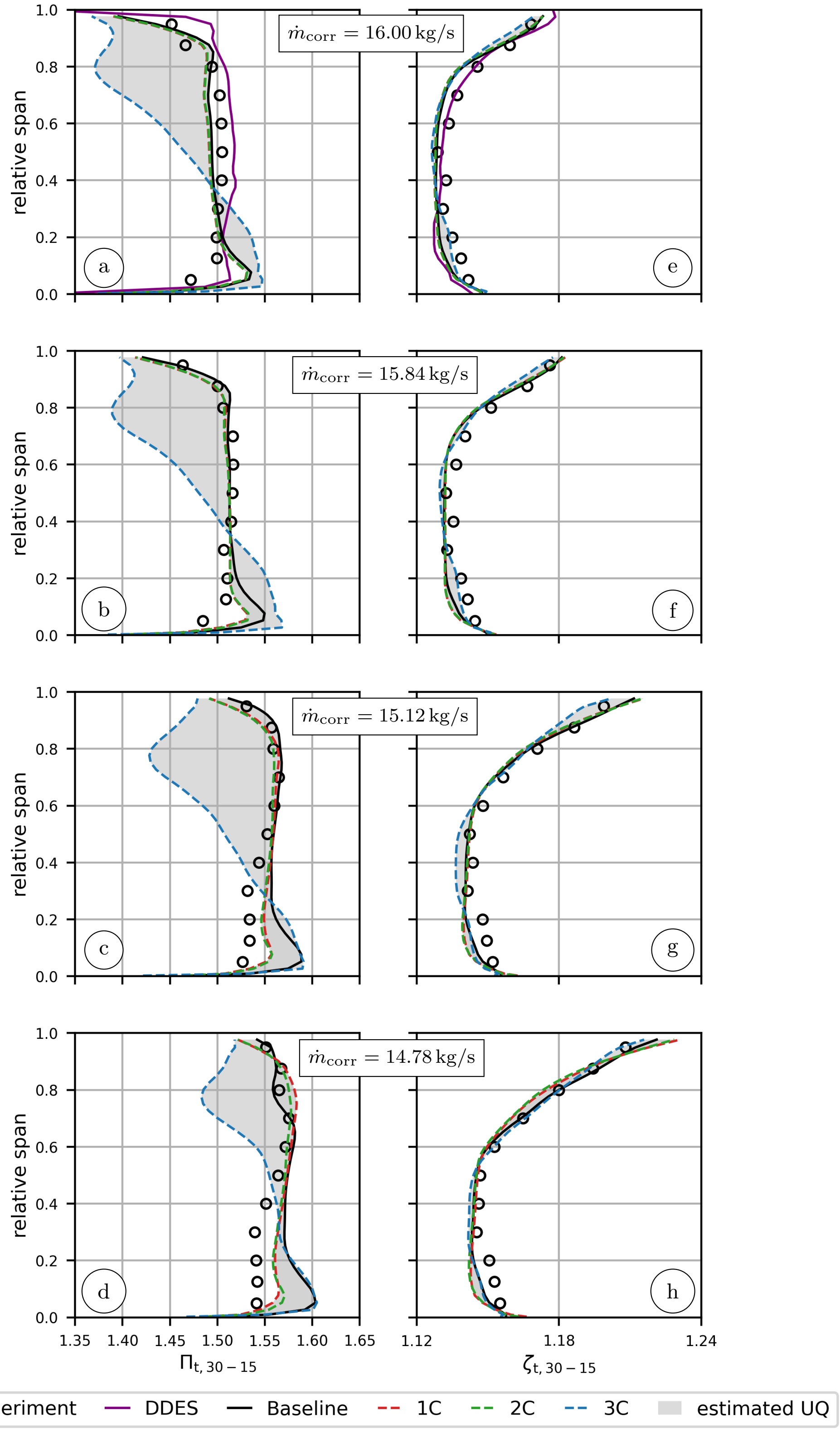

Figure 7.7.: Uncertainty estimates for predicting radial profiles of the total pressure ratio ((a), (b), (c), (d)) and the total temperature ratio ((e), (f), (g), (h)) at ME30 for four different operating points. The total pressure and temperature ratio is computed using circumferentially area-averaged quantities at ME30 and the integral area-averaged quantities at ME15.

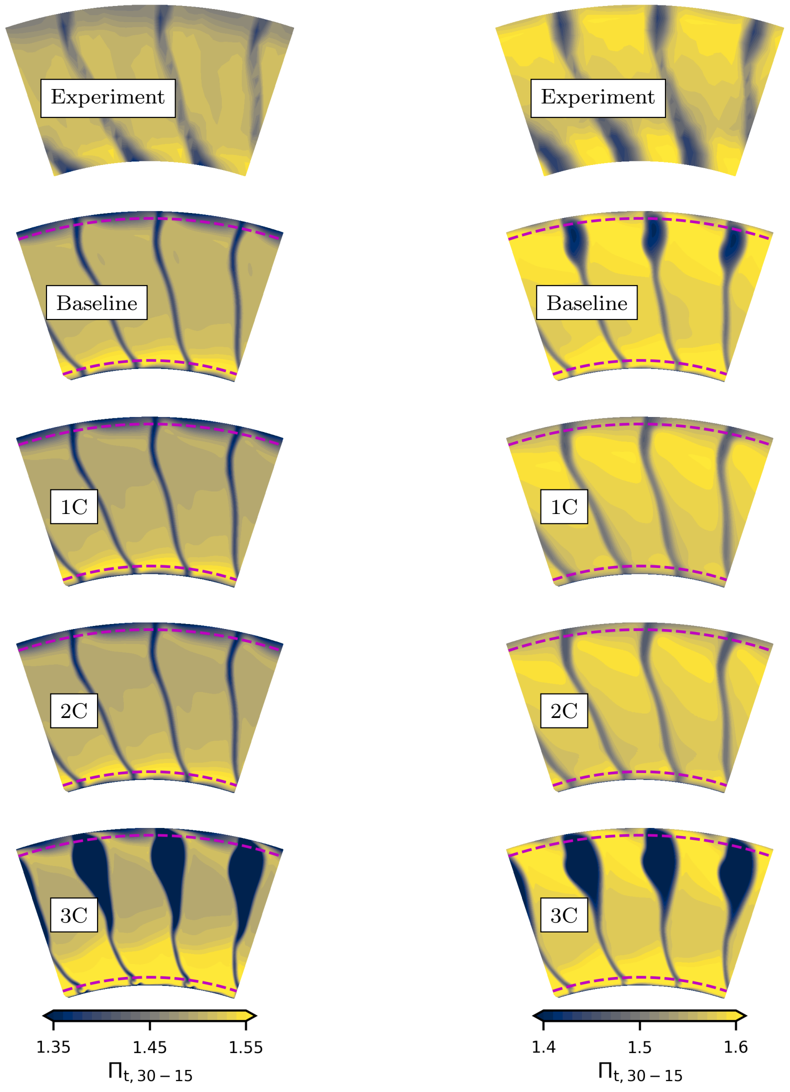

(a) $\dot{m}_{\mathrm{corr}} = 16.00$ kg/s (b) $\dot{m}_{\mathrm{corr}} = 14.78$ kg/s

Figure 7.8.: Comparison of total pressure wake losses at ME30 for two different operating points. The total pressure and ratio is computed using the integral area-averaged total pressure at ME15. Red dashed lines indicate the radial measurement window in the experimental setup.

et al. [75] have shown experimentally that the stator hub cavity increases the hub corner separation and is a contributor to the total pressure losses. As the current CFD setup neglects this cavity completely, it is not expected to match the experiments in this region. This is also addressed in Section 7.4.6, where we highlight capabilities and limitations of the applied UQ framework. Additionally, the wakes of the baseline, 1C and 2C simulation are predicted to be too sharp in comparison to the experiment, as can be observed in Fig. 7.8. It is important to acknowledge that the measured data are constrained by the spatial resolution inherent in the experiment. In general, 1C and 2C perturbations tend to reduce the overpredicted pressure rise in all considered operating points but especially in the hub region for lower mass flow rates (see Fig. 7.7a to Fig. 7.7d), which indicates that the corner separation is characterised by anisotropic rather than isotropic Reynolds

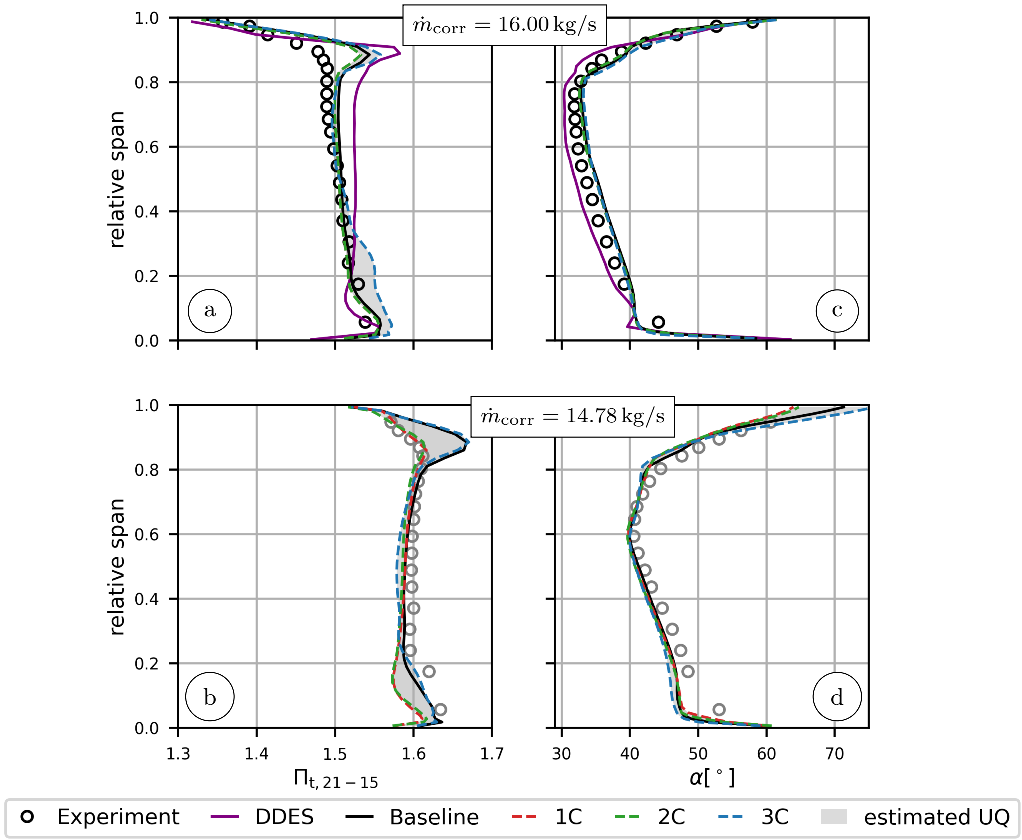

Figure 7.9.: Uncertainty estimates for predicting radial profiles of the total pressure ratio ((a), (b)) and the flow angle ((c), (d)) at ME21 for two different operating points. The total pressure ratio is computed using circumferentially area-averaged total pressure at ME21 and the integral area-averaged total pressure at ME15. Note: The experimental data presented in (b) and (d) were obtained by personal communication with Fabian Klausmann. As the underlying operation point ($\dot{m}_{\text{corr}} = 14.66\,\text{kg/s}$) varies slightly from the numerical one ($\dot{m}_{\text{corr}} = 14.78\,\text{kg/s}$), the markers are grayed out.

stresses. Perturbing the Reynolds stress tensor towards the isotropic state, massively affects the total pressure increase for higher mass flow rates. This means that the overprediction at the hub becomes larger, while the tip region is massively underpredicted, indicating near-tip trailing edge separation. This is supported by Fig. 7.13b presenting increased circumferentially area-averaged turbulent kinetic energy in the upper half of the annulus at ME30. Approaching the numerical stall limit, the over- and underprediction of experimental data by 3C simulation is reduced. Although the near hub regions seems to be sensitive to Reynolds stress tensor perturbation and, as already mentioned before, the 3C perturbation produces actual worst case total pressure, there is almost no coverage of the experimental and the DDES predicted total pressure ratios at ME30. Consequently, the turbulence model seems to be over-confident based on the total pressure prediction. Considering the total temperature ratio $\zeta_{t,30-15}$ at ME30 in Fig. 7.7e to Fig. 7.7h, the variation by means of tensor perturbations is small. Therefore, we can conclude that the effect of eigenvalue perturbation on the prediction of the total temperature is moderate.

ME21 enables us to analyze the flow directly behind the rotor. Unfortunately, radial measurement data are not available for $\dot{m}_{\text{corr}} = 14.78\,\text{kg/s}$ at ME21, that is why Fig. 7.9b

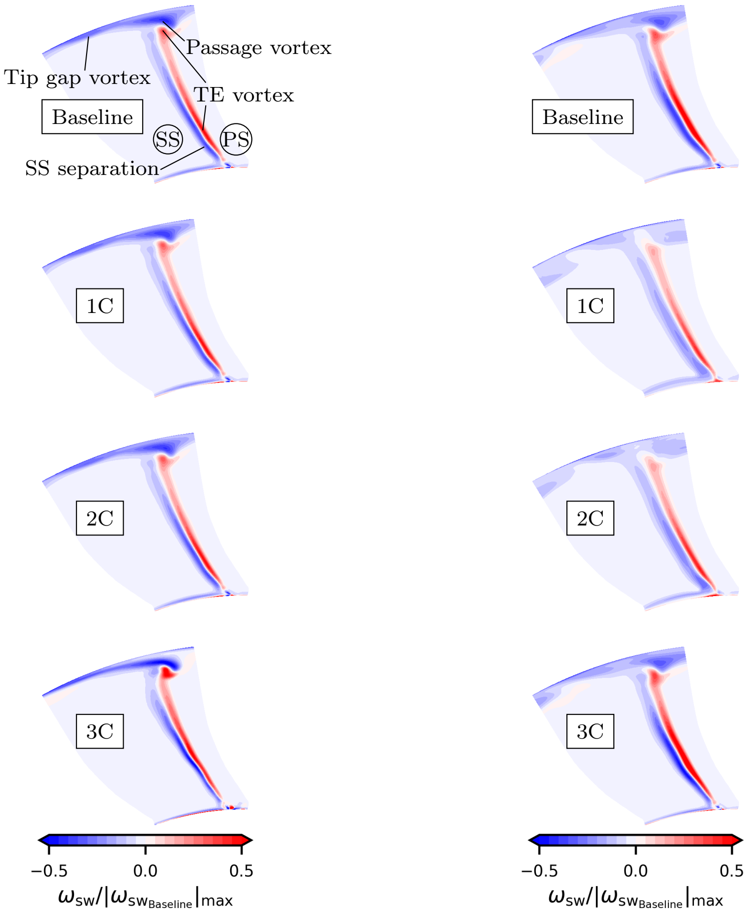

(a) $\dot{m}_{\mathrm{corr}} = 16.00$ kg/s (b) $\dot{m}_{\mathrm{corr}} = 14.78$ kg/s

Figure 7.10.: Comparison of secondary flow structures indicated by the streamwise vorticity at ME21 for two different operating points. The local streamwise vorticity was normalized using the maximum absolute value of the streamwise vorticity occurring at ME21 in the baseline simulation.

and Fig. 7.9d show experimental measurements at $\dot{m}_{\mathrm{corr}} = 14.66\,\mathrm{kg/s}$. Although the simulation results align well with the experimentally measured flow angle at the design speed in Fig. 7.9c, the total pressure ratio in Fig. 7.9a is overpredicted above 60% span by the RANS baseline simulation, due to the representation of the rotor tip vortex. Between 10% and 60% span the total pressure profiles are in accordance with the measurements. Nevertheless, the transitional DDES proves the existence of the total pressure increase due to the representation of the tip-leakage flow (see discussion on that by Möller et al. [114]). RANS also overpredicts the pressure increase in the very near hub region. Except for the tip and hub region at $\dot{m}_{\mathrm{corr}} = 14.78\,\mathrm{kg/s}$, perturbing the Reynolds stress tensor towards 1C and 2C lead to a minor decrease of the total pressure ratio, while the flow angle is rather unaffected by this modification. Keeping in mind that the relative perturbation magnitude for 1C and 2C is significantly higher for the lower mass flow rate compared to the design point, we can conclude that the tip-leakage flow and the separation in the hub region (similarly to ME30) is prone to changes in the Reynolds stress tensor's anisotropy. The 3C perturbation leads to a pressure increase at the design mass flow rate in Fig. 7.9a. As opposed to this, the usage of $\Delta_B = 0.09$ at $\dot{m}_{\mathrm{corr}} = 14.78\,\mathrm{kg/s}$ results

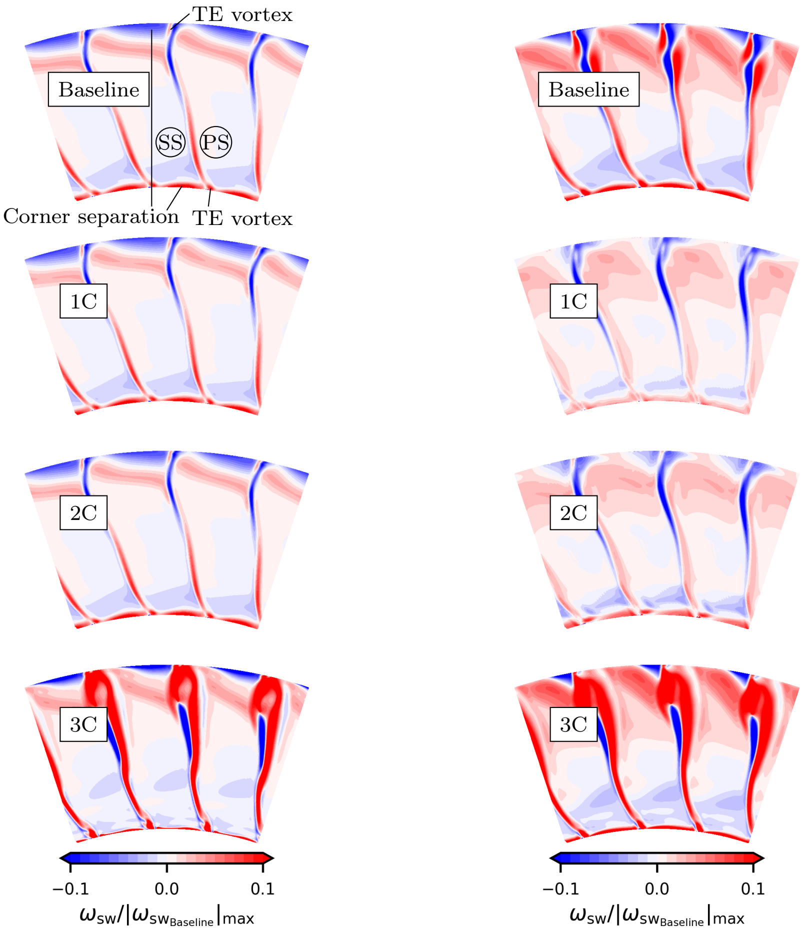

(a) $\dot{m}_{\mathrm{corr}} = 16.00$ kg/s

(b) $\dot{m}_{\mathrm{corr}} = 14.78$ kg/s

Figure 7.11.: Comparison of secondary flow structures indicated by the streamwise vorticity at ME30 for two different operating points. The local streamwise vorticity was normalized using the maximum absolute value of the streamwise vorticity occurring at ME30 in the baseline simulation.

in almost unaffected total pressure ratio for 3C perturbation in Fig. 7.9c. Moreover, all considered eigenspace perturbations have moderate effect on the flow angle. This seems plausible as the turbulence modeling is not expected to have significant impact on the flow turning.

The streamwise vorticity

$$\omega_{\mathrm{sw}} = \frac{U_i \epsilon_{ijk} \frac{\partial U_k}{\partial x_j}}{\sqrt{U_q U_q}} \tag{7.11}$$

enables an analysis of the secondary flow structures in the reference planes ME21 and ME30. The vortex system behind the rotor is mainly dominated by a strong passage vortex on the SS, which originates from the leading edge (LE) (see Fig. 7.10). The flow at the tip gap of the rotor travels from PS to SS, merging with the passage vortex. The overpredicted total pressure ratio at 90% span, as discussed above (see Fig. 7.9), can be attributed to this secondary flow structure. Additionally, there are two vortices coming from the PS near the trailing edge (TE). The rotor's SS separation covers large parts of the entire span (cf. Fig. 7.12a), causing increased streamwise vorticity in all considered

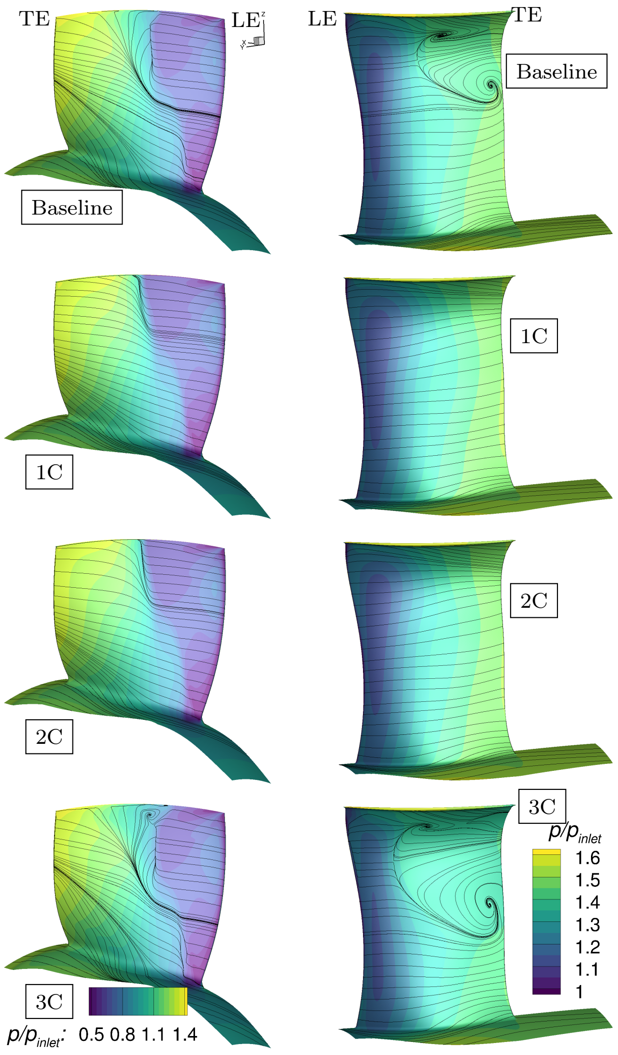

(a) Rotor (b) Stator

Figure 7.12.: The effect of perturbing the eigenspace of the Reynolds Stress tensor on static surface pressure and surface streamtraces on the hub and SS at $\dot{m}_{\text{corr}} = 14.78$ kg/s.

simulations. On the one hand, the 1C and 2C simulations only have limited effect on the vortex system at the design operation point. This is in accordance with the observations in Fig. 7.9, keeping in mind that the perturbation magnitude is rather small. On the other hand, 1C and 2C perturbations lead to mitigated secondary flows with the SS separation reduced in radial direction at $\dot{m}_{\text{corr}} = 14.78\,\text{kg/s}$ (see Fig. 7.10b and Fig. 7.12a). In contrast to the 1C and 2C perturbations, the perturbation towards the isotropic limiting state does not alter the secondary flows at the near stall operation point. However, 3C perturbation leads to the formation of a separated vortex structure from the tip wall and increases the vorticity formed by the TE vortices at $\dot{m}_{\text{corr}} = 16.00\,\text{kg/s}$.

Figure 7.11 presents the secondary flow at ME30. The flow behind the stator reveals the existence of two corner separations at hub and tip, which can be also identified in Fig. 7.12b. Furthermore, the flow past the TE causes the formation of vortices at hub and tip. Throttling of the compressor leads to a massive increase of streamwise vorticity (e.g. see baseline simulation in Fig. 7.11b). Moreover, additional concentrated

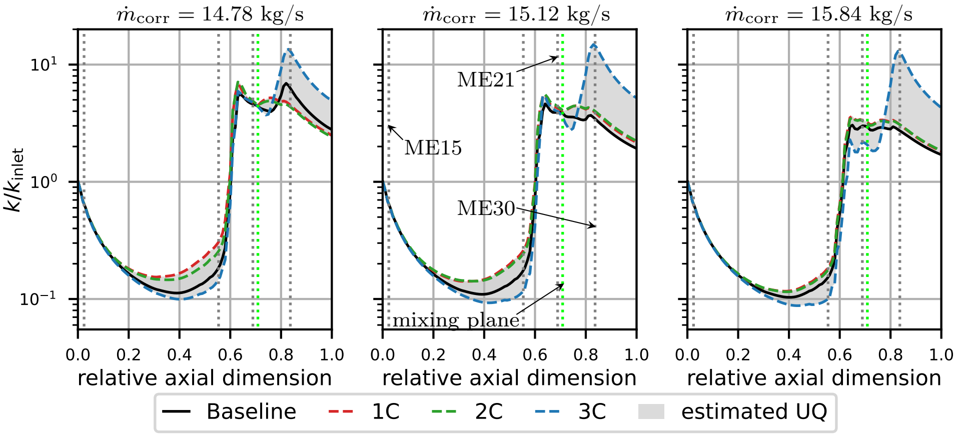

(a) Circumferentially and radially area-averaged turbulent kinetic energy over axial dimension of the compressor

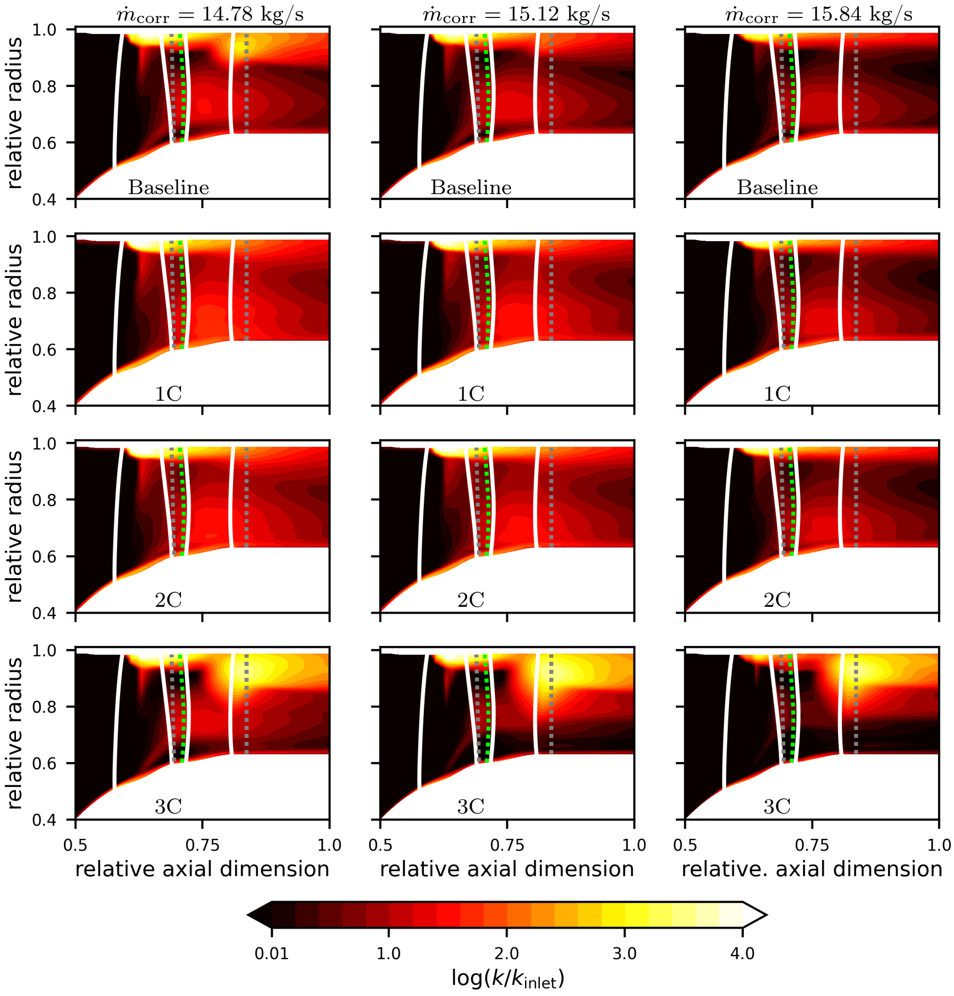

(b) Circumferentially area-averaged 2D turbulent kinetic energy distribution in the core part of the compressor (zoom)

Figure 7.13.: Comparison of turbulent kinetic energy distribution throughout the compressor for three different operating points. Reference planes are shown by dotted gray lines, while the mixing plane interface between rotor and stator is marked in light green. White lines in (b) indicate the contours of rotor and stator.

secondary flow structures occur, if the simulation is close the achievable numerical stall limit (e.g. baseline and 3C). These additional structures can be also identified on the SS in Fig. 7.12b. The eigenvalue perturbations of the Reynolds stress tensor generally follow similar trends as already described for ME21. To emphasize, one clearly sees that 3C perturbation underestimates the total pressure ratio in Fig. 7.7 and Fig. 7.8 above 40% span by producing massive vortex structures at ME30.

7.4.4. Effect of anisotropy on turbulent kinetic energy level

The reason for the observed behavior is the impact of the anisotropy on the actual level of turbulence. The resulting distribution of the turbulent kinetic energy is presented in Fig. 7.13 for three operating points $\dot{m}_{\mathrm{corr}} = 14.78\,\mathrm{kg/s}$, $\dot{m}_{\mathrm{corr}} = 15.12\,\mathrm{kg/s}$ and $\dot{m}_{\mathrm{corr}} = 15.84\,\mathrm{kg/s}$. Following the theoretically derived relationship between the production of turbulent kinetic energy and the componentiality of turbulence [56, 97][5], the turbulence production will be minimized by approaching the isotropic limit and maximized for the 1C state[6]. This can be observed in the upstream section before the rotor (relative axial dimension $\lessapprox 0.58$) in Fig. 7.13a, as the turbulence production is altered accordingly in the boundary layers at hub and tip. The circumferentially and radially area-averaged distribution of k is mostly unaffected by the eigenspace perturbation in the rotor section,

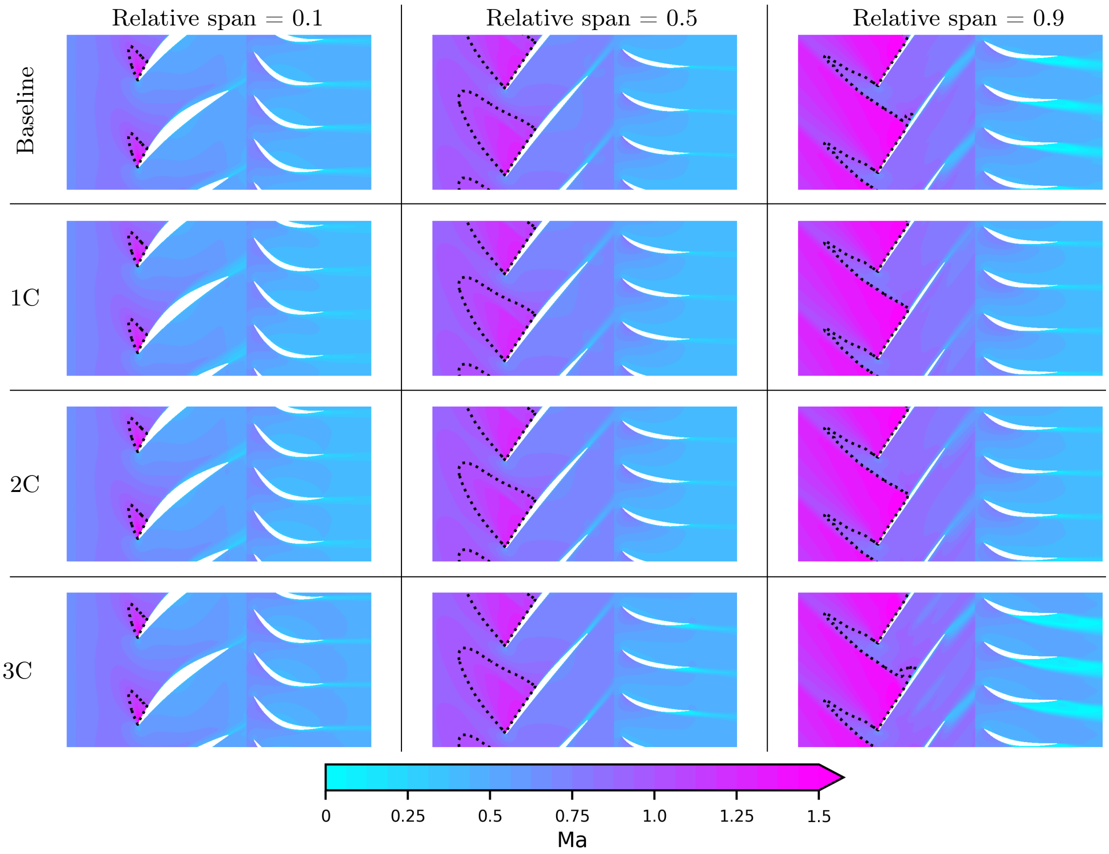

Figure 7.14.: Analysis of shock position and wake width prediction by illustrating the relative Mach number distribution for three constant relative span levels at $\dot{m}_{\mathrm{corr}} = 14.78\,\mathrm{kg/s}$. Dashed lines indicate $\mathrm{Ma} = 1$.

---

[5] Details can be found in Appendix B.

[6] This is only valid if the velocity gradients are identical (cf. Eq. (7.7) and [97]).

as the increase of turbulence is mainly attributed to the superposition of occurring flow phenomena such as the formation of tip-leakage flow. The effect of a modified componentiality of the Reynolds stress tensor can be observed in the stator section again, where 3C turbulence creates large separation zones (cf. Fig. 7.12b) leading to increased turbulent kinetic energy. Compared with the baseline simulation, the one- and two-component perturbation tends to decrease the turbulence level close to ME30 due to the suppression of separation zones at the near stall operation point (cf. Fig. 7.12b).

7.4.5. Shock-boundary layer interaction

Additionally, we analyze the Mach number distributions across several constant radial planes. Figure 7.14, presenting the Mach number for $\dot{m}_{\mathrm{corr}} = 14.78\,\mathrm{kg/s}$, confirms the previously described observations. Both the baseline and 3C simulation lead to massive separation in the stator tip region (relative span=0.9) (cf. Fig. 7.12b), while the one- and two-component perturbations result in sharper wakes with less losses. The region covering transient flow increases from hub to tip, which can be also seen in Fig. 7.12a. The position of the shock in the passage of the rotor section is unaffected, whereas the shock's interaction with the boundary layer shows noticeable effects due to the eigenspace perturbation. Unfortunately, there is no measurement data available to judge the shock location predicted by RANS. That is the reason, why we included the numerical results based on the DDES at least for the design point in Fig. 7.15, showing the isentropic Mach

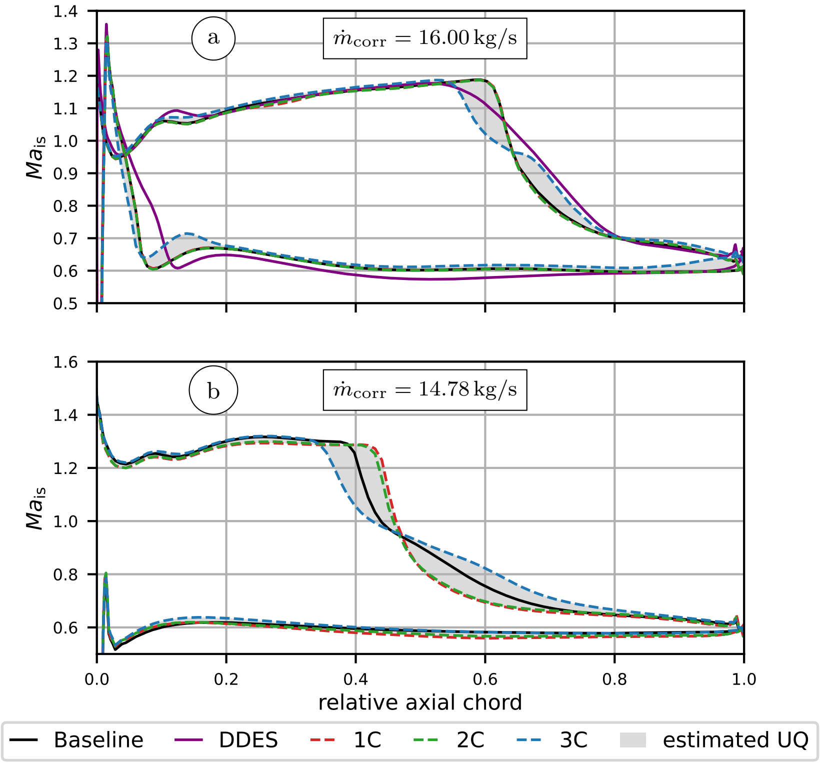

Figure 7.15.: Uncertainty estimates for the isentropic Mach number distribution at 90% span of the rotor for two different operating points.

number

$$\mathrm{Ma}_{\mathrm{is}} = \sqrt{\left(\left(\frac{p_{\mathrm{t},21}}{p}\right)^{\frac{\gamma-1}{\gamma}} - 1\right)\frac{2}{\gamma-1}} \tag{7.12}$$

at 90% of the rotor span. Comparing the baseline RANS with the high-fidelity DDES simulation reveals some differences in shock-location onset and steepness of the SS pressure increase. Nevertheless, the estimated uncertainty based on the EPF almost envelopes the DDES predicted drop in $\mathrm{Ma}_{\mathrm{is}}$. In accordance to the observations by Emory et al. [33], the isotropic perturbation lead to an earlier shock, while the 1C and 2C perturbations postpone the shock-location. This becomes especially noticeable in off-design points (see Fig. 7.15b), when the relative perturbation magnitude increases for the 1C and 2C eigenvalue perturbations.

7.4.6. Capabilities and limitations of the EPF

The aim of the EPF is to quantify the epistemic uncertainties of LEVMs. Indeed, a turbomachinery designer is interested in attributing the effect of the turbulence model's uncertainty on certain design QoI. In the current work, this is achieved by perturbing the Reynolds stress tensor towards three limiting states of turbulence, propagating these states and observing the influence on QoI. However, the relation between the 1C-, 2C- and 3C limiting state of the Reynolds stress tensor and some QoI is anything but linear. Consequently, the EPF seeks to estimate the uncertainty intervals rather than create extreme states for some QoI. Furthermore, we need to discuss the obvious judgment of the presented uncertainty intervals with respect to certain high-fidelity or measurement data, which is often done. There is no guarantee that the simulation results, obtained by the EPF, overlap with reference data. The main reason is that the eigenvalue perturbation is only able to account for epistemic uncertainties limited to the turbulence model's representation of the turbulent state. Nevertheless, the LEVM's assumption that the Reynolds stress and strain-rate tensor have identical eigendirections (cf. Eq. (7.1)) is not necessarily valid. Thus, the incorporation of physically constrained eigenvector perturbations, as done in previous work [97], aiming to account for any misalignment with the eigenspace of the strain-rate tensor, is missing in the current analysis. Furthermore, other sources of uncertainties related to RANS simulations are not considered by the Reynolds stress tensor perturbations. In the current configuration of the TUDa-GLR-OpenStage compressor these might include the neglect of certain components (e.g. cavity), the inaccurate representation of the geometry (such as tip gap and fillet radii), the assumption of steady-state flow conditions, the application of the mixing plane approach at rotor-stator interface, the use of 32 instead of 29 stator blades and, last but not least, the choice of the boundary conditions. Although we compare the RANS data with transitional DDES based on the research of Möller et al. [114] in order to mitigate geometrical uncertainties, there are still notable disparities in the simulation setups. These include variances in the approach to steady versus unsteady simulations, different numerical schemes and the application of multiple turbulence modeling modifications. Consequently, these simulations are not fully comparable. Therefore, it cannot be expected that the estimated uncertainties based on the EPF envelope the high-fidelity DDES. This is yet another illustration of the EPF's potential, as well as its limitations. Additionally, the achievable uncertainty intervals on QoI such as the total pressure ratio or the overall isentropic efficiency of the compressor, are mainly affected by the prescribed amount of relative perturbation Δ_B. In the current study, we seek for worst case scenarios attributed to the maximum perturbation of the Reynolds stresses while still assuring convergence of the simulations. For this very reason, the presented uncertainties show the general trends of each individual eigenvalue perturbation. In a real-world application, a designer would probably not try to perturb as much as possible across the entire speedline. Based on expert knowledge or machine learning strategies, a sensible strategy for future applications may be the application of non-uniform, more moderate eigenspace perturbations, both spatially in the computational domain and across multiple operating points.

7.5. Conclusion

We have presented the first multi-row turbomachinery application of the Reynolds stress tensor EPF to assess turbulence modeling uncertainty for the design speedline of the transonic TUDa-GLR-OpenStage compressor. Through comparison with measurement and transitional DDES data, we validate the ability of the EPF to quantify the epistemic uncertainties, showcasing its potential for complex turbomachinery simulations. In pursuit of worst case scenarios to ascertain the most conservative estimation of inherent turbulence modeling uncertainties, it is imperative to apply non-uniform relative perturbation magnitudes across the various operating points of the compressor and across different states of turbulence componentiality (1C, 2C and 3C). The flow characteristics of the compressor allowed greater eigenvalue perturbation for 1C and 2C close to the numerical stall limit, whereas the perturbation towards the isotropic state could be increased near the design point.

Our current investigation underscores the sensitivity of determining the numerical stall limit of the compressor to the anisotropy of the Reynolds stress tensor, presenting a significant enhancement in accordance with the experimental stall limit compared to the baseline LEVM simulation. Consequently, orthotropic eddy viscosity models have the potential to provide stability improvements similar to conventional turbulence modeling enhancements. We postulate that this phenomenon can be attributed to the influence of turbulence componentiality on the turbulence production. The evaluated radial profiles of total pressure also demonstrate that corner separations, and to some extent, the tip-leakage flow, are susceptible to changes in the shape of the Reynolds stress tensor ellipsoid. Although the baseline RANS model accurately captures the flow physics in the midsection, regions near the hub and tip consistently reveal deviations from measurements and pose challenges to designers. Therefore, the shown results based on the eigenvalue perturbation might be of great interest for turbomachinery designers and the turbulence modeling community. Finally, it was found that introducing substantial levels of anisotropy to the Reynolds stress tensor influences the dynamics of shock-boundary layer interaction, specifically affecting the location of the shock. The emphasized impacts of physically constrained perturbations to the shape of the Reynolds stress tensor offer new insights for future turbulence modeling approaches. The aim of these insights is to eliminate the need for non-physically constrained adjustments (often referred to as *tweaking*) to the model in order to achieve a more accurate representation of compressor flow physics.

Last but not least, the current research paper, contributes to the evaluation of the epistemic turbulence modeling uncertainties for multi-row turbomachinery configurations, with a specific focus on the TUDa compressor. In future research, the inclusion of physically constrained eigenvector perturbations could complete the view of the true model-form uncertainty in the representation of the Reynolds stress tensor. As we have made the most conservative estimates, we believe that the next plausible step is to incorporate local perturbations in areas where LEVMs tend to fail while reducing the perturbation where the models are known to perform well.

8. Discussion

This research centered around the quantification of epistemic model-form uncertainty for RANS turbulence closure models. After the term *uncertainty* in CFD has been clarified in Chapter 2, the origin of uncertainty in RANS turbulence modeling was introduced in Chapter 3. Following the derived need to account for the model-form uncertainty of turbulence models, a framework incorporating physics-based perturbations to the eigenspace of the Reynolds stress tensor was presented. This EPF has been implemented in DLR's turbomachinery research and design solver TRACE that is developed and utilized in strong cooperation with MTU Aero Engines AG. Thus, this integration adheres to high quality standards with respect to testing and validation, ensuring consistent and reliable results. The implementation of the EPF into the existing solver required several adjustments with respect to appropriate user control, correct treatment of boundary conditions and adequate schedule of the perturbations in the iteration of the steady RANS approach. This thesis presents the review of the implementation of the EPF based on its conceptual idea and subsequent adaptations of the methodology. Besides the successful application of random forests to predict the expected deviations in Reynolds stress anisotropy in Chapter 4 and the application of eigenspace perturbation for a multi-row compressor application in Chapter 7, this thesis exemplifies the necessary V&V in Chapter 5 and Chapter 6. Although, the EPF has been extensively applied in academia and industry-partnered research, the conducted V&V revealed that there are some shortcomings and limitations that have been addressed in this research. Hereby, the framework has been improved to produce physics-constrained and consistent results for its future applications. The application of the framework to the turbulent boundary layer flow in a 1D channel, the separating flow in a converging-diverging channel, the flow around the NACA 4412 airfoil and finally the flow of the TUDa-GLR-OpenStage compressor served to validate the current implementation. The obtained results have been presented in the form of a cumulative dissertation, consisting of previously published peer-reviewed research.

8.1. Methodological coherence and development across publications

One of the key challenges of this dissertation lies in addressing the methodological coherence across the four underlying publication. While all these studies are based on a shared methodology, which is the eigenspace perturbation of the Reynolds stress tensor, each publication incorporates specific modifications, extensions and applications tailored to its research questions and contextual requirements. Although these adaptations were necessary to increase the scientific and applied insights of each study, it might give the impression that the methodological implementation of the EPF and its application exhibit a certain lack of coherence.

Consequently, the following section provides an analysis of the methodological commonalities, difference and the rationale behind each decision made. This discussion aims to demonstrate how the shared EPF was adapted and applied in every publication and still aligns with the overall research objectives of this thesis.

The simulation results presented in Chapter 4 are based on the implementation of the EPF as outlined by Iaccarino et al. [66] and Mishra et al. [107]. Key differences between this initial implementation and the final version of the framework in TRACE are the usage of a moderation factor (see Eq. (4.11)) for addressing the convergence issue of the perturbed simulations and the permutation of first and third eigenvector, which at that time reflected the prevailing approach in the literature. The main purpose of this research was to explore a data-driven, local perturbation of eigenvalues on the basis of the existing and validated implementation of the EPF[1].

However, as issues in application of the initially formulated EPF persisted, an initiated verification of the implementation laid the foundation for subsequent investigations, presented in Chapter 5 and Chapter 6, following a progressive research structure. Initially, Chapter 5 identifies the lack of self-consistency of the earlier implementation, which relied on the moderation factor by Mishra et al. [107], and suggests a novel approach to converged simulation results. Building on this, Chapter 6 derives a new constraint for the eigenvector perturbation replacing the eigenvector permutation by Iaccarino et al. [66]. These two formulations supersede the initial implementation as applied in Chapter 4 and only rely on uniform perturbation in the entire computational domain. This change in approach was motivated by the findings of the research in Chapter 4, which demonstrated the challenges in training a generalizing machine learning model to predict inaccuracies in the Reynolds stress anisotropy combined with the fact, that even a perfect model prediction still suffers from the limitations of the EPF (see detailed discussion in the following section). Additionally, it became evident that the application of non-local perturbations can be insightful for the turbulence modeling community without necessitating extensive training of machine learning models in advance (as will be also discussed in the following summarizing Section 8.2).

In the context of assessing the EPF regarding its capabilities for turbomachinery applications, the study of the multi-row compressor test case in Chapter 7 mainly intends to provide practical guidance and analyze the resulting uncertainties. While this research builds upon the implementation developed in Chapter 5 and Chapter 6, it does not consider distinct perturbation of eigenvectors. This decision was partly due to the need to first establish and present an approach to handle eigenvalue perturbations across the entire speedline of a compressor, which, per se, required substantial effort and focus. In addition, retrospective analysis of Chapter 6 revealed that excluding eigenvector perturbations would have led to nearly identical uncertainty intervals for the converging-diverging test case (see also study in Section 3.5.2). This observation underscores the potential for meaningful insights, although relying solely on eigenvalue perturbations, as further elaborated in the subsequent section.

8.2. Summary of the research findings

The novel contributions offered by this thesis are listed in Section 1.4.1. While these contributions are relevant from a theoretical and researching point of view, this section aims to highlight important findings for practical application purposes and to provide guidance for CFD practitioners and turbomachinery designers, willing to use the EPF in the future.

---

[1] At the time, validation referred to the agreement of the results between the implementation in TRACE and those reported in the literature for identical test cases.

8.2.1. Additional six perturbed simulations required and effects on attainable solution space for QoI

Due to the modification to the EPF, presented in this thesis, it requires six[2] simulations in addition to the baseline RANS simulation featuring an unperturbed turbulence model to assess the uncertainty of the turbulence model. Three of them result from targeting the eigenvalues at the corners of the barycentric triangle associated with the turbulence componentiality (1C, 2C, 3C). Each of them can be supplemented by perturbing the orientation of the principal axes of the Reynolds stress tensor ellipsoid by rotating the eigenvectors, resulting in three additional simulations. While the eigenvalue perturbation is controlled via a relative perturbation $\Delta_B \in [0,1]$, the angle for the eigenvector rotation was found to be $\alpha \in [0,\pi/4]$ (see derivation of this limit in Chapter 6).

Aligning with the initially postulated idea of aiming for enveloping uncertainty bounds by creating limiting states of the Reynolds stress tensor, the user of the EPF is encouraged to perturb the eigenspace to these limiting states, $\Delta_B = 1$ and $\alpha = \pi/4$. This procedure is driven by the plausible observation that the more the Reynolds stress tensor is altered from its native form (which is restricted by the Boussinesq approximation in LEVMs), the more the obtained result for a certain QoI changes (see Section 3.5.2). However, the relationship between any perturbation to the Reynolds stress tensor's eigenspace and the solution of the RANS equations is strongly non-linear. Consequently, it cannot be ensured that a certain output QoI changes proportionally to these perturbation. In other words, choosing the perturbations of eigenvalues and/or eigenvectors as strong as possible, does not necessarily lead to upper or lower limits for QoI. Nonetheless, it is a good approximation that could also be observed in this thesis and by other researchers, such as Emory [36], Gorlé et al. [56] and Zeng et al. [173].

Moreover, it is just a sophisticated guess that the 1C, 2C or 3C state of the Reynolds tress tensor, really results in an extreme state for certain QoI. Similarly, although the derivations for rotating the eigenvector matrix of the Reynolds stress tensor around the second eigenvector are based on physical observations in this thesis, the resulting eigenvector matrix is only one out of an infinite number of possible realizations, represented by the specific rotation axis (axes) and the respective rotation angle(s) (see Mishra and Iaccarino [106] for details). The following ramifications are threefold. Firstly, analyzing the results of the EPF can and will show areas for some QoI, where the unperturbed baseline RANS simulation forms the bound. In order to accurately assess the sensitivity of the RANS result with respect to the eigenspace of the Reynolds stress tensor, an infinite set (or at least a significant number) of simulations, representing any location inside the barycentric triangle and any possible rotation of eigenvectors, would be required. Additionally, it might be also not suffice to assume that all eigenvalues and eigenvectors have to be perturbed to identical directions with identical perturbation strength to obtain the most conservative estimations for QoI. Nevertheless, as this is not feasible, especially for industrial purposes, this thesis demonstrates by example the provision of reasonable intervals for certain QoI based on the proposed EPF compared with excessive sampling of the possible solution space of the anisotropy tensor in Section 3.5.2. Consequently, targeting for the three corners of the barycentric triangle represents an appropriate approach leading to sufficient information on the uncertainty. Secondly, the resulting bounds of the EPF do not necessarily overlap with reference data, based on high-fidelity simulations or experimental measurements. This can be concluded directly from the fundamentals of the RANS equations, as certain QoI is not necessarily a linear combination of the limiting states of turbulence. Moreover, there are always other uncertainties and errors involved, which are not addressed by the EPF, potentially preventing the coverage of reference data. Thirdly, although the true eigenvalues of the Reynolds stress tensor are a convex combination of the eigenvalues at these limiting states [170] and the true eigenvectors can also be determined by transforming the strain-rate tensor's eigenbasis (as shown in e.g. Matha and Morsbach [95]), the EPF is not designed to represent the true (correct) eigenspace. Thus, the EPF does not per se prohibit states of the Reynolds stress tensor, which contradict real-world observations, such as 3C turbulence in boundary layers.

---

[2] The set of additional simulations reduces to five if $\Delta_B = 1$ for the 3C (isotropic) perturbation due to the degeneration of the Reynolds stress tensor into a sphere making a rotation of its eigenvectors unnecessary. However, this perturbation is hardly possible due to upcoming convergence issues, discussed in the following.

Given that the perturbation of the Reynolds stress tensor within the limits of the eigenspace does not inherently guarantee to obtain the limiting state for QoI and a frequent complete sampling from the physically permissible space of the Reynolds stress tensor is unfeasible, this thesis recommends incorporating the unperturbed RANS results to mark the final model-form uncertainty. This strategy balances the required computational resources and the practical necessity of assessing uncertainty comprehensively while making reasonable assumptions within the EPF[3].

8.2.2. Convergence issues and their consequences

As discussed in detail in Chapter 4 to Chapter 7, the extreme states of the Reynolds stress tensor, are often not feasible in practical simulations. Upcoming numerical convergence issues, when altering the shape and orientation of the Reynolds stress tensor, prevent the attainment of the promising special states using $\Delta_B = 1$ and/or $\alpha = \pi/4$. Consequently, the strategy in this thesis was to always find the largest possible perturbations (eigenvalue and/or eigenvector) that still result in stable steady-state solutions (referring to not applying data-driven eigenvalue perturbations as in Chapter 4). Following this approach, the intervals controlling the eigenvalue ($\Delta_B \in [0, 1]$) and eigenvector ($\alpha \in [0, \pi/4]$) perturbations have to be discretized with a reasonable number of sampling points and applied iteratively in reversed order in CFD simulations. Subsequently, this procedure requires the appropriate definition of convergence criteria. In the current thesis, integral values at interfaces, such as outlet pressure or blade forces, as well as local surface quantities, such as pressure and friction coefficients, and locally probed mean flow quantities, such as mean velocity, have been used to decide on appropriate convergence. Consequently, the results obtained in this thesis can be considered as worst case yet converged results. Nevertheless, there is no unique general metric to assess convergence in this context, and it is in the user's responsibility to conduct this analysis appropriately. Otherwise, the obtained results derived from the EPF are considered to be futile. Indeed, there are a couple of publications that have applied the EPF for DUU task [108, 51, 87]. These researchers have had to use a great set of simulations in order to find the attainable perturbation for each design, applied only minimum amount of perturbations (such they can be sure that all perturbed simulations for every design converge) or managed to deal with an excessive number of non-converged runs (if no iterative procedure to find attainable perturbation parameters is conducted). Contrary to the approach of finding the largest possible perturbations, turbomachinery designers willing to use the EPF to add credibility to their RANS simulations could already benefit from adding at least *some* amount of perturbation to get an indication regarding the sensitivity of the analyzed QoI. Additionally, incorporating non-local perturbations (as already mentioned in the conclusion section of Chapter 7) may also be beneficial for DUU tasks. The latter is discussed in the following section with a focus on the turbulence modeling community.

---

[3] The assumptions in the EPF are referred to as *best guesses you can make* without usage of additional resources or data-informed enhancements.

8.2.3. Local vs. non-local perturbations and derived insights for the turbulence modeling community

In general, the EPF is motivated by the expectation that an accurate representation of the Reynolds stress tensor inevitably leads to accurate predictions for mean flow field quantities[4] and concurrently the prevailing inaccurate modeling assumptions, such as the linear eddy viscosity hypothesis, leading to inherent flaws for certain flow conditions. But these modeling assumptions are not uniformly violated across the entire flow field, instead they vary in extent and magnitude. To address these local inaccuracies, researchers have developed methods that introduce local perturbations through marker functions [33, 34, 54, 56]. Such markers are often limited to the considered data set and lack universality, unless they are directly measurable characteristics, such as the deviation from parallel shear flow. Furthermore, designing these markers or sensors requires profound knowledge of the turbulence model's flaws, which might also be limited to a specific flow phenomenon of the considered application. That is the reason, why data-driven machine learning approaches have emerged as effective alternative using existing high-fidelity data to improve the prediction of model-form uncertainty by predicting regions suffering from potential turbulence model deficits [30, 61, 32].

In this thesis, random forest regression was applied to introduce and moderate perturbations to the Reynolds stress tensor in areas, where a discrepancy in its anisotropy (represented by the eigenvalues) was expected. The application of local perturbations was found to significantly reduce the estimated uncertainty interval, resulting in less conservative estimations by the framework. As highlighted in Section 1.4.1, Chapter 4 adopts the approach of Heyse et al. [61], extends the number of test cases, completes the methodology by considering eigenvector perturbation and adds extensive model validation. Nevertheless, the study also revealed the challenge of training a universal machine learning model to predict the discrepancy in representing the Reynolds stress tensor anisotropy. This difficulty arises mainly due to the vast amount of well-resolved data required, encompassing different geometries, flow phenomena and operation conditions. Given the inherent limitation in data availability, an extrapolation metric was evaluated to estimate the *a priori* confidence of the prediction. Furthermore, there is no guarantee that a perfect prediction for the deviation of the true anisotropy tensor would result in an overlap with QoI of reference data, following the identical line of argumentation as in Section 8.2.1 referring to the non-linearity of the system.

However, although the turbulence modeling assumptions are not fully satisfied everywhere in the computational domains featuring different flow physics, the results obtained for QoI are often predicted sufficiently accurately for practical CFD purposes. Otherwise, turbulence models would not have been utilized for such a long period, contributing significantly to advancements in turbomachinery designs [25]. There is always the possibility of obtaining accurate results using RANS turbulence models, especially when remembering the distinction between error and uncertainty (see Chapter 2) - where uncertainty represents a potential inaccuracy. A prominent example is the error/uncertainty cancellation often cited by engineers and CFD practitioners.

---

[4] In practise, *correct* Reynolds stresses may have to be specially treated in the RANS approach, because of the potential ill-conditioning of the equations [167, 13].

As a result of the described experiences, observations and inferred analyses, this thesis suggests to apply the methodology using non-local perturbations in order to enable the turbulence modeling community to identify areas in the flow that are most sensitive to the eigenspace of the Reynolds stress tensor, coinciding with the chosen approach for the most conservative UQ in this thesis. For example, the simulation results in the present dissertation show the greatest sensitivity to Reynolds stress tensor perturbation in the separation and reattachment region of the converging-diverging channel, or in areas close to the hub and tip contour and in the region of shock-boundary layer interaction for the TUDa compressor. An illustrative but simple example is the turbulent channel flow in Section 5.2.4. When comparing RANS and DNS data, the discrepancy with respect to the anisotropy of the Reynolds stress becomes most noticeable close to the wall. However, almost any baseline RANS turbulence model is able to predict the velocity profile accurately. When applying uniform perturbations by the EPF, the velocity profiles are not notably affected in the region close to the wall. Greater sensitivity with respect to the eigenspace can be observed in the outer part of the boundary layer[5]. Consequently, the key takeaway for the turbulence modeling community, referring to the example of the turbulent boundary layer would be, if there would be some differences between RANS results and high-fidelity data, anisotropic Reynolds stress tensor modeling could modify the agreement just in this outer part of the velocity profile.

8.2.4. Eigenspace perturbation and its effect on the turbulence production

This research focused on the appropriate perturbation of the orientation of the Reynolds stress tensor ellipsoid, referring to the perturbation of the eigenvectors, motivated by two key considerations. On the one hand, the Boussinesq approximation postulates identical eigendirections for the strain-rate tensor and the Reynolds stress tensor, which was proven to be incorrect for many cases. On the other hand, the perturbation of the eigenvectors enables to indirectly modify the turbulence level once the eigenvalues have already been perturbed. This thesis proposes a perturbation of the eigenvectors, relying on a tensor rotation around the second eigenvector. Based on derivations for 1D boundary layer flow, it was concluded that the rotation angle should be between 0 and $\pi/4$ in order to ensure realizable dynamics resulting from the perturbed Reynolds stress tensor. Since wall-bounded flows are present in any relevant turbomachinery configuration, the derivation remains valid under the chosen strategy of applying uniform perturbations. The rotation approach is mathematically equivalent to the eigenvector perturbation approach by Iaccarino et al. [66] and setting the angle to $\pi/2$, which was identified to result in negative eddy viscosity, countergradient transport of momentum and negative turbulence production. The eigenvector rotation in combination with the eigenvalue perturbation impact the turbulence level due to the incorporation of perturbed Reynolds stresses in the turbulence production term (cf. details in Appendix B).

Although the actual values of the turbulence production term vary case by case, there are two states of turbulence that should be highlighted, as they contribute massively to the overall uncertainty estimation. While 1C perturbations (without altering the eigenvector alignments) increase the turbulence production term, 3C perturbations (with and without eigenvector perturbation) tend to create the smallest turbulence production term under the challenge of achieving converged simulation results, as mentioned in Section 8.2.2. These simulations establish the envelope for QoI most commonly, highlighting the importance of turbulence level adjustments for the prediction of the uncertainty interval. This is consistent with other studies that have directly introduced a discrepancy term for the turbulent kinetic energy in Eq. (3.24) [19].

---

[5] The predicted uncertainty is acknowledged to be exaggerated from a turbulence modeling and engineering point of view, as the baseline RANS model is capable of matching the reference data quite well.

Hence, there is a potential for reducing the set of additional simulations to obtain similar or at least sufficient information regarding the potential turbulence model uncertainty. Due to the strong impact of the perturbation on the turbulence production term and the actual level of turbulence, an enveloping model for QoI could, in principle, be reduced to the 1C and 3C simulations in most of the cases, also making any perturbation of eigenvectors obsolete. This strategy might seem contradictory to the objective of targeting for extreme states of the Reynolds stress tensor. Especially as highlighted by Mishra and Iaccarino [106], who derived that only the combination of eigenvalue and eigenvector perturbation is able to really extend the isotropic eddy viscosity model to an orthotropic and anisotropic one (see Appendix C). However, setting aside these theoretical considerations and focusing on the actual impact of the perturbations on the solutions of the RANS equations, this reduction in the required number of simulations could facilitate more frequent usage of the EPF in simulation-based optimization and certification tasks.

9. Conclusions and outlook

The EPF is currently the only published framework for addressing physics-constrained uncertainty estimation of the Reynolds stress tensor representation in RANS turbulence models. This underscores its importance for building up credibility in CFD simulations. However, to explore the future potential of this framework it is imperative to conclude several key aspects. Drawing on the conducted research and outlined observations, this chapter aims to provide recommendations regarding the usability of the EPF, as well as to derive conclusions for its future applications and related research. Additionally, this sections seeks to emphasize the potential benefits and limitations of the methodology, aligning with the research objectives in Section 1.2. Many of these considerations are directly connected to the highlighted novel contributions of this thesis mentioned in Section 1.4.1 and the summarized research findings presented in Section 8.2.

9.1. Conclusions

First and foremost, considering all the examined and highlighted aspects of this thesis, the application of the eigenspace perturbations to the Reynolds stress tensor should be regarded as an *uncertainty estimation* approach rather than an *uncertainty quantification* methodology, aligning with considerations by others researchers, such as Emory [36] and Xiao et al. [170]. Since the EPF is primarily motivated and explicitly designed to introduce physics-constrained perturbations to the Reynolds stress tensor, this research has contributed significantly to preserving its physical foundations while integrating the framework into the flow solver TRACE. The theoretical analysis and conceptual review of the implementation was successfully completed. The considerations, analyses and suggestions presented in this thesis are important for attaining appropriate estimation of turbulence modeling uncertainty using the EPF in the future. The novel derived implementation in TRACE differs from the one in any other flow solver up to date, addressing shortcomings that previously violated physical principles and conceptual ideas of the eigenspace perturbation methodology.

Beyond advancing the methodology itself, this thesis has also enriched the understanding of epistemic uncertainties in RANS turbulence models and refined their interpretation when estimated using the EPF. Leveraging recent advancements presented in Chapter 5 and Chapter 6, the EPF can now be applied without concerns about the meaningfulness of the obtained intervals and violating the initial underlying physical motivation. However, selective perturbation of eigenvalues and eigenvectors of the Reynolds stress tensor, coupled with the presence of additional other uncertainties in CFD, means that the resulting intervals are far from providing rigorous bounds.

Currently, the EPF is not yet ready for seamless integration into everyday industrial workflows. Challenges, such as convergence issues and the necessity to identify the greatest perturbation possible, hinder its practical utility in automated design iteration cycles. Nonetheless, this thesis has demonstrated the readiness of the EPF for complex turbomachinery applications. Notably, dealing with the convergence issues has culminated in the identification of a worst case scenario approach - perturbing as much as possible while retaining steady-state converged results. The described usage concludes the suggested application of the EPF, underscoring the practical guidance offered by this thesis. When applied to the multi-row compressor test case, the approach enabled exploration of how individual perturbations affect the compressor's stability and performance, providing valuable insights into its behavior under turbulence modeling uncertainty. These findings enhance the utility of the EPF as a diagnostic and exploratory tool, shedding light on the sensitivity with respect to the Reynolds stress tensor's anisotropy.

If users and developers of this framework remain aware of its limitations, while adhering to its conceptual principles, linked to its capabilities, the application of the EPF will help to explore the possible solution space of the RANS approach, moving beyond the linear eddy viscosity assumption. Focusing solely on the turbulence model uncertainty by using the interval approach of the EPF offers plausible numerical results based on deterministic model predictions on the one hand, without the underlying requirement to create bounds that bridge the gap between high-fidelity simulations or experimental measurements and RANS simulations on the other hand. Consequently, the EPF is unsuitable for CFD practitioners and designers, who are interested in enveloping certain reference data or establishing any probability distribution. Likewise, the application of the EPF alone is not sufficient to explore the comprehensive uncertainty associated with the RANS approach, as it represents only a partial uncertainty.

Finally, the insights gained from increased sensitivity to the Reynolds stress tensor's eigenspace can provide estimates on the potential impact of future turbulence model enhancements, fostering improved predictive capabilities and enhanced reliability of CFD simulations.

9.2. Outlook

The focus of this thesis has been set on fully turbulent setups, while turbomachinery flows are also characterized by laminar flows and in particular by the phenomenon of laminar to turbulent transition necessitating dedicated transition modeling [102]. Chu et al. [18, 19] have begun examining the impact of the EPF on the coupling of turbulence and transition modeling for transitional flows. However, most prominent transition models, such as the one proposed by Langtry and Menter [82], modify the turbulence generation in the k transport equation of the turbulence model by scaling P_k, that is also influenced by the eigenspace of the Reynolds stress tensor, with an additional term called intermittency. A sophisticated study is needed to compare the application with and without additional transition modeling, particularly when applying the provided consistent implementation of the EPF in TRACE, in order to determine whether combining a transition model with the eigenspace perturbation enhances information gain or not.

Furthermore, the applications of the Reynolds stress tensor perturbations and the derived inferences for uncertainty estimations are performed for steady RANS simulations in this thesis. However, turbulent flows, particularly turbomachinery flows, are unsteady by definition. As time-consuming SRS are not expected to enter daily industrial design processes, (unsteady) RANS or harmonic balance methods representing the highest level of modeling unsteady effects in turbomachinery [44, 3, 70]. Therefore, it may be the next step to evaluate the capabilities of the EPF focusing on unsteady turbomachinery flows[1].

Besides the frequently discussed perturbations of the Reynolds stress tensor and its effects on QoI, researchers are encouraged to evaluate the effects on the budget terms of the turbulence model's transport equations besides the turbulence production term, as current literature lacks insights into this aspect. These analyses may be especially interesting for the turbulence modeling community and to gain a deeper understanding of the indirect effects of the EPF on the transport equations.

All presented EPF results in this thesis are conducted on simulation grids that showed sufficiently mesh-independent solutions for the baseline RANS simulation. It was inferred that the chosen mesh must be reasonably well resolved to obtain appropriate results using the EPF. This practical choice aimed to minimize the computational effort in finding an appropriate grid for each and every perturbation. However, there is a need for future research and publications dedicated to address this topic especially for turbomachinery applications[2].

Early studies analyzing the sign of the turbulence production term under eigenvector perturbation for complex configurations, similar to the presented compressor flow in Chapter 7, indicate that the constraints derived in Chapter 6 can be also applied in similar manner to 3D test cases. Nevertheless, there needs to be a detailed discussion on the eigenvector rotation approach in upcoming research. Besides, future research should compare the resulting uncertainty estimates that are created with and without eigenvector perturbation and by relying on the full set of six versus a conceivable set of only two eigenspace perturbations for a broad range of test cases (see discussions in Section 8.2.4). However, if meaningful insights can be achieved with only two additional simulations, the application of the EPF becomes drastically more feasible in future DUU tasks.

Studies like the ones from Gorlé et al. [55][3] or Emory [36][4] underscore the necessity of integrating multiple uncertainties to develop credibility in CFD frameworks for future design tasks. Besides inflow condition uncertainties, other simplifications, such as the overall usage of RANS, the steady-state assumption, the usage of mixing planes in turbomachinery configurations, the neglect of surface roughness and manufacturing tolerances were accepted and not accounted for in terms of uncertainty consideration in this thesis. In order to provide a complete perspective for simulation-driven design and certification, future research activities are encouraged to build upon the verified and validated EPF in TRACE and to incorporate several sources of uncertainty in a mixed manner, similar to the approach of Granados-Ortiz and Ortega-Casanova [57].

---

[1] Gori et al. [50] has already analyzed the sensitivity of the eigenspace perturbation with respect to the time-step size for flow around an airfoil using the SU2 solver, no applications have been made to more complex turbomachinery flows featuring inherent unsteady but periodic effects.

[2] Gori et al. [50] demonstrated that one should not expect identical trends for the grid resolution dependency between the baseline (unperturbed) and every single simulation featuring any perturbation of the Reynolds stresses. However, their conclusion that was primarily based on the onset of instabilities during stall for the NACA 0012 airfoil, a scenario notoriously difficult to predict for RANS models in a steady simulation, leaves a number of questions unanswered.

[3] Gorlé et al. [55] emphasized that combining multiple sources of uncertainties, such as inflow and turbulence model uncertainty, is challenging but can provide a comprehensive view of the overall uncertainty for wind flows in urban environments.

[4] Emory [36] investigated a large set of inflow uncertainty mixed with the combustor model uncertainty and the eigenvalue perturbation of the Reynolds stress tensor for a scramjet.

Nomenclature

Abbreviations

1C	One-component turbulence
1D	One-dimensional
2C	Two-component axisymmetric turbulence
2D	Two-dimensional
3C	Three-component, isotropic turbulence
3D	Three-dimensional
ABM	Anisotropy Barycentric Map
AIAA	American Institute of Aeronautics and Astronautics
AIM	Anisotropy Invariant Map
ASME	American Society of Mechanical Engineers
CFD	Computational Fluid Dynamics
CFL	Courant-Friedrichs-Lewy
DDES	Delayed Detached-Eddy Simulation
DLR	German Aerospace Center
DNS	Direct Numerical Simulation
DUU	Design Under Uncertainty
EPF	Eigenspace Perturbation Framework
GLR	Fachgebiet Gasturbinen, Luft- und Raumfahrtantriebe
GPPS	Global Power and Propulsion Society
ISA	International Standard Atmosphere
KDE	Kernel Density Estimation
LE	Leading edge
LES	Large Eddy Simulation
LEVM	Linear Eddy Viscosity Model
ME	Measurement plane (German: Messebene)
NACA	National Advisory Committee for Aeronautics
OEM	Original Equipment Manufacturer
PCS	Principal Coordinate System
PS	Pressure side
QoI	Quantity of Interest
RANS	Reynolds-averaged Navier-Stokes
RGB	Red Green Blue
RMSE	Root Mean Square Error
RSM	Reynolds Stress Model
SAF	Sustainable Aviation Fuels
SRS	Scale-Resolving Simulation
SS	Suction side
TE	Trailing edge

TRACE	Turbomachinery Research Aerodynamics Computational Environment
TUDa	Technische Universität Darmstadt
UQ	Uncertainty Quantification
V&V	Verification and Validation

Latin symbols

$\mathbf{a}$	Reynolds stress anisotropy tensor
A	Reciprocal of the probability density with respect to uniform distribution inside a cuboid
$\mathbf{A}, \mathbf{B}, \mathbf{C}, \mathbf{X}, \mathbf{Y}, \mathbf{Z}$	Exemplary Reynolds stress tensors
c	Chord length; symbolic for constants of turbulence model
c_f	Skin friction coefficient
c_p	Pressure coefficient; heat capacity at constant pressure
c_v	Heat capacity at constant volume
C_{i_C}	Barycentric weights for ith componentiality
d	Wall distance; number of features for KDE
d_KDE	Extrapolation distance based on KDE
$\mathbf{D}$	Epistemic discrepancy between $\boldsymbol{\tau}_\mathrm{true}$ and $\boldsymbol{\tau}_\mathrm{modeled}$
e	Internal energy
f	Moderation factor
f_KDE	Probability density function based on KDE
$\mathbf{G}$	Shortened notation: $\mathbf{G} = \mathbf{v}^T\mathbf{R}\mathbf{v}$
h	Enthalpy
H	Height
I, II, II	Tensor invariants
k	Turbulent kinetic energy
$K(k)$	Gaussian kernel with t as symbolic input quantity
$\mathbf{K}$	Shortened notation: $\mathbf{K} = \mathbf{T}/\mathbf{S}^-$
L	Characteristic length
L_T	Turbulent length scale
m	Symbolic for variables of the turbulence model
$\dot{m}$	Mass flow rate
Ma	Mach number
$\mathcal{M}$	Symbolic for turbulence model
n	Number; rotational speed
$\boldsymbol{n}$	Arbitrary test vector ($\forall \boldsymbol{n} \in \mathbb{R}^n$)
n_x, n_y, n_y	Number of grid cells in each cartesian coordinate direction
n_Trees	Number of regressions trees for random forest
$\mathcal{N}$	Symbolic for the Navier-Stokes equations
p	Pressure; perturbation magnitude in barycentric coordinates
P_k	Turbulence production term
Pr	Prandtl number
$\boldsymbol{q}$	Heat flux vector
q_i	ith physical flow feature
$\mathbf{Q}$	Transformation tensor from eigenvalues to barycentric coordinates: $\boldsymbol{x} = \mathbf{Q}\boldsymbol{\lambda}$
$\mathcal{Q}$	Union of raw input quantities
R	Gas constant
$\mathbf{R}$	Rotation tensor
Re	Reynolds number

Re_c	Reynolds number based on chord c
Re_H	Reynolds number based on channel height H
Re_τ	Reynolds number based on friction velocity u_τ
$\mathbf{S}$	Strain-rate tensor
$\mathcal{T}$	Symbolic for functional form of turbulence model
t	Time
T	Temperature
$\mathbf{T}$	Shortened notation: $\mathbf{T} = \mathbf{v}\boldsymbol{\Lambda}_{(\mathrm{t})}\mathbf{v}^T$
Tu	Turbulence intensity
$\boldsymbol{u}$	Cartesian velocity vector $\boldsymbol{u} = (u_1, u_2, u_3)^T$
u_τ	Friction velocity
$\boldsymbol{U}$	Favre-averaged cartesian velocity vector $\boldsymbol{U} = (U_1, U_2, U_3)^T$
U_B	Bulk velocity based on U_1
$\mathbf{v}$	Eigenvector matrix of Reynolds stress (anisotropy) tensor $\mathbf{v} = (\boldsymbol{v_1}, \boldsymbol{v_2}, \boldsymbol{v_3})$
$\boldsymbol{v_i}$	i*th* Eigenvector of Reynolds stress (anisotropy) tensor
$\boldsymbol{x}$	Cartesian coordinate vector $\boldsymbol{x} = (x, y, z)^T = (x_1, x_2, x_3)^T$; barycentric coordinate vector $\boldsymbol{x} = (x, y)^T$

Greek symbols

α	Rotation angle for eigenvector perturbation; flow angle; exemplary element in normalization
β	Normalization factor
γ	Heat capacity ratio
δ	Characteristic dimension; arbitrary delta
δ_{ij}	Kronecker delta
Δ_B	Relative perturbation magnitude for eigenvalue perturbation
ϵ	Turbulent dissipation rate
ϵ_{ijk}	Levi-Civita symbol
ζ_T	Total temperature ratio
η_is	Isentropic efficiency
θ_i	i*th* eigenvalue of $\mathbf{K}$
$\boldsymbol{\Theta}$	Eigenvalue matrix of $\mathbf{K}$
ι	Arbitrary delta
κ	Heat conductivity
λ_i	i*th* eigenvalue of Reynolds stress anisotropy tensor
$\boldsymbol{\lambda}$	Eigenvalue vector of Reynolds stress anisotropy tensor
$\boldsymbol{\Lambda}$	Eigenvalue matrix of Reynolds stress anisotropy tensor
μ	Molecular viscosity
μ_T	Turbulent eddy viscosity multiplied with density
ν	Kinematic viscosity
ν_T	Turbulent eddy viscosity
ξ_i	i*th* eigenvalue of Reynolds stress tensor
$\boldsymbol{\xi}$	Eigenvalue vector of Reynolds stress tensor
$\boldsymbol{\Xi}$	Eigenvalue matrix of Reynolds stress tensor
Π_T	Total pressure ratio
ρ	Density
σ	Bandwidth for KDE
$\boldsymbol{\sigma}$	Viscous stress tensor
τ_w	Wall shear stress

$\boldsymbol{\tau}$	Reynolds stress tensor
ϕ	Symbolic quantity for averaging
ψ_i	$i th$ eigenvalue of strain-rate tensor
$\boldsymbol{\Psi}$	Eigenvalue matrix of strain-rate tensor
ω	Specific turbulent dissipation rate
ω_{sw}	Streamwise vorticity
$\boldsymbol{\Omega}$	Rotation-rate tensor

Decorations and operators

$\overline{\Box}$	Reynolds-average quantity, time-averaged quantity
$\Box'$	Fluctuating part of a Reynolds-averaged quantity
$\widetilde{\Box}$	Favre-averaged quantity
$\Box''$	Fluctuating part of a Favre-averaged
$\Box^*$	Perturbed quantity
$\Box^+$	Nondimensionalized quantity based on friction velocity u_τ
$\Box^-$	Traceless tensor or property of traceless tensor
-1	Inverse/pseudoinverse of a tensor
$\hat{\Box}$	Normalized quantity $\hat{\alpha} = \frac{\alpha}{\lvert\alpha\rvert + \lvert\beta\rvert}$
$\tilde{\Box}$	Test data sample
$\lvert\Box\rvert$	Absolute-value norm
$\lvert\lvert\Box\rvert\rvert$	Euclidean norm
$\langle\Box_1, \Box_2\rangle_F$	Frobenius inner product between tensor $\Box_1$ and tensor $\Box_2$
$\det(\Box)$	Determinant of a tensor
$\mathrm{diag}(\Box)$	Diagonal tensor
$\mathrm{tr}(\Box)$	Trace of a tensor
$\Delta\Box$	Difference, discrepancy
∇	Nabla operator
$\partial\Box_1/\partial\Box_2$	Partial derivative of $\Box_1$ with respect to $\Box_2$
#	Number (of)

Sub- and superscripts

0	Reference location 0
1C	One-component turbulence
2C	Two-component turbulence
3C	Isotropic turbulence
15	Quantity at ME15 of TUDa stage
21	Quantity at ME21 of TUDa stage
30	Quantity at ME30 of TUDa stage
$\mathbf{a}$	Reynolds stress anisotropy tensor
$\mathbf{A}, \mathbf{B}, \mathbf{C}, \mathbf{X}, \mathbf{Y}, \mathbf{Z}$	Property of exemplary Reynolds stress tensors
$\alpha\alpha, \beta\beta, \alpha\beta, \gamma\gamma$	Tensor entry
corr	Corrected quantity to ISA conditions
DNS	Based on DNS
exp	Experimentally determined value
f	Moderated with factor f
(i)	$i th$ training data sample
ij, in, nl, jl	Tensor entry

∞	Free stream
is	Isentropic
ISA	Quantity at International Standard Atmosphere
max	Maximum
mean	Mean
min	Minimum
modeled	Modeled
pred	Predicted
PCS	In the Principal Coordinate System
$\mathrm{PCS}_{\mathbf{S}}$	In the Principal Coordinate System of strain-rate tensor
real	Real quantity
ref	Reference
rotated	Rotated
RANS	Based on RANS
stall	Quantity at compressor stall
$\mathbf{S}$	Strain-rate tensor
(t)	Target barycentric state
i, j, k, q	Vector entry or index
t	Total quantity
test	Based on test data
train	Based on training data
true	True
T	Turbulent quantity; transpose of a vector or tensor

List of Figures

1.1. Schematic representation of key aspects of turbulence. 2

2.1. Overview of errors and uncertainties in CFD. 11

3.1. Sources of uncertainty in RANS turbulence models at different levels according to Duraisamy et al. [29]. 18
3.2. Conceptual difference of non-parametric and parametric approaches for assessing the uncertainty of RANS turbulence modeling to explore the possible solution space of the Reynolds stress tensor, inspired by Xiao and Cinnella [169] and Soize [142]. 19
3.3. Schematic representation of the relationship between anisotropy $\mathbf{a}$ (gray) and the traceless strain-rate tensor $\mathbf{S}^-$ (orange) in the eigenbasis defined by the eigenvectors $\boldsymbol{v_i}$. As $\mathbf{a}$ and $\mathbf{S}^-$ are not positive semi-definite, the magnitude of the eigenvalues λ_i and ψ_i^- is plotted according to Kratz et al. [79]. The Reynolds stress tensor featuring identical principal axes as the anisotropy tensor behaves in similar manner as the anisotropy tensor. . . . 25
3.4. Representation of the eigenvalue perturbation within the ABM and its effect on the shape of the Reynolds stress tensor ellipsoid. The eigenvalue perturbation towards the 2C limiting state is shown exemplarily. 26
3.5. Effect of Δ_B when targeting for the 1C limiting state on the solution of the converging-diverging channel without modifying the eigenvectors of the Reynolds stress tensor; legend in (b) applies also for (a), (c), (d) and (e). 28
3.6. Effect of sampled states inside the barycentric triangle on the solution of the converging-diverging channel without modifying the eigenvectors of the Reynolds stress tensor; legend in (b) applies also for (c), (d) and (e). . 29
3.7. Effect of α when perturbing the eigenvalues to the 1C limiting state on the solution of the converging-diverging channel; legend in (a) applies also for (b). 30
3.8. Flow chart of the final implemented version of the EPF in TRACE. 33

4.1. Schematic representation of the eigenvalue perturbation approach. 40
4.2. Implementation of the UQ framework within the CFD solver suite TRACE. 45
4.3. Schematic turbulent channel flow setup. 48
4.4. Schematic periodic hill setup. 48
4.5. Schematic wavy wall setup. 49
4.6. Schematic converging-diverging setup. 50
4.7. Schematic NACA 4412 setup. 51
4.8. Training accuracy (solid / left) and testing accuracy (dashed / right) based on RMSE for selection of hyperparameters in scenario I. 53

4.9. Relationship between the RMSE of the prediction for the converging-diverging channel and the mean value of the KDE extrapolation metric (standard deviation of the extrapolation metric is shown as the horizontal bars). All 56 input features are considered for the prediction and training of the random forest models, while only q_1, q_2, q_3, q_7 and q_8 are used to compute d_{KDE}. 55
4.10. Barycentric coordinates for the selected flow cases; legend of (b) corresponds to (a) and (c) as well. 56
4.11. Frequency of the target quantity p for the selected flow cases; vertical axis correspond to (a), (b) and (c). 56
4.12. Verification of extrapolation metric based on converging-diverging channel. 57
4.13. Evaluated metric and perturbation magnitude for the NACA 4412 profile. 57
4.14. Surface quantities for the flow around NACA 4412 including data-free evaluation of the uncertainty estimates for the Menter SST $k-\omega$ turbulence model; legend in (a) applies also for (b). 60
4.15. Comparison of the effect of identical model predicted perturbation magnitude p on the relative perturbation magnitude Δ_B. 61
4.16. Surface quantities for the flow around NACA 4412 including data-driven evaluation of the uncertainty estimates for the Menter SST $k-\omega$ turbulence model; legend in (a) applies also for (b). 62

5.1. Representation of the Reynolds stress tensor as an ellipsoid; eigenvalues ξ_i and eigenvectors $\boldsymbol{v_i}$ are highlighted. 69
5.2. AIM of the Reynolds stress tensor comparing second and third invariant of respective anisotropy tensor. The corners of the triangle (1C, 2C, 3C) represent the componentiality of turbulence (see Table 5.1). 70
5.3. ABM representing the eigenvalues of the anisotropy tensor and its effect on the shape of the Reynolds stress tensor ellipsoid. The eigenvalue perturbation towards the two-component limiting state of turbulence is shown schematically. 72
5.4. Comparison of the perturbation trajectory for RANS channel flow data at $\mathrm{Re}_\tau = 1000$ (blue dots) in barycentric coordinates. The trajectories for selected RANS data points (τ_{ij}) are created by increasing $f = 0...1$ with and without eigenvector perturbation targeting the one-component limiting state of turbulence $\tau^*_{ij} = \tau_{ij_{1\mathrm{C}}}$ (orange dot). 75
5.5. Transition from tensor **A** to **B** (defined in Appendix 5.D) featuring identical eigenvectors by increasing $f = 0...1$ (see Eq. (5.16)). The intermediate brown-colored states in (a), (b) and (c) correspond to the states with $f \in [0.2, 0.4, 0.6, 0.8]$ in (d) and (e). 76
5.6. Transition from tensor **A** to **C** (defined in Appendix 5.D) featuring different eigenvector by increasing $f = 0...1$ (see Eq. (5.16)). The intermediate brown-colored states in (a), (b) and (c) correspond to the states with $f \in [0.2, 0.4, 0.6, 0.8]$ in (d) and (e). 77
5.7. Schematic turbulent channel flow setup. 80
5.8. Barycentric coordinates of DNS data and RANS simulation using the Menter SST k-ω model. Data points are colored according to their distance from the wall. 80
5.9. Comparison of the resulting uncertainty bounds for the streamwise velocity profile of turbulent channel flow simulation derived by the EPF. 81
5.10. Comparison of the resulting barycentric coordinates of the perturbed Reynolds stress tensors for the turbulent boundary layer profiles. 81

6.1. Representation of the eigenvalue perturbation within the barycentric triangle and its effect on the shape of the Reynolds stress tensor ellipsoid. . . 90
6.2. Schematics of steady, fully developed 1D boundary layer flow. 91
6.3. Comparison of the effect of the eigenspace perturbation on the turbulence production term P_k in case of fully developed boundary layer flow. Effect of pure eigenvalue perturbation is shown in (a), while (b) presents the effect, when combining the permutation of the eigenvectors $\boldsymbol{v_1}$ and $\boldsymbol{v_3}$ and eigenvalue perturbation within the barycentric triangle. 93
6.4. Rotation of the eigenvector matrix of the Reynolds stress tensor around second eigenvector $\boldsymbol{v_2}$ by α. The schemtical impact of the rotation on the Reynolds stress tensor ellipsoid is shown in (a). (b) shows the effect of eigenvector rotation on the Reynolds shear stress component and the turbulence production. This plot is created based on assuming 1D boundary layer flow, as sketched in Fig. 6.2. The eigenvectors of τ_{ij} presented in Eq. (6.19) are rotated by α. The resulting τ_{12} and P_k (see Eq. (6.17)) are evaluated subsequently. 94
6.5. Distribution of the turbulence production term $P_{k_{\text{rotated}}}$, when rotating the eigenvectors of the Reynolds stress tensor around the second eigenvector by $\alpha = \pi/4$. For better interpretability the resulting production is scaled by the unperturbed turbulence production P_k. The magenta line indicates $U_1 = 0$. 95
6.6. Rotation around the second eigenvector of the Reynolds stress tensor by $\alpha|_{P_k=0}$ leads to zero turbulence production. In order to better classify the discrepancy from $\pi/4$, the determined angle $\alpha|_{P_k=0}$ is presented as a fraction of $\pi/4$. The magenta line indicates $U_1 = 0$. 96
6.7. Estimated turbulence model uncertainty for the streamwise velocity inside the converging-diverging channel based on the EPF. $U_{1_{0,\text{max}}}$ is the maximum streamwise velocity of the baseline simulation at x/H=0. The settings for every eigenspace perturbation of the Reynolds stress tensor can be found in Table 6.1. 98
6.8. Turbulence model uncertainty based on the EPF for the friction coefficient $c_f = \tau_w / \left(\frac{1}{2}\rho_0 U^2_{1_{0,\text{max}}}\right)$ at upper and bottom wall of the converging-diverging channel. The quantities with subscript 0 indicate that they are extracted at $x/H = 0$. The settings for every eigenspace perturbation of the Reynolds stress tensor can be found in Table 6.1. 99
6.9. Turbulence model uncertainty based on the EPF for the pressure coefficient $c_p = (p - p_0) / \left(\frac{1}{2}\rho_0 U^2_{1_{0,\text{max}}}\right)$ at upper and bottom wall of the converging-diverging channel. The quantities with subscript 0 indicate that they are extracted at $x/H = 0$. The settings for every eigenspace perturbation of the Reynolds stress tensor can be found in Table 6.1. 99
6.10. Evolution and comparison of the turbulent kinetic energy within the converging-diverging channel between DNS data [85] (a), RANS baseline (b) and EPF simulations applying perturbed Reynolds stress tensors (c)-(h) (see Table 6.1). 100
6.11. Comparison of modifying eigenvectors of the Reynolds stress tensor. . . . 102
6.12. Introduction of the converging-diverging setup. 103
6.13. Evolution of the area averaged outlet pressure over iteration count for the simulation using eigenvector permutation without any eigenvalue perturbation. 104

6.14. Streamwise velocity inside the converging-diverging channel based on pure eigenvector permutation without any eigenvalue perturbation. The snapshots are taken every 1000 iteration, while the mean $U_{1_{\mathrm{mean}}}$ and the standard deviation $\mathrm{std}(U_1)$ are determined between 400.000 to 500.000 iterations. 104

6.15. Streamwise velocity inside the converging-diverging channel for simulation #2 (see Table 6.1) using moderated eigenvector perturbation and eigenvalue modification towards the one-component limiting state. The snapshots are taken every 1000 iteration, while the mean $U_{1_{\mathrm{mean}}}$ and the standard deviation $\mathrm{std}(U_1)$ are determined between 400.000 to 500.000 iterations. . 104

7.1. Representation of the Reynolds stress tensor's eigenvalue perturbation within the barycentric triangle. Its effect on the shape of the Reynolds stress tensor is shown by the ellipsoid visualizations, when approaching the vertices of the triangle. 108

7.2. 3D illustration of the considered TUDa compressor configuration. The simulated single passage is colored in pink, while reference locations are highlighted as well. 110

7.3. Effect of the grid resolution on the prediction of the total pressure ratio (top) and the isentropic efficiency (bottom) by RANS simulations at design speed. 111

7.4. Attainable relative perturbation magnitude Δ_B over corrected mass flow rate for eigenvalue perturbation of the Reynolds stress tensor towards the three limiting states of turbulence. 112

7.5. Illustration of the turbulent state of the Reynolds stress tensor at ME30 and $\dot{m}_{\mathrm{corr}} = 14.78$ kg/s. (a) presents the RGB coloring according to the location of each data point inside the barycentric triangle, which is shown in (b). 113

7.6. Estimated turbulence modeling uncertainty for the global compressor performance quantities total pressure ratio (top) and isentropic efficiency (bottom) at 100% speedline and comparison with experimental data. The mass flow rates for subsequent detailed analysis are highlighted by magenta dashed lines ($\dot{m}_{\mathrm{corr}} \in [14.78\ \mathrm{kg/s}, 15.12\ \mathrm{kg/s}, 15.84\ \mathrm{kg/s}, 16.00\ \mathrm{kg/s}]$). . . . 114

7.7. Uncertainty estimates for predicting radial profiles of the total pressure ratio ((a), (b), (c), (d)) and the total temperature ratio ((e), (f), (g), (h)) at ME30 for four different operating points. The total pressure and temperature ratio is computed using circumferentially area-averaged quantities at ME30 and the integral area-averaged quantities at ME15. . . 116

7.8. Comparison of total pressure wake losses at ME30 for two different operating points. The total pressure and ratio is computed using the integral area-averaged total pressure at ME15. Red dashed lines indicate the radial measurement window in the experimental setup. 117

7.9. Uncertainty estimates for predicting radial profiles of the total pressure ratio ((a), (b)) and the flow angle ((c), (d)) at ME21 for two different operating points. The total pressure ratio is computed using circumferentially area-averaged total pressure at ME21 and the integral area-averaged total pressure at ME15. Note: The experimental data presented in (b) and (d) were obtained by personal communication with Fabian Klausmann. As the underlying operation point ($\dot{m}_{\mathrm{corr}} = 14.66\,\mathrm{kg/s}$) varies slightly from the numerical one ($\dot{m}_{\mathrm{corr}} = 14.78\,\mathrm{kg/s}$), the markers are grayed out. 118

7.10. Comparison of secondary flow structures indicated by the streamwise vorticity at ME21 for two different operating points. The local streamwise vorticity was normalized using the maximum absolute value of the streamwise vorticity occurring at ME21 in the baseline simulation. 119
7.11. Comparison of secondary flow structures indicated by the streamwise vorticity at ME30 for two different operating points. The local streamwise vorticity was normalized using the maximum absolute value of the streamwise vorticity occurring at ME30 in the baseline simulation. 120
7.12. The effect of perturbing the eigenspace of the Reynolds Stress tensor on static surface pressure and surface streamtraces on the hub and SS at $\dot{m}_{\text{corr}} = 14.78$ kg/s. 121
7.13. Comparison of turbulent kinetic energy distribution throughout the compressor for three different operating points. Reference planes are shown by dotted gray lines, while the mixing plane interface between rotor and stator is marked in light green. White lines in (b) indicate the contours of rotor and stator. 122
7.14. Analysis of shock position and wake width prediction by illustrating the relative Mach number distribution for three constant relative span levels at $\dot{m}_{\text{corr}} = 14.78\,\text{kg/s}$. Dashed lines indicate $\text{Ma} = 1$. 123
7.15. Uncertainty estimates for the isentropic Mach number distribution at 90% span of the rotor for two different operating points. 124

List of Tables

1.1. Summary of the considered articles in this thesis. 6

4.1. Raw flow features for constructing the invariant basis. 43
4.2. Physical flow features. 44
4.3. Scenarios for hyperparameter study: x means part of training data, ∘ means testing data. 52
4.4. Prediction accuracy of random forest: x means part of training data, ∘ means not part of training data, red highlights data sets used for evaluation of RMSE. 54
4.5. Moderation factor f for every perturbed UQ simulation of NACA 4412. Application of $\Delta_B \leq 1$ in the data-driven approach necessitates a distinction between $P_{k_{\min}}$ and $P_{k_{\max}}$ for 3C. 59

5.1. Turbulence componentiality and limiting states of turbulence with respect to the eigenvalues of the Reynolds stress tensor ξ_i and the anisotropy tensor λ_i. 71

6.1. Selected turbulent target states (componentiality), Δ_B for the eigenvalue modifications and α for the eigenvector rotations of the Reynolds stress tensor perturbation applied to the flow within the converging-diverging channel. 97

7.1. Number of grid points / 10^6 used for the RANS grid convergence study presented in Fig. 7.3. 110

Bibliography

[1] AIAA. Guide: Guide for the Verification and Validation of Computational Fluid Dynamics Simulations. In *AIAA G-077-1998*. 2002.

[2] E. Anderson, Z. Bai, C. Bischof, S. Blackford, J. Demmel, J. Dongarra, J. Du Croz, A. Greenbaum, S. Hammarling, A. McKenney, and D. Sorensen. *LAPACK Users' Guide*. Society for Industrial and Applied Mathematics, Philadelphia, PA, third edition, 1999.

[3] G. Ashcroft, C. Frey, H.-P. Kersken, E. Kügeler, and N. Wolfrum. On the Simulation of Unsteady Turbulence and Transition Effects in a Multistage Low Pressure Turbine: Part I Verification and Validation. volume 2C: Turbomachinery of *Turbo Expo: Power for Land, Sea, and Air*, page V02CT42A042, 2018.

[4] S. Banerjee, R. Krahl, F. Durst, and C. Zenger. Presentation of anisotropy properties of turbulence, invariants versus eigenvalue approaches. *Journal of Turbulence*, 8: N32, 2007.

[5] J. Bardina, J. H. Ferziger, and R. S. Rogallo. Effect of rotation on isotropic turbulence: computation and modelling. *Journal of Fluid Mechanics*, 154:321–336, 1985.

[6] B. Basara. Employment of the second-moment turbulence closure on arbitrary unstructured grids. *International Journal for Numerical Methods in Fluids*, 44(4): 377–407, 2004.

[7] O. Bidar, S. R. Anderson, and N. Qin. Sensor placement for data assimilation of turbulence models using eigenspace perturbations. *Physics of Fluids*, 36(1):015144, 2024.

[8] B. Blais and F. Bertrand. On the use of the method of manufactured solutions for the verification of CFD codes for the volume-averaged Navier–Stokes equations. *Computers & Fluids*, 114:121–129, 2015.

[9] J. Blazek. *Computational Fluid Dynamics: Principles and Applications (Third Edition)*. Butterworth-Heinemann, Oxford, third edition edition, 2001.

[10] A. Bleh, C. Morsbach, and J. Backhaus. Investigating the Nature and Invariance of Field Inversion based on Transition in a Turbine Cascade. In *ASME Turbo Expo 2022: Turbomachinery Technical Conference and Exposition, GT 2022*, 2022.

[11] L. Breiman. Random Forests. *Machine Learning*, 45:5–32, 2001.

[12] L. Breiman. Bagging predictors. *Machine Learning*, 24:123–140, 2004.

[13] B. P. Brener, M. A. Cruz, R. L. Thompson, and R. P. Anjos. Conditioning and accurate solutions of Reynolds average NavierStokes equations with data-driven turbulence closures. *Journal of Fluid Mechanics*, 915:A110, 2021.

[14] M. Breuer, N. Peller, C. Rapp, and M. Manhart. Flow over periodic hills – Numerical and experimental study in a wide range of Reynolds numbers. *Computers & Fluids*, 38(2):433 – 457, 2009.

[15] S. L. Brunton, B. R. Noack, and P. Koumoutsakos. Machine learning for fluid mechanics. *Annual Review of Fluid Mechanics*, 52:477–508, 2020.

[16] H. Choi and P. Moin. Grid-point requirements for large eddy simulations: Chapman's estimates revisited. *Physics of Fluids*, 24:011702, 2012.

[17] K.-S. Choi and J. L. Lumley. The return to isotropy of homogeneous turbulence. *Journal of Fluid Mechanics*, 436:59–84, 2001.

[18] M. Chu, X. Wu, and D. E. Rival. Quantification of Reynolds-averaged-Navier–Stokes model-form uncertainty in transitional boundary layer and airfoil flows. *Physics of Fluids*, 34(10):107101, 2022.

[19] M. Chu, X. Wu, and D. E. Rival. Model-form uncertainty quantification of Reynolds-averaged Navier–Stokes modeling of flows over a SD7003 airfoil. *Physics of Fluids*, 34(11):117105, 2022.

[20] A. Cimarelli, A. Leonforte, E. De Angelis, A. Crivellini, and D. Angeli. On negative turbulence production phenomena in the shear layer of separating and reattaching flows. *Physics Letters A*, 383(10):1019–1026, 2019.

[21] D. Coles and A. J. Wadcock. Flying-Hot-wire Study of Flow Past an NACA 4412 Airfoil at Maximum Lift. *AIAA Journal*, 17(4):321 – 329, 1979.

[22] L. W. Cook, A. A. Mishra, J. P. Jarrett, K. E. Willcox, and G. Iaccarino. Optimization under turbulence model uncertainty for aerospace design. *Physics of Fluids*, 31 (10):105111, 2019.

[23] T. Craft, B. Launder, and K. Suga. Development and application of a cubic eddy-viscosity model of turbulence. *International Journal of Heat and Fluid Flow*, 17(2): 108–115, 1996.

[24] L. F. Cremades Rey, D. F. Hinz, and M. Abkar. Reynolds Stress Perturbation for Epistemic Uncertainty Quantification of RANS Models Implemented in OpenFOAM. *Fluids*, 4(2), 2019.

[25] J. D. Denton. Some Limitations of Turbomachinery CFD. volume 7: Turbomachinery, Parts A, B, and C of *Turbo Expo: Power for Land, Sea, and Air*, pages 735–745, 2010.

[26] Divisional Board Aeronautics. Towards zero-emission avaition - How DLR's Aviation Reasearch Strategy supports the European Green Deal 2050. Aeronatics programme strategy, German Aerospace Center (DLR), 2021.

[27] DLR, German Aerospace Center, Institute of Propulsion Technology. TRACE User Guide. `http://www.trace-portal.de/userguide/trace/index.html`, accessed April 2022.

[28] E. Dow and Q. Wang. Quantification of Structural Uncertainties in the k -w Turbulence Model. In *52nd AIAA/ASME/ASCE/AHS/ASC Structures, Structural Dynamics and Materials Conference*. 2011.

[29] K. Duraisamy, G. Iaccarino, and H. Xiao. Turbulence Modeling in the Age of Data. *Annual Review of Fluid Mechanics*, 51:357–377, 2019.

[30] W. Edeling, G. Iaccarino, and P. Cinnella. Data-Free and Data-Driven RANS Predictions with Quantified Uncertainty. *Flow, Turbulence and Combustion*, 100: 593–616, 2018.

[31] A. Eidi, R. Ghiassi, X. Yang, and M. Abkar. Model-form uncertainty quantification in RANS simulations of wakes and power losses in wind farms. *Renewable Energy*, 179:2212–2223, 2021.

[32] A. Eidi, N. Zehtabiyan-Rezaie, R. Ghiassi, X. Yang, and M. Abkar. Data-driven quantification of model-form uncertainty in Reynolds-averaged simulations of wind farms. *Physics of Fluids*, 34(8):085135, 2022.

[33] M. Emory, R. Pecnik, and G. Iaccarino. Modeling Structural Uncertainties in Reynolds-Averaged Computations of Shock/Boundary Layer Interactions. In *49th AIAA Aerospace Sciences Meeting including the New Horizons Forum and Aerospace Exposition*. 2011.

[34] M. Emory, J. Larsson, and G. Iaccarino. Modeling of structural uncertainties in Reynolds-averaged Navier-Stokes closures. *Physics of Fluids*, 25(11):110822, 2013.

[35] M. Emory, G. Iaccarino, and G. M. Laskowski. Uncertainty Quantification in Turbomachinery Simulations. volume 2C: Turbomachinery of *Turbo Expo: Power for Land, Sea, and Air*, page V02CT39A028, 2016.

[36] M. A. Emory. *Estimating model-form uncertainty in Reynolds-averaged Navier-Stokes closures*. Dissertation, Stanford University, Department of Mechanical Engineering, 2014.

[37] European Commision and Directorate-General for Research and Innovations. *Fly the Green Deal: Europe's vision for sustainable aviation*. Publications Office of the European Union, 2022.

[38] L. Eça, M. Hoekstra, A. Hay, and D. Pelletier. On the construction of manufactured solutions for one and two-equation eddy-viscosity models. *International Journal for Numerical Methods in Fluids*, 54(2):119–154, 2007.

[39] L. Eça, M. Hoekstra, A. Hay, and D. Pelletier. Verification of RANS solvers with manufactured solutions. *Engineering with Computerss*, 23:253–270, 2007.

[40] M. H. Faber. On the Treatment of Uncertainties and Probabilities in Engineering Decision Analysis. *Journal of Offshore Mechanics and Arctic Engineering*, 127(3): 243–248, 2005.

[41] J. Faragher. Probabilistic Methods for the Quantification of Uncertainty and Error in Computational Fluid Dynamics Simulations. Aeronatics programme strategy, Defence Sciency and Technology Organisation, Air Vehicle Division of the Australian Government, Victoria (Australia), 2004.

[42] N. Fard Afshar, D. Kozulovic, S. Henninger, J. Deutsch, and P. Bechlars. Turbulence anisotropy analysis at the middle section of a highly loaded 3D linear turbine cascade using Large Eddy Simulation. *Journal of the Global Power and Propulsion Society*, 7:71–84, 2023.

[43] G. G. Fleming, I. de Lépinay, and R. Schaufele. Environmental Trends in Aviation to 2050. In *Innovation for a green transition*, pages 24–31. 2022.

[44] M. Franke, T. Röber, E. Kügeler, and G. Ashcroft. Turbulence Treatment in Steady and Unsteady Turbomachinery Flows. In *V European Conference on Computational Fluid Dynamics ECCOMAS CFD 2010*, 2010.

[45] C. García-Sánchez, D. Philips, and C. Gorlé. Quantifying inflow uncertainties for CFD simulations of the flow in downtown Oklahoma City. *Building and environment*, 78:118–129, 2014.

[46] B. Gayen and S. Sarkar. Negative turbulent production during flow reversal in a stratified oscillating boundary layer on a sloping bottom. *Physics of Fluids*, 23(10): 101703, 2011.

[47] G. Geiser, J. Wellner, E. Kügeler, A. Weber, and A. Moors. On the Simulation and Spectral Analysis of Unsteady Turbulence and Transition Effects in a Multistage Low Pressure Turbine. 141(5), 2019.

[48] S. Geman, E. Bienenstock, and R. Doursat. Neural Networks and the Bias/Variance Dilemma. *Neural Computation*, 4:1–58, 1992.

[49] G. Gori. Estimating Model-Form Uncertainty in RANS Turbulence Closures for NICFD Applications. In *Proceedings of the 4th International Seminar on Non-Ideal Compressible Fluid Dynamics for Propulsion and Power*, pages 72–81, Cham, 2023. Springer Nature Switzerland.

[50] G. Gori, O. Le Maître, and P. Congedo. On the sensitivity of structural turbulence uncertainty estimates to time and space resolution. *Computers & Fluids*, 229: 105081, 2021.

[51] G. Gori, O. Le Maître, and P. Congedo. A confidence-based aerospace design approach robust to structural turbulence closure uncertainty. *Computers & Fluids*, 246:105614, 2022.

[52] C. Gorlé and G. Iaccarino. A framework for epistemic uncertainty quantification of turbulent scalar flux models for Reynolds-averaged Navier-Stokes simulations. *Physics of Fluids*, 25(5):055105, 2013.

[53] C. Gorlé, M. Emory, J. Larsson, and G. Iaccarino. Epistemic uncertainty quantification for RANS modeling of the flow over a wavy wall. *Center for Turbulence Research Annual Research Briefs, Stanford Univ., Stanford, CA*, pages 81–91, 2012.

[54] C. Gorlé, J. Larsson, M. Emory, and G. Iaccarino. The deviation from parallel shear flow as an indicator of linear eddy-viscosity model inaccuracy. *Physics of Fluids*, 26(5):051702, 2014.

[55] C. Gorlé, C. Garcia-Sanchez, and G. Iaccarino. Quantifying inflow and RANS turbulence model form uncertainties for wind engineering flows. *Journal of Wind Engineering and Industrial Aerodynamics*, 144:202–212, 2015. Selected papers from the 6th International Symposium on Computational Wind Engineering CWE 2014.

[56] C. Gorlé, S. Zeoli, M. Emory, J. Larsson, and G. Iaccarino. Epistemic uncertainty quantification for Reynolds-averaged Navier-Stokes modeling of separated flows over streamlined surfaces. *Physics of Fluids*, 31(3):035101, 2019.

[57] F.-J. Granados-Ortiz and J. Ortega-Casanova. Quantifying & analysing mixed aleatoric and structural uncertainty in complex turbulent flow simulations. *International Journal of Mechanical Sciences*, 188:105953, 2020.

[58] Z. Hao and C. Gorlé. Quantifying turbulence model uncertainty in Reynolds-averaged Navier–Stokes simulations of a pin-fin array. Part 1: Flow field. *Computers & Fluids*, 209:104641, 2020.

[59] X. He and F. Klausmann. RANS Capabilities for Transonic Axial Compressor: A Perspective from GPPS CFD Workshop. 2023.

[60] X. He, M. Zhu, K. Xia, K. S. Fabian, J. Teng, and M. Vahdati. Validation and verification of RANS solvers for TUDa-GLR-OpenStage transonic axial compressor. *Journal of the Global Power and Propulsion Society*, 7:13–29, 2023.

[61] J. F. Heyse, A. A. Mishra, and G. Iaccarino. Estimating RANS model uncertainty using machine learning. *Journal of the Global Power and Propulsion Society*, (May): 1–14, 2021.

[62] C. Hirsch. *Numerical Computation of Internal and External Flows (Second Edition)*. Butterworth-Heinemann, Oxford, second edition edition, 2007.

[63] J. A. Hoeting, D. Madigan, A. E. Raftery, and C. T. Volinsky. Bayesian model averaging: a tutorial (with comments by M. Clyde, David Draper and E. I. George, and a rejoinder by the authors. *Statistical Science*, 14(4):382 – 417, 1999.

[64] S. D. Hornshøj-Møller, P. D. Nielsen, P. Forooghi, and M. Abkar. Quantifying structural uncertainties in Reynolds-averaged Navier–Stokes simulations of wind turbine wakes. *Renewable Energy*, 164:1550–1558, 2021.

[65] Z. Huang, A. Mishra, and G. Iaccarino. A Nonuniform Perturbation to Quantify RANS Model Uncertainties. *Center for Turbulence Research Annual Research Briefs, Stanford Univ., Stanford, CA*, pages 223–232, 2020.

[66] G. Iaccarino, A. A. Mishra, and S. Ghili. Eigenspace perturbations for uncertainty estimation of single-point turbulence closures. *Phys. Rev. Fluids*, 2:024605, 2017.

[67] IEA. World Energy Outlook 2023. Technical report, International Energy Agency (IEA), 2023.

[68] M. Ihme, W. T. Chung, and A. Mishra. Combustion machine learning: Principles, progress and prospects. *Progress in Energy and Combustion Science*, 91:101010, 2022.

[69] C. Jiang, R. Vinuesa, R. Chen, J. Mi, S. Laima, and H. Li. An interpretable framework of data-driven turbulence modeling using deep neural networks. *Physics of Fluids*, 33(5):055133, 2021.

[70] L. Junge. *A new harmonic balance approach using multidimensional time*. Dissertation, German Aerospace Center, Ruhr-Universität Bochum, Bochum, Germany, 2023.

[71] G. Karniadakis. Quantifying Uncertainty in CFD. *Journal of Fluids Engineering-transactions of the ASME*, 124(1):2–3, 2002.

[72] M. Kato and B. Launder. The Modelling of Turbulent Flow Around Stationary and Vibrating Square Cylinders. In *9th Symposium on Turbulent Shear Flows*, pages 10.4.1–10.4.6, 1993.

[73] A. D. Kiureghian and O. Ditlevsen. Aleatory or epistemic? Does it matter? *Structural Safety*, 31(2):105–112, 2009. Risk Acceptance and Risk Communication.

[74] F. Klausmann, D. Franke, J. Foret, and H.-P. Schiffer. Transonic compressor Darmstadt - Open test case Introduction of the TUDa open test case. *Journal of the Global Power and Propulsion Society*, 6:318–329, 2022.

[75] F. Klausmann, N. Kilian, X. He, D. Franke, B. Schmidt, and H.-P. Schiffer. Transonic Compressor Darmstadt Open Test Case: Experimental Investigation of Stator Secondary Flows and Hub Leakage. *Journal of Turbomachinery*, 146(10):101007, 2024.

[76] F. S. Klausmann, D. Spieker, and H.-P. Schiffer. Transonic compressor Darmstadt Open Test Case – unsteady aerodynamics and stall inception. *Journal of the Global Power and Propulsion Society*, 8:52–61, 2024.

[77] A. N. Kolmogorov. Equations of turbulent motion in an incompressible fluid. *Proceedings of the USSR Academy of Sciences*, 30:299–303, 1941.

[78] D. Kozulovic and T. Röber. Modelling the Streamline Curvature Effects in Turbomachinery Flows. In *Proceedings of the ASME Turbo Expo*, 2006. Paper No. GT2006-90265.

[79] A. Kratz, C. Auer, M. Stommel, and I. Hotz. Visualization and Analysis of Second-Order Tensors: Moving Beyond the Symmetric Positive-Definite Case. *Computer Graphics Forum - State of the Art Reports*, 1:49 – 74, 2013.

[80] G. Lamberti and C. Gorlé. Uncertainty Quantification for RANS Predictions of Wind Loads on Buildings. In *Proceedings of the XV Conference of the Italian Association for Wind Engineering*, pages 402–412, Cham, 2019. Springer International Publishing.

[81] L. Langston. Secondary Flows in Axial TurbinesA Review. *Annals of the New York Academy of Sciences*, 934(1):11–26, 2001.

[82] R. B. Langtry and F. R. Menter. Correlation-Based Transition Modeling for Unstructured Parallelized Computational Fluid Dynamics Codes. *AIAA Journal*, 47(12):2894–2906, 2009.

[83] J. B. Lasserre. A trace inequality for matrix product. *IEEE Trans. Automatic Control*, 40(1500), 1995.

[84] B. E. Launder, D. P. Tselepidakis, and B. A. Younis. A second-moment closure study of rotating channel flow. *Journal of Fluid Mechanics*, 183:63–75, 1987.

[85] J. Laval and M. Marquillie. Direct Numerical Simulations of Converging–Diverging Channel Flow. In *Progress in Wall Turbulence: Understanding and Modeling*, pages 203–209, 2011.

[86] M. Lee and R. D. Moser. Direct numerical simulation of turbulent channel flow up to $Re_\tau \approx 5200$. *Journal of Fluid Mechanics*, 774:395–415, 2015.

[87] A. Li, T. Wang, J. Chen, Z. Huang, and G. Xi. Adjoint Design Optimization Under the Uncertainty Quantification of Reynolds-Averaged Navier-Stokes Turbulence Model. *AIAA Journal*, pages 1–12, 2024.

[88] J. Li, T. Liu, G. Zhu, Y. Li, and Y. Xie. Uncertainty quantification and aerodynamic robust optimization of turbomachinery based on graph learning methods. *Energy*, 273:127289, 2023.

[89] F. Lien and M. Leschziner. Assessment of turbulence-transport models including non-linear rng eddy-viscosity formulation and second-moment closure for flow over a backward-facing step. *Computers & Fluids*, 23(8):983–1004, 1994.

[90] J. Ling and J. Templeton. Evaluation of machine learning algorithms for prediction of regions of high Reynolds averaged Navier Stokes uncertainty. *Physics of Fluids*, 27(8):085103, 2015.

[91] G. Louppe. *Understanding Random Forests: From Theory to Practice.* Dissertation, 2014.

[92] J. L. Lumley. Computational Modeling of Turbulent Flows. In *Advances in Applied Mechanics*, volume 18, pages 123 – 176. Elsevier, 1979.

[93] J. L. Lumley and G. R. Newman. The return to isotropy of homogeneous turbulence. *Journal of Fluid Mechanics*, 82(1):161–178, 1977.

[94] M. Matha and K. Kucharczyk. Applicability of machine learning in uncertainty quantification of turbulence models. Technical report, Summarizing white paper on recent findings, 2022.

[95] M. Matha and C. Morsbach. Extending turbulence model uncertainty quantification using machine learning. In *NeurIPS - Thirty-fifth Conference on Neural Information Processing Systems | Fourth Workshop on Machine Learning and the Physical Sciences*, 2021.

[96] M. Matha and C. Morsbach. Improved self-consistency of the Reynolds stress tensor eigenspace perturbation for uncertainty quantification. *Physics of Fluids*, 35(6): 065130, 2023.

[97] M. Matha and C. Morsbach. Physically constrained eigenspace perturbation for turbulence model uncertainty estimation. *Physics of Fluids*, 36(2):025153, 2024.

[98] M. Matha, K. Kucharczyk, and C. Morsbach. Assessment of data-driven Reynolds stress tensor perturbations for uncertainty quantification of RANS turbulence models. In *AIAA AVIATION 2022 Forum*, 2022.

[99] M. Matha, K. Kucharczyk, and C. Morsbach. Evaluation of physics constrained data-driven methods for turbulence model uncertainty quantification. *Computers & Fluids*, 255:105837, 2023.

[100] M. Matha, F. Möller, C. Bode, C. Morsbach, and E. Kügeler. Advanced Methods for Assessing Flow Physics of the TU Darmstadt Compressor Stage: Part 2 - Uncertainty Quantification of RANS Turbulence Modeling. volume 12C: Turbomachinery Design Methods and CFD Modeling for Turbomachinery; Ducts, Noise, and Component Interactions of *Turbo Expo: Power for Land, Sea, and Air*, page V12CT32A013, 2024.

[101] M. Matha, F. M. Möller, C. Bode, C. Morsbach, and E. Kügeler. Advanced Methods for Assessing Flow Physics of the TU Darmstadt Compressor Stage: Uncertainty Quantification of RANS Turbulence Modeling. *Journal of Turbomachinery*, 147(8): 081004, 2025.

[102] R. E. Mayle. The Role of Laminar-Turbulent Transition in Gas Turbine Engines. volume 5: Manufacturing Materials and Metallurgy; Ceramics; Structures and Dynamics; Controls, Diagnostics and Instrumentation; Education; IGTI Scholar Award; General of *Turbo Expo: Power for Land, Sea, and Air*, page V005T17A001, 1991.

[103] F. Menter. Zonal Two Equation k-w Turbulence Models for Aerodynamic Flows. In *23rd Fluid Dynamics, Plasmadynamics, and Lasers Conference*. 1994.

[104] F. Menter, M. Kuntz, and R. Langtry. Ten years of industrial experience with the SST turbulence model. *Turbulence, Heat and Mass Transfer*, 4:625 – 632, 2003.

[105] A. A. Mishra and G. Iaccarino. Uncertainty Estimation for Reynolds-Averaged Navier–Stokes Predictions of High-Speed Aircraft Nozzle Jets. *AIAA Journal*, 55 (11):3999–4004, 2017.

[106] A. A. Mishra and G. Iaccarino. Theoretical analysis of tensor perturbations for uncertainty quantification of Reynolds averaged and subgrid scale closures. *Physics of Fluids*, 31(7):075101, 2019.

[107] A. A. Mishra, J. Mukhopadhaya, G. Iaccarino, and J. Alonso. Uncertainty Estimation Module for Turbulence Model Predictions in SU2. *AIAA Journal*, 57(3): 1066–1077, 2019.

[108] A. A. Mishra, J. Mukhopadhaya, J. Alonso, and G. Iaccarino. Design exploration and optimization under uncertainty. *Physics of Fluids*, 32(8):085106, 2020.

[109] G. Mompean, S. Gavrilakis, L. Machiels, and M. Deville. On predicting the turbulence-induced secondary flows using nonlinear k-ϵ models. *Physics of Fluids*, 8(7):1856–1868, 1996.

[110] J.-F. Monier, N. Poujol, M. Laurent, F. Gao, J. Boudet, S. Aubert, and L. Shao. LES Investigation of Boussinesq Constitutive Relation Validity in a Corner Separation Flow. volume 2C: Turbomachinery of *Turbo Expo: Power for Land, Sea, and Air*, page V02CT42A023, 2018.

[111] F. Montomoli. Future Developments. In *Uncertainty Quantification in Computational Fluid Dynamics and Aircraft Engines*, pages 195–196. Springer International Publishing, Cham, 2019.

[112] C. Morsbach. *Reynolds Stress Modelling for Turbomachinery Flow Applications*. Dissertation, German Aerospace Center, Technische Universität Darmstadt, Darmstadt, Germany, 2017.

[113] J. Mukhopadhaya, B. T. Whitehead, J. F. Quindlen, J. J. Alonso, and A. W. Cary. Multi-fidelity modeling of probabilistic aerodynamic databases for use in aerospace engineering. *International Journal for Uncertainty Quantification*, 10(5):425–447, 2020.

[114] F. M. Möller, P. G. Tucker, Z.-N. Wang, C. Bode, C. Morsbach, M. Matha, and P. Sivel. Advanced Methods for Assessing Flow Physics of the TU Darmstadt Compressor Stage: Part 1 Transitional Delayed Detached-Eddy Simulation. volume 12C: Turbomachinery Design Methods and CFD Modeling for Turbomachinery; Ducts, Noise, and Component Interactions of *Turbo Expo: Power for Land, Sea, and Air*, page V12CT32A037, 2024.

[115] H. N. Najm. Uncertainty Quantification and Polynomial Chaos Techniques in Computational Fluid Dynamics. *Annual Review of Fluid Mechanics*, 41:35–52, 2009.

[116] NASA, National Aeronautics and Space Administration. Turbulence modeling resource database. `https://turbmodels.larc.nasa.gov/index.html`, accessed April 2022.

[117] M. J. Nauta. Separation of uncertainty and variability in quantitative microbial risk assessment models. *International Journal of Food Microbiology*, 57(1):9–18, 2000.

[118] N. Nigam, S. Mohseni, J. Valverde, S. Voronin, J. Mukhopadhaya, and J. J. Alonso. A toolset for creation of multi-fidelity probabilistic aerodynamic databases. In *AIAA Scitech 2021 Forum*, page 0466, 2021.

[119] W. Oberkampf and C. Roy. *Verification and Validation in Scientific Computing.* Cambridge University Press, 2010.

[120] W. L. Oberkampf and T. G. Trucano. Verification and Validation in Computational Fluid Dynamics. *Progress in aerospace sciences*, 2002.

[121] W. L. Oberkampf, S. M. DeLand, B. M. Rutherford, K. V. Diegert, and K. F. Alvin. Error and uncertainty in modeling and simulation. *Reliability Engineering & System Safety*, 75(3):333–357, 2002.

[122] F. Pedregosa, G. Varoquaux, A. Gramfort, V. Michel, B. Thirion, O. Grisel, M. Blondel, P. Prettenhofer, R. Weiss, V. Dubourg, J. Vanderplas, A. Passos, D. Cournapeau, M. Brucher, M. Perrot, and E. Duchesnay. Scikit-learn: Machine Learning in Python. *Journal of Machine Learning Research*, 12:2825–2830, 2011.

[123] S. B. Pope. *Turbulent Flows.* Cambridge University Press, 2000.

[124] S. V. Poroseva, M. Y. Hussaini, and S. L. Woodruff. Improving the Predictive Capability of Turbulence Models Using Evidence Theory. *AIAA Journal*, 44(6): 1220–1228, 2006.

[125] N. Razaaly, G. Gori, G. Iaccarino, and P. M. Congedo. Optimization of an orc supersonic nozzle under epistemic uncertainties due to turbulence models. In *GPPS 2019-Global Power and Propulsion Society*, 2019.

[126] O. Reynolds. IV. On the dynamical theory of incompressible viscous fluids and the determination of the criterion. *Philosophical Transactions of the Royal Society of London. (A.)*, 186:123–164, 1895.

[127] P. J. Roache. *Verification and validation in computational science and engineering*, volume 895. Hermosa Albuquerque, NM, 1998.

[128] S. Rochhausen. *Modellierung des turbulenten Wärmeflusses in Turbomaschinenströmungen.* Dissertation, Dissertation Ruhr-Universität Bochum, 2018.

[129] P. Roe. Approximate Riemann solvers, parameter vectors, and difference schemes. *Journal of Computational Physics*, 43(2):357–372, 1981.

[130] R. Rossi. *Passive scalar transport in turbulent flows over a wavy wall.* Dissertation, Università degli Studi di Bologna, Bologna, Italy, 2006.

[131] U. Sahlin, I. Helle, and D. Perepolkin. “This Is What We Don’t Know”: Treating Epistemic Uncertainty in Bayesian Networks for Risk Assessment. *Integrated Environmental Assessment and Management*, 17(1):221–232, 2020.

[132] S. Salvadori. Uncertainty Quantification in CFD: The Matrix of Knowledge. In *Uncertainty Quantification in Computational Fluid Dynamics and Aircraft Engines*, pages 33–66. Springer International Publishing, Cham, 2019.

[133] R. D. Sandberg and V. Michelassi. The Current State of High-Fidelity Simulations for Main Gas Path Turbomachinery Components and Their Industrial Impact. *Flow, Turbulence and Combustion*, 102:797–848, 2019.

[134] D. Schlüß, C. Frey, and G. Ashcroft. Consistent Non-Reflecting Boundary Conditions For Both Steady And Unsteady Flow Simulations In Turbomachinery Applications. In *7th European Congress on Computational Methods in Applied Sciences And Engneering*, pages 7403–7422, 2016.

[135] F. G. Schmitt. About Boussinesq’s turbulent viscosity hypothesis: historical remarks and a direct evaluation of its validity. *Comptes Rendus Mécanique*, 335(9):617–627, 2007. Joseph Boussinesq, a Scientist of bygone days and present times.

[136] U. Schumann. Realizability of Reynolds-Stress Turbulence Models. *Physics of Fluids*, 20:721–725, 1977.

[137] D. Scott. *Multivariate density estimation: Theory, practice, and visualization: Second edition.* 2015.

[138] R. Senge, S. Bösner, K. Dembczyński, J. Haasenritter, O. Hirsch, N. Donner-Banzhoff, and E. Hüllermeier. Reliable classification: Learning classifiers that distinguish aleatoric and epistemic uncertainty. *Information Sciences*, 255:16–29, 2014.

[139] A. P. Singh and K. Duraisamy. Using field inversion to quantify functional errors in turbulence closures. *Physics of Fluids*, 28(4):045110, 2016.

[140] A. P. Singh, K. Duraisamy, and Z. J. Zhang. Augmentation of Turbulence Models Using Field Inversion and Machine Learning. In *55th AIAA Aerospace Sciences Meeting.* 2016.

[141] R. C. Smith. *Uncertainty Quantification: Theory, Implementation, and Application.* Society for Industrial and Applied Mathematics, USA, 2013.

[142] C. Soize. A comprehensive overview of a non-parametric probabilistic approach of model uncertainties for predictive models in structural dynamics. *Journal of Sound and Vibration*, 288(3):623–652, 2005. Uncertainty in structural dynamics.

[143] P. Spalart and M. Shur. On the sensitization of turbulence models to rotation and curvature. *Aerospace Science and Technology*, 1(5):297–302, 1997.

[144] A. Spencer and R. Rivlin. Isotropic integrity bases for vectors and second-order tensors. *Archive for Rational Mechanics and Analyis*, 9:45 – 63, 1962.

[145] C. G. Speziale. On turbulent secondary flows in pipes of noncircular cross-section. *International Journal of Engineering Science*, 20(7):863–872, 1982.

[146] C. G. Speziale. Analytical Methods for the Development of Reynolds-Stress Closures in Turbulence. *Annual Review of Fluid Mechanics*, 23(1):107–157, 1991.

[147] Stanford University, Aerospace Design Lab of the Department of Aeronautics and Astronautics. SU2 code (version 7.4.0 "Blackbird"). `https://github.com/su2code/SU2`, accessed December 2022.

[148] F. Stern, R. V. Wilson, H. W. Coleman, and E. G. Paterson. Comprehensive Approach to Verification and Validation of CFD Simulations—Part 1: Methodology and Procedures . *Journal of Fluids Engineering*, 123(4):793–802, 2001.

[149] W. Sutherland. LII. The viscosity of gases and molecular force. *The London, Edinburgh, and Dublin Philosophical Magazine and Journal of Science*, 36(223): 507–531, 1893.

[150] C. Tebaldi and Knutti. *Philosophical transaction of the royal society A: mathematical, physical and engineering sciences*, 365:2053–2075, 2007.

[151] L. Terentiev. *The Turbulence Closure Model Based on Linear Anisotropy Invariant Analysis.* Dissertation, Friedrich-Alexander-Universität Erlangen-Nürnberg (FAU), 2006.

[152] R. L. Thompson, A. A. Mishra, G. Iaccarino, W. Edeling, and L. Sampaio. Eigenvector perturbation methodology for uncertainty quantification of turbulence models. *Phys. Rev. Fluids*, 4:044603, 2019.

[153] B. Tracey, K. Duraisamy, and J. Alonso. Application of Supervised Learning to Quantify Uncertainties in Turbulence and Combustion Modeling. In *51st AIAA Aerospace Sciences Meeting including the New Horizons Forum and Aerospace Exposition.* 2013.

[154] P. Tucker. Computation of unsteady turbomachinery flows: Part 1 - Progress and challenges. *Progress in Aerospace Sciences*, 47(7):522–545, 2011.

[155] P. Tucker. Trends in turbomachinery turbulence treatments. *Progress in Aerospace Sciences*, 63:1–32, 2013.

[156] J. Tyacke, N. Vadlamani, W. Trojak, R. Watson, Y. Ma, and P. Tucker. Turbomachinery simulation challenges and the future. *Progress in Aerospace Sciences*, 110: 100554, 2019.

[157] G. D. van Albada, B. van Leer, and W. W. Roberts, Jr. A comparative study of computational methods in cosmic gas dynamics. *Astronomy and Astrophysics*, 108 (1):76–84, 1982.

[158] B. van Leer. Towards the ultimate conservative difference scheme. V. A second-order sequel to Godunov's method. *Journal of Computational Physics*, 32(1):101–136, 1979.

[159] J.-X. Wang, R. Sun, and H. Xiao. Quantification of uncertainties in turbulence modeling: A comparison of physics-based and random matrix theoretic approaches. *International Journal of Heat and Fluid Flow*, 62:577–592, 2016.

[160] J.-X. Wang, J. Wu, J. Ling, G. Iaccarino, and H. Xiao. A comprehensive physics-informed machine learning Framework for predictive turbulence modeling. 2018.

[161] D. Wilcox. *Turbulence modelling for CFD.* DCW Industries, La Cañada, USA, 3rd edition edition, 2006.

[162] S. Wojtkiewicz, M. Eldred, J. R. Field, A. Urbina, and J. Red-Horse. Uncertainty quantification in large computational engineering models. In *19th AIAA Applied Aerodynamics Conference*. 2001.

[163] J.-L. Wu, J.-X. Wang, and H. Xiao. A Bayesian Calibration–Prediction Method for Reducing Model-Form Uncertainties with Application in RANS Simulations. *Flow, Turbulence and Combustion*, 97:761 – 786, 2016.

[164] J.-L. Wu, J.-X. Wang, H. Xiao, and J. Ling. A Priori Assessment of Prediction Confidence for Data-Driven Turbulence Modeling. *Flow, Turbulence and Combustion*, 99(1):25–46, 2017.

[165] J.-L. Wu, H. Xiao, and E. Paterson. Physics-informed machine learning approach for augmenting turbulence models: A comprehensive framework. *Phys. Rev. Fluids*, 3:074602, 2018.

[166] J.-L. Wu, R. Sun, S. Laizet, and H. Xiao. Representation of stress tensor perturbations with application in machine-learning-assisted turbulence modeling. *Computer Methods in Applied Mechanics and Engineering*, 346:707–726, 2019.

[167] J.-L. Wu, H. Xiao, R. Sun, and Q. Wang. Reynolds-averaged Navier–Stokes equations with explicit data-driven Reynolds stress closure can be ill-conditioned. *Journal of Fluid Mechanics*, 869:553–586, 2019.

[168] K. Xia, X. He, M. Zhu, F. S. Klausmann, J. Teng, and M. Vahdati. Endwall geometric uncertainty and error on the performance of TUDA-GLR-OpenStage transonic axial compressor. *Journal of the Global Power and Propulsion Society*, 7: 113–126, 2023.

[169] H. Xiao and P. Cinnella. Quantification of model uncertainty in RANS simulations: A review. *Progress in Aerospace Sciences*, 108:1–31, 2019.

[170] H. Xiao, J.-L. Wu, J.-X. Wang, R. Sun, and C. Roy. Quantifying and reducing model-form uncertainties in Reynolds-averaged Navier–Stokes simulations: A data-driven, physics-informed Bayesian approach. *Journal of Computational Physics*, 324:115–136, 2016.

[171] H. Xiao, Wang, and R. G. Ghanem. A random matrix approach for quantifying model-form uncertainties in turbulence modeling. *Computer Methods in Applied Mechanics and Engineering*, 313:941–965, 2017.

[172] T. Zang, M. Hemsch, M. Hilburger, S. Kenny, J. Luckring, P. Maghami, S. Padula, and W. Stroud. Needs and Opportunities for Uncertainty-Based Multidisciplinary Design Methods for Aerospace Vehicles. 2002.

[173] F. Zeng, T. Zhang, D. Tang, J. Li, and C. Yan. Structural uncertainty quantification of Reynolds-averaged Navier–Stokes closures for various shock-wave/boundary layer interaction flows. *Chinese Journal of Aeronautics*, 2023.

A. RANS equations implemented and solved within this thesis

The following equations are implemented and solved in TRACE using the RANS approach:

$$\frac{\partial \rho}{\partial t} + \frac{\partial}{\partial x_i}\left(\rho U_i\right) = 0 \tag{A.1}$$

$$\frac{\partial}{\partial t}\left(\rho U_i\right) + \frac{\partial}{\partial x_j}\left(\rho U_j U_i\right) = -\frac{\partial p}{\partial x_i} + \frac{\partial}{\partial x_j}\left[2\mu\left(S_{ij} - \frac{1}{3}S_{kk}\delta_{ij}\right) - \rho\tau_{ij}\right] \tag{A.2}$$

$$\begin{aligned}\frac{\partial}{\partial t}\left[\rho\left(c_v T + \frac{U_i U_i}{2}\right)\right] + \frac{\partial}{\partial x_j}\left[U_j \rho\left(c_p T + \frac{U_i U_i}{2}\right)\right] \\ = \frac{\partial}{\partial x_j}\left[\left(\frac{c_p \mu}{\mathrm{Pr}} + \kappa_{\mathrm{T}}\right)\frac{\partial T}{\partial x_j}\right] \\ + \frac{\partial}{\partial x_j}\left[U_i\left(2\mu\left(S_{ij} - \frac{1}{3}S_{kk}\delta_{ij}\right) - \rho\tau_{ij}\right)\right] .\end{aligned} \tag{A.3}$$

The specific heat capacity at constant volume and pressure are replaced by

$$c_v = \frac{R}{\gamma - 1} \text{ and } c_p = \frac{R}{\gamma\left(\gamma - 1\right)} , \tag{A.4}$$

while the dynamic viscosity is determined using Sutherland's constants and relationship [149]

$$\mu = \mu_{\mathrm{ref}}\left(\frac{T}{T_{\mathrm{ref}}}\right)^{\frac{3}{2}}\frac{T_{\mathrm{ref}} + S_{\mathrm{ref}}}{T + S_{\mathrm{ref}}} . \tag{A.5}$$

By applying an unperturbed turbulence model, the Reynolds stress tensor τ_{ij} is determined according to Eq. (3.17) and the simplifications of neglecting the main diagonal entries, as described in Section 3.5.4. The turbulent heat conductivity κ_{T} is modeled using the turbulent Prandtl number and the introduction of the turbulent eddy viscosity. As this thesis only focuses on the steady RANS equations, the derivative with respect to the physical time $\partial\square/\partial t$ must vanish. The equations simplify to

$$\frac{\partial}{\partial x_i}\left(\rho U_i\right) = 0 \tag{A.6}$$

$$\frac{\partial}{\partial x_j}\left(\rho U_j U_i\right) = -\frac{\partial p}{\partial x_i} + \frac{\partial}{\partial x_j}\left[2\left(\mu + \mu_{\mathrm{T}}\right)\left(S_{ij} - \frac{1}{3}S_{kk}\delta_{ij}\right)\right] \tag{A.7}$$

$$\begin{aligned}\frac{\partial}{\partial x_j}\left[U_j \rho\left(c_p T + \frac{U_i U_i}{2}\right)\right] = \frac{\partial}{\partial x_j}\left[c_p\left(\frac{\mu}{\mathrm{Pr}} + \frac{\mu_{\mathrm{T}}}{\mathrm{Pr}_{\mathrm{T}}}\right)\frac{\partial T}{\partial x_j}\right] \\ + \frac{\partial}{\partial x_j}\left[U_i\left(2\left(\mu + \mu_{\mathrm{T}}\right)\left(S_{ij} - \frac{1}{3}S_{kk}\delta_{ij}\right)\right)\right] .\end{aligned} \tag{A.8}$$

If the eigenspace perturbation is used to account for the model-form uncertainties of the underlying turbulence model, the Reynolds stresses can be taken directly from the perturbed stresses obtained via perturbed eigenvalues and eigenvectors based in Eq. (3.24).

$$\frac{\partial}{\partial x_i}\left(\rho U_i\right) = 0 \tag{A.9}$$

$$\frac{\partial}{\partial x_j}\left(\rho U_j U_i\right) = -\frac{\partial p}{\partial x_i} + \frac{\partial}{\partial x_j}\left[2\mu\left(S_{ij} - \frac{1}{3}S_{kk}\delta_{ij}\right) - \rho\tau^*_{ij}\right] \tag{A.10}$$

$$\begin{aligned}\frac{\partial}{\partial x_j}\left[U_j\rho\left(c_pT + \frac{U_iU_i}{2}\right)\right] &= \frac{\partial}{\partial x_j}\left[c_p\left(\frac{\mu}{\mathrm{Pr}} + \frac{\mu_\mathrm{T}}{\mathrm{Pr}_\mathrm{T}}\right)\frac{\partial T}{\partial x_j}\right] \\ &+ \frac{\partial}{\partial x_j}\left[U_i\left(2\mu\left(S_{ij} - \frac{1}{3}S_{kk}\delta_{ij}\right) - \rho\tau^*_{ij}\right)\right] \ .\end{aligned} \tag{A.11}$$

B. Relationship between the turbulence production and the eigenspace of the Reynolds stress tensor

The turbulence production term can be expressed as the Frobenius inner product between the Reynolds stress and the strain-rate tensor

$$P_k = -\tau_{ij} \frac{\partial U_i}{\partial x_j} = -\tau_{ij} \cdot S_{ij} = -\langle \boldsymbol{\tau}, \mathbf{S} \rangle_F \ . \tag{B.1}$$

According to Lasserre [83], the bounds of the Frobenius inner product based on two hermitian tensors can be written in terms of their respective eigenvalues. Since the Reynolds stress and the strain-rate tensor are real symmetric[1], the turbulence production term is limited according to

$$P_k \in [\xi_1 \psi_3 + \xi_2 \psi_2 + \xi_3 \psi_1,\, \xi_1 \psi_1 + \xi_2 \psi_2 + \xi_3 \psi_3] \ , \tag{B.2}$$

with ξ_i (representing the eigenvalues of the Reynolds stress tensor) and ψ_i (representing the eigenvalues of the strain-rate tensor) arranged in decreasing order.
The Frobenius inner product essentially measures the alignment of two tensors. This means, that for a given set of eigenvalues ξ_i and ψ_i, the turbulence production term gets maximized, if the eigenvectors of $\boldsymbol{\tau}$ and $\mathbf{S}$ are identical. Minimum turbulence production would require the permutation of the first and last eigenvector of the Reynolds stress tensor[2], thereby aligning the eigenvectors of strain-rate and Reynolds stress tensor in the least favorable configuration.

As the relationship between eigenvalues of the anisotropy tensor and the Reynolds stress tensor is defined as

$$\boldsymbol{\lambda} = \frac{\boldsymbol{\xi}}{k} - \frac{2}{3} \ , \tag{B.3}$$

finding the limiting states of turbulence that lead to either maximum or minimum turbulence production is equivalent to determine the states that maximize $\lambda_1\psi_1 + \lambda_2\psi_2 + \lambda_3\psi_3$ and minimize $\lambda_1\psi_3 + \lambda_2\psi_2 + \lambda_3\psi_1$. Since the trace of the anisotropy vanishes per definition, $\lambda_1 + \lambda_2 + \lambda_3 = 0 \rightarrow \lambda_3 = -(\lambda_1 + \lambda_2)$. Based on the idea of Gorlé et al. [56], the ordering of the eigenvalues $\psi_1 \geq \psi_2 \geq \psi_3$ requires

$$\psi_2 = \psi_1 - \delta \tag{B.4}$$

$$\psi_3 = \psi_1 - \delta - \iota \text{ with } \delta,\iota \geq 0 \ . \tag{B.5}$$

Hence finding the maximum of $\lambda_1\psi_1 + \lambda_2\psi_2 + \lambda_3\psi_3$ can be simplified to

$$\max\left(\lambda_1\psi_1 + \lambda_2\psi_2 + \lambda_3\psi_3\right) \tag{B.6}$$

$$\xrightarrow{\text{simplifies to}} \max\left(\lambda_1\psi_1 + \lambda_2\left(\psi_1 - \delta\right) - \left(\lambda_1 + \lambda_2\right)\left(\psi_1 - \delta - \iota\right)\right) \tag{B.7}$$

$$\xrightarrow{\text{simplifies to}} \max\left(\lambda_1\left(\delta + \iota\right) + \lambda_2\iota\right) \ . \tag{B.8}$$

---

[1] Thus, they satisfy the requirement for being hermitian.

[2] Permuting the eigenvalues directly would violate $\xi_1 \geq \xi_2 \geq \xi_3$; however, the identical effect with respect to the obtained tensor ellipsoid (see e.g. Fig. 6.4a) can be achieved by permuting the eigenvectors.

Inserting the eigenvalues of the anisotropy tensor at the limiting states of turbulence (cf. Table 5.1) into the expression of Eq. (B.8) leads to:

- 1C → $\frac{4}{3}\delta + \frac{2}{3}\iota$
- 2C → $\frac{1}{3}\delta + \frac{2}{3}\iota$
- 3C → 0 .

As Eq. (B.8) aims for the maximum, $\frac{4}{3}\delta+\frac{2}{3}\iota \geq \frac{1}{3}\delta+\frac{2}{3}\iota \geq 0 \rightarrow 1\mathrm{C} \geq 2\mathrm{C} \geq 3\mathrm{C}$. Consequently, 1C turbulence is able to maximizes the turbulence production term, if the Reynolds stress and strain-rate tensor share identical eigenvectors, while at the isotropic limit (3C) the smallest value of turbulence production is expected[3].
In similar manner, finding the minimum of $\lambda_1\psi_3 + \lambda_2\psi_2 + \lambda_3\psi_1$ is equivalent to

$$\min\left(\lambda_1\psi_3 + \lambda_2\psi_2 + \lambda_3\psi_1\right) \tag{B.9}$$

$$\xrightarrow{\text{simplifies to}} \min\left(\lambda_1\left(\psi_1 - \delta - \iota\right) + \lambda_2\left(\psi_1 - \delta\right) - \left(\lambda_1 + \lambda_2\right)\psi_1\right) \tag{B.10}$$

$$\xrightarrow{\text{simplifies to}} \min\left(-\lambda_1\left(\delta + \iota\right) - \lambda_2\delta\right) \ . \tag{B.11}$$

Inserting the eigenvalues of the anisotropy tensor at the limiting states of turbulence (cf. Table 5.1) into the expression of Eq. (B.11) leads to:

- 1C → $-\frac{2}{3}\delta - \frac{4}{3}\iota$
- 2C → $-\frac{2}{3}\delta - \frac{1}{3}\iota$
- 3C → 0 .

As Eq. (B.11) aims for the minimum, $-\frac{2}{3}\delta - \frac{4}{3}\iota \leq -\frac{2}{3}\delta - \frac{1}{3}\iota \leq 0 \rightarrow 1\mathrm{C} \leq 2\mathrm{C} \leq 3\mathrm{C}$. Thus, 1C turbulence creates the smallest (potentially negative) turbulence production term, if the first and third eigenvectors of the Reynolds stress tensor are permuted.

In addition, Chapter 6, in particular Fig. 6.3, highlights, that the amount of turbulence production changes linearly when altering the state of the eigenvalues on a parallel trajectory to the connecting line from state 1C to 3C for the example of a fully developed boundary layer flow (the contour level of Fig. 6.3 are orthogonal on the connecting line from 1C to 3C). As the sampled states of the barycentric coordinates in Fig. 3.6a are chosen such, that they also form orthogonal lines on 1C-3C, e.g. sample 28, 38, 49 or samples 6, 12, 19 and 27, combined with the fact, that the converging-diverging channel contains boundary layer like flows in large parts of the domain, one can also observe identical turbulence production terms at these lines of samples. The resulting streamwise velocity profiles in Fig. 3.6b show the strong impact of the turbulence production term, as the profiles belonging the states on these perpendicular lines show identical results, although the entries of the perturbed Reynolds stress tensor differ due to the different states of anisotropy. However, this observation was only possible due to the boundary layer like flow topology in the converging-diverging channel.

---

[3] It is disagreed with the conclusions drawn by Gorlé et al. [56], who argued, that 3C always leads to zero turbulence production. Although it is shown in Section 6.3 that zero turbulence production occures at 3C for certain specific flow scenarios.

C. Physical rationale of the eigenspace perturbations of the Reynolds stress tensor

The theoretical foundation of the EPF was initially described by Mishra and Iaccarino [106]. This section tries to clarify and extend the derivations for compressible flows.

In general, the anisotropy tensor can be decomposed into eigenvalues and eigenvectors according to

$$a_{ij} = v_{in}\Lambda_{nl}v_{jl} \ . \tag{C.1}$$

If the Boussinesq assumption in Eq. (3.17) is applied for LEVMs, the anisotropy is defined via the strain-rate tensor and its eigenspace

$$\begin{aligned} a_{ij} &= -2\frac{\nu_\mathrm{T}}{k}\left(S_{ij} - \frac{1}{3}S_{kk}\delta_{ij}\right) && \text{(C.2)} \\ &= -2\frac{\nu_\mathrm{T}}{k}S^-_{ij} && \text{(C.3)} \\ &= -2\frac{\nu_\mathrm{T}}{k}v_{in}\boldsymbol{\Psi}^-_{nl}v_{jl} \ , && \text{(C.4)} \end{aligned}$$

whereby S^-_{ij} represents the traceless strain-rate tensor and $\boldsymbol{\Psi}^-$ consists of the strain-rate tensor's eigenvalues $\psi^-_i = \psi_i - \frac{S_{kk}}{3}$. While the relationship between the eigenvalues of the anisotropy and the traceless strain-rate tensor is defined as

$$\lambda_i = -2\frac{\nu_\mathrm{T}}{k}\psi^-_{(4-i)} \text{ for } i = 1,2,3 \ , \tag{C.5}$$

given the ordered anisotropy tensor's eigenvectors $\boldsymbol{v_i}$.

C.1. Eigenvalue perturbation

The anisotropy tensor under eigenvalue perturbation (according to Eq. (3.25)) can be written as

$$\begin{aligned} \mathbf{a}^* &= \mathbf{v}\boldsymbol{\Lambda}^*\mathbf{v}^T && \text{(C.6)} \\ &= \mathbf{v}\left(\left(1-\Delta_B\right)\boldsymbol{\Lambda} + \Delta_B\begin{pmatrix} \lambda_{(t)_1} & 0 & 0 \\ 0 & \lambda_{(t)_2} & 0 \\ 0 & 0 & \lambda_{(t)_3} \end{pmatrix}\right)\mathbf{v}^T && \text{(C.7)} \\ &= \left(1-\Delta_B\right)\mathbf{v}\boldsymbol{\Lambda}\mathbf{v}^T + \Delta_B\mathbf{v}\boldsymbol{\Lambda}_{(\mathrm{t})}\mathbf{v}^T && \text{(C.8)} \\ &= -2\frac{\nu_\mathrm{T}}{k}\left(1-\Delta_B\right)\mathbf{v}\boldsymbol{\Psi}^-\mathbf{v}^T + \Delta_B\mathbf{v}\boldsymbol{\Lambda}_{(\mathrm{t})}\mathbf{v}^T && \text{(C.9)} \\ &= -2\frac{\nu_\mathrm{T}}{k}\left(1-\Delta_B\right)\mathbf{S}^- + \Delta_B\mathbf{T} \ . && \text{(C.10)} \end{aligned}$$

In the principal axes of the strain-rate tensor (eigenvectors) the perturbed anisotropy tensor can be expressed via

$$\mathbf{a}^*|_{\mathrm{PCS}_\mathbf{S}} = -2\frac{\nu_\mathrm{T}}{k}\left(1-\Delta_B\right)\boldsymbol{\Psi}^- + \Delta_B\boldsymbol{\Lambda}_{(\mathrm{t})} \ . \tag{C.11}$$

A tensor $K_{ij} = \frac{T_{ij}}{S^-_{ij}} = v_{in}\Theta_{nl}v_{jl}$ is introduced, which has to have identical eigendirections, resulting in $\mathbf{K}$, $\mathbf{T}$ and $\mathbf{S}$ being simultaneously diagonalizable. Hence, the relationship between the diagonal eigenvalue tensors is

$$\boldsymbol{\Theta} = \frac{\boldsymbol{\Lambda}_{(\mathrm{t})}}{\boldsymbol{\Psi}^-} \ , \tag{C.12}$$

which is only valid if $\psi^-_k \neq 0$. Consequently, the perturbed Reynolds stress anisotropy tensor in the principal axes of the strain-rate tensor can be expressed as

$$\mathbf{a}^*|_{\mathrm{PCS}_\mathbf{S}} = \underbrace{-2\frac{\nu_\mathrm{T}}{k}\left(1-\Delta_B\right)}_{\text{scalar}}\boldsymbol{\Psi}^- + \underbrace{\Delta_B\boldsymbol{\Theta}}_{\text{diagonal tensor}}\boldsymbol{\Psi}^- \ . \tag{C.13}$$

This expression shows that the eigenvalue perturbation is able to assign different scalars (comparable to the turbulent eddy viscosity) along the orthogonal axes of the Reynolds stress tensor, changing the turbulent medium to an orthotropic one. However, this is true for any perturbation of the eigenvalues with the except of approaching the 3C state, as $\boldsymbol{\Theta}$ results being the zero matrix.

C.2. Eigenvector perturbation

The anisotropy tensor under eigenvector perturbation (according to Eq. (3.28)) can be written as

$$\begin{aligned}
\mathbf{a}^* &= \mathbf{v}^*\boldsymbol{\Lambda}\left(\mathbf{v}^*\right)^T && \text{(C.14)}\\
&= \mathbf{R}\mathbf{v}\boldsymbol{\Lambda}\left(\mathbf{R}\mathbf{v}\right)^T && \text{(C.15)}\\
&= \mathbf{R}\mathbf{v}\boldsymbol{\Lambda}\mathbf{v}^T\mathbf{R}^T && \text{(C.16)}\\
&= -2\frac{\nu_\mathrm{T}}{k}\mathbf{R}\mathbf{v}\boldsymbol{\Psi}^-\mathbf{v}^T\mathbf{R}^T \ . && \text{(C.17)}
\end{aligned}$$

In the principal axes of the strain-rate tensor $\mathbf{S}$ defined by the unperturbed eigenvectors $\mathbf{v}$, the anisotropy tensor becomes

$$\begin{aligned}
\mathbf{a}^*|_{\mathrm{PCS}_\mathbf{S}} &= -2\frac{\nu_\mathrm{T}}{k}\mathbf{v}^T\mathbf{R}\mathbf{v}\boldsymbol{\Psi}^-\mathbf{v}^T\mathbf{R}^T\mathbf{v} && \text{(C.18)}\\
&= -2\frac{\nu_\mathrm{T}}{k}\mathbf{v}^T\mathbf{R}\mathbf{v}\boldsymbol{\Psi}^-\left(\mathbf{v}^T\mathbf{R}\mathbf{v}\right)^T && \text{(C.19)}\\
&= -2\frac{\nu_\mathrm{T}}{k}\mathbf{G}\boldsymbol{\Psi}^-\mathbf{G}^T \ . && \text{(C.20)}
\end{aligned}$$

The tensor $\mathbf{G}$ represents the tensor containing the rotated eigenvectors in the original principal axes. As $\mathbf{G}$ is typically not a diagonal matrix, the anisotropy tensor in the principal axes of the strain-rate tensor contains off-diagonal elements under eigenvector perturbation. Consequently, the relationship between the strain-rate tensor and the anisotropy tensor shows that the eigenvector perturbation turns the turbulence model into an anisotropic eddy viscosity model.

Curriculum Vitae

Personal Data

NAME	Marcel Matha
DATE OF BIRTH	05 October 1991
PLACE OF BIRTH	Bad Mergentheim, Germany
NATIONALITY	German

Employment

Since 10/2017	Research assistant at INSTITUTE OF PROPULSION TECHNOLOGY *German Aerospace Center (DLR)* Department *Numerical Methods* Cologne, Germany
10/2016 - 03/2017	Working Student at DAIMLER AG Sindelfingen, Germany
10/2015 - 12/2015	Intern at SAP SE, Business Unit Aerospace and Defense Walldorf, Germany
04/2014 - 09/2014	Intern at TESAT SPACECOM GMBH & CO. KG Backnang, Germany
10/2013 - 09/2016 (intermittent)	Student assistant at INSTITUTE OF AIRCRAFT PROPULSION SYSTEMS *University of Stuttgart* Stuttgart, Germany

Education

04/2015 - 10/2017	**Master of Science** in **AEROSPACE ENGINEERING** **University of Stuttgart**, Stuttgart, Germany
01/2016 - 05/2016	**Semester abroad** at **FACULTY OF ENGINEERING** **National University of Singapore**, Singapore
10/2011 - 03/2015	**Bachelor of Science** in **AEROSPACE ENGINEERING** **University of Stuttgart**, Stuttgart, Germany
02/2002 - 05/2011	**Abitur** **Martin-Schleyer Gymnasium**, Lauda-Königshofen, Germany